

DTIC FILE COPY

4

RADC -TR-89-8, Vol I (of two)
Final Technical Report
April 1989



AD-A213 895

SCANNABLE MILLIMETER WAVE ARRAYS

Polytechnic University

Arthur A. Oliner

APPROVED FOR PUBLIC RELEASE; DISTRIBUTION UNLIMITED.

DTIC
ELECTE
OCT 30 1989
S Q E D

ROME AIR DEVELOPMENT CENTER
Air Force Systems Command
Griffiss Air Force Base, NY 13441-5700

89 10 30 116

This report has been reviewed by the RADC Public Affairs Division (PA) and is releasable to the National Technical Information Service (NTIS). At NTIS it will be releasable to the general public, including foreign nations.

RADC-TR-89-8, Vol I (of two) has been reviewed and is approved for publication.

APPROVED:



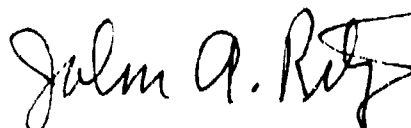
HANS P. STEYSKAL
Project Engineer

APPROVED:



JOHN K. SCHINDLER
Director of Electromagnetics

FOR THE COMMANDER:



JOHN A. RITZ
Directorate of Plans & Programs

If your address has changed or if you wish to be removed from the RADC mailing list, or if the addressee is no longer employed by your organization, please notify RADC (EEAA) Hanscom AFB MA 01731-5000. This will assist us in maintaining a current mailing list.

Do not return copies of this report unless contractual obligations or notices on a specific document require that it be returned.

UNCLASSIFIED

SECURITY CLASSIFICATION OF THIS PAGE

REPORT DOCUMENTATION PAGE				Form Approved OMB No. 0704-0188	
1a. REPORT SECURITY CLASSIFICATION UNCLASSIFIED			1b. RESTRICTIVE MARKINGS N/A		
2a. SECURITY CLASSIFICATION AUTHORITY N/A			3. DISTRIBUTION/AVAILABILITY OF REPORT Approved for public release; distribution unlimited.		
2b. DECLASSIFICATION/DOWNGRADING SCHEDULE N/A					
4. PERFORMING ORGANIZATION REPORT NUMBER(S) POLY-WRI-1543-88			5. MONITORING ORGANIZATION REPORT NUMBER(S) RADC-TR-89-8, Vol I (of two)		
6a. NAME OF PERFORMING ORGANIZATION Polytechnic University		6b. OFFICE SYMBOL (If applicable)	7a. NAME OF MONITORING ORGANIZATION Rome Air Development Center (EEAA)		
6c. ADDRESS (City, State, and ZIP Code) Weber Research Institute 333 Jay Street Brooklyn NY 11201			7b. ADDRESS (City, State, and ZIP Code) Hanscom AFB MA 01731-5000		
8a. NAME OF FUNDING/SPONSORING ORGANIZATION Rome Air Development Center		8b. OFFICE SYMBOL (If applicable) EEAA	9. PROCUREMENT INSTRUMENT IDENTIFICATION NUMBER F19628-84-K-0025		
8c. ADDRESS (City, State, and ZIP Code) Hanscom AFB MA 01731-5000			10. SOURCE OF FUNDING NUMBERS		
	PROGRAM ELEMENT NO. 61102F	PROJECT NO. 2305	TASK NO. J3	WORK UNIT ACCESSION NO. 44	
11. TITLE (Include Security Classification) SCANNABLE MILLIMETER WAVE ARRAYS					
12. PERSONAL AUTHOR(S) Arthur A. Oliner					
13a. TYPE OF REPORT Final		13b. TIME COVERED FROM Apr 84 to Jan 87		14. DATE OF REPORT (Year, Month, Day) April 1989	
15. PAGE COUNT 298					
16. SUPPLEMENTARY NOTATION					
17. COSATI CODES			18. SUBJECT TERMS (Continue on reverse if necessary and identify by block number)		
FIELD	GROUP	SUB-GROUP	Millimeter waves, antennas, leaky waves, scanning arrays, printed circuit arrays, nonradiative dielectric (NRD) guide, groove guide, microstrip line.		
09	05				
09	01				
19. ABSTRACT (Continue on reverse if necessary and identify by block number)					
<p>The complexity usually associated with scanning arrays at millimeter wavelengths produces fabrication difficulties, so that alternative methods are needed that employ simpler structures. This Final Report describes such an alternative scanning approach, and presents a group of new and simpler radiating structures suitable for millimeter-wave applications.</p> <p>The new class of scanning arrays described here achieves scanning in two dimensions by creating a one dimensional array of leaky-wave line-source antennas. The individual line sources are fed from one end and are scanned in elevation by electronic means or by varying the frequency. Scanning in the cross plane, and therefore in azimuth, is produced by phase shifters arranged in the feed structure of the one-dimensional array of line sources.</p> <p>Within the sector of space over which the arrays can be scanned, the radiation has negligible cross polarization, no blind spots and no grating lobes. These are significant, and also</p> <p style="text-align: right;">(Cont'd)</p>					
20. DISTRIBUTION/AVAILABILITY OF ABSTRACT <input checked="" type="checkbox"/> UNCLASSIFIED/UNLIMITED <input type="checkbox"/> SAME AS RPT. <input type="checkbox"/> DTIC USERS			21. ABSTRACT SECURITY CLASSIFICATION UNCLASSIFIED		
22a. NAME OF RESPONSIBLE INDIVIDUAL HANS STEYKAL			22b. TELEPHONE (Include Area Code) (617) 377-2052		22c. OFFICE SYMBOL RADC/EEAA

DD Form 1473, JUN 86

Previous editions are obsolete.

SECURITY CLASSIFICATION OF THIS PAGE

UNCLASSIFIED

UNCLASSIFIED

Block 19 (Cont'd)

unusual advantages. The novel features in the study reported here relate mainly to the new structures employed for the individual leaky-wave line sources and their combination into arrays, but also to analyses of the interactive effects produced when scanning occurs in both planes simultaneously.

The analyses of the various antenna structures are believed to be accurate, and for most of the antennas they are notable for resulting in transverse equivalent networks in which all the elements are in closed form, so that the dispersion relations for the propagation properties of the leaky-wave structures are also in closed form. It should be added that for all the array structures the analyses take all mutual coupling effects into account.

Although these studies are predominantly theoretical in nature, sets of careful measurements were made for two of the novel leaky-wave line-source antennas: the foreshortened NRD guide structure and the offset-groove-guide antenna. The agreement with the theoretical calculations was excellent in both cases.

In the Final Report, seven different novel antennas are described, of which four are leaky-wave line sources that scan in elevation, and three are arrays that scan in two dimensions. They represent examples of the new class of scannable antennas that are simple in configuration and suitable for millimeter wavelengths.

This Final Report is composed of 12 Chapters, of which the first is an introduction and summary, the second discusses some general features of our approach to the analysis of arrays, and the twelfth contains the list of references. Chapters III through XI discuss in detail our comprehensive studies on the various specific antennas; the material is presented under three broad categories; NRD guide antennas, groove guide antennas, and printed-circuit antennas. Because of the binding problems created by the size of this report, it is being printed in a two-volume format.

Accession For	
NTIS CRA&I	<input checked="checked" type="checkbox"/>
DTIC TAB	<input checked="checked" type="checkbox"/>
Unannounced	<input type="checkbox"/>
Justification	
By	
Distribution/	
Availability Codes	
Dist	Avail and/or Special
A-1	



UNCLASSIFIED

TABLE OF CONTENTS

I.	SUMMARY OF PROGRAM GOALS AND ACCOMPLISHMENTS	1
A.	PROGRAM GOALS AND APPROACHES	1
B.	OVERVIEW OF THE NEW ANTENNA STRUCTURES	6
1.	Background	6
2.	The New Antenna Structures	7
a.	NRD Guide Antennas	10
b.	Groove Guide Antennas	13
c.	Printed-Circuit Antennas	17
II.	ARRAYS OF LEAKY-WAVE LINE SOURCES	25
A.	TYPICAL ARRAY STRUCTURES AND THEIR UNIT CELLS	26
B.	PROPERTIES OF THE UNIT CELL WAVEGUIDE	36
C.	THE MODE FUNCTIONS FOR THE UNIT CELL WAVEGUIDE	42
D.	ANALYTICAL EXPRESSIONS FOR RADIATION PATTERNS OF LEAKY-WAVE ANTENNAS	44
	NRD GUIDE ANTENNAS	47
III.	THE ASYMMETRIC NRD GUIDE LEAKY-WAVE LINE SOURCE	51
A.	DESCRIPTION OF THE ASYMMETRIC LEAKY-WAVE ANTENNA	54
B.	LEAKAGE WITHIN THE PARALLEL-PLATE REGION	56
1.	Analysis and Numerical Results	56
2.	Behavior Near Cutoff	65
C.	ANTENNA WITH FINITE SIDE WALLS: COUPLING EFFECTS	71
1.	The Transverse Equivalent Network	71
2.	Coupling Effects in the Propagation Characteristics	74
a.	Qualitative Features	74
b.	Quantitative Results	77

IV.	SCANNABLE ARRAY OF NRD GUIDE LINE SOURCES	91
A.	DESCRIPTION AND OPERATION OF THE ARRAY	93
B.	ANALYSIS OF THE ARRAY	96
	1. Unit Cell Wavenumber Relations	96
	2. Transverse Equivalent Network of the Unit Cell	99
C.	PERFORMANCE FEATURES	104
	1. Behavior When the Cross-Plane Scan Angle is Zero	104
	2. Behavior as the Cross-Plane Scan Angle is Varied	104
	a. Coupling with Channel-Guide Leaky Modes	105
	b. Departure from Conical Scan	125
	c. Absence of Blindness Effects	128
	GROOVE GUIDE ANTENNAS	139
V.	A NEW EQUIVALENT NETWORK FOR THE CONSTITUENT E-PLANE TEE JUNCTION	143
A.	THE NEW EQUIVALENT NETWORK	144
B.	COMPARISONS WITH MEASUREMENTS	150
	1. Comparisons for a Slit-Coupled E-Plane Tee Junction	150
	2. Comparisons for a Slit That Couples Two Parallel Guides in E-Plane Fashion	154
VI.	THE L-SHAPED LEAKY-WAVE LINE SOURCE	163
A.	DOMINANT MODE AND HIGHER MODE PROPERTIES OF GROOVE GUIDE: A SUMMARY	164
	1. The Dominant Mode	164
	2. The Higher Modes, Which Are All Leaky	164
B.	THE L-SHAPED ANTENNA	169
	1. Theoretical Description	169
	2. Numerical Results	177

VII.	THE OFFSET-GROOVE-GUIDE LEAKY-WAVE LINE SOURCE	187
A.	PRINCIPLES AND THEORETICAL DESCRIPTION	189
	1. Structure and Principle of Operation	189
	2. The Transverse Equivalent Network	192
	3. The Dispersion Relation	196
B.	NUMERICAL RESULTS FOR THE PROPAGATION BEHAVIOR	198
	1. Structures with a Flatter Aspect Ratio	198
	2. Aspect Ratio Equal to that of Rectangular Waveguide	204
	3. Variations with Frequency	208
C.	COMPARISON OF RESULTS WITH AN ALTERNATIVE THEORETICAL APPROACH	215
D.	EFFECTS DUE TO FINITE STUB LENGTH	220
	1. Modification of the Dispersion Relation	221
	2. Coupling with Another Leaky Mode	223
	a. Variations with Stub Length	224
	b. Variations with Stub Offset	229
	c. Variations with Frequency	235
VIII.	MEASUREMENTS AT MILLIMETER WAVE- LENGTHS ON THE OFFSET-GROOVE-GUIDE ANTENNA	243
A.	THE STRUCTURE UNDER MEASUREMENT	244
B.	MEASUREMENT METHODS	247
	1. Wavenumbers	247
	2. Radiation Patterns	247
C.	WAVENUMBER DATA	253
	1. Preliminary Theoretical Calculations	253
	2. Comparisons Between Theory and Measurements	256
	3. Design Considerations for Tapered Apertures for Sidelobe Control	258
	4. Vector Field Distributions	266

D.	RADIATION PATTERNS	270
	1. Calculations for the Near Field Patterns	270
	2. Comparisons Between Theory and Measurement	271
	PRINTED-CIRCUIT ANTENNAS	285
IX.	MICROSTRIP LINE LEAKY-WAVE STRIP ANTENNAS	289
A.	BACKGROUND AND MOTIVATION	289
B.	THE NATURE OF THE LEAKAGE FROM HIGHER MODES ON MICROSTRIP LINE	292
	1. The Radiation Region and Leaky Modes	292
	2. The Two Forms of Leakage	294
	3. The Ratio of Powers in the Surface Wave and the Space Wave	296
C.	ANALYSIS AND PROPERTIES OF THE LEAKY MODES	304
	1. Derivation of Accurate Expression for the Propagation Characteristics	304
	2. Numerical Comparisons with the Literature	310
D.	STEEPEST-DESCENT PLANE FORMULATIONS	315
	1. Motivation	315
	2. Review of Some Properties of the Steepest-Descent Representation	316
	3. Steepest-Descent Plane Plots for Microstrip Line Higher Modes	324
	a. Microstrip Line with Open Top Using the Cross-Section Dimensions of Boukamp and Jansen	325
	b. The Boukamp-Jansen Structure with a Covered Top	334
	c. The Menzel Antenna Structure	336
E.	INVESTIGATIONS RELATING TO MENZEL'S ANTENNA	341
	1. Description of Menzel's Antenna	341
	2. Analysis of Menzel's Antenna in Leaky Mode Terms	343
	3. Parametric Dependences for Antenna Design	350
	4. Performance When Properly Designed as a Leaky-Wave Antenna	355

X.	A NOVEL ARRAY OF PRINTED-CIRCUIT UNIFORM LEAKY-WAVE LINE SOURCES	367
A.	DESCRIPTION AND OPERATION OF THE ARRAY	369
	1. Evolution of the Array Structure	369
	2. Principle of Operation	371
B.	DERIVATION OF THE EQUIVALENT NETWORK FOR THE CONSTITUENT TEE JUNCTION	374
	1. Can the Network Form be Symmetrical?	375
	2. How the Dielectric Filling in the Main Guide is Taken into Account	376
	a. Symmetric Magnetic Field Excitation	377
	b. Symmetric Electric Field Excitation	380
	c. Small Aperture Calculation for B_a/Y_o	382
	3. Putting Together the Remaining Pieces	385
	a. The Stub Guide Contribution B_s/Y_o	385
	b. The Turns Ratio n_{cs}	387
	c. The Complete Network	390
C.	TRANSVERSE EQUIVALENT NETWORK FOR THE ARRAY OF PRINTED-CIRCUIT LINE SOURCES	393
	1. Unit Cell Properties	393
	2. Complete Transverse Equivalent Network	396
	3. The Dispersion Relation	398
D.	PERFORMANCE WITHOUT CROSS-PLANE SCAN	401
	1. Variations with Dimensional Ratios	402
	2. Variations with Frequency	419
E.	EFFECTS OF CROSS-PLANE SCANNING	434
	1. Small Cross-Plane Scan Angles	437
	2. Large Cross-Plane Scan Angles	443
	a. Variations with Stub Guide Height	443
	b. Variations with Slit Location	446
	3. Variations with Imposed Phase Shift	449
	a. Wavenumber Variations	449
	b. Conical Scan Dependence	456

XI.	A NOVEL ARRAY OF PRINTED-CIRCUIT PERIODIC LEAKY-WAVE LINE SOURCES	465
A.	STRUCTURE AND PRINCIPLE OF OPERATION	467
B.	GENERAL PERFORMANCE CONSTRAINTS USING THE k_o vs. β_n DIAGRAM	471
	1. Description of the k_o vs. β_n Diagram	471
	2. Some Constraint Conditions	474
C.	TRANSVERSE EQUIVALENT NETWORK	479
	1. Equivalent Network for the Array of Periodic Slits on a Metal-Coated Air-Dielectric Interface	479
	2. The Full Transverse Equivalent Network	484
D.	ELEVATION ANGLE PERFORMANCE WITHOUT CROSS SCAN	489
E.	EFFECTS OF CROSS-PLANE SCANNING	501
XII.	REFERENCES	523

I.	SUMMARY OF PROGRAM GOALS AND ACCOMPLISHMENTS	1
A.	PROGRAM GOALS AND APPROACHES	1
B.	OVERVIEW OF THE NEW ANTENNA STRUCTURES	6
	1. Background	6
	2. The New Antenna Structures	7
	a. NRD Guide Antennas	10
	b. Groove Guide Antennas	13
	c. Printed-Circuit Antennas	17

I. SUMMARY OF PROGRAM GOALS AND ACCOMPLISHMENTS

A. PROGRAM GOALS AND APPROACHES

Scanning arrays for millimeter wavelengths involve special problems because of the small sizes of the constituents of the array. The complexity usually associated with scanning arrays, and particularly two-dimensional phased arrays, produce fabrication difficulties, so that alternative methods that involve simpler structures should be investigated. The primary goal of this program is to devise and examine new scanning methods and/or new radiating structures that are simpler in configuration and thus suitable for millimeter-wave applications. This program has therefore focused on an alternative, but not new, approach to two-dimensional scanning, and has devised and examined *new structures* that employ this approach and are simple in configuration.

This *alternative approach* is to achieve scanning in two dimensions by creating a one-dimensional array of line-source antennas. The individual line sources, fed from one end, are *leaky-wave antennas* that are scanned electronically or electro-mechanically, or by frequency scanning if that is permitted by the system. Such scanning would be essentially in elevation. Scanning in the cross plane, and therefore in azimuth, is produced by *phase shifters* arranged in the feed structure of the one-dimensional array of line sources.

As with any class of antennas, the antennas devised and studied on this program, and described here, are most suitable for certain applications and unsuitable for others. They also have certain very interesting advantages as well as limitations, as we discuss below. It may be mentioned now that the arrays can be scanned over a limited sector of space, but within that sector the radiation has *pure single polarization*, with *no blind spots* and with *no grating lobes*.

The novel contributions in this program relate to the structures employed for the individual leaky-wave line sources and their combination into arrays, and also to the studies of the interactive effects produced when scanning occurs in both planes simultaneously. In addition, several basic new features of interest to fundamental electromagnetics emerged in the course of the investigations; among them are the nature of the leakage from higher modes on microstrip line, which is studied with the help of the steepest-descent plane, and unexpected coupling effects between two types of leaky mode, which are explored analytically here in some detail for perhaps the first time.

The analyses of the various structures are believed to be accurate, and for most of the structures they are notable for resulting in transverse equivalent networks in which the elements are all expressed in *closed form*, so that the dispersion relations for the propagation properties of the structures are also in closed form. As a byproduct of the analyses of the antennas based on groove guide, we have developed a new and improved network for an E-plane tee junction for which the parameters are both accurate and in very simple closed form. It should be added that for all of the array structures the analyses take *all mutual coupling effects* into account.

The studies are predominantly *theoretical* in nature. In one case, however, for the offset-groove-guide line source, a novel leaky-wave antenna derived from the groove guide, a set of careful *measurements* were made that showed excellent agreement with our theoretical calculations. These experiments are also described in this report. (Careful measurements that also agreed very well with our theoretical results were made previously on another of our leaky-wave line sources, the foreshortened NRD guide antenna, which was discussed in detail in the Final Report on the predecessor contract. That material has since been published.)

Most of the novel leaky-wave line sources investigated on this program have two principal features. *First*, they form longitudinally *continuous apertures*, making the antennas relatively simple to construct. All but one of the antennas, the last one to be described in this report, have that feature. The remaining antenna involves a printed-circuit periodic array of metal strips, where the periodicity permits some added flexibility in performance while retaining the simplicity desired. *Second*, they are based on *low-loss waveguides* so that the leakage loss (which produces the radiation) dominates over the intrinsic (metal and/or dielectric) loss. Two low-loss waveguides were selected on which to base several novel leaky-wave antennas. These waveguides were the groove guide and the NRD (nonradiative dielectric) guide, which is a new variant of H guide. The printed-circuit arrays to be described have slightly more loss but they possess other important advantages.

In this Final Report, we discuss in detail *seven* different novel antennas, of which four are leaky-wave line sources that scan in elevation, and three are arrays that scan in two dimensions. These antennas are grouped into three broad categories: NRD Guide Antennas, Groove Guide Antennas, and Printed-Circuit Antennas. An overview of the structures of these antennas and some of their principal features is presented in the next section, B. Details of how these antennas operate, together with their analyses and performance results, are contained in Chaps. III and IV for the NRD guide antennas, Chaps. V through VIII for the groove guide antennas, and

Chaps. IX through XI for the printed-circuit antennas. All references are grouped together in Chap. XII.

The two-dimensional arrays are comprised of linear arrays of leaky-wave line sources, which themselves yield scannable narrow beams in elevation in the longitudinal plane, with wide fan beams in the cross plane. When these line sources are arranged parallel to each other in an array, the array can then produce a pencil beam scannable in two dimensions within a restricted region of space. Scanning in the cross plane in phased-array fashion is achieved by placing a given phase shift between successive line sources. This mode of operation is common to all three of the arrays discussed in this report.

The analyses for all of the arrays employ a *unit cell* for the external periodic environment, in which phase-shift walls take into account the effects of scan in the cross plane. The individual line sources are analyzed using a transverse equivalent network, in which the radiating open end is representative of the environment of a single lone line source. In the two-dimensional array, the environment of the line source is very different, and the unit cell now becomes the termination on the transverse equivalent network. That unit cell termination changes with scan and automatically takes into account all mutual coupling effects; the resonances of the complete network reveal the array performance as a function of scan angle in both scan planes. Because the approach is common to all the arrays analyzed here, and because it is not familiar to everyone, the unit-cell approach is described in some detail in Chap. II. Included in that section are some array structures and their unit cells, some properties of the unit cell waveguide, and some basic relations for leaky-wave line sources.

The present contract, for which this Final Report is written, covers the 34-month period ending January 31, 1987. The study of leaky-wave line sources based on low-loss waveguides was actually begun on the predecessor contract, Contract No. F19628-81-K-0044. Under that contract, the properties of the NRD guide and the groove guide were examined, including the leaky higher mode spectrum of groove guide, and several leaky-wave line sources based on these guides were analyzed in detail. Complete papers on the two most important of these line-source antennas have since been published. They are referred to in Sec. B below. The line-source antennas described in the present report are different from the previous ones, and are improvements over them for reasons given under B.

The results achieved during the first half of the present contract period have been presented in the Mid-Period Report, dated January 31, 1986. Since that report was

not widely distributed, two major portions of that report are included in context in the present Final Report, and some new information obtained since that time on those topics has been incorporated as well. The sections in the present report corresponding to those portions are Chap. III, on the asymmetric NRD guide leaky-wave line source, and Chap. IX, on microstrip leaky-wave strip antennas.

It is a pleasure to acknowledge the valuable contributions made by colleagues and students to this overall study. As is evident from the Table of Contents, the large scope of this program was made possible only through their devoted interest and collaboration. These collaborators were Professor P. Lampariello of the University of Rome "La Sapienza," Italy, and his student F. Frezza; Professor H. Shigesawa of Doshisha University, Kyoto, Japan, and his colleague, Dr. M. Tsuji; Professor S. T. Peng of the New York Institute of Technology and his students; Professor Xu Shanjia of the University of Science and Technology of China, Hefei, Anhui, China, who was a Visiting Scholar at Polytechnic University; Dr. K. S. Lee, a former Ph.D. student who is now at Texas Instruments, Dallas; and Dr. M. Guglielmi, a former Ph.D. student who is now Assistant Professor at Polytechnic University. The specific areas of collaboration for each are indicated in each of the respective chapters. In connection with the foreshortened NRD guide leaky-wave line-source antenna, completed on the predecessor contract, I wish to acknowledge the important contributions of Dr. A. Sanchez, a former Ph.D. student who is now with RCA/Astro-Space Division, Princeton, and Professor Q. Han, who was a Visiting Scholar but has since returned to the Huazhong (Central China) University of Science and Technology, Wuhan, China. Aside from the students, these collaborators made their contributions at no cost to the contract. The full scope of the effort was not evident when the proposal was submitted; as a result, some portions of these studies, namely, some of the fundamental as opposed to applicational aspects, were supported by the Joint Services Electronics Program, Contract No. F49620-85-C-0078.

As indicated above, the remainder of this Final Report is organized in the following manner. Section B, immediately following, contains an overview of the various antennas and their principal features. Then Chap. II describes the unit-cell approach employed in the analysis of the two-dimensional arrays, covering how the unit cells are obtained for various structures and presenting the properties of the unit cells. Also included are some general results for the leaky-wave line sources. Chapters III through XI then present detailed descriptions of the principles of operation, analyses of the behavior, and numerical results for the seven different new antennas examined in course of this study. The sections are grouped into three broad categories: NRD Guide Antennas (Chaps. III and IV), Groove Guide Antennas

(Chaps. V through VIII), and Printed-Circuit Antennas (Chaps. IX through XI). All of the references are grouped together in Chap. XII.

B. OVERVIEW OF THE NEW ANTENNA STRUCTURES

1. Background

The arrays described here that are capable of two-dimensional scan within a certain sector in space are comprised of a linear phased array of parallel leaky-wave line sources. Scanning in one plane (elevation, along the axis of the line sources) is provided by a frequency scan or an electronic scan of the leaky-wave line sources, whereas scanning in the cross plane (resulting in azimuth scan) is obtained in the usual phased-array manner. The radiation from these arrays is designed to have pure polarization (no cross polarization) and to encounter no grating lobes, and the analyses show that no blind spots occur.

Both the line sources themselves and the arrays that comprise them are novel. We present here seven novel antenna structures, four of which are leaky-wave line-source antennas and three of which are arrays of line sources. In fact, two of the three arrays employ line sources that are not directly any of the four line-source antennas to be described, but are outgrowths of them or were suggested by them. Each of the four line-source antennas is of interest in its own right, however.

A leaky-wave line-source antenna is basically an open waveguide possessing a mechanism that permits a slow leakage of power along the length of the waveguide. This slow leakage is characterized by a phase constant β and a leakage constant α , and these quantities are the end products of any analysis of a leaky-wave structure. The relations between β and α and the properties of an actual leaky-wave antenna, such as the angle of maximum radiation, the beam width, and the sidelobe distribution, are standard. For the convenience of the reader, some general properties of leaky-wave antennas, and their relations to β and α , are summarized at the end of Chap. II.

Leaky-wave antennas for the millimeter-wave range face two main problems. The first relates to the small wavelengths involved, which require small waveguide dimensions and pose fabrication difficulties. The second problem is higher metal loss; for antennas that are many wavelengths long, the leakage (which results in radiation) may compete with the intrinsic waveguide loss, and the antenna design can be adversely affected. We overcome the first of these problems by considering leaky-wave structures with *longitudinally continuous apertures*, and the second by basing the antennas on *low-loss waveguides*. Of the possible low-loss waveguides that have been proposed over the years, we have selected two on which to base our new leaky-wave antennas: the *groove guide* and the *nonradiative dielectric (NRD) guide*.

Alternatively, *printed-circuit antennas* offer great flexibility in design combined with simplicity in structure, and they lend themselves to lithographic fabrication techniques. We have therefore examined such antennas as well, and we have concentrated on them in the later stages of this program. The longitudinally continuous apertures mentioned above do indeed offer simplicity in structure, but the scan in elevation is therefore limited to the forward quadrant only. The use of a *periodic* aperture would permit scan in the backward quadrant and part or all of the forward quadrant, and in a printed-circuit form the advantage of simplicity in structure is retained. The last of the three arrays to be described is based precisely on such a periodic structure.

Several different *mechanisms* have been introduced to produce the necessary leakage from a waveguiding structure whose dominant mode is purely bound. These mechanisms include asymmetry, foreshortening of the structure's cross section, and the use of leaky higher modes. As will be seen, most of the antennas employ asymmetry, but two are based on leaky higher modes, and one antenna on the predecessor contract used the foreshortening technique.

Many other new radiating structures, beyond the ones we have examined, may be devised by applying these mechanisms in an imaginative way. We should remember, however, that our selections were limited by the requirement that we can analyze the structures accurately as well.

2. The New Antenna Structures

The antenna structures examined in this program fall into three broad categories, depending on the guiding structure on which they are based. These three categories are (a) NRD guide antennas, (b) Groove guide antennas, and (c) Printed-circuit antennas.

The Final Report on the predecessor contract [1]* described several new antenna structures, and treated two of them in substantial detail. One of them was based on the groove guide, and it employed the principle of asymmetry to produce radiation from the ordinarily bound dominant mode. The second was based on the NRD (nonradiative dielectric) guide, and used the principle of foreshortening to produce the required radiation. Full papers on both of these leaky-wave structures have since been published [2-5]. These antenna structures will now be described briefly as an introduction to the basic principles involved as well as to show what their limitations were and why it was necessary to devise improved structures.

* All the references are listed in Chap. XII.

The basic symmetrical nonradiating *groove guide* is shown on the left-hand side of Fig. 1.1. The leaky-wave antenna, shown on the right-hand side of Fig. 1.1, differs from the nonradiating groove guide structure in that a continuous metal strip of narrow width has been added to the guide in *asymmetrical* fashion. Without that strip, the field of the dominant mode of the symmetrical groove guide is evanescent vertically, so that the field has decayed to negligible values as it reaches the open upper end. The function of the asymmetrically placed metal strip is to produce some amount of net horizontal electric field, which in turn sets up a mode akin to a TEM mode between the parallel plates. The field of that mode propagates at an angle all the way to the top of the waveguide, where it leaks away. The bottom of the guide is closed to prevent radiation from the bottom as well.

We thus have available a leaky-wave line-source antenna based on the asymmetry mechanism and simple in concept. The value of the real part of the propagation wavenumber (or phase constant) β of the leaky wave is governed primarily by the properties of the original unperturbed groove guide, and the value of the leakage constant α is controlled by the width and location of the perturbing strip.

The antenna structure in Fig. 1.1 is clear in principle, and has the desirable feature that β and α can be controlled essentially independently, but it is a structure that would be difficult to build at millimeter wavelengths. It thus becomes necessary to devise new antenna structures that are *simpler in configuration*. We shall shortly discuss two of these that are based on the groove guide.

The nonradiating *NRD guide* and the early leaky-wave antenna based on it are shown on the left-hand and right-hand sides, respectively, of Fig. 1.2. As was the case for the symmetrical groove guide, the field in the air regions of the standard NRD guide is evanescent vertically and will decay to negligible values as it reaches the open ends. The leaky wave antenna is created simply by decreasing the distance d between the dielectric strip and the top of the metal plates. When distance d is small, the fields have not yet decayed to negligible values at the upper open end, and therefore some power leaks away. The upper open end forms the antenna aperture, and the aperture amplitude distribution is tapered by varying the distance d as a function of the longitudinal variable z . No radiation is produced from the lower open end because the plates in the air region are kept sufficiently long.

This leaky-wave antenna, which employs the foreshortening mechanism, is seen to be very simple in structure. The polarization of the antenna radiation is seen to be predominantly *vertical*, in view of the primary electric field orientation in the basic

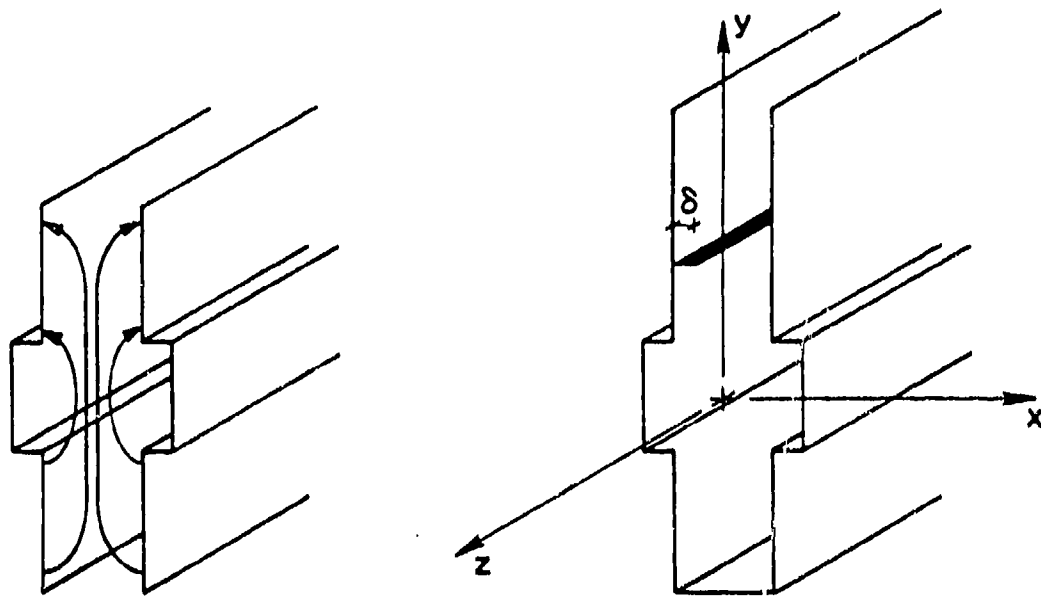


Fig. 1.1 The basic symmetrical nonradiating groove guide is shown on the left, together with typical electric field lines. On the right is the leaky-wave antenna produced by adding a continuous narrow metal strip (shown black) in asymmetrical fashion.

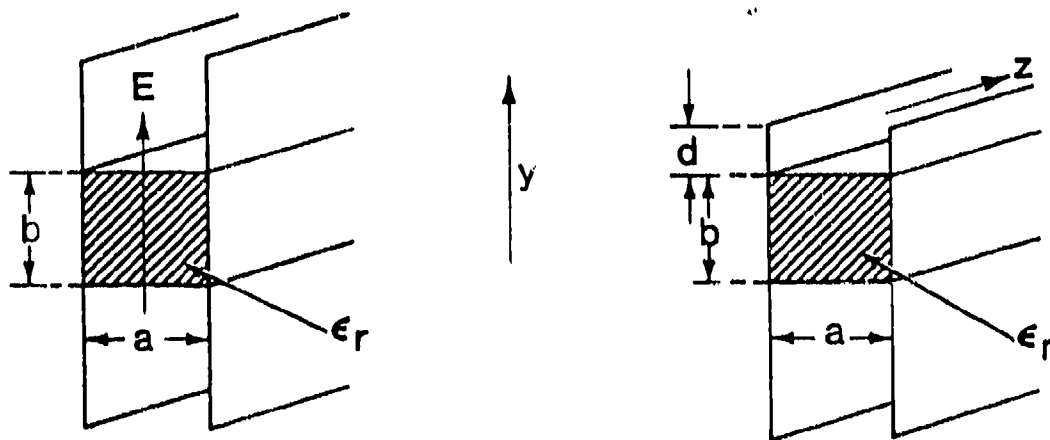


Fig. 1.2 The basic nonradiative dielectric (NRD) guide is shown on the left; on the right is the foreshortened-top leaky-wave antenna, where leakage is controlled by distance d .

waveguide. It turns out, however, that there is also a small amount of off-axis horizontal polarization, due to the small components of horizontal electric field at the vertical walls. If *pure* polarization is required, then another structure is preferable.

a. NRD Guide Antennas

In an attempt to achieve a *leaky-wave line-source antenna* that yields pure polarization (no cross polarization), the *asymmetry* mechanism was applied to the NRD waveguide. The leaky-wave antenna that resulted is shown, together with the original nonradiating NRD guide, in Fig. 1.3. The antenna structure is bisected so as to simplify its structure and permit radiation from one end only.

The asymmetry is produced by introducing a small air gap of thickness t in the dielectric block. As a result, a small amount of net horizontal electric field is created, which produces a mode in the parallel-plate air region akin to a TEM mode. That mode then propagates at an angle between the parallel plates until it reaches the open end and leaks away. It is necessary to maintain the parallel plates in the air region sufficiently long that the vertical electric field component of the original mode has decayed to negligible values at the open end. Then the TEM-like mode, with its horizontal electric field, is the only field left, and the field polarization is then *pure*. (The discontinuity at the open end does not introduce any cross-polarized field components.) The antenna structure is also seen to be simple in configuration.

The analysis of the behavior of this line-source antenna is presented in Chap. III, together with various performance curves. It is shown that when the air-gap thickness t is varied the phase constant β changes only a little but the leakage constant α varies substantially, as we would like. Some very interesting behavior for α as a function of dielectric width b near to the cutoff of the mode is described and explained.

Of particular importance is the odd behavior found in certain ranges when the length c of the parallel plates is varied. The behavior was originally totally unexpected and inexplicable. It was then realized that *coupling* was occurring between two different leaky modes supportable by the structure. One leaky mode is the desired one, and the other is a modification of the so-called channel-guide mode. Since both modes are leaky, with complex propagation wavenumbers, they can couple only when *both* the α values and the β values of each are equal. Nevertheless, such coupling does occur for large leakage rates and for large values of length c . To avoid the complications in performance due to this coupling phenomenon, the antenna design should avoid making length c unnecessarily long, and attention should be paid to whether or not the leakage rate is too high (resulting in very large beam widths).

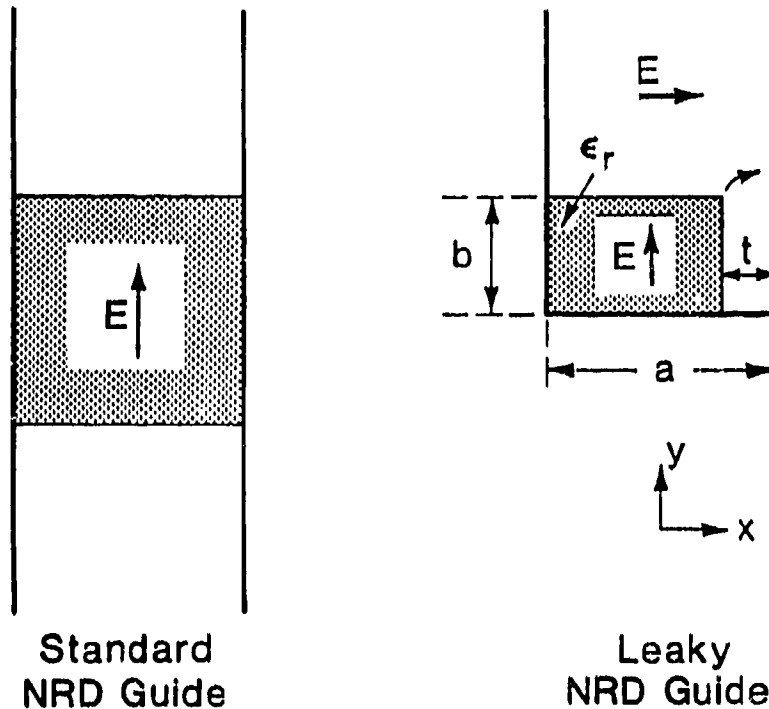


Fig. 1.3 The standard NRD guide, on the left, and the leaky NRD guide antenna produced by creating an asymmetric air gap of thickness t and bisecting the structure horizontally. (Treated in Chap. III.)

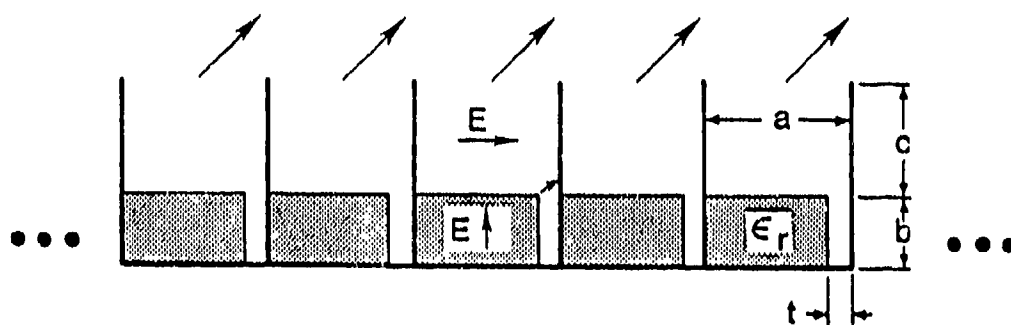


Fig. 1.4 A linear phased array of parallel NRD guide leaky-wave line sources, of the type shown in Fig. 1.3, that produces two-dimensional scanning, with negligible cross-polarization, and without blind spots or grating lobes. (Treated in Chap. IV.)

If the coupling cannot be avoided, advice is given in this report (in several places) regarding how the problem can be gotten around in a satisfactory way.

The analytical description of the nature of this leaky-wave coupling is of basic interest in itself, and may represent the first appearance of such an analysis. In any case, it turns out that such coupling can occur whenever the radiation involves the parallel plate stubs. Since those stubs are needed to achieve the desired pure polarization, they have been incorporated into all the antenna structures discussed in this report. This means that concern regarding the effect of such coupling also appears in the other antennas to be described, and, in fact, the coupling effects are investigated more carefully and fully for some of the other line-source antennas (and arrays as well).

Chapter IV describes how these NRD guide line-source antennas can be placed into an *array* to produce two-dimensional scanning. The structure is shown in Fig. 1.4. The linear array of parallel NRD guide line sources will scan in the cross plane, as shown, with an angle that depends on the phase shift introduced between the successive line sources. The radiation in pencil beam form will scan in both elevation and azimuth in a conical scan manner. The spacing between the line sources is such that *no grating lobes* can occur, and *pure polarization* (horizontal in this configuration) can be maintained. An accurate analysis shows that *no blind spots* appear anywhere.

The accurate analysis is based on a *unit-cell approach* that automatically takes all mutual coupling effects into account. The essential features of the unit-cell approach are described in Chap. II. The unit-cell approach is itself well-known, having been introduced some time ago for phased arrays [6] and described in detail in a book [7]. In the known form, however, the wavenumber k_z along the axis z of the line sources is imposed and real (as k_x is here). In our array problem, k_z is complex, i.e., $k_z = \beta - j\alpha$, and is not known beforehand. There are therefore *new features* in our unit-cell analysis.

As the phase shift between line sources increases (and the beam is scanned further in the cross plane and therefore in azimuth), the effective load impedance on the end of the unit cell departs further from a matched load condition. It is found that for large azimuth scan angles the coupling effect observed for the line-source antenna occurs here as well, raising the need to be alert in the array design and to keep the length c no longer than is necessary to eliminate the cross polarization.

b. *Groove Guide Antennas*

As explained above, the first version of the asymmetric groove guide leaky-wave antenna, shown on the right-hand side of Fig. 1.1, works well in principle and possesses desirable features but would be difficult to build at millimeter wavelengths. New structures that are simpler in configuration were therefore sought.

The *simplest* of these is shown on the right-hand side of Fig. 1.5. It is also based on the groove guide, but it employs the first higher antisymmetric mode, which is itself leaky. (In fact, all higher modes of groove guide are leaky.) The electric field of that higher mode is sketched on the full groove guide on the left-hand side of Fig. 1.5. Due to the symmetry of the structure and the directions of the electric field lines, the structure can be bisected twice to yield the greatly simplified structure on the right-hand side.

The derivation of the final L-shaped structure may also be viewed in two alternative ways. First, before the horizontal bisection but after the vertical one, the structure can be regarded as an asymmetrical groove guide which would then leak by virtue of asymmetry. The second way is to observe that the final structure, after the double bisection, resembles a rectangular waveguide with a large off-center stub fed by its dominant mode. Our derivation was the one described first above, i.e., from the leaky higher mode viewpoint.

The analysis and subsequent discussion of the L-shaped configuration are presented in Chap. VI. The analysis employs a transverse equivalent network that is based on a *new equivalent network for an E-plane tee junction*. The tee junction network is then bisected to conform to the bisected antenna structure. The equivalent network for the tee junction is a new one, and it is notable in that the expressions for the elements of the network are in *simple closed form*, and yet are very accurate. As a result, the dispersion relation is also in simple closed form, so that the values of phase constant β and leakage constant α are then obtained quickly. The new tee-junction equivalent network is discussed in Chap. V.

The configuration of the L-shaped leaky-wave line-source antenna is indeed *simple*, and it can be easily fed when we view it as derived from a rectangular waveguide. It suffers from an important limitation, however, in that it leaks very strongly for most geometric aspect ratios. This antenna is therefore useful only for applications that require *wider beams*. Further details regarding the properties of this antenna are contained in Chap. VI.

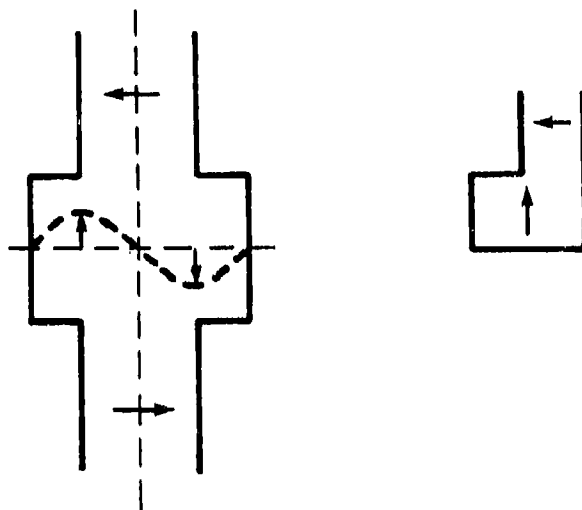


Fig. 1.5

The L-shaped leaky-wave antenna on the right, a particularly simple structure, is derived from the groove guide on the left when it supports the first higher antisymmetric mode and is then bisected both horizontally and vertically. Some key electric field directions are indicated. (Treated in Chap. VI.)

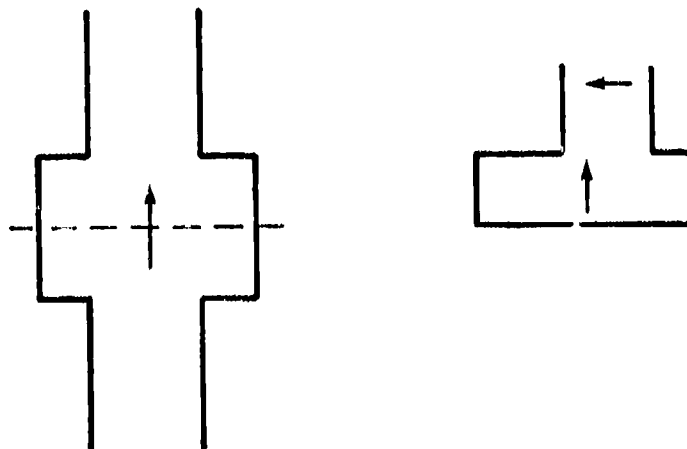


Fig. 1.6

The offset-groove-guide leaky-wave antenna on the right is derived from the groove guide on the left when it supports the dominant mode but is bisected horizontally and then made asymmetrical by offsetting the stub portion at the top. The antenna possesses many desirable features. (Treated in Chaps. VII and VIII.)

The next challenge to be addressed was how to devise a structure that would retain most of the simplicity of the L-shaped antenna but provide the *versatility* with respect to beam width that the L-shaped structure lacked. We were fortunate, and the answer was found in the *offset-groove-guide* leaky-wave antenna. The structure of this antenna is shown in Fig. 1.6, together with that of the ordinary groove guide antenna operated in its dominant mode. This antenna structure is treated in detail in Chap. VII.

In the antenna structure on the right-hand side of Fig. 1.6, the groove guide is bisected horizontally and then the stub portion is placed off center (offset). The asymmetry introduced induces a net horizontal electric field which in turn produces a TEM-like mode that propagates at an angle between the stub guide plates to the open top and then leaks away. One can alternatively view the antenna structure as a rectangular waveguide with an open stub that is offset from the center position, a view that is reinforced when comparison is made with the L-shaped structure in Fig. 1.5, which can then be regarded as corresponding to the extreme off-center position.

When the stub is centered, the structure is that of groove guide (bisected horizontally), which is known to be nonradiating. The centered stub may be alternatively viewed as a slotted section cut in rectangular waveguide. For small off-center positions of the stub, the leakage rate will be small, yielding radiated beams of narrow width. When the offset is increased, α will increase and the beam width will increase. We therefore have a relatively simple leaky-wave antenna, easily fed from a rectangular waveguide, that permits great versatility with respect to beam width by simply adjusting the location of the stub guide.

This line-source antenna also possesses other important virtues. The sidelobe level and distribution of any line-source antenna can be prescribed by appropriately specifying the antenna's aperture distribution. That means that the aperture of the antenna must be tapered in some specified fashion. For an easy design, one must be able to vary the leakage constant α while keeping the phase constant β the same. Not all leaky-wave antennas will permit this separation. From the numerical results obtained in Chap. VII, however, it is seen that such separability is indeed present for the offset-groove-guide antenna, so that beams with low sidelobe levels can be designed using this structure.

An additional advantage follows from the fact that the antenna is filled with only one medium, namely air. As a result, it is known (and also shown in Chap. VII) that the beam width remains constant when the beam is scanned in elevation as one changes the frequency.

The analysis of this antenna, presented in detail in Chap. VII, is based on the use of the new E-plane tee junction network discussed in Chap. V. Although the results were expected to be accurate, an additional, independent, check was provided by calculating the values of α and β by an *entirely different* theoretical approach, that of mode matching. As shown in Chap. VII, the comparison was found to be excellent over a wide range of parameters, thus providing added confidence with respect to the accuracy of the results.

Because of the finite length of the stub guide, the coupling between two leaky modes, the desired one and a modified channel-guide mode, that was discussed for the asymmetric NRD guide antenna, also occurs here as well when the stub is long and the leakage rate is high. The phenomenon is examined in detail in Chap. VII. Again, the complications introduced by this coupling can be avoided by suitable design, principally by keeping the stub length no longer than it needs to be to eliminate cross polarization.

Because of the many advantages of the offset-groove-guide leaky-wave antenna (relatively simple structure, easy to feed, versatile with respect to beam width, ability to vary α while keeping β essentially constant so that designs can be made for low sidelobes, and constancy of beam width with frequency scan), it was decided that experiments to verify the theoretical predictions would be valuable. The details regarding the *measurements* that were made are described in Chap. VIII.

An antenna structure was built and then fed using standard rectangular waveguide, of cross section 4.8 mm by 2.4 mm, and measurements were taken over the frequency range 40 GHz to 60 GHz. Measurements were taken of α and β , and also of the radiation patterns over this frequency range. The beam width was found experimentally to remain constant to within about 0.1° over this frequency range. In all cases, the comparisons with theory were found to be excellent.

The next step was to examine the properties of an *array* of these very desirable leaky-wave line sources. An array that employed these line-source elements *directly* would suffer from two disadvantages. First, the spacing between line sources would need to be greater than $\lambda_0/2$, so that grating lobes would no longer be automatically avoided. Second, the array structure would be mechanically more complex than the one in Fig. 1.4, for the array of NRD guide line sources. Because of these considerations, we finally adopted a *printed-circuit version* of such an array, which retains all of the principal virtues of the offset-groove-guide line source but overcomes the two disadvantages expressed above. That array is treated in detail in Chap. X, and

some additional comments regarding it are made below.

c. *Printed-Circuit Antennas*

The steadily increasing interest within the past few years with respect to printed-circuit antennas caused us to think about how such structures could be adapted to the general goals of this program. The first step was to examine *microstrip line*. After an extensive investigation, which is reported in detail in Chap. IX, we emerged with a variety of very interesting results, ranging from new basic material on the properties of higher modes on microstrip line to a particularly simple new leaky-wave structure -- just a length of uniform microstrip line excited in its first higher mode, as shown in Fig. 1.7. In large part, this study was motivated by some confusion in the literature regarding what happens to microstrip line higher modes as they approach cutoff, and also to a traveling-wave patch antenna whose mode of operation was unclear. Upon recognition that the higher modes become leaky near cutoff, everything fell into place and the confusions all became clarified. In the process, much was learned of a basic nature, and the behavior of the microstrip leaky-wave strip antennas became clearly understood analytically and numerically.

As a new leaky-wave antenna, the microstrip strip antenna has the great virtue of being extremely simple in configuration -- just a uniform length of microstrip line, but excited in its first higher mode. On the other hand, it is not a versatile structure. For example, the beam width cannot be adjusted independently of the angle of the beam maximum, as is true for the offset-groove-guide antenna. If one attempts to taper the aperture distribution to reduce the sidelobe level, the only parameter that can be changed is the strip width. But if the strip width is modified to adjust the value of α , the value of β changes also. The extreme simplicity thus limits the versatility. The antenna is simple and cheap, however, and its performance is predictable analytically, so that it should be useful for certain limited applications.

A parallel array of such microstrip leaky-wave strip antennas would be practical if no scanning in azimuth is planned. Once such scanning is performed, it is highly likely that blind spots would result. After some thought, a printed-circuit array emerged that is an amalgam of the microstrip array and an array of offset-groove-guide line sources, but retains the versatility and other advantages of the offset-groove-guide antenna. The cross section of that printed-circuit array structure is shown in Fig. 1.8, and the array is examined in detail in Chap. X.

The leaky-wave line sources themselves are new. They are *printed-circuit versions*,

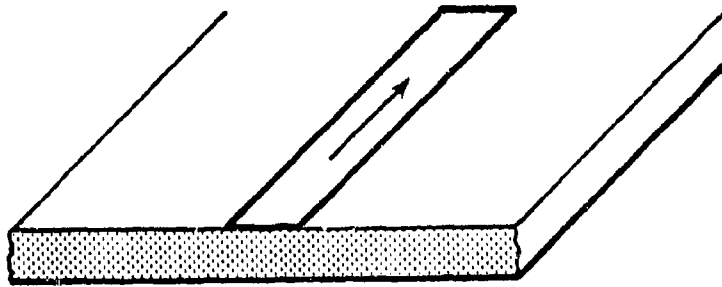


Fig. 1.7 An extremely simple leaky-wave antenna in microstrip line: just a uniform strip but excited in the first higher mode. (Treated in Chap. IX.)

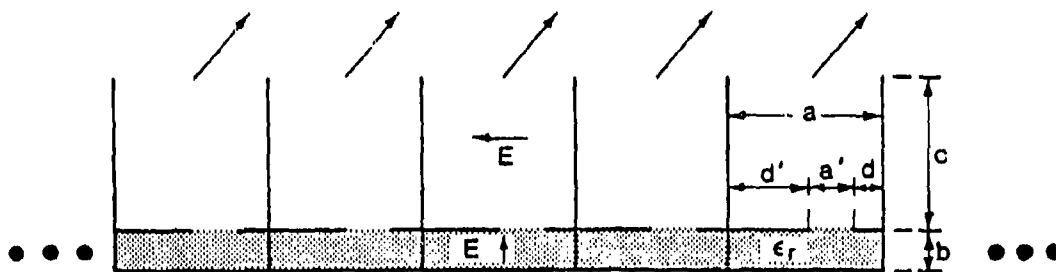


Fig. 1.8 A printed-circuit form of a linear array of leaky-wave line sources that produces two-dimensional scanning, where the line sources themselves are also new, being a printed-circuit version of the offset-groove-guide antenna shown in Fig. 1.6. As with the array in Fig. 1.4, this array is notable for the absence of cross polarization, grating lobes and blind spots. (Treated in Chap. X.)

with modifications, of the offset-groove-guide leaky-wave antenna described above. These individual line-source antennas are then arranged parallel to each other in a line array, with each fed from one end, and with some imposed phase shift between them to produce the desired azimuth scan angle.

The physical mechanism of leakage from the individual line sources is the following. Although the initial structure was derived by bisecting groove guide and then offsetting its upper stub, the individual line source in the printed-circuit version in Fig. 1.8 may best be viewed as a flat dielectric-filled rectangular waveguide with an unsymmetrical longitudinal continuous slit on its top wall, leaking power into an air-filled upper stub of finite length. Width a must be chosen so as to satisfy two conditions: (a) the TE_{10} mode with its vertical electric field in the dielectric-filled rectangular guide is above cutoff, and (b) the mode in the parallel-plate stub region with vertical electric field is below cutoff. The rectangular waveguide, which is fed from one end, then leaks through the slit into the parallel-plate stub guide above. The asymmetric location of the slit excites both a horizontal and a vertical electric field in the stub region. The horizontal electric field corresponds to a TEM mode that travels up at an angle between the parallel plates of length c , and radiates from the open end at the top. The condition on width a causes the mode with the vertical electric field to be below cutoff. The radiation into space thus has *pure* horizontal electric field polarization. The second of the two conditions on width a also eliminates any grating lobes with respect to scan in azimuth.

The structure would be neater and simpler if the stubs were not present. The antenna would then still radiate, but the radiation would be cross polarized. In addition, there would very likely be blind spots present in the array application. *With* the stubs present, however, our accurate analysis indicates that *no blindness effects occur*. The stubs are a structural nuisance, of course, but they serve to eliminate both cross polarization and blindness problems. It is highly likely that the introduction of such stubs into other forms of phased arrays (where scanning in both planes are obtained using phase shifters) would also produce both benefits and thereby improve performance.

If the slit were centered within width a there would be no radiation. Small shifts of the slit off center result in small leakage rates, whereas larger shifts result in larger leakage per unit length. Since the width of the radiated beam is directly proportional to this leakage rate, we have available a very simple mechanism to control the beam width. Thus, the beam width can readily be varied over a wide range by simply changing the location of the slit within the width a . The structure therefore yields

versatile performance in addition to pure polarization, no grating lobes, and no blind spots.

The analysis of the array again treats the array in terms of unit cells, where the termination on the unit cell employs a rigorous equivalent circuit taken from the Waveguide Handbook [8]. The overall transverse equivalent network also incorporates a new modification of the tee junction network discussed above, to take into account the dielectric filling of the feed portion of the array and the unsymmetrical location of the slit.

The numerical results show that for this structure one can vary α but keep β essentially constant, by changing either the off-center location of the slit or the width of the slit. Thus, one can readily design the taper necessary for controlling the sidelobe level. One advantage over the offset-groove-guide antenna in this connection is that here the whole taper can be fabricated lithographically.

The calculations also show that no blind spots are encountered. On the other hand, the leaky-wave coupling effects discussed earlier occur here as well when the stub length c is long, but only for very large azimuth scans. Again, these effects are easily avoided when length c is not excessive.

It was mentioned earlier that, due to the fact that the radiating apertures are *longitudinally uniform* (except when modified slightly by tapering to control sidelobes), the scanning in elevation is limited to the *forward quadrant*, or at least most of it. Then, when phase shifts are introduced between successive line sources, the two-dimensional scan takes the form of a conical scan. The reason for specifying that the apertures be longitudinally uniform was to ease the difficulty of fabricating the structures at millimeter wavelengths. However, when the apertures are fabricated lithographically this requirement can be lifted to a large extent. For example, instead of an aperture comprised of a longitudinally uniform slit, we could employ an aperture containing an array of *periodic strips*. It would not be harder to fabricate lithographically, and it would permit *greater flexibility in scan coverage*.

If the period of the periodic strips were selected properly relative to the frequency and the other dimensions, the $n = -1$ space harmonic of the periodic array of strips would become fast and would leak power away at some angle. The angular coverage in elevation would then comprise the backward quadrant and some or all of the forward quadrant, depending on the parameter values. An array of the type we have been considering is illustrated in Fig. 1.9, and a detailed discussion of its properties is presented in Chap. XI.

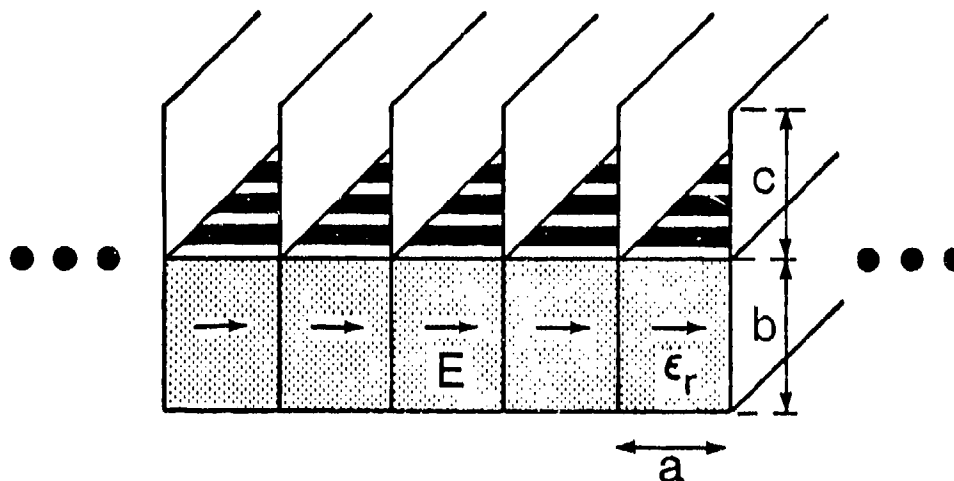


Fig. 1.9

A linear phased array of leaky-wave line sources in which the individual line-source elements are longitudinally periodic, rather than uniform as in the other arrays, in order to provide greater scan coverage. The array also takes advantage of printed-circuit technology, and possesses, in the same fashion as the arrays in Figs. 1.4 and 1.8, the virtues of pure polarization, no grating lobes and no blind spots. (Treated in Chap. XI.)

It is easy to dream up a variety of array structures that should work well, but we are also restricted by the fact that we must be able to analyze the array accurately. We therefore present the array shown in Fig. 1.9. The individual line sources are each fed by a dielectric-filled rectangular waveguide placed on its side, so as to create a horizontal electric field polarization. The electric field lines are then perpendicular to the metal baffles, so that the spacing between them can be whatever we wish; in particular, we can make them less than about $\lambda_0/2$ so that grating lobes are automatically avoided. We can also view the structure as a grounded dielectric layer with a metal grating on it. The periodic structure produces an infinity of space harmonics, but proper design will permit only the $n = -1$ space harmonic to be fast along the surface, and all the other space harmonics, including the basic $n = 0$ one, will be slow. (A systematic method for achieving a proper design is presented in Chap. XI in the context of the wavenumber (k_0 vs. β_n) diagram, which also provides excellent physical insight.) The fast space harmonic will then become propagating in

the air regions in the vertical direction. As a result, a mode akin to a TEM mode in each parallel-plate region will propagate at an angle toward the open top and will leak power away. Since only the $n = -1$ space harmonic is fast, there will be only a single radiating beam.

The analysis of this array and numerical results for it are presented in Chap. XI, where it is shown that when the ratio of strip width to period is varied the value of α changes greatly but the value of β is modified only very slightly. This behavior is just what we seek so that the beam width and the angle of the beam maximum can be specified essentially independently, and so that the antenna aperture can be tapered to control the sidelobe level.

For the dielectric constant value selected, this array can scan in elevation through the whole backward quadrant, past broadside and then about 20° into the forward quadrant. The angular coverage can be increased when ϵ_r is made larger, but we must take care that the second mode remains below cutoff. However, the angular coverage is already much greater than that obtained with the uniform apertures. Also, when the strips are singly periodic as indicated, the broadside angle corresponds to a stop band, and scanning in that narrow angular region must be omitted. By pairing the strips a quarter-guide-wavelength apart at the broadside angle, cancellation can occur and the array can be scanned through broadside as well, but we have not explored that option in this study.

We also find that the other array attributes occur here as well; there is no cross polarization and no blind spots are found. The important feature in this last array is that the appropriate use of a periodic, rather than a uniform, aperture permits a larger and more flexible scan coverage.

II.	ARRAYS OF LEAKY-WAVE LINE SOURCES	25
A.	TYPICAL ARRAY STRUCTURES AND THEIR UNIT CELLS	26
B.	PROPERTIES OF THE UNIT CELL WAVEGUIDE	36
C.	THE MODE FUNCTIONS FOR THE UNIT CELL WAVEGUIDE	42
D.	ANALYTICAL EXPRESSIONS FOR RADIATION PATTERNS OF LEAKY-WAVE ANTENNAS	44

II. ARRAYS OF LEAKY-WAVE LINE SOURCES

As mentioned in Chap. I, a scannable two-dimensional array can be created by forming a *one-dimensional array of leaky-wave line sources*. A variety of leaky-wave line sources can be employed in this connection, including the ones developed and analyzed under the predecessor contract and described in its Final Report [1]. These individual line-source antennas were analyzed using a transverse equivalent network in which the radiating open end was representative of the environment of the *single* lone line source. In the *array* of such line sources, the radiating environment is of course quite different, and it will, in fact, change as the array is scanned in azimuth.

The array of line sources is periodic in the array direction, and our method of analysis is to treat the external periodic environment by a *unit-cell approach*. This automatically accounts for all mutual coupling effects and provides information on all the effects of scan. The radiating termination on the unit cell modifies the transverse equivalent network, and the resonances of this transverse network yield the properties of the leaky wave guided along the line sources.

A key new feature of the array analysis is therefore the determination of the *active admittance* of the unit cell in the two-dimensional environment as a function of scan angle. This active admittance corresponds to the *input* admittance to the external radiating region, and it is appended to the remainder of the transverse equivalent network, the latter being different for each of the line sources. The active admittance itself will be the same for several different line sources, however, and may therefore be viewed as a *canonical* constituent.

The *unit-cell approach* is treated here, where it is first shown how canonical unit cell structures can be utilized in connection with several different line sources. The nature of the unit cell's phase-shift walls as a function of scan angle is elaborated, and the relations between the various transverse wavenumbers and the scan angles are examined. These considerations and relations are common to the analyses of all the arrays treated in this report, and that is why this material is presented here, in this separate chapter. For the same reason, we also include here, in Sec. D below, some material regarding radiation patterns and their relation to the leaky wave properties β and α .

A. TYPICAL ARRAY STRUCTURES AND THEIR UNIT CELLS

The two-dimensional structures, which are scannable in both elevation and azimuth, consist of a linear array of leaky-wave line sources. Phase shifters associated with the feed structure at one end of these line sources produce the scan in the cross plane and therefore in azimuth. The scan in elevation, which for these uniform leaky-wave antennas is restricted to a 45° or 60° sector of the forward quadrant, is produced by some electronic or electro-mechanical scanning mechanism, or by frequency scan, if desired. The line sources which are arrayed can be any one of the antennas discussed in Chap. I. Some typical array structures employing these line sources are discussed below. The external environment for these leaky-wave structures becomes altered when they are arranged in array fashion, and, furthermore, this environment varies with the azimuth scan angle.

The two-dimensional arrays under investigation are then traveling-wave antennas in one plane, and phased-array line-source elements in the other. The constituent traveling-wave antennas are the leaky-wave line sources, and they are arranged into a periodic linear array and fed from one end.

If the line-source element is the L-shaped antenna (discussed in Chap. VI and based on the groove guide) shown in Fig. 2.1, a top view and a cross-section view of the array of such leaky-wave line sources would be those shown in Figs. 2.2(a) and 2.2(b). The array would have period a in the x direction, and dimension a must be slightly greater than $\lambda_o/2$, where λ_o is the free-space wavelength. The individual

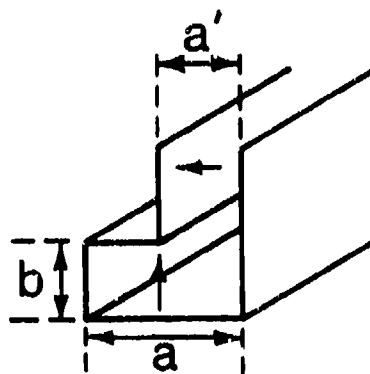
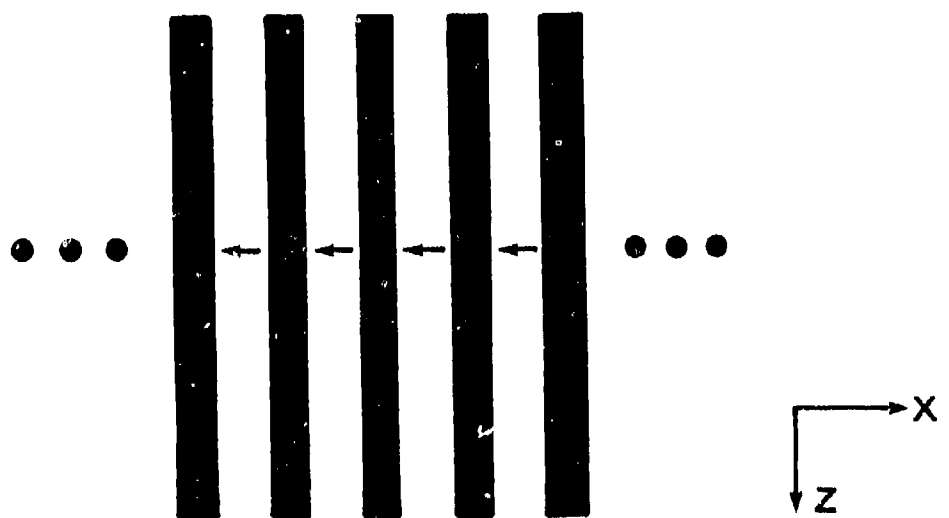
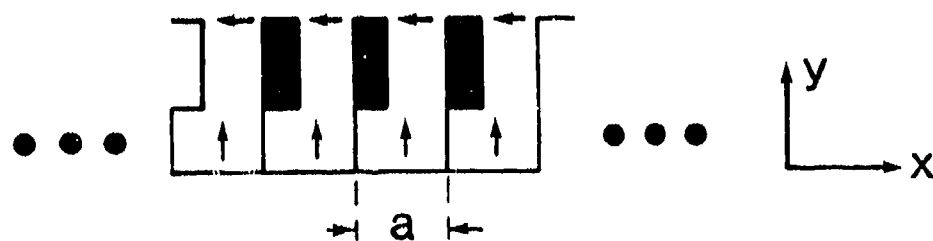


Fig. 2.1 L-shaped leaky-wave line-source antenna based on groove guide, and discussed in Chap. VI. The arrows represent electric field lines.



(a) Top View



(b) Cross Section View

Fig. 2.2

Linear array of line sources in which each line source is the leaky-wave L-shaped antenna shown in Fig. 2.1. The arrows represent the directions of the electric field lines in the various regions, and the solid portions indicate metal.

elements are fed at one end with the electric field vertical, as shown; the energy that leaks has its electric field horizontal, so that the radiation is *horizontally* polarized. The two-dimensional array is seen to be structurally quite simple.

If the line-source element selected is the antenna shown in Fig. 2.3, a cross-section view of the resulting array is that appearing in Fig. 2.4. The structure is more complicated than that in Fig. 2.2, but it is largely similar. The array period is again a , which must be slightly larger than $\lambda_o/2$. The radiation is again horizontally polarized. Added in Fig. 2.4 is a set of lines at an angle representing radiation at that scan angle in the xy plane, which of course depends on the phasing between neighboring line-source elements. The analysis for the line-source element in Fig. 2.3 has been discussed in detail in a pair of papers [2,3].

In Fig. 2.6, we see the cross section of the array formed by using the foreshortened NRD guide antennas in Fig. 2.5 as line-source elements in the array. This line-source antenna has been described in the literature [4,5]. The structure is seen to be comprised of both metal and dielectric, but in a very simple form. The excitation electric field is vertical, as seen in Fig. 2.6, and the radiation is now *vertically* polarized, in contrast to that in Figs. 2.2 and 2.4. The array period is again called a but now it is *less* than $\lambda_o/2$, in keeping with the requirement of NRD guide. If it is desired that the period should be larger, the walls between the line-source elements could simply be made a bit thicker.

The next illustrative array cross section is shown in Fig. 2.8, where the leaky-wave antenna employed as the line source is the one shown in Fig. 2.7. The line source is based on the NRD guide, but the asymmetry mechanism is employed so that the radiation is *horizontally* polarized when the structure is oriented as shown. The structure is again simple, and the array period is again a , with $a < \lambda_o/2$, as in Fig. 2.6. This line source is discussed in Chap. III, and the array is treated in Chap. IV.

From Figs. 2.2, 2.4, 2.6 and 2.8, we note that a variety of line-source leaky-wave antennas is available to place in an array to produce scanning in two dimensions. If desired, other leaky-wave line sources can be employed, including the very versatile offset-groove-guide antenna discussed in Chap. VII, or the very simple microstrip line strip antenna treated in Chap. IX. In addition, a class of novel *printed-circuit* arrays may be used. Two members of this class are discussed in detail in this report, the first employing uniform leaky-wave line sources and the second using periodically modulated line sources. The cross sections of these two arrays are presented in Figs. 1.8 and 1.9, respectively, of Chap. I, and their analyses and performance features are covered in Chaps. X and XI, respectively.

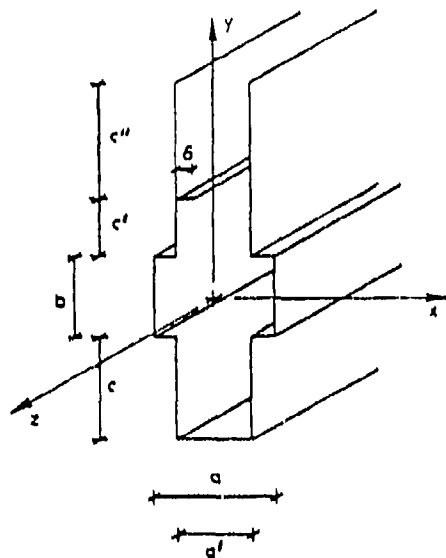


Fig. 2.3

Leaky-wave line-source antenna based on groove guide, where leakage is produced by the introduction of an asymmetric continuous metal strip.

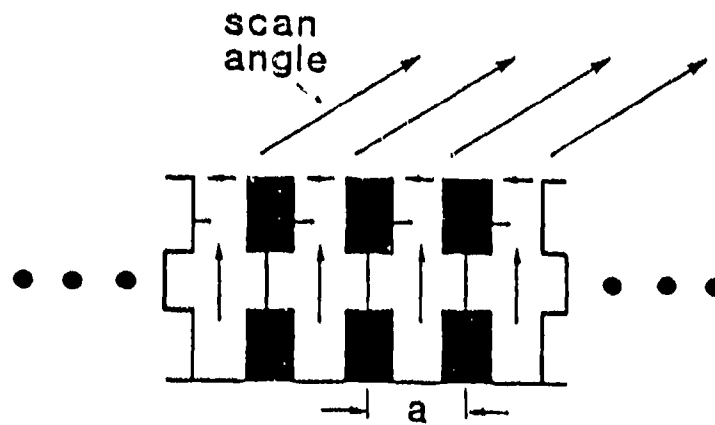


Fig. 2.4

Linear array of line sources in which each line source is the leaky-wave antenna in Fig. 2.3. The arrows within the guides represent electric field lines; the arrows outside indicate the direction of cross-plane scan.

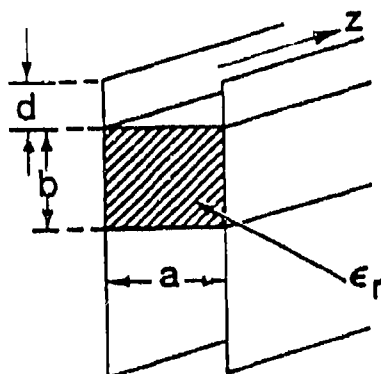


Fig. 2.5 Leaky-wave line-source antenna based on the NRD guide, where leakage is produced by foreshortening the top of the guide.

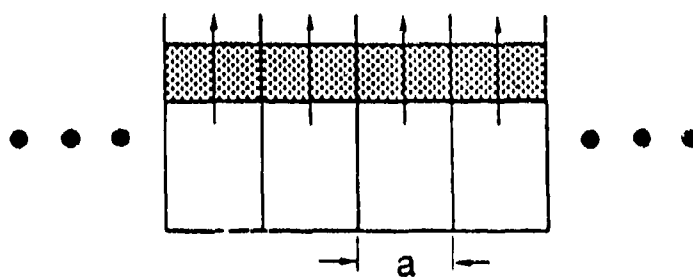


Fig. 2.6 Linear array of line sources in which each line source is the NRD guide leaky-wave antenna in Fig. 2.5, with vertically polarized radiation.

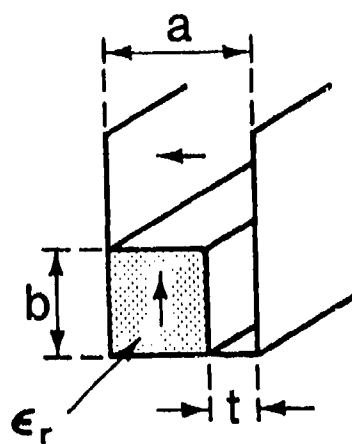


Fig. 2.7 Leaky-wave line-source antenna based on the NRD guide, where leakage is produced by asymmetry. The arrows represent electric field lines.

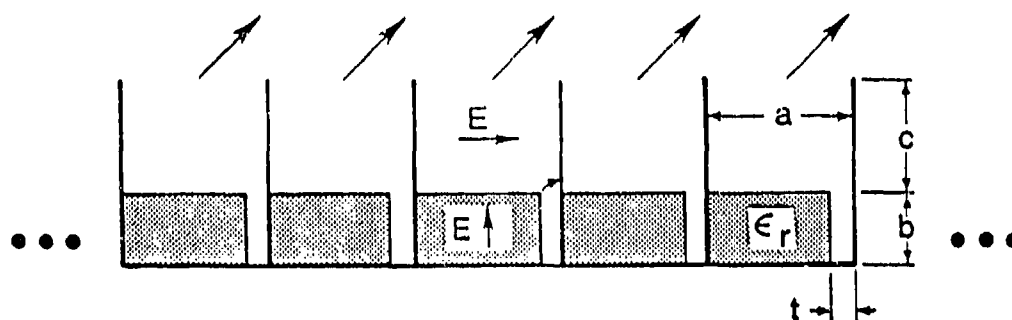


Fig. 2.8 Linear array of line sources in which each line source is the NRD guide leaky-wave antenna in Fig. 2.7.

All the structures are relatively simple, although some are simpler than others. The structural simplicity is of key importance when the array is to be used at millimeter wavelengths. Lithographic methods may be used to create the apertures on the printed-circuit arrays.

We also see that either horizontally polarized or vertically polarized radiation can be achieved, and that the period of the array can be made less than $\lambda_o/2$ or slightly greater than $\lambda_o/2$. When the groove guide antennas are used as the array elements, the array period must be greater than $\lambda_o/2$ (unless the array is dielectric loaded). However, the NRD guide antennas permit the array spacing to be *less* than $\lambda_o/2$; also, by using thicker wall separations the array spacing can be increased, if desired. The NRD guide line-source elements therefore provide an added advantage. The printed-circuit arrays are also designed to have array spacings less than $\lambda_o/2$, so that grating lobes are automatically avoided.

The individual line-source antennas were analyzed by establishing a suitable transverse equivalent network for each of the structures, and then by applying the transverse resonance condition to obtain the dispersion relation for the complex propagation constant $\beta - j\alpha$ of the leaky mode producing the radiation. In each case, the radiating open end is represented by a complex impedance or a complex admittance, placed at the end of an appropriate transmission line.

When the leaky-wave line source is made part of a linear array of such line sources, the external environment of the line source obviously changes, and the line sources in the array become mutually coupled. The mutual coupling effects are rigorously taken into account by selecting a *unit cell* appropriate to the periodicity of the array, and by placing *phase-shift walls* that correspond to the phase shift conditions at the boundary walls of the unit cell.

As an example, a leaky-wave line source when *isolated* appears in Fig. 2.3. When an *array* of such line sources is employed, the more complex structure that results was shown in Fig. 2.4. When the external array environment is accounted for rigorously by a unit cell, the array structure of Fig. 2.4 may be replaced rigorously by the *unit cell* shown in Fig. 2.9. The side walls of the unit cell of parallel-plate form in the external region have a phase shift relative to each other that corresponds to the angle of scan in the xy plane in Fig. 2.2. The transverse equivalent network that represents the unit cell structure in Fig. 2.9 is *identical in form* with that representing the isolated line source, but the equations characterizing the terminal admittance are now very different and may be much more complicated. In fact, these equations must also

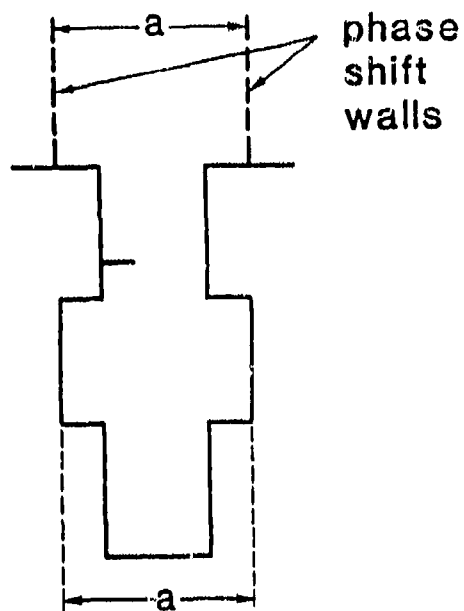


Fig. 2.9 Unit cell model of the array of groove guide line sources shown in Fig. 2.4.

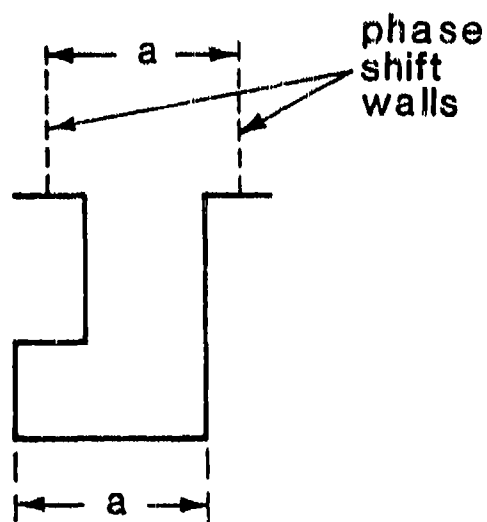


Fig. 2.10 Unit cell model of the array of L-shaped line sources shown in Fig. 2.2(b). The outside portion, contained by the phase-shift walls, is identical to that in Fig. 2.9 but is shifted laterally with respect to the base of the L-shaped structure.

include changes with scan angle.

The external structure of the unit cell in Fig. 2.9 is seen to be symmetrical, since the basic line source has a symmetric outer periphery, the asymmetry being *inside* in the form of an asymmetrically placed strip. A corresponding unit cell arrangement for the array structure shown in Fig. 2.2(b) appears somewhat unsymmetrical, however, as seen in Fig. 2.10, since the outer periphery of the isolated line source is unsymmetrical. It is important to recognize, though, that the *outside* portions of the unit cell in both Figs. 2.9 and 2.10 are the *same*.

Unit cells corresponding to the arrays in Figs. 2.6 and 2.8 are somewhat simpler than those shown in Figs. 2.9 and 2.10. For example, the unit cell for the array in Fig. 2.8 is seen in Fig. 2.11. On the other hand, the outside portion of the unit cell for the array in Fig. 2.6 would look the same as that in Fig. 2.11, but the input admittance for each of them would be quite different because the electric field polarizations for each are different.

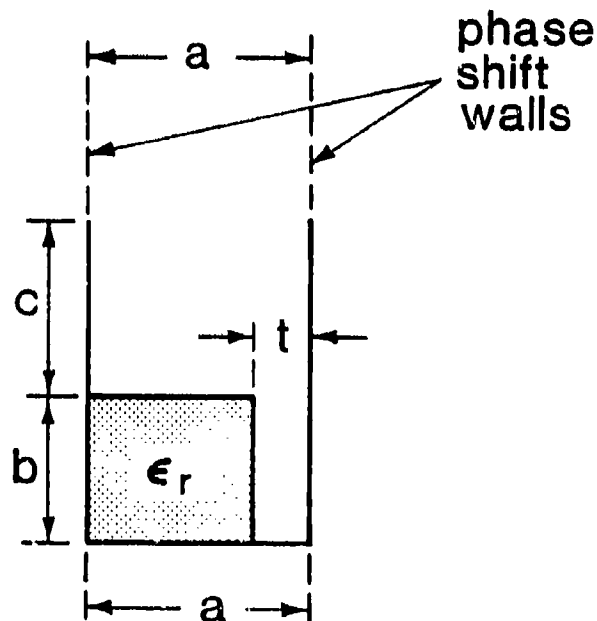


Fig. 2.11 Unit cell model of the array of asymmetrical NRD guide line sources shown in Fig. 2.8.

The basic *new* element in the analysis is the determination of the *active* impedance or admittance of the outside portion of the unit cell, the term "active" indicating that the line source is in its array environment and that all mutual coupling effects are accounted for, including the modifications that occur when the scan angle in azimuth is changed. For those cases for which the leakage is horizontally polarized, that is, for the structures corresponding to Figs. 2.2, 2.4, and 2.8, the results for broadside radiation in azimuth (cross-scan angle equal to zero) becomes particularly simple. The active impedance must then reduce to the known result for a capacitive change in height, since the phase-shift walls become a pair of electric walls, or short circuits. The unit cell shown in Fig. 2.11 becomes trivially simple in that limit since the short-circuit walls in the structure simply continue onward and the junction discontinuity disappears altogether.

The determination of the active impedance or admittance usually offers the most important challenge in the analysis, but it corresponds only to an *intermediate stage* in it. The active impedance must then be placed into the transverse equivalent network for the unit cell to make it complete, and the transverse resonance condition must be applied to derive the dispersion relation, which then yields the phase and leakage constants for the leaky-wave antenna placed in its array environment.

For the unit cell in Fig. 2.11, with horizontal polarization, the active input admittance may be obtained from a simple analytic continuation of a rigorous solution presented in the Waveguide Handbook [8]. The details are contained in Chap. IV.

B. PROPERTIES OF THE UNIT CELL WAVEGUIDE

Let us consider the region in space *above* the periodic array of leaky-wave line sources, shown in Fig. 2.12. Because the field is periodic, we may select a unit cell with phase-shift walls, as seen in Fig. 2.12, where the scan-dependent phase difference between the walls, or phase shift per unit cell, is equal to $k_{xop}a$, where a is the period and k_{xop} is the wavenumber in the x direction determined by the phase shifters. Wavenumber k_{xop} , where subscripts o and p signify "lowest mode" and "periodic region," respectively, is therefore *imposed* on the system and may be regarded as given. When all leaky-wave line sources are fed in phase, $k_{xop} = 0$ and the beam points at zero azimuth angle. For convenience, as a measure of the scan, we may view k_{xop} as related to an angle θ_x in the xy plane as

$$\sin \theta_x = k_{xop} / k_o \quad (2.1)$$

where θ_x is measured from the broadside direction, and k_o is the free space wavenumber. The relation between θ_x and the usual polar angle θ is indicated later.

Due to the periodicity, space harmonics are excited, and Floquet's theorem requires that the n-th space harmonic wavenumber k_{xnp} be related to k_{xop} by

$$k_{xnp} = k_{xop} + 2\pi n / a \quad (2.2)$$

The space harmonics with respect to the x direction correspond to *modes in the unit cell*, where the transmission direction is vertical, i.e., the y direction. The wavenumber k_{ynp} of the n-th mode in the unit cell waveguide is given by

$$k_{ynp}^2 = k_o^2 - k_{xnp}^2 - k_z^2 \quad (2.3)$$

where k_{xnp} contains a dependence on the period a , as seen in (2.2). For the lowest mode, we have

$$k_{yop}^2 = k_o^2 - k_{xop}^2 - k_z^2 \quad (2.4)$$

and it is noted that k_{yop} is independent of period a . The mode corresponds, therefore, to a plane wave propagating at an angle to both the x and z directions, and will be above cutoff for any value of the period. When $k_{xop} = 0$, meaning no imposed phase shift in the x direction, k_{yop} is clearly above cutoff since k_z must be less than k_o for propagation along z. For a sufficiently large value of k_{xop} , however, the mode will go below cutoff, indicating that the beam will disappear.

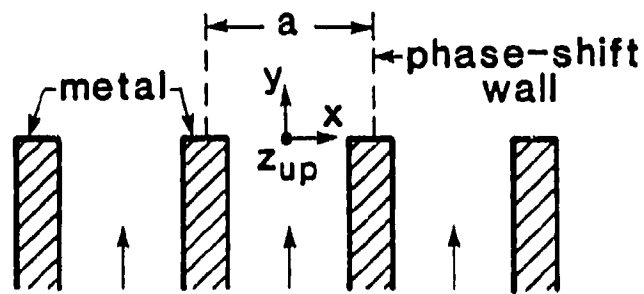


Fig. 2.12 Placement of unit cell with phase-shift walls in a periodic array of leaky-wave line sources.

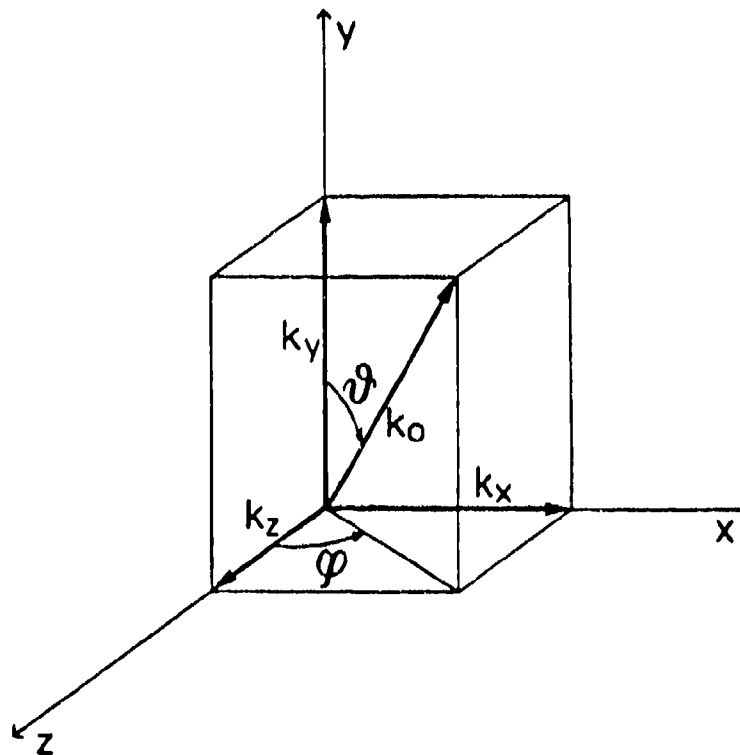


Fig. 2.13 Polar coordinate system showing the relations with the wavenumbers.

Let us note that the properties of the unit cell are well known for the case for which $k_z = 0$, or when k_z is present due to an *imposed* phase shift in the z direction. The picture is less familiar when k_z arises due to *leakage*, so that $k_z = \beta - j\alpha$, as in our case. Furthermore, k_z in our case is not known beforehand but is instead the end product of the analysis. These features concerning k_z introduce a *new element* into these considerations.

We generally wish to operate the system so that only one beam is radiated, and we therefore need to know what value of period a to choose to avoid the second mode being above cutoff in the unit cell waveguide, corresponding to the onset of a grating lobe in space. The next mode corresponds to $n = -1$ in (2.2), so that (2.3) yields

$$k_{y,-1,p}^2 = k_o^2 - k_z^2 - (k_{xop} - \frac{2\pi}{a})^2 \quad (2.5)$$

To avoid the presence of the grating lobe, $k_{y,-1,p}^2 \leq 0$, so that (2.5) becomes

$$(k_o^2 - k_z^2) \leq (k_{xop} - \frac{2\pi}{a})^2 \quad (2.6)$$

or

$$\left[1 - \left(\frac{k_z}{k_o} \right)^2 \right]^{1/2} \leq \frac{\lambda_o}{a} - \frac{k_{xop}}{k_o} \quad (2.7)$$

so that

$$a \leq \frac{\lambda_o}{\left[1 - (k_z/k_o)^2 \right]^{1/2} + (k_{xop}/k_o)} \quad (2.8)$$

When $k_z = 0$, it is well known that a can be less than λ_o for a grating lobe to appear when $k_{xop} \neq 0$. Relation (2.8) further tells us that when $k_z \neq 0$ the period a must be increased again before the grating lobe can be present.

The relations between the wavenumbers and the *polar coordinate system* become clear from Fig. 2.13. Consistent with the coordinates in Fig. 2.12, the angle ϕ in Fig. 2.13 is measured from the z axis in the xz plane. We then have the usual relations

$$\begin{aligned} k_x &= k_{xop} = k_o \sin \theta \sin \phi \\ k_z &= \beta = k_o \sin \theta \cos \phi \\ k_y &= k_{yop} = k_o \cos \theta \end{aligned} \quad (2.9)$$

Thus, θ_x , defined in (2.1), and θ_z , correspondingly defined as

$$\beta = k_o \sin \theta_z \quad (2.10)$$

become

$$\begin{aligned} \sin \theta_x &= \sin \theta \sin \phi \\ \sin \theta_z &= \sin \theta \cos \phi \end{aligned} \quad (2.11)$$

It was remarked above in connection with (2.4) that if k_{xop} is increased sufficiently, corresponding to a given value of k_z , the radiating beam will disappear. Let us examine that statement in the light of the angles introduced above. Assume that β/k_o , and therefore $\sin \theta_z$ from (2.10), is specified, and that k_{xop}/k_o , or $\sin \theta_x$, is varied. For propagation of the lowest mode, k_{yop}^2 in (2.4) must be greater than zero, so that we may write

$$\left(\frac{k_{xop}}{k_o}\right)^2 + \left(\frac{k_z}{k_o}\right)^2 \leq 1 \quad (2.12)$$

On use of (2.1), (2.10) and (2.11), (2.12) becomes

$$\sin^2 \theta \sin^2 \phi + \sin^2 \theta \cos^2 \phi \leq 1$$

so that the condition for mode cutoff as k_{xop} increases is

$$\sin \theta = 1 \text{ or } \theta = 90^\circ \quad (2.13)$$

What is occurring, then, as k_{xop} increases from zero to its maximum value before cutoff, is that the beam is undergoing *conical scan*, beginning at the highest value of θ in the yz plane and then decreasing in θ while increasing in ϕ until the beam finally hits the horizontal xz plane.

It is also easy to obtain a simple expression relating the angles at the extremes of the conical scan. When the phase shift between the line sources is zero, $k_{xop} = 0$ and $\phi = 0$, so that $\sin \phi = 0$ and $\cos \phi = 1$. Then, from (2.9), we have

$$\sin \theta = k_z / k_o \quad (2.14)$$

When the beam hits the ground in the conical scan, $\theta = 90^\circ$, from (2.13), so that $\cos \theta = 0$ and $\sin \theta = 1$. Then, from (2.9), we find

$$\cos \phi = k_z / k_o \quad (2.15)$$

By comparing (2.14) and (2.15), we see that

$$\cos \phi_{\theta = 90^\circ} = \sin \theta_{\phi = 0}$$

from which we note that

$$\phi_{\theta = 90^\circ} + \theta_{\phi = 0} = 90^\circ \quad (2.16)$$

or

$$\phi_{k_y = 0} + \theta_{k_x = 0} = 90^\circ \quad (2.17)$$

Of course, we have implicitly assumed here that α is small, so that $k_z \approx \beta$.

The unit cell waveguide can be represented by a *transmission line* for each of its modes. For the lowest mode, which we assume is the only propagating mode, the transmission line is characterized by its propagation wavenumber k_{yop} and its characteristic admittance Y_{op} . The wavenumber k_{yop} has already been discussed above, but the characteristic admittance cannot be specified until we know the field polarization. Some general observations can be made nevertheless.

Since the leaky-wave line-source structures are *uniform* longitudinally, and any dielectric material is removed from the junction between the feed parallel-plate guide and the space above, the mode types are *separable* if designated correctly. The total field is separable into fields characterized by an H_z but no E_z , or an E_z but no H_z . The corresponding mode types are, respectively, the $H^{(z)}$ -type and $E^{(z)}$ -type modes, alternatively known as the $LSE^{(xy)}$ and $LSM^{(xy)}$ modes. The corresponding electric field polarizations are horizontal and vertical polarizations.

The characteristic admittances corresponding to these modes are [9]

$$Y_{op} = \frac{k_o^2 - k_z^2}{\omega \mu k_{yop}} \quad (2.18)$$

and

$$Y_{op} = \frac{\omega \epsilon k_{yop}}{k_o^2 - k_z^2} \quad (2.19)$$

for the H -type and E -type modes, respectively. The mode functions for the unit cell waveguide are discussed next for the case of horizontal polarization; the considerations are dual for vertical polarization.

For horizontal polarization, with the electric field of the lowest mode horizontal in the feed parallel-plate guide (i.e., $E = E_x$ only), the problem becomes greatly simplified when the azimuth angle is zero, that is, for $k_{xop} = 0$. The phase-shift walls then become electric walls, and the radiating junction discontinuity reduces to a step in parallel-plate guide for structures like those in Figs. 2.9 and 2.10. The result is even simpler for the structure in Fig. 2.11 since the unit cell walls then become simply an extension of the parallel-plate guide walls, and the discontinuity disappears altogether. Unfortunately, no corresponding simplification occurs for vertical polarization, where the phase-shift walls become magnetic walls.

C. THE MODE FUNCTIONS FOR THE UNIT CELL WAVEGUIDE

Inside the *parallel-plate guide*, the mode functions are all of sine or cosine form. For the horizontal polarization case, the modes are all $H^{(z)}$ -type (or $LSE^{(xy)}$) modes, meaning that there is no E_z component. In every plane parallel to the aperture, which is an xz plane with y perpendicular to it, the electric field of every mode has only an x component, so that the $\underline{e}_n(x, z)$ mode functions possess an \underline{x}_0 component only. The $\underline{h}_n(x, z)$ mode functions can have both \underline{x}_0 and \underline{z}_0 components.

From our papers [2,3] on the asymmetric strip antenna based on groove guide, we have

$$e_{x0}(x, z) = \frac{1}{\sqrt{a'}} e^{-jk_z z} = -h_{z0}(x, z) \quad (2.20)$$

$$e_{x1}(x, z) = \frac{\sqrt{2}}{\sqrt{a'}} \sin \frac{\pi x}{a'} e^{-jk_z z} = -h_{z1}(x, z) \quad (2.21)$$

where a' is the width of the parallel plate guide.

In the *periodic unit cell*, the mode functions e_{xn} and h_{zn} have the form

$$e_{xn}(x, z) = A e^{-jk_{xnp} x} e^{-jk_z z} \quad (2.22)$$

$$h_{zn}(x, z) = -A e^{-jk_{xnp} x} e^{-jk_z z} \quad (2.23)$$

where

$$k_{xnp} = k_{xop} + 2\pi n/a \quad (2.24)$$

which we treated in Sec. B. The negative sign in (2.23) follows from the coordinate system choice, and is the same as that in (2.20) and (2.21). To find A we employ the normalization condition

$$\int_0^a \int_0^a \underline{y}_0 \times \underline{e}_n \cdot \underline{h}_n^* dx dz = 1 \quad (2.25)$$

which yields $A = 1/\sqrt{a'}$. Coefficient A may be taken to be real since any phase

factor can be placed in the exponent so that it then drops out. We thus may write

$$h_{np}(x, z) = -z_0 \frac{1}{\sqrt{a}} e^{-jk_{xp}x} e^{-jk_z z} \quad (2.26)$$

with k_{xp} given by (2.24). The subscript p in h_{np} signifies "periodic."

If we let subscript g signify the parallel-plate "guide," then we should recognize that h_{ng} and h_{np} do not correspond one for one. The sum of the h_{ng} terms would go from 0 to ∞ , whereas that for the h_{np} terms runs from $-\infty$ to ∞ .

D. ANALYTICAL EXPRESSIONS FOR RADIATION PATTERNS OF LEAKY-WAVE ANTENNAS

This section contains considerations that are common to all the leaky-wave antennas under investigation, and for this reason the material is presented here.

Line-source antennas are characterized by three specifications: the angle θ_m of maximum radiation, the 3 dB beam width $\Delta\theta$, and the sidelobe level and distribution. These specifications will differ depending on the application for which the antenna is designed. Leaky-wave structures, as a special class of line-source antennas, are characterized by two quantities: the normalized phase constant β/k_o and the normalized leakage constant α/k_o . There exist *simple rules of thumb* that relate the values of θ_m and $\Delta\theta$ to the β/k_o and α/k_o of the leaky-wave structure. The first of these is

$$\sin \theta_m \approx \beta/k_o \quad (2.27)$$

where θ_m is the angle of maximum radiation measured from the broadside direction. Then, one must choose some length L for the antenna aperture. The length is selected as a compromise between antenna efficiency and excessive length, and it is usually chosen so that 90% or so of the power is radiated, with the remaining 10% absorbed by a matched load. This length is related to the α/k_o of the leaky-wave structure by

$$\frac{L}{\lambda_o} \approx \frac{0.183}{\alpha/k_o} \quad (2.28)$$

The beam width $\Delta\theta$ is determined primarily by the aperture length L , but it is also influenced by the aperture field distribution. It can vary somewhat, being narrowest for a constant aperture field and wider for sharply peaked distributions. A simple middle-of-the-range result is provided by the following expression:

$$\Delta\theta \approx \frac{1}{(L/\lambda_o) \cos \theta_m} \quad (2.29)$$

where $\Delta\theta$ is in radians. For a constant aperture distribution, the unity factor in the numerator should be replaced by 0.88. When the leaky-wave structure is maintained uniform along its length, its aperture distribution is exponentially decaying; when the length L corresponds to 90% power radiation, the beam width given by (2.29) is almost exactly 10% too large. For such a distribution, the unity factor should be replaced by 0.91.

Our next consideration involves the *full radiation patterns* that result from different aperture field distributions. It is well known that the power radiation pattern $R(\theta)$ is given by

$$R(\theta) \sim \left| k_o \int G_p(z) e^{jk_o z \sin \theta} dz \right|^2 \cos^2 \theta \quad (2.30)$$

where, as before, θ is measured from the broadside direction. The j in the exponent corresponds to the usual time dependence $\exp(j\omega t)$; if, as in the steepest-descent-plane considerations discussed in Chap. IX, the time dependence is $\exp(-i\omega t)$, we simply replace j by $-i$.

When the amplitude of the aperture distribution is *constant*,

$$G_p(z) = e^{-j\beta z} \quad (2.31)$$

meaning that the field along the aperture consists of a traveling wave of constant amplitude along the aperture length. Substitution of (2.31) into (2.30) and subsequent integration yields the well-known result

$$R(\theta) \sim (k_o L \cos \theta)^2 \frac{\sin^2 \left[(\beta/k_o - \sin \theta) k_o L / 2 \right]}{\left[(\beta/k_o - \sin \theta) k_o L / 2 \right]^2} \quad (2.32)$$

When the geometry of the leaky-wave antenna is maintained uniform along the antenna length, the aperture field distribution is *exponentially decaying*, i.e.,

$$G_p(z) = e^{-j(\beta - j\alpha)z} \quad (2.33)$$

If the antenna length is infinite, one finds, after substituting (2.33) into (2.30) and integrating,

$$R(\theta) \sim \frac{\cos^2 \theta}{(\alpha/k_o)^2 + (\beta/k_o - \sin \theta)^2} \quad (2.34)$$

This pattern does not produce any sidelobes.

If the antenna length is L , use of (2.33) in (2.30) yields

$$R(\theta) \sim \frac{1 + e^{-2k_o L (\alpha/k_o)} - 2e^{-k_o L (\alpha/k_o)} \cos \left[(\beta/k_o - \sin \theta) k_o L \right]}{(\alpha/k_o)^2 + (\beta/k_o - \sin \theta)^2} \cos^2 \theta \quad (2.35)$$

-47- / 48

NRD GUIDE ANTENNAS

III.	THE ASYMMETRIC NRD GUIDE LEAKY-WAVE LINE SOURCE	51
A.	DESCRIPTION OF THE ASYMMETRIC LEAKY-WAVE ANTENNA	54
B.	LEAKAGE WITHIN THE PARALLEL-PLATE REGION	56
	1. Analysis and Numerical Results	56
	2. Behavior Near Cutoff	65
C.	ANTENNA WITH FINITE SIDE WALLS: COUPLING EFFECTS	71
	1. The Transverse Equivalent Network	71
	2. Coupling Effects in the Propagation Characteristics	74
	a. Qualitative Features	74
	b. Quantitative Results	77

III. THE ASYMMETRIC NRD GUIDE LEAKY-WAVE LINE SOURCE

(With: Prof. H. Shigesawa, Dr. M. Tsuji
Doshisha University, Kyoto, Japan
and Prof. S.T. Peng, Mr. K.M. Sheng
New York Institute of Technology,
Old Westbury, NY)

Nonradiative dielectric (NRD) guide is one of the newer waveguides for millimeter wave use, and it shows promise for application to millimeter wave integrated circuits. It is basically a modification of H guide where the plate separation is reduced to less than half of a free-space wavelength; because of this change, discontinuity structures that maintain the symmetry of the waveguide become purely *reactive*, and components can be built readily and connected together in integrated circuit fashion. Yoneyama and Nishida, who first proposed [9] the NRD guide, have also designed and measured many components for this guide type, and have demonstrated its attractiveness. The basic NRD guide (together with the primary orientation of the electric field) is shown in Fig. 3.1(a).

The Final Report on the predecessor contract [1] presented the details of a thorough study on the *first antenna* proposed by anyone that is based on NRD guide. That antenna employed a *foreshortened top* (or side, depending on orientation) to achieve the desired leakage, and produced a polarization that was the same as that of the main electric field component in the basic waveguide. In addition, careful and systematic measurements were performed that demonstrated excellent agreement with the theory. That study is complete, and detailed results have been published [4,5].

A second antenna, that is treated here, is based on a different leakage mechanism, that of *asymmetry*. The asymmetry is produced by introducing an air gap between the dielectric region and one of the metal plates. For the antenna application, the structure is also bisected so that radiation occurs from the top only. The resulting configuration appears in Fig. 3.1(b). A description of the antenna and a discussion of its leakage mechanism are presented in Sec. A.

It was first recognized that some of the early results obtained for the leakage could be applied to the problem of cross talk produced by an inadvertently created small air gap that occurred within some NRD guide integrated circuitry. Results were calculated for certain parameter values, and considerations were given to what gap

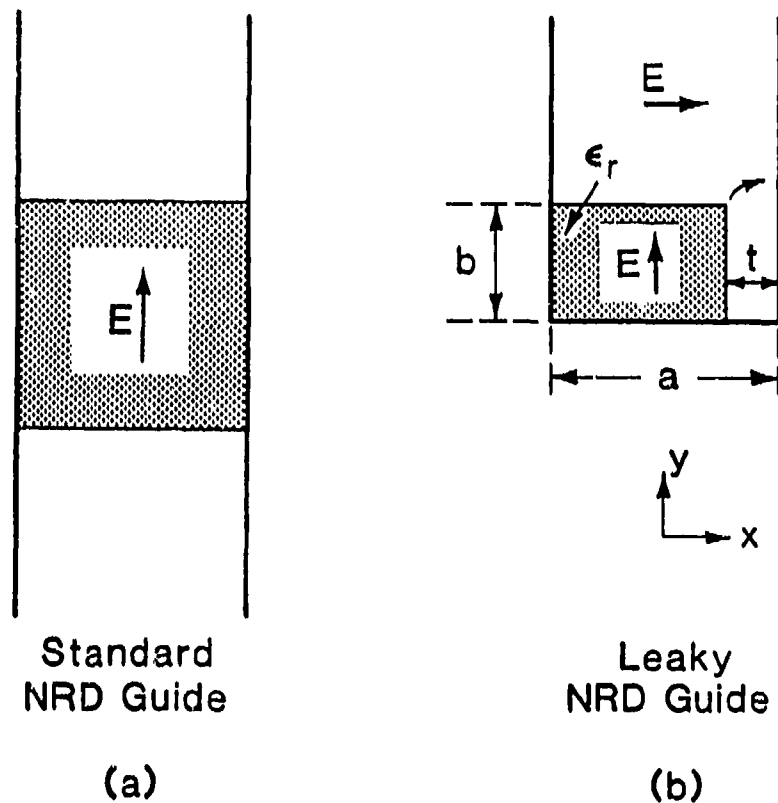


Fig.3.1 (a) NRD (nonradiative dielectric) guide, which is like H guide except that the spacing a is made less than $\lambda_o/2$ to insure that discontinuities are reactive.

(b) Structure obtained when the NRD guide is bisected and an air gap is introduced between the dielectric strip and one metal side wall. The modifications produced in the electric fields are also shown.

size is permissible before any noticeable effect is introduced. Some of the results of that investigation were presented at the 1985 IEEE International Microwave Symposium and summarized in its Digest [10].

Those results were derived for a structure for which the parallel-plate walls were extended to *infinity*. The length of those walls must of course be finite in a practical antenna, but it turns out that the results for infinite walls yield all the basic parametric dependences and performance insights, and the structure is then easier to analyze.

For the application to cross talk within NRD guide integrated circuitry, infinite-length walls are appropriate; it also turns out, as will be shown in Chap. IV, that the results for infinitely long walls are exactly correct when applied to the linear array of NRD guide line sources, shown in Fig. 1.4 of Chap. I, when all the line sources in the array are in phase, so that the cross-plane scan angle is zero.

Many new and more recent results are presented in Sec. B for the antenna with infinitely long walls, or, as phrased there, for leakage within the parallel-plate region. Included there are the method of analysis and various numerical results. Parametric dependences are shown, and some insights are presented into the unusual propagation wavenumber behavior just above cutoff.

The study of an actual antenna with parallel-plate walls of *finite* length is described in Sec. C. The analysis of the behavior of the leakage constant α and the phase constant β as a function of the length of the walls yielded some interesting and unexpected new effects. These initially puzzling effects were found to result from the simultaneous presence of *another* leaky mode, and the *coupling* between the two leaky modes over certain parameter ranges. These results are particularly important because it was found later that such coupling, with resultant complex behavior, occurs in other configurations as well (see discussions and examples in Chaps. IV, VII and X). These effects in an NRD guide antenna were discussed in two symposia and summarized in the respective Digests [11,12].

This new NRD guide leaky-wave antenna, based on asymmetry, is of interest because of its simple configuration, its large range of leakage rates (so that a large range of beam widths can be achieved), its ease of connection with NRD guide integrated circuitry, and the fact that its width is less than half a wavelength. This last point is of particular interest when the antenna is used as a line source in a phased array of such line sources, since grating lobes would then automatically be eliminated. The interesting performance features of a phased array of such NRD guide line sources are described in Chap. IV.

A. DESCRIPTION OF THE ASYMMETRIC LEAKY-WAVE ANTENNA

The leakage mechanism for this type of antenna is best understood by examining Figs. 3.1(a) and (b). Figure 3.1(a) represents the cross section of the nonradiating NRD guide. The principal electric field component is shown, and is seen to be parallel to the metal walls. The mode guided in the axial (longitudinal) direction is thus not the dominant mode, but the lowest mode of opposite polarization. A discontinuity that maintains the symmetry, such as a change in width b , will be purely reactive for this mode (provided that plate spacing a is maintained less than $\lambda_o/2$), whereas the same discontinuity for the dominant mode would produce leakage into the TEM mode on both sides. The lengths of the walls in Fig. 3.1 are not specified, but let us assume that they are of finite length and that they are sufficiently long that the evanescent transverse field in the air regions of the mode discussed above has negligible amplitude at the open ends.

In the second structure, that in Fig. 3.1(b), the asymmetrically placed air gap introduces new field components, as is shown in the figure for the electric field. As is seen, the distortion of the electric field lines produces a net horizontal electric field, thereby exciting the TEM mode in the parallel plate region away from the dielectric strip. Since the TEM mode will propagate at all frequencies, it will carry power away from the dielectric strip region at an angle toward the opening at the top, thereby producing *power leakage*.

Although the NRD guide will operate satisfactorily as a waveguide whether the guided mode is fast or slow, the antenna with the asymmetric air gap will radiate only when the guided wave is *fast*. This requirement follows readily from the wavenumbers. For the TEM mode, which is the $n = 0$ transverse mode,

$$k_o^2 = k_z^2 + k_{yo}^2, \text{ or } k_{yo} = [k_o^2 - k_z^2]^{1/2} \quad (3.1)$$

where k_z is the wavenumber of the guided wave (in the axial direction), and k_{yo} is the transverse wavenumber in the y direction in the outer air regions. If the guided wave is a fast wave, $k_o > k_z$, so that k_{yo} is real; for a slow wave, k_{yo} is imaginary, and the wave is evanescent transversely. (Actually, k_z and k_{yo} will possess small imaginary parts when leakage occurs, so that k_z and k_{yo} are really complex, but the simple physical idea presented above is still valid.)

For an actual leaky-wave antenna, the antenna aperture amplitude distribution is tapered to control the side lobes. In this structure, such a taper can be produced easily

by simply changing the thickness of the air gap, beginning with it completely closed and then gradually (in distance) opening it. Other NRD guide structures may be devised that are also based on the introduction of asymmetry, and that therefore leak in the same fashion. F. Schwering [13] has recently proposed two interesting ones that also lend themselves easily to tapering the aperture amplitude distribution so as to lower the sidelobe level. These two structures do not introduce an air gap but instead place a perturbing mechanism directly on the top of the dielectric-air interface in the symmetrical NRD guide of Fig. 3.1(a) (after bisection). One proposed structure has a small dielectric strip placed at the air-dielectric interface next to one of the parallel-plate walls; for the tapering, the width or height of the strip would be modified. The second structure has a metal strip that would be deposited asymmetrically on the air-dielectric interface, perhaps next to one of the walls. The tapering would be performed by varying the width of the metal strip, a task that could be accomplished lithographically all at once by employing a mask.

B. LEAKAGE WITHIN THE PARALLEL-PLATE REGION

1. Analysis and Numerical Results

We first consider the case for which the parallel-plate walls are infinitely long in Fig. 3.1(b). The leakage then occurs into a parallel-plate region. As mentioned above, this special case corresponds exactly to the situation in which the linear array of NRD guide line sources discussed in Chap. IV is phased so that the cross-plane scan angle is zero. The results here will be applied directly in Chap. IV. In addition, however, the analysis for walls of infinite length is simpler than the one for walls of finite length, yet the results obtained here yield all the basic performance information and parametric dependences.

In the analysis, we view the cross section of the structure in the vertical (y) direction. A dielectric step junction is then seen to be present at the interface between the air and the dielectric regions in Fig. 3.1(b). At that junction, all the *transverse* modes are excited in both the air region and the partially dielectric-filled region. How to designate these transverse modes appropriately becomes a minor problem. In the air region, it is easy since there is only one medium in the parallel plate region, and only the TEM transverse mode is above cutoff. To be more precise, since that "TEM" mode propagates at an angle to the longitudinal (z) axis, we should designate it as the TE_0 mode with respect to the y direction (but TEM in its actual angle of propagation). For the partially dielectric-filled parallel-plate region, three transverse modes are above cutoff, but to designate them in TE or TM terms we must view them with respect to the x direction since separability into such modes occurs only in the x direction. One of the three modes (which of course are all surface-wave modes) is the exciting mode, which is the (lowest) TE_1 surface-wave mode viewed in the x direction. The other two are the lowest and the first higher TM surface-wave modes, and they are excited by the dielectric step junction. The (lowest) TM_0 mode corresponds to the TEM mode in the air region mentioned above, viewed in a different direction. The (other) TM_1 mode is degenerate with the TE_1 mode in the limit of vanishing air gap. The remaining modes on both sides are evanescent, and are therefore stored in the vicinity of the junction and contribute to its reactive nature.

When these same transverse modes are viewed with respect to the y direction, their designations change. We recognize that these modes will bounce back and forth between the side walls in Fig. 3.1(b), so that they are hybrid modes when viewed in the y direction. The TE_1 mode when viewed in the x direction then becomes the $(H_1)_x$ -type mode or the $(LSE_1)_{yz}$ mode when viewed in the y direction. Similarly,

the TM_1 mode becomes the $(E_1)_x$ -type or $(LSM_1)_{yz}$ mode. The notation $(H)_x$ -type means that the mode does not propagate in the x direction but is separable in that direction as an H or TE mode; $(LSE)_{yz}$ means that the mode contains only the electric field in the longitudinal section defined by the yz plane. Either notation is cumbersome (and neither has been "standardized") but each is actually clear. The TM_0 surface-wave mode viewed in the x direction becomes the $(E_0)_x$ -type or $(LSM_0)_{yz}$ mode; in the air region, the hybrid nature is lost and the mode becomes simply the TE_0 mode mentioned earlier.

The propagation characteristics of the leaky-wave structure were obtained by a *mode-matching procedure* in the transverse (y) direction similar to that described in detail for the analysis of leakage from dielectric strip waveguides [14,15]. Thirty transverse modes (15 TE and 15 TM) in each region were included in the computer program. Of the modes in the air-filled parallel-plate region, only the TEM mode at an angle, or, more correctly, the TE_0 mode, is above cutoff, so it is the only mode to contribute to the leakage of power. Curves for both the normalized phase constant β/k_0 and the normalized leakage constant α/k_0 as a function of the normalized dielectric strip width b/λ_0 are presented in Figs. 3.2 and 3.3, with the normalized air gap thickness t/λ_0 as a parameter.

Although accurate quantitative curves are presented, we are concerned first with their *qualitative* behavior. The effect of the air gap is to *speed up* the wave, which is to be expected since more of the wave is now in the air region. The values of β/k_0 are therefore lowered somewhat by the air gap. The behavior of α requires more detailed consideration. Since the theory neglects material losses, the value of α is zero in the absence of a gap; the value of α (or α/k_0 , when we normalize it to the free-space wavenumber) thus represents only the leakage itself.

In the curves of α/k_0 in Fig. 3.3, we note that, as the width b increases, there appear three main features. *First*, the curves in the neighborhood of $b/\lambda_0 = 0.15$ to 0.20 undergo a change in the curvature. This variation occurs in the vicinity of cutoff, as the nature of the attenuation changes from radiative above cutoff to primarily reactive below cutoff. The location of cutoff may also be noted in Fig. 3.2, where the curves approach $\beta/k_0 = 0$. *Second*, we observe a general decrease in the value of α/k_0 as b/λ_0 increases. As one moves away from cutoff, the angle that the pair of surface waves makes with the metal bottom and the upper wall of the dielectric strip becomes closer to grazing, with the result that the amount of TE-TM coupling becomes reduced. The leakage power is therefore correspondingly reduced.

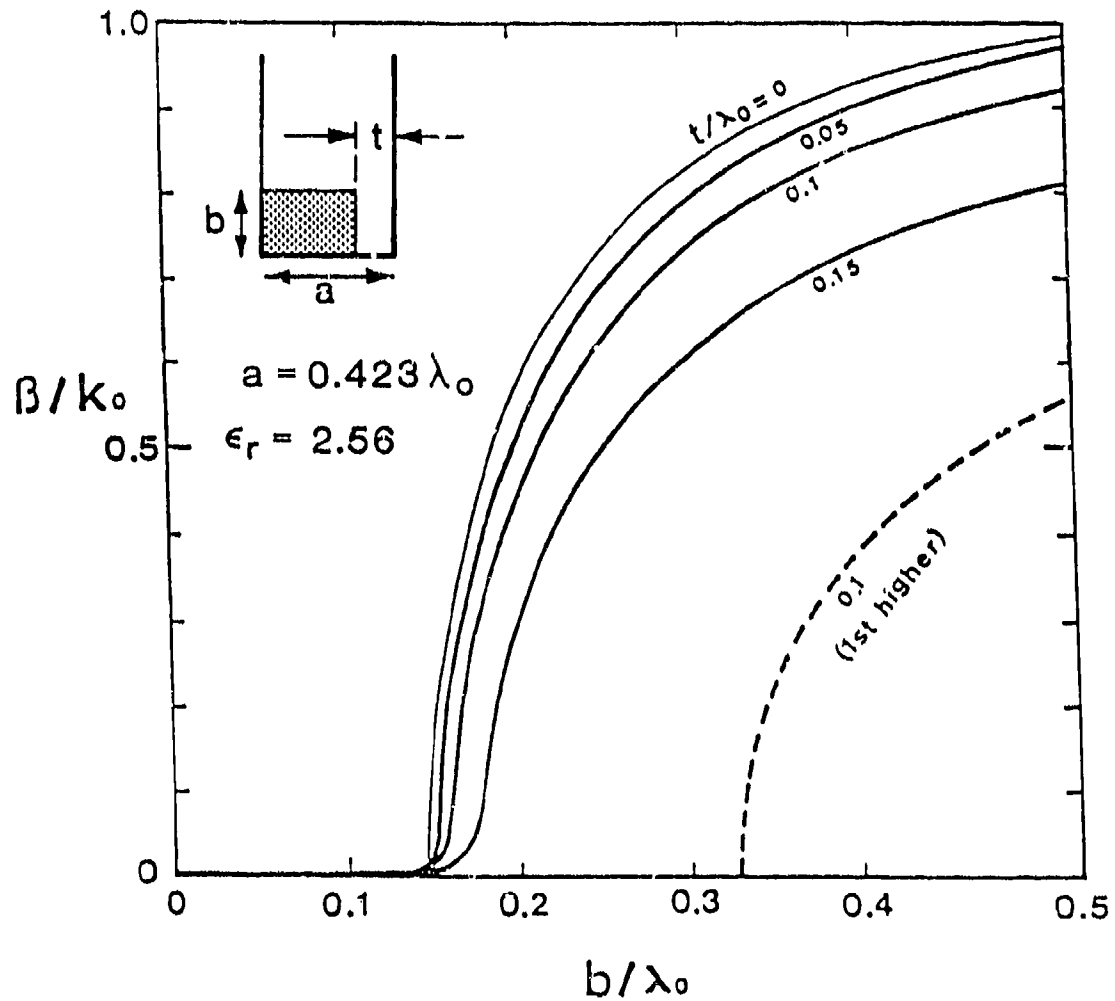


Fig. 3.2

Curves of the normalized phase constant as a function of the dielectric width, with the air gap thickness as a parameter. The solid lines refer to the dominant mode, and the dashed line to the first higher mode.

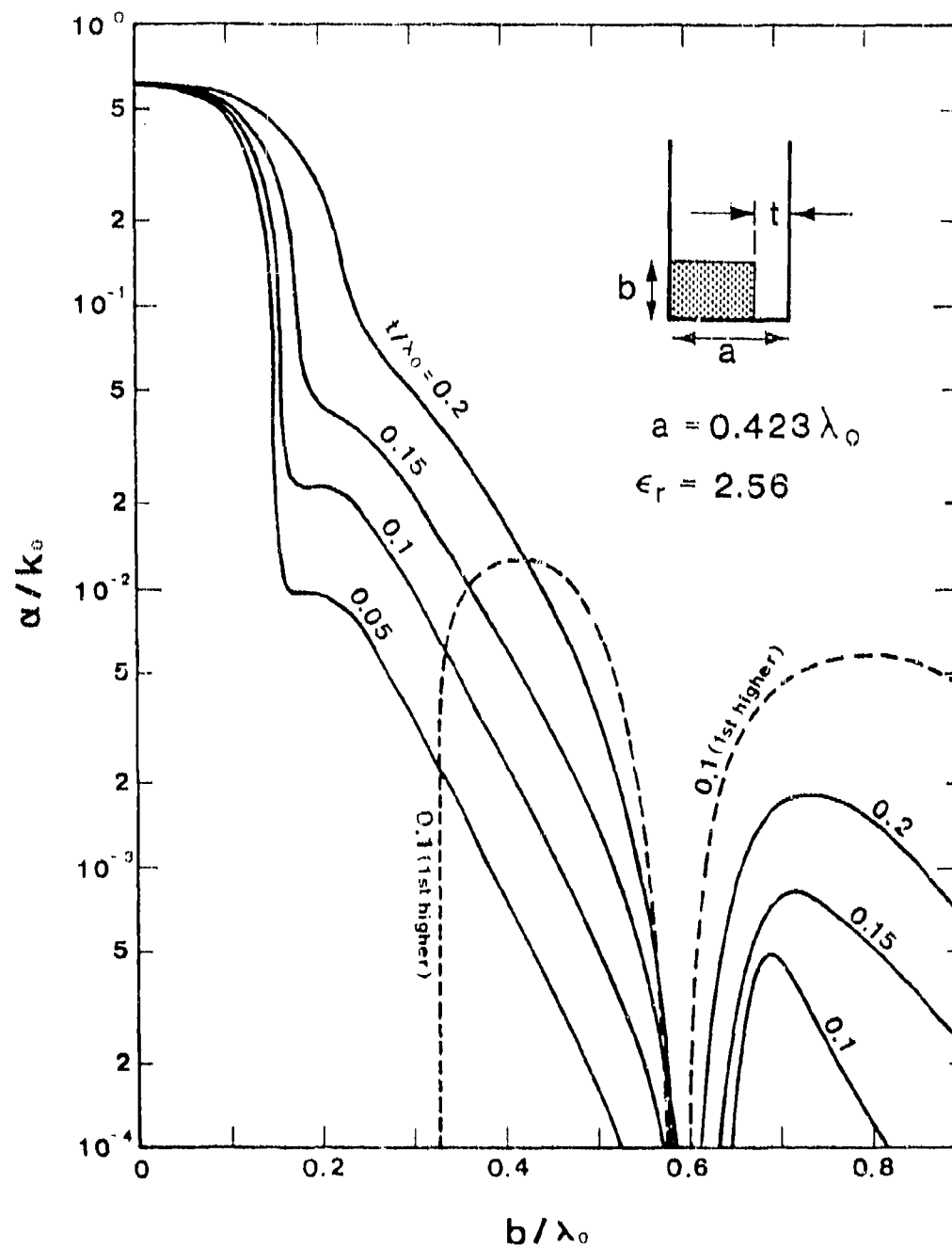


Fig. 3.3 Same as for Fig. 3.2, but for the normalized leakage constant.

The *third* main qualitative feature in Fig. 3.3 is the presence of a pronounced dip in the vicinity of $b/\lambda_0 = 0.6$. This dip is due physically to the mode-converted TM surface waves that bounce back and forth at an angle between the top of the dielectric strip and the metal bottom wall. At appropriate widths, a cancellation effect occurs and the value of α is reduced sharply. It is therefore interesting to note that the α itself is due to the leaking TEM wave in the parallel-plate region, but the strong dip in the value of α relates to the TM surface waves in the dielectric strip region.

Some *similar* qualitative features in the behavior of α as a function of strip width was found for leakage from dielectric strip waveguides [15]. The same basic TE-TM mode conversion at the strip sides produced both the α itself and the sharp cancellation effects in those cases as well. Another interesting similarity is that the dominant mode in each of these waveguide types can never leak, but that the lowest mode of the *opposite* polarization can leak. Furthermore, the power that leaks away has a polarization *opposite* to that possessed by the main portion of the guided mode, in contrast to the situation for customary leaky-wave antennas. These qualitative similarities exist despite certain important geometric differences between the present structure (Fig. 3.1 (b)) and the dielectric strip waveguides.

Nevertheless, there are important *differences* between these guide types. One difference between them is that the leakage power is carried by a TEM mode in the NRD guide structure rather than by a surface wave. A more important difference relates to the behavior as the dielectric strip width b approaches zero. In the dielectric strip guides, the outside region can always support a surface wave in some direction, so that its effective dielectric constant for the basic transverse mode is real and positive. In contrast, the outside region in the asymmetric NRD guide structure, corresponding simply to the parallel plates, is below cutoff for the basic transverse mode (the TE_1 mode in the y direction), so that its effective dielectric constant in that region is negative real. As a result, the lowest longitudinal guided mode for the overall structure is above cutoff for *any* value of dielectric strip width in the case of dielectric strip guides, whereas, for the structure in Fig. 3.1(b), the longitudinal guided mode will go *below cutoff* if the strip width b becomes sufficiently small. This feature explains why the curves in Figs. 3.2 and 3.3 demonstrate a cutoff at a non-zero value of width b .

Also shown in Fig. 3.2 and 3.3, are dashed curves representing the behavior of the first higher mode, for $t/\lambda_0 = 0.1$. There are some interesting features regarding their characteristics (for example, the behavior at and below cutoff is different from that for the dominant mode) but we shall not discuss them here.

The variation of b/k_o as a function of the air gap thickness t/λ_o is given in Fig. 3.4, where dielectric width b/λ_o appears as a parameter. In agreement with Fig. 3.3, we observe that the leakage rate falls substantially as b/λ_o is increased, approaching the sharp drop in α/k_o as $b/\lambda_o \approx 0.6$. As expected, the leakage rate increases as t/λ_o is made larger.

To assess the relative magnitude of the leakage, it is useful to compare it with measured values of *metal wall and dielectric losses* encountered in NRD guide. Yoneyama has found that for teflon the measured wall and dielectric losses at 50 GHz amount to about 5 dB/m. The ordinate quantity α/k_o in Figs. 3.3 and 3.4 expresses the leakage in terms of nepers per wavelength, divided by 2π . The measured losses at 50 GHz thus translate into the value 5.5×10^{-4} on the ordinate scale in Figs. 3.3 and 3.4. When we superimpose that value on these curves, we obtain some quantitative measure of when the leakage becomes meaningful. With that measure, we see that a gap of $t/\lambda_o = 0.01$, which is about 2.5% of the plate spacing, yields a leakage value that is less than the measured losses for $b/\lambda_o > 0.25$ or so. For b/λ_o about 0.6, on the other hand, the leakage is negligible for all gap thicknesses.

The dependence of β/k_o on the value of the dielectric constant ϵ_r is presented in Fig. 3.5, with air gap t/λ_o as a parameter for two different values of b/λ_o . Changing the size t of the air gap, for small values of t , has little effect on the values of β/k_o , in agreement with Fig. 3.2. Varying the dielectric constant and the dielectric width do change β/k_o significantly. Note that when the value of ϵ_r is increased sufficiently the longitudinal guided wave is no longer a fast wave; β/k_o exceeds unity then and the structure no longer leaks.

The corresponding curves for α/k_o as a function of ϵ_r appear in Fig. 3.6. Consistent with the information in Fig. 3.4, we see that α/k_o depends strongly on both t and b . What is interesting here is that the leakage rate α appears to be affected relatively little by changing ϵ_r until the value is reached corresponding to $\beta/k_o = 1$, at which the guided wave becomes slow and all leakage stops.

The ordinate scale on the right-hand side of Fig. 3.5 represents the angle of the radiated beam, as shown in the inset in that figure. In the design procedure, we see that the angle of the main beam can be influenced to first order by the choice of ϵ_r , and that the leakage rate, from Fig. 3.6, will then be affected to second order only.

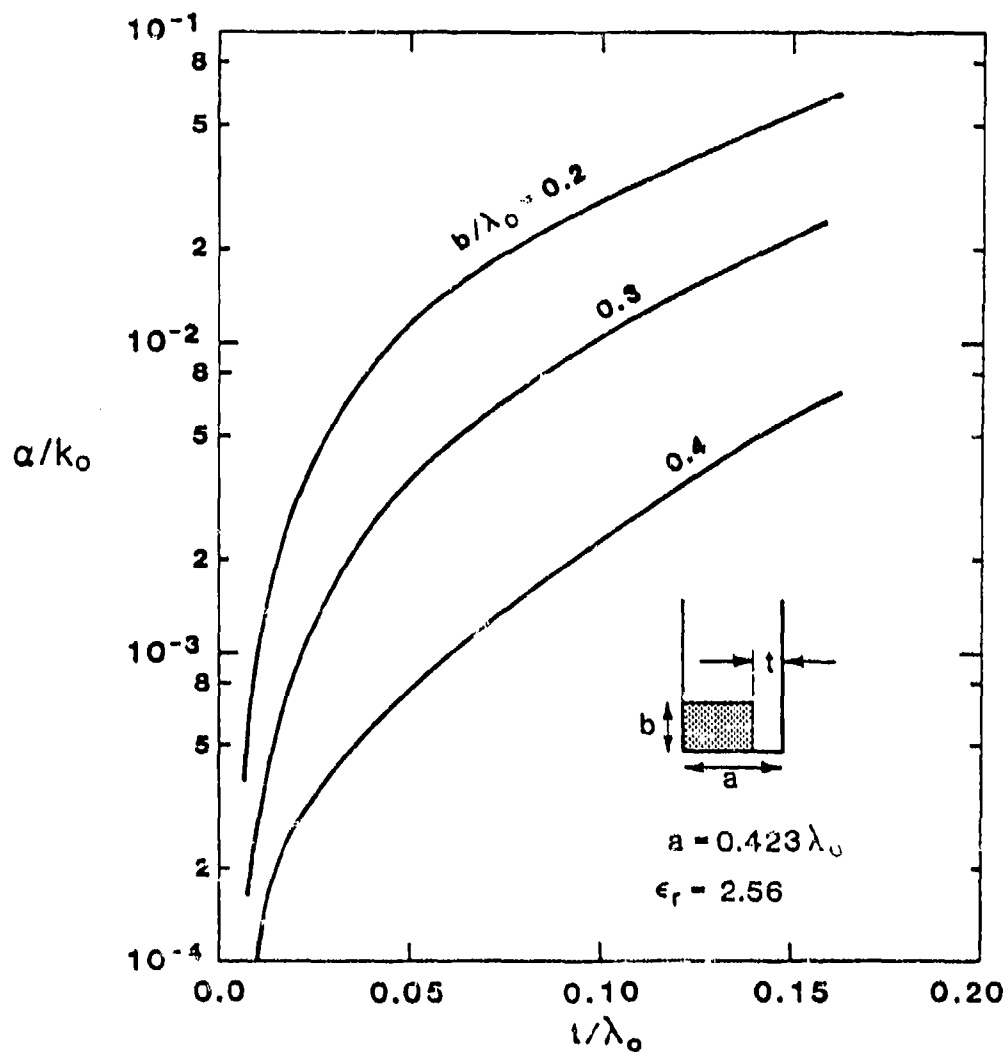


Fig. 3.4

The variation of the normalized leakage constant as a function of the air gap thickness, with the dielectric width as a parameter.

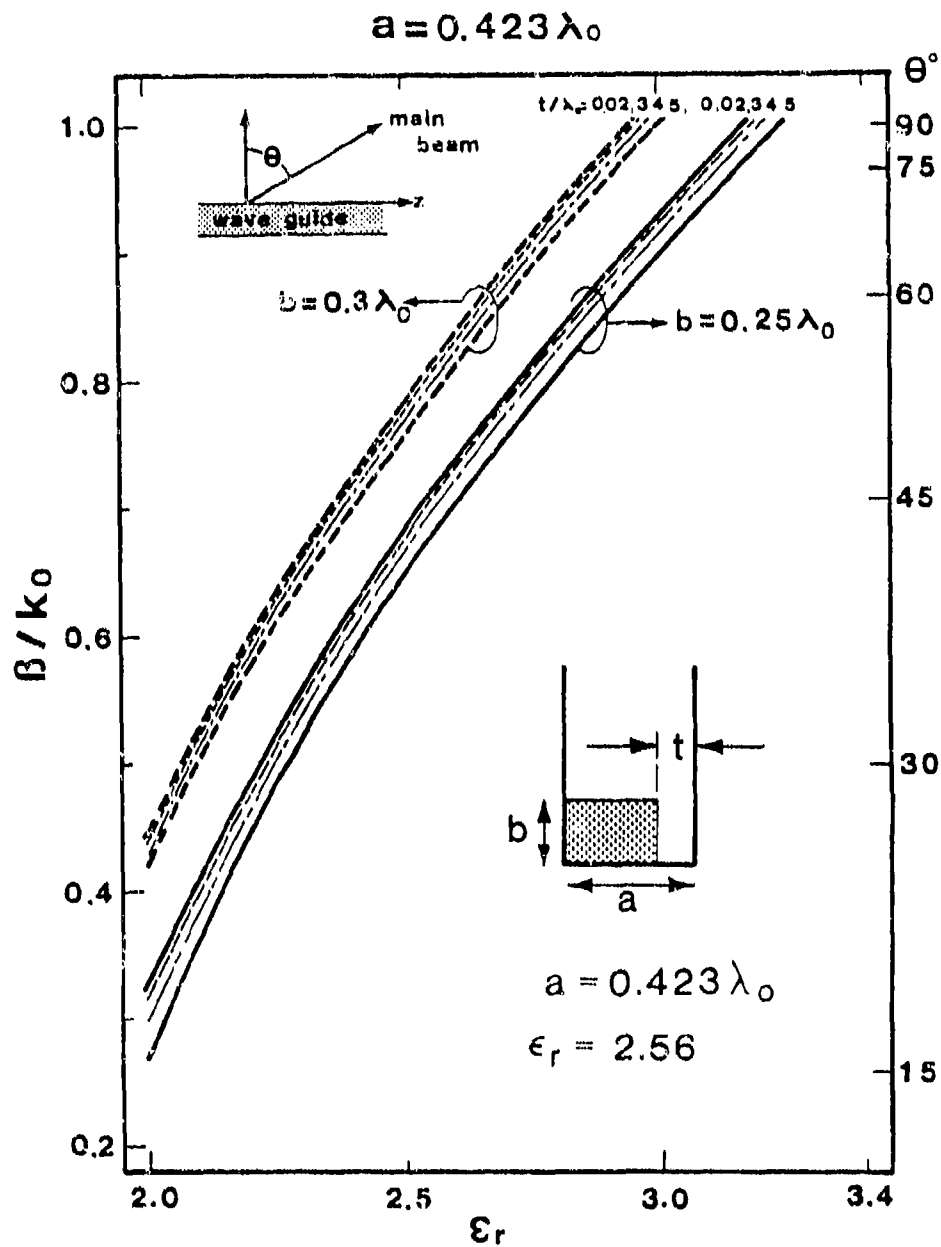


Fig. 3.5 Dependence of the normalized phase constant β/k_0 and the beam angle θ in degrees on the dielectric constant, for two different dielectric widths b/λ_0 and with the air gap thickness t/λ_0 as a parameter.

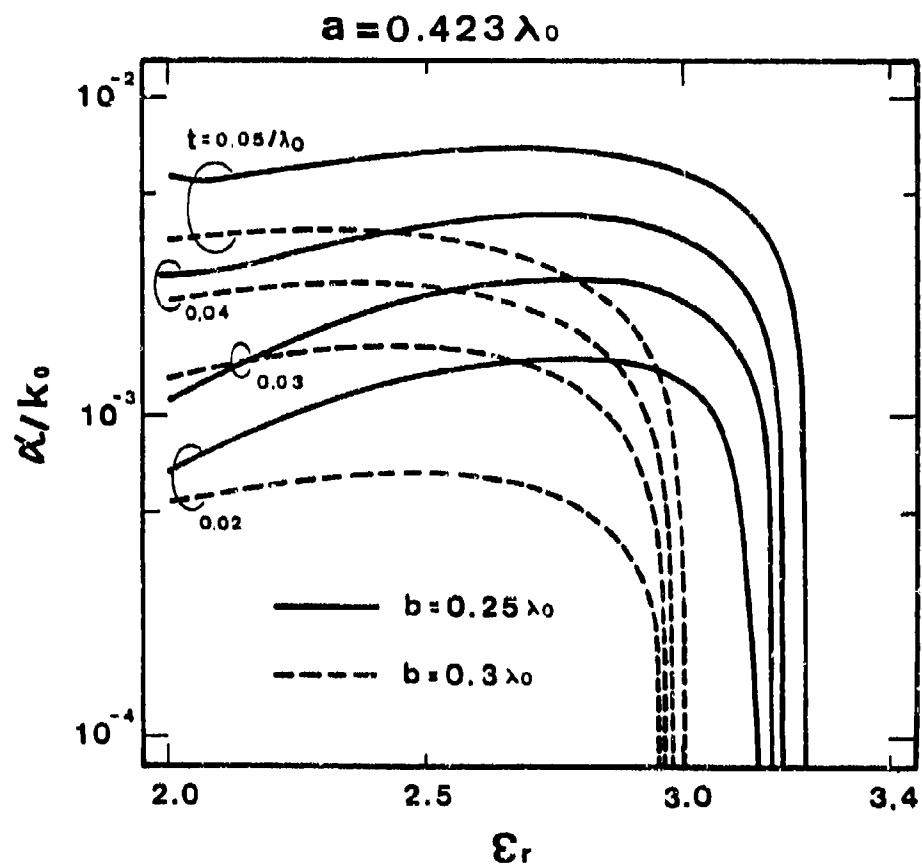


Fig. 3.6

Same as for Fig. 3.5, but for the normalized leakage constant α/k_0 .

2. Behavior Near Cutoff

The variation of α/k_o as a function of b/λ_o in the vicinity of cutoff, as shown in Fig. 3.3, indicates some interesting behavior, and caused us to inquire further into this region. In Fig. 3.7 we present corresponding results for additional values of t/λ_o that are *smaller* than the original set, and we also extend the curves down to zero width for the dielectric material (i.e., $b/\lambda_o = 0$). Also shown in Fig. 3.7 is a dashed line that corresponds to the curve for the reactive attenuation of the NRD guide basic mode (for $t/\lambda_o = 0$) below cutoff; the cutoff occurs at $b/\lambda_o = 0.145$.

For the values of t/λ_o less than 0.05 we find that the curves exhibit a distinct peak and then decrease to some minimum value just before cutoff; below cutoff, the reactive contribution rapidly becomes dominant. As expected, the value of maximum attenuation decreases as the thickness of the air gap goes to zero. We observe, however, that for all the curves, and particularly for those for larger values of t/λ_o , the total attenuation constant is higher than the reactive value alone, indicating that some power leakage still occurs in the region below cutoff.

The behavior *just above cutoff* suggests that two competing effects may be occurring there. To obtain further clarification, we changed the value of the metal plate spacing a , thereby modifying slightly the value of b/λ_o corresponding to cutoff. Calculations of α/k_o vs. b/λ_o were then repeated for the case $t/\lambda_o = 0.05$, a median value for which only a very small dip was found in Fig. 3.7. The resulting curve for the new value of $a/\lambda_o = 0.45$ is shown in Fig. 3.8, together with the curve for $a/\lambda_o = 0.423$ copied from Fig. 3.7 for comparison. Also shown are the dashed curves for each value of a/λ_o corresponding to the purely reactive attenuation due to the NRD guide mode below cutoff, as in Fig. 3.7.

The new curve in Fig. 3.8 demonstrates that a small shift in the cutoff location can produce a rather different-looking result, strengthening the belief that something else is changing rapidly exactly in that region. The shift in the cutoff to a lower value of b/λ_o caused a clear peak to appear, followed by a sharp dip, similar to the behavior in Fig. 3.7 for smaller values of t/λ_o .

The end points for α/k_o corresponding to $b/\lambda_o = 0$ may be independently checked in a simple way. We recognize that as $b \rightarrow 0$ the value of k_{y10} of the exciting $n = 1$ mode approaches zero. More precisely, the decay rate $|k_{y10}|$ in the air region goes to zero, with the field spreading out in the vertical direction. From the sum-of-squares relation for that mode for the air region

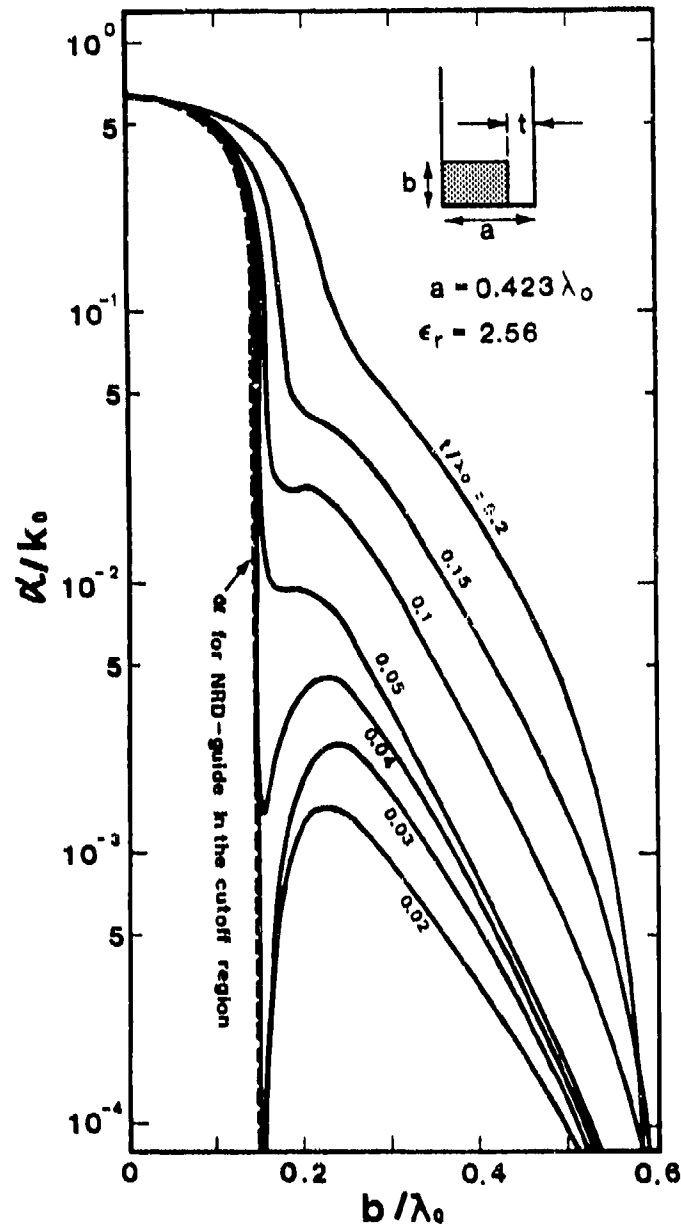


Fig. 3.7

Curves for the normalized leakage constant as a function of dielectric width, with stress on the region near and below cutoff. These plots go beyond those in Fig. 3.3 in that additional curves are included for lower values of air gap thickness, and all curves are extended to zero dielectric width. The dashed curve represents the reactive attenuation below cutoff for the basic NRD guide mode (for $t/\lambda_0 = 0$).

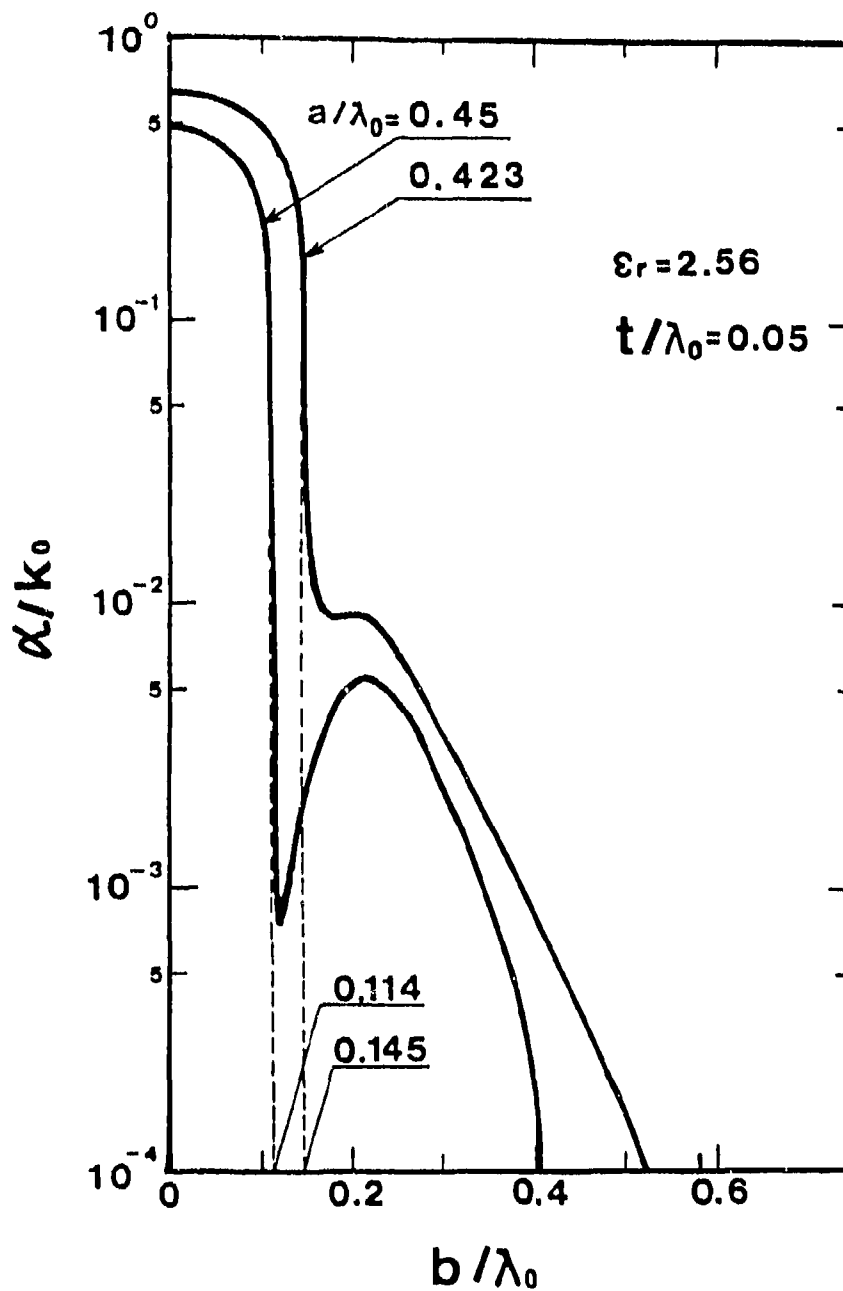


Fig. 3.8

Curves similar to those in Fig. 3.7, except only for $t/\lambda_0 = 0.05$ and for two different values of plate spacing a/λ_0 . A small change is produced in the location of the cutoff, but a large change in the shape of the curve.

$$k_o^2 = k_x^2 + k_{y10}^2 + k_z^2 = (\pi/a)^2 + 0 - \alpha^2 \quad (3.2)$$

where we have set $k_z = -j\alpha$ since we are far below cutoff, we obtain

$$\frac{\alpha}{k_o} = \left[\left(\frac{\lambda_o}{2a} \right)^2 - 1 \right]^{1/2} \quad (3.3)$$

Using (3.3), we find $\alpha/k_o = 0.630$ and 0.484 , respectively, for $a/\lambda_o = 0.423$ and 0.450 ; these values are seen to agree very well with the end points in Fig. 3.8. It should be noted that a different result would be found if the frequency, rather than dielectric width b , were made to approach zero. The vertical decay rate would still become zero, but k_o would also become zero, so that $\alpha = \pi/a$, and α/k_o would diverge.

Returning to the possible competing effect mentioned above, let us first assume that the conversion of power from the exciting $n = 1$ mode into the leaking TEM mode at an angle is due primarily to the dielectric corner junction discontinuity at the air-dielectric interface. The relative amount of power converted, and thus the structure's leakage rate, should therefore be proportional to the relative magnitude of the field of the exciting mode at the air-dielectric interface. That field magnitude should be given to a very good approximation by the corresponding value for the NRD guide basic mode (setting $t/\lambda_o = 0$). Next, we recall that the value of $|k_{y10}|$, the decay rate in the air region for the exciting $n = 1$ mode, varies with the value of b/λ_o . As a result, the field distribution in the y direction, in both the air and dielectric regions, will change as b/λ_o is varied.

The solid curve in Fig. 3.9 represents the ratio of the square of the normal component field at the air-dielectric interface to the total power in the cross section, for the NRD guide basic mode, as a function of b/λ_o . The total power was obtained by integrating the Poynting vector over the cross section. This ratio would be expected to have a maximum at some intermediate value of b/λ_o , since near zero the field is spread out greatly and the value at the interface would be negligible, whereas for very large values almost all the power resides in the dielectric region, with the value at the interface becoming small. Also appearing in Fig. 3.9 is the dashed curve for the case $t/\lambda_o = 0.1$ (note that b/λ_o is not taken down to zero in Fig. 3.9). It is very interesting that the value of b/λ_o for the peak in the solid curve corresponds very closely to that for the subsidiary peak in the dashed curve. The sharp drop in the solid curve for

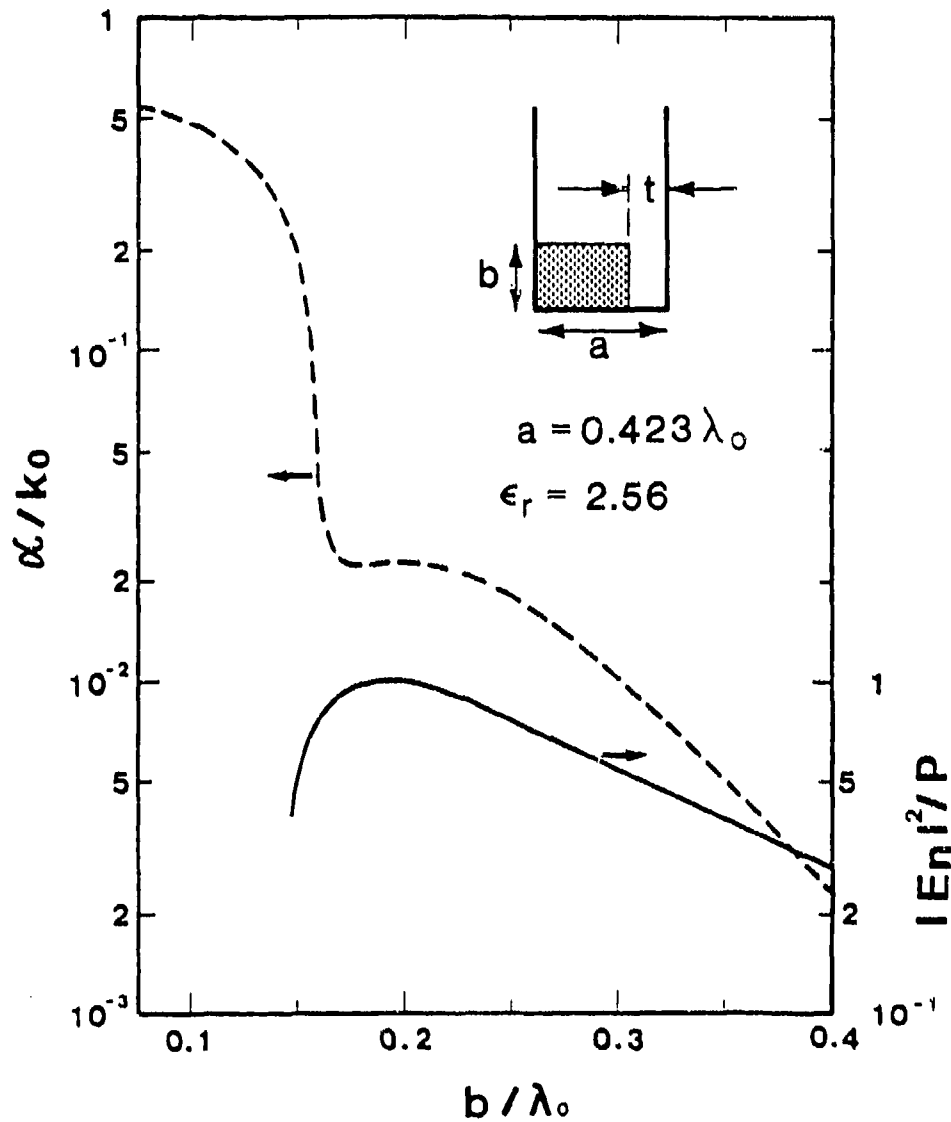


Fig. 3.9

Curve (solid), as a function of dielectric width b/λ_0 , of the ratio of the square of the normal component of the electric field at the air-dielectric interface to the total power for the NRD guide basic mode. Also shown (dashed) is the variation with b/λ_0 of α/k_0 for $t/\lambda_0 = 0.1$, taken from Fig. 3.7. The peak in the solid curve occurs near cutoff and explains the peculiar bump in the dashed curve.

lower values of b/λ_o also appear to explain the drops in the curves of α/k_o in Fig. 3.7 for the lower values of t/λ_o and in Fig. 3.8 for $a/\lambda_o = 0.45$. Thus, the leakage loss rate (or alternatively the power converted into the leaking TEM mode at an angle) closely tracks the variation with b/λ_o of the normal electric field component at the air-dielectric interface.

C. ANTENNA WITH FINITE SIDE WALLS: COUPLING EFFECTS

The discussions in Sec. B present much information that is relevant to line-source antenna performance, but those considerations and numerical values apply when the side walls are taken to be infinitely long, so that the radiation occurs into a parallel-plate region. In order to radiate into free space, one must make the side walls *finite* in length, as shown in Fig. 3.10. The change required in the transverse equivalent network is examined first, and then the very interesting possible coupling effects are treated. It is important to understand the complications introduced by the coupling, so as to know how to avoid them or how to take them into account in a straightforward way.

1. The Transverse Equivalent Network

The difference in the transverse equivalent network for this modified structure and that for the one with infinite side walls resides only in the treatment of the TEM mode at an angle in the air region. When the side walls are infinite, the transmission line representative of the TEM mode is simply terminated by its characteristic admittance. For side walls of finite length, that transmission line must be terminated by the equivalent network that characterizes an abruptly ended parallel-plate line carrying a TEM mode incident at an angle on that termination. Fortunately, the required equivalent network for that termination is given in the Waveguide Handbook [8], Sec. 4.6a, pp. 179-183. The network is simple in form, and the expressions for it are rigorous.

Since the network for the termination is an element of a *transverse* equivalent network, we recognize that the wavenumber normal to that termination is the transverse wavenumber k_{y_0} , and we must modify the notation accordingly. In our notation, the structure and the equivalent network for the termination are presented in Fig. 3.11. We should also note that the network becomes particularly simple, consisting only of a conductance, when the reference plane for the network is shifted from the geometric termination by distance d .

One may instead employ an alternative network representation consisting of a conductance and a susceptance in parallel, located directly at the geometric termination. That network form was actually used by us in connection with the line-source antennas based on groove guide and analyzed in Chaps. VI and VII. The details in that form are contained in Sec. B, 1 of Chap. VI, where the expressions are given as (6.23) to (6.25) and the network is shown in Fig. 6.6. It is quite a matter of choice as to which network form to select.

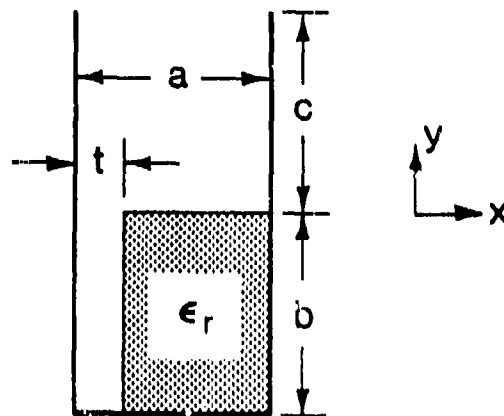


Fig. 3.10 Cross section of the NRD guide leaky-wave antenna based on the asymmetry introduced by the air gap of thickness t . The side walls have finite length c .

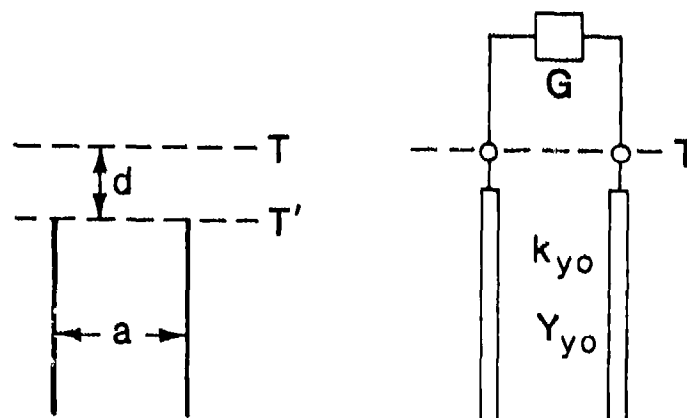


Fig. 3.11 Structure and equivalent network for the radiating open end in the cross section of the NRD guide leaky-wave antenna shown in Fig 3.10. The network form becomes particularly simple when the reference plane is located at T, a distance d from the actual termination. Taken from the Waveguide Handbook [8], but with our notation.

For the network form shown in Fig. 3.11, the expressions for the network parameters, taken from the Waveguide Handbook but restated in our notation, are the following. At the reference plane T located at a distance d given by

$$k_{y0} d = x \ln \frac{2e}{\gamma x} - S_1(x;0,0) \quad (3.4)$$

the equivalent network is simply a conductance

$$\frac{G}{Y_{y0}} = \tanh \frac{\pi x}{2} \quad (3.5)$$

where

$$x = k_{y0} \frac{a}{2\pi}, \quad e = 2.718, \quad \gamma = 1.781 \quad (3.6)$$

$$S_1(x;0,0) = \sum_{n=1}^{\infty} \left[\sin^{-1} \frac{x}{n} - \frac{x}{n} \right] \quad (3.7)$$

These results are valid for $x < 1$.

All of the other modes in the parallel-plate guide region have decayed to negligible values as they reach the open termination a distance c away from the end of the dielectric strip in Fig. 3.10. The transmission lines representing those modes in the complete mode-matching network are thus terminated in their respective (essentially reactive) characteristic admittances, as mentioned above. The transmission line for the TEM mode an an angle (actually the TE_0 mode) is terminated by the conductance in (3.5) at a distance $c + d$ from the end of the dielectric region. We note, of course, that d is not a fixed distance but a function of transverse wavenumber k_{y0} , and is in fact slightly complex due to the leakage.

2. Coupling Effects in the Propagation Characteristics

a. Qualitative Features

By applying the transverse resonance condition to the complete transverse equivalent network, including the mode-matching process, we can compute the complete propagation behavior for the structure in Fig. 3.10. We are interested in particular in the variation of β/k_o and α/k_o as a function of the width c of the side walls. One reason for such interest is that c is the new parameter; the other reason is that as c changes β/k_o may remain fairly constant and α/k_o may vary, so that tapering the value of c might offer another way to control the antenna's sidelobes.

Because the discontinuity at the open end of the cross section would produce a reflection, we expected that a mild standing wave would be produced along the width c ; we then anticipated that α/k_o should vary periodically with width c , at least for low values of leakage. Our expectations were borne out for low values of α/k_o , as we show later. When we obtained the computed results for larger values of leakage, however, we found them unexpected and puzzling. It was only after some time and effort that the explanation became clear. It should be added that the primary credit for the solution of the puzzle must go to my collaborators Shigesawa and Tsuji, who conducted the actual calculations in Kyoto.

Illustrations of what we found for α/k_o vs. the length c of the parallel-plate region for both small and large values of leakage rate are given in Fig. 3.12. As seen, for small values of α/k_o the curve is nicely periodic, as expected. For a larger value of α/k_o , the result is not periodic, and in fact the curve continues to decrease monotonically for higher values of c/λ_o . Clearly, some new factor must be present to account for the completely different behavior.

The initially puzzling effects at larger values of leakage are due to the simultaneous presence of *another* leaky mode, and the *coupling* between the two leaky modes. The additional leaky mode is similar to the so-called *channel-guide* mode that was first described some thirty years ago in connection with a class of leaky-wave antennas based on rectangular waveguide with an open side wall. The only difference is that here the cross section is dielectric loaded near the closed end, where the field of that mode is weakest. As width c is increased, higher order solutions of the channel-guide mode are created, corresponding to additional half cycles of field variation in the y direction in the cross section.

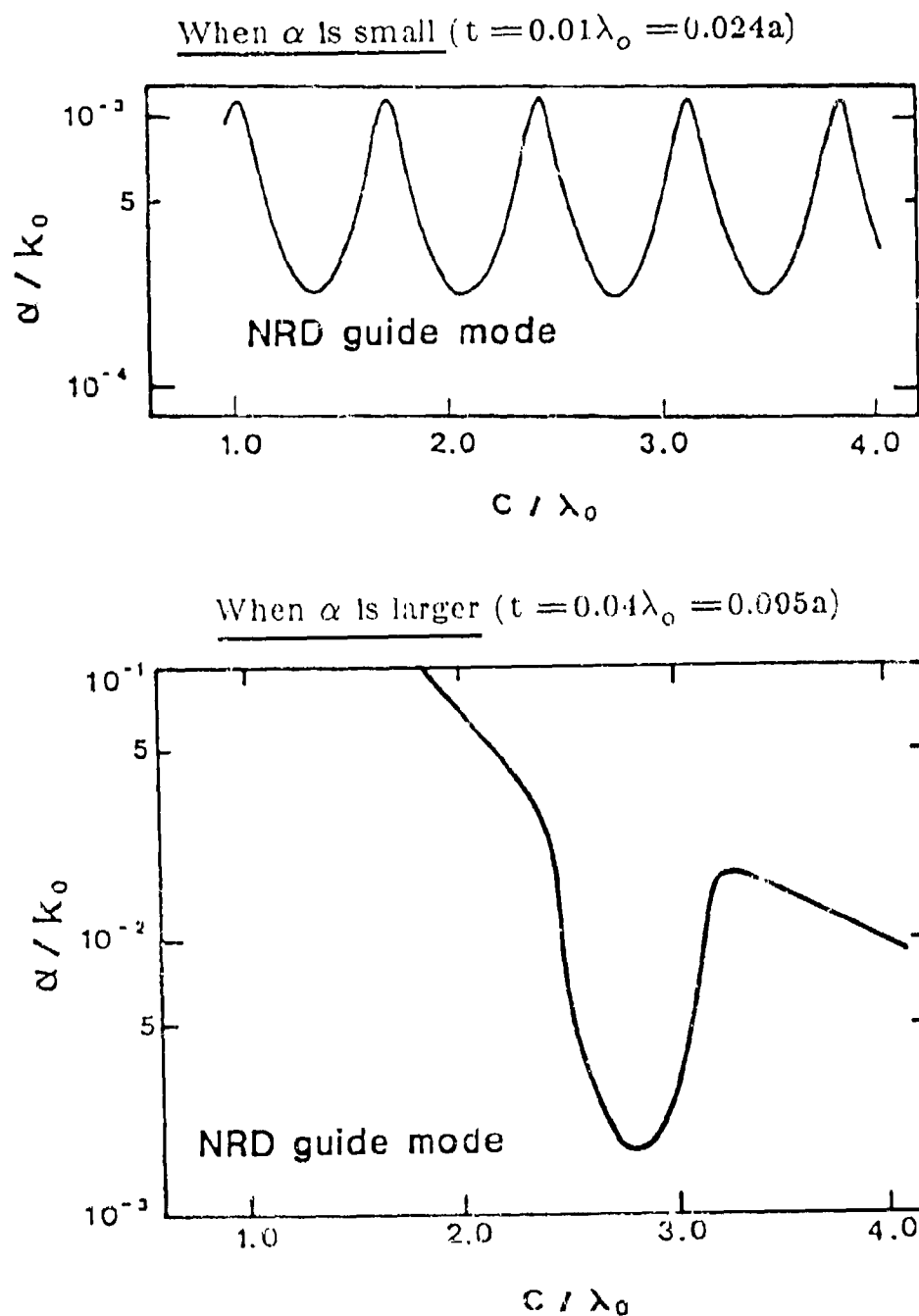
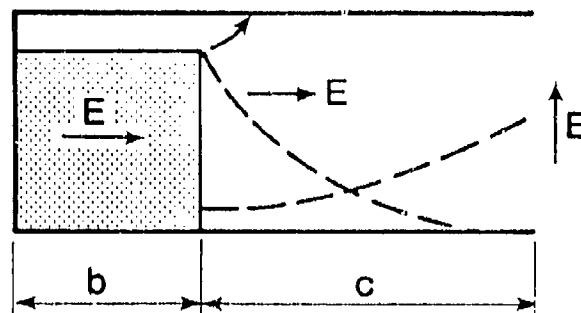
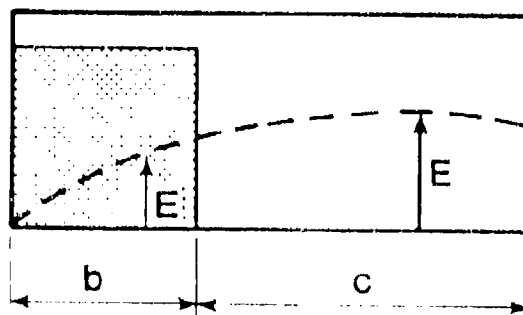


Fig. 3.12 The different behaviors found for the normalized leakage constant α/k_0 , as the length c of the metal parallel plates is increased for small and large values of leakage rate. For small values, the periodic variation is what was expected; the peculiar behavior for large values shows that some added factor is present.

These channel-guide solutions are completely different from the NRD guide mode, for which most of the field is concentrated in the dielectric region and then leaks away from that region at a relatively slow rate. To put it another way, the NRD guide mode is successively reflected by the top of the dielectric strip (though incompletely because leakage occurs), whereas the channel-guide mode is successively reflected by the open end of the parallel-plate guide (again incompletely). In addition, the electric field orientations of the two modes in the dielectric region are at right angles to each other,



NRD guide mode



Modified channel guide mode

Fig. 3.13 Sketches of the electric field variations and orientations for the NRD guide mode and the channel-guide mode, illustrating their differences. For convenience the structures have been placed on their sides.

and the main part of the power in the NRD guide mode resides in the dielectric region whereas most of the channel-guide mode power is in the air region. Some of these distinctions are made clear in the sketches in Fig. 3.13, where the structures are placed on their sides for convenience.

These two types of leaky mode are thus very different from one another, but if the values of *both* α and β for each are equal they can *couple* to each other since they have field components in common.

b. Quantitative Results

With reference to Fig. 3.10, calculations were made for plate spacing $a = 0.423\lambda_0$ (the value chosen originally by Yoneyama and Nishida [9]), dielectric strip width $b = 0.25\lambda_0$, and dielectric constant $\epsilon_r = 2.56$; the air gap thickness t was taken as the parameter, and the normalized leakage constant α/k_0 and phase constant β/k_0 were determined as a function of the length c of the side walls.

The first results we shall examine are those for a *small* air gap, i.e., for $t = 0.01\lambda_0$, presented in Fig. 3.14. We expected, for the leaky NRD guide mode, that β/k_0 would remain almost constant as c/λ_0 is increased, and that α/k_0 would vary periodically over that same range of c/λ_0 . We observe that from Fig. 3.14 that we indeed *do* obtain that behavior for the curves labeled NRD guide mode. In addition, however, we obtain a set of other curves, which are completely independent of the first ones, and which correspond to a set of channel-guide modes.

For this value of t , however, these modes do *not* couple. The β/k_0 values always cross, but the values of α/k_0 for the channel-guide modes are much larger than those for the NRD guide mode. The situation is made clear by reference to points A in Fig. 3.14; we note that the β/k_0 values coincide, but that at that value of c/λ_0 the α/k_0 values differ by more than an order of magnitude. For significant coupling to occur, *both* the β/k_0 and the α/k_0 values must be close to each other.

If not for the behavior for the larger values of t/λ_0 , where coupling does occur, we would probably never have noticed the other (channel-guide) set of solutions. Let us next examine the results for $t = 0.03\lambda_0$, which seems to be a transition value; the curves appear in Fig. 3.15. If we looked only at the NRD guide mode curves for c/λ_0 less than 3.0 or so, which is a quite large value for length c , we would not suspect anything. Here again, there are always crossings in the β/k_0 curves, so we must examine how closely the α/k_0 values approach each other. Interestingly, the α/k_0

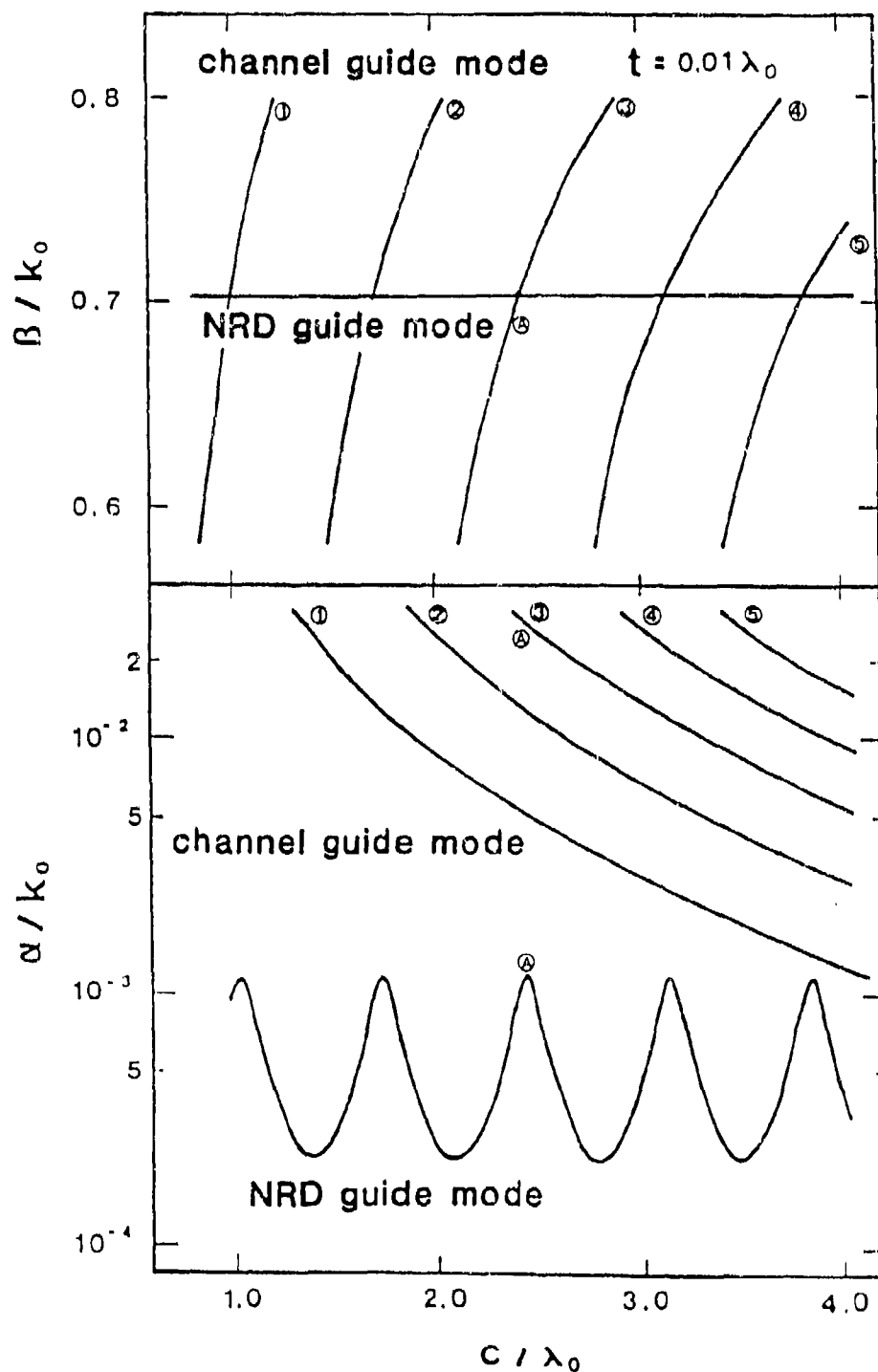


Fig. 3.14

Variations of β/k_0 and α/k_0 with normalized length c/λ_0 of metal parallel plates, for the NRD guide antenna shown in Fig. 3.10 when the parameter values are $a/\lambda_0 = 0.423$, $b/\lambda = 0.250$, $\epsilon_r = 2.56$, and $t/\lambda_0 = 0.01$. For this *small* air gap, no coupling occurs between the NRD guide mode and the channel-guide mode solutions.

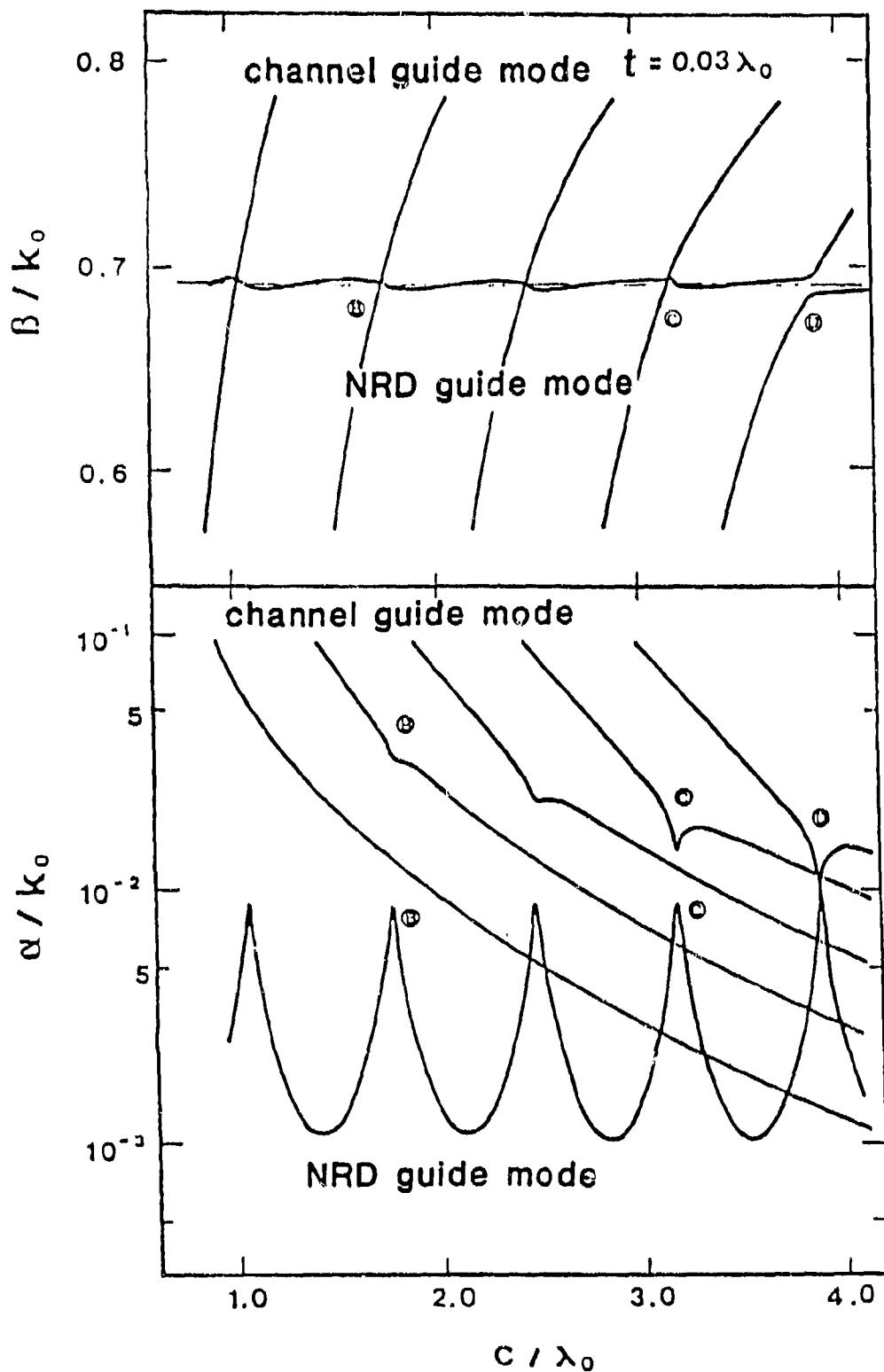


Fig. 3.15

Same as for Fig. 3.14, but for $t/\lambda_0 = 0.03$. Coupling effects are beginning to occur for larger values of c/λ_0 .

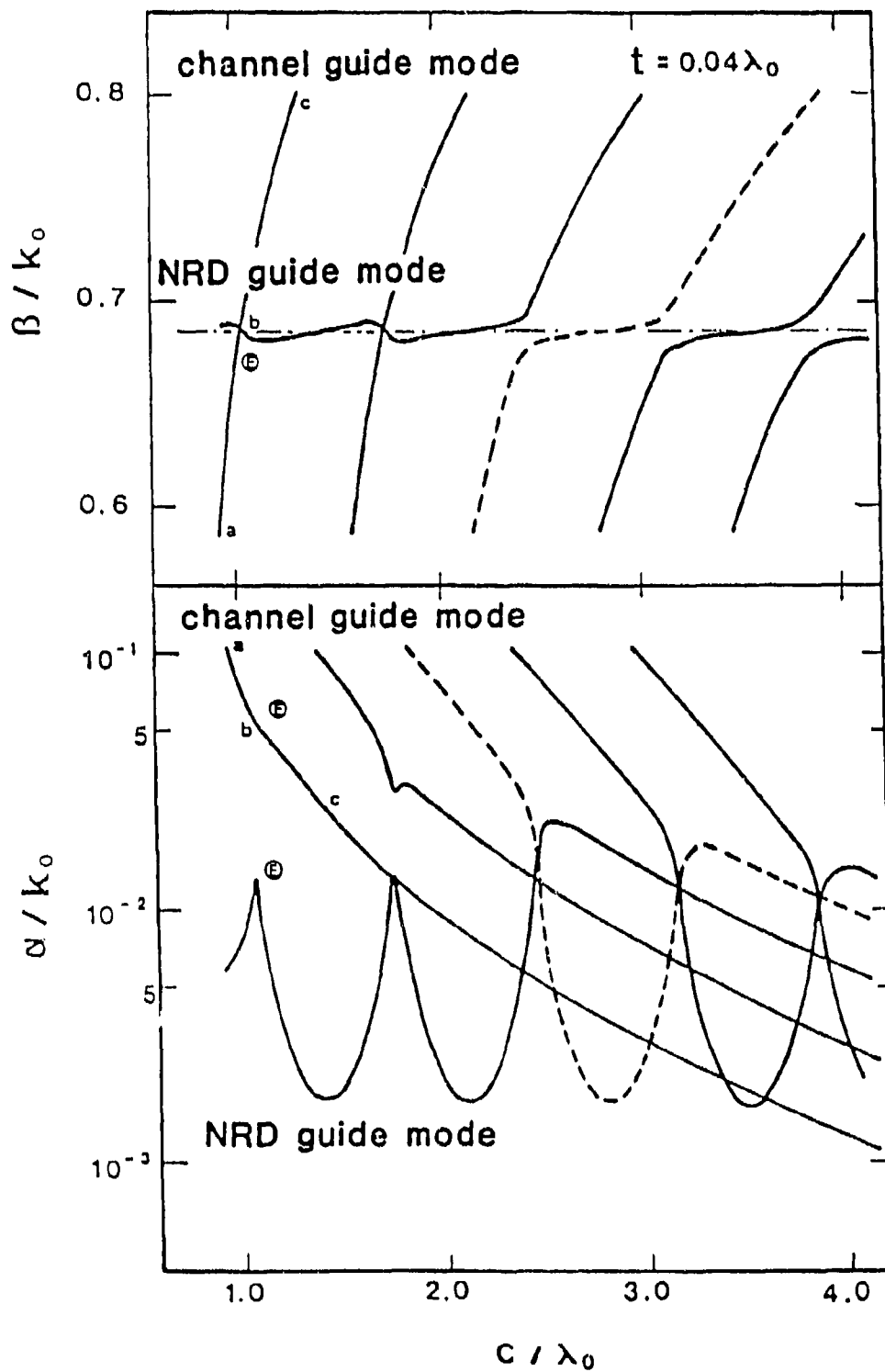


Fig. 3.16

Same as for Fig. 3.14, but for $t/\lambda_0 = 0.04$. Coupling effects are pronounced for large values of c/λ_0 ; the dashed lines show how the modes actually interchange within one interaction region.

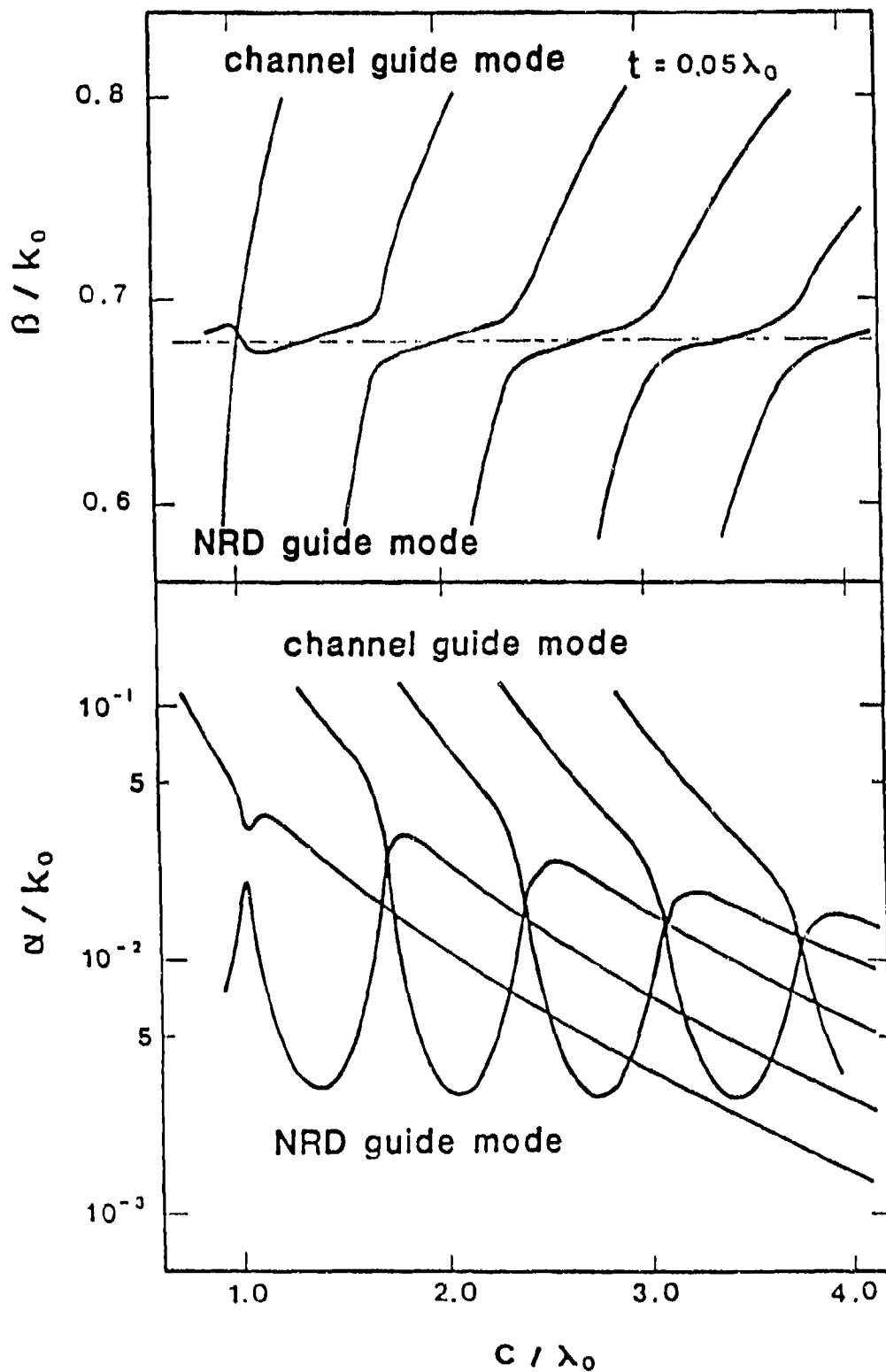


Fig. 3.17 Same as for Fig. 3.14, but for $t/\lambda_0 = 0.05$. Strong coupling is seen to occur almost everywhere for this larger value of leakage.

values become closer as c/λ_o increases, and the corresponding values are indicated in Fig. 3.15 by the letters B, C and D. For points B, only the channel-guide mode curve seems to be influenced, and only slightly since the values are not that much alike yet. The coupling becomes stronger at point C, while at point D the coupling is so strong that characteristic coupling behavior already occurs. We observe that *curve splitting* (directional coupling behavior) is produced in the β/k_o plot, and that the α/k_o curves cross and *interchange* with each other.

The coupling behaviors for *larger* values of air gap thickness t appear in Figs. 3.16 and 3.17. We again observe that the coupling becomes stronger as c/λ_o increases, noting that for point E on Fig. 3.16 the coupling is still negligible, and that it can be ignored even for values of c/λ_o less than 2 or so. As t/λ_o increases, and the leakage for the NRD guide mode increases, the α/k_o values for the two modes become close to each other and the mode coupling and conversion effects grow stronger and occur for smaller values of c/λ_o .

The behavior in the coupling region itself is actually rather complicated. To help clarify the behavior, one interaction region is shown *dashed* for both α/k_o and β/k_o in Fig. 3.16. As one follows the dashed curves, one sees that the two modes actually fully *interchange* with each other. Additional information is provided by the letters a, b and c on the lowest channel-guide mode curves, showing the correspondences between points on the β/k_o and α/k_o curves.

Several questions arise regarding how one can proceed with the design of a leaky-wave antenna in view of these complications in the dispersion behavior. First, we recall that for small values of t and/or for small values of c the coupling effects are absent or minimal. In such regions of operation, the solutions are independent but in principle both mode types are present. If we excite the NRD guide leaky mode, how strongly will the channel-guide leaky mode be excited as a result? It is believed that it will be rather weakly excited, since the field of the channel-guide mode is weakest where the NRD guide field is strongest. In addition, over most of the structure their field polarizations are opposite; they couple mainly, when they do, at the radiating open end. Thus, the exciting $n = 1$ NRD guide mode cannot strongly excite the channel-guide mode. For a special case in another structure, the offset-groove-guide antenna, that supports the channel-guide mode in addition to the desired mode of opposite basic polarization, we may look at Figs. 8.16 and 8.17 of Chap. VIII. These figures present a vector electric field plot for each of the two modes, showing the field strengths and field directions at each point in a grid of many points. The modes involved are sufficiently similar to those in the NRD guide antenna that a look at

those plots should be helpful in showing how the two modes differ.

Perhaps one could estimate the amplitude of the channel-guide mode excited by an NRD guide mode, but, in any case, it would be low compared to that for the NRD guide mode. At worst, its presence would result in a low-power spurious beam. Experiment would furnish reliable proof. In this connection, we may again refer to Chap. VIII, where measurements were performed at 50 GHz on an offset-groove-guide leaky-wave antenna. No evidence was found experimentally of any spurious beam.

Assuming, therefore, that the channel-guide mode can be safely ignored in those regions for which the coupling is not strong, the next step would be to make the value of c , the length of the metallic side walls, *as small as possible*. What determines how small we can make that length? We wish the radiation to possess only the polarization associated with the TEM mode in the parallel-plate guide. That means that c must be sufficiently long that the evanescent field of the basic $n = 1$ mode in the air region has decayed to negligible values as it reaches the open end. We thus determine the value of c that yields an acceptably low value for that undesired polarization, and specify that length in the design. In the air region, we have that the wavenumber in the y direction for that $n = 1$ mode is given by

$$\frac{k_{y1}}{k_o} = \left[1 - \left(\frac{k_z}{k_o} \right)^2 - \left(\frac{k_{x1}}{k_o} \right)^2 \right]^{1/2} \quad (3.8)$$

where

$$\frac{k_z}{k_o} \approx \frac{\beta}{k_o} \quad \text{and} \quad \frac{k_{x1}}{k_o} = \frac{\lambda_o}{2a} \quad (3.9)$$

For our geometry, $a/\lambda_o = 0.423$ and an average value for β/k_o can be taken as 0.69 (from Figs. 3.14 to 3.17). We then find that $k_{y1}/k_o = -j 0.93$, which represents a large decay rate. As a result, for $c/\lambda_o = 0.50$, the square of the field at the open end is down by 26 dB, which is quite sufficient for most needs. We can thus select a value of c that is not greater than $\lambda_o/2$, and perhaps a bit less, thereby permitting us to avoid the coupling regions even for the worst case for which we have calculations, i.e., $t = 0.05\lambda_o$.

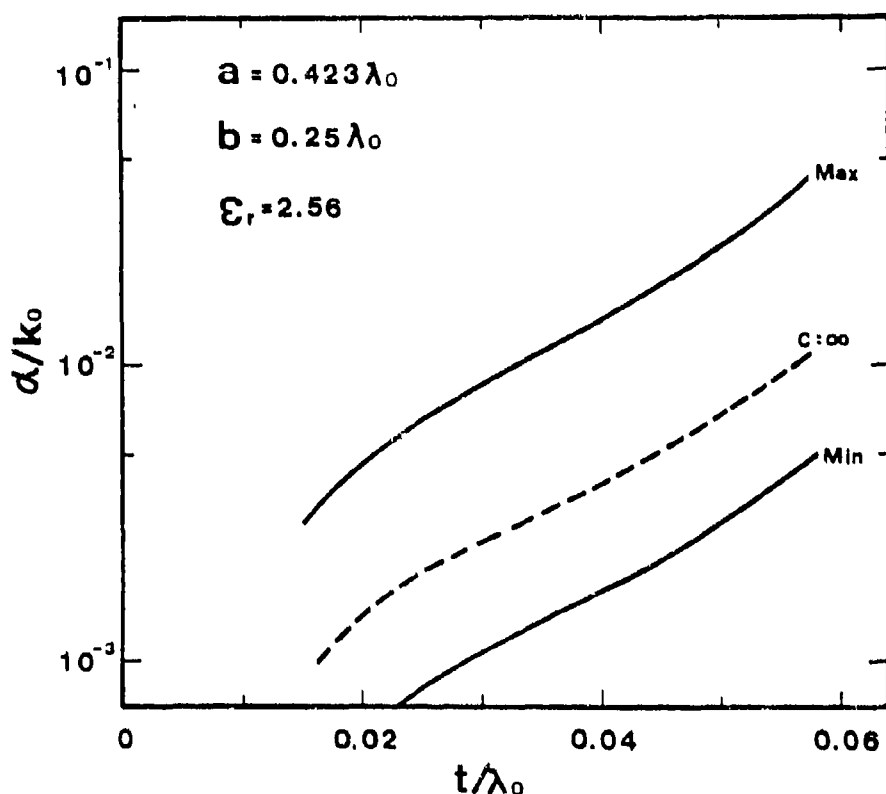


Fig. 3.18 The value of α/k_0 varies in periodic fashion as c/λ_0 is changed in those regions for which coupling is absent. The curves here indicate the range in that variation as a function of t/λ_0 , when $b/\lambda_0 = 0.25$.

In those regions in which coupling is *absent*, we saw (as in Figs. 3.14 and 3.15) that β/k_0 remains fairly flat as c/λ_0 is changed, but that α/k_0 undergoes a rather large variation, in periodic fashion as c/λ_0 is increased. By appropriately selecting the value of c , therefore, we can adjust the leakage rate within a fairly wide range. That range changes with the value of air gap thickness t , of course, and the curves in Fig. 3.18 tell us what that range is as a function of t/λ_0 , for dielectric width $b/\lambda_0 = 0.25$. From Fig. 3.18 we see that the difference between the maximum and minimum values (the crests and the troughs in the periodic variation of α/k_0) is somewhat less than an order of magnitude, and that it increases slowly as t/λ_0 increases. Of course, the median value increases strongly as the air gap is made wider. Also shown in that plot is the dashed curve representing the value for $c = \infty$; the dashed curve possesses the same variation with t/λ_0 , but it lies a little lower than the median value.

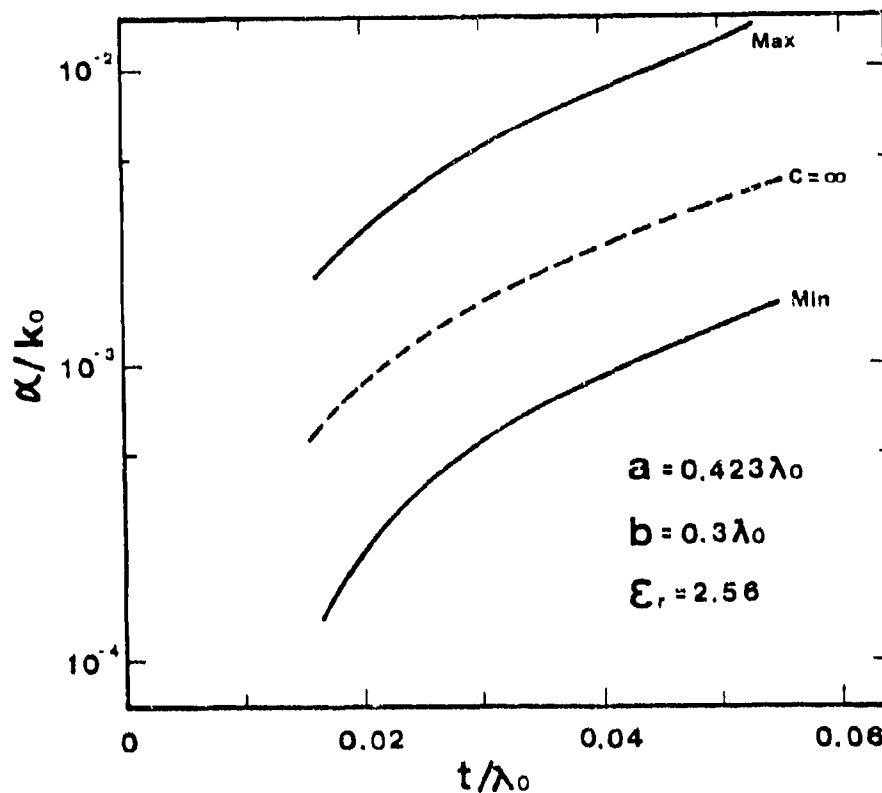


Fig. 3.19 Same as for Fig. 3.18, but for $b/\lambda_0 = 0.30$.

The results of a similar calculation for a wider dielectric region, namely, $b/\lambda_0 = 0.30$, are presented in Fig. 3.19. The qualitative behavior is similar, but the values of α/k_0 are lower (consistent with Fig. 3.3). The dashed curve for $c = \infty$ is again seen to furnish a good approximation to the median values, but a bit smaller than those would actually be.

As the air gap thickness t increases, the curve of β/k_0 vs. c/λ_0 remains less constant, and exhibits some fluctuation in a periodic fashion. The amplitude of that fluctuation, expressed in per cent, is plotted in Fig. 3.20 as a function of t/λ_0 , for two different values of b/λ_0 . The fluctuation increases rapidly with t/λ_0 , but it is seen to remain quite small, when we note that the ordinate scale is greatly expanded.

The final question in this sequence is: approximately what beam widths correspond to the values of t/λ_0 in Figs. 3.14 through 3.17? The beam width $\Delta\theta$ depends on the

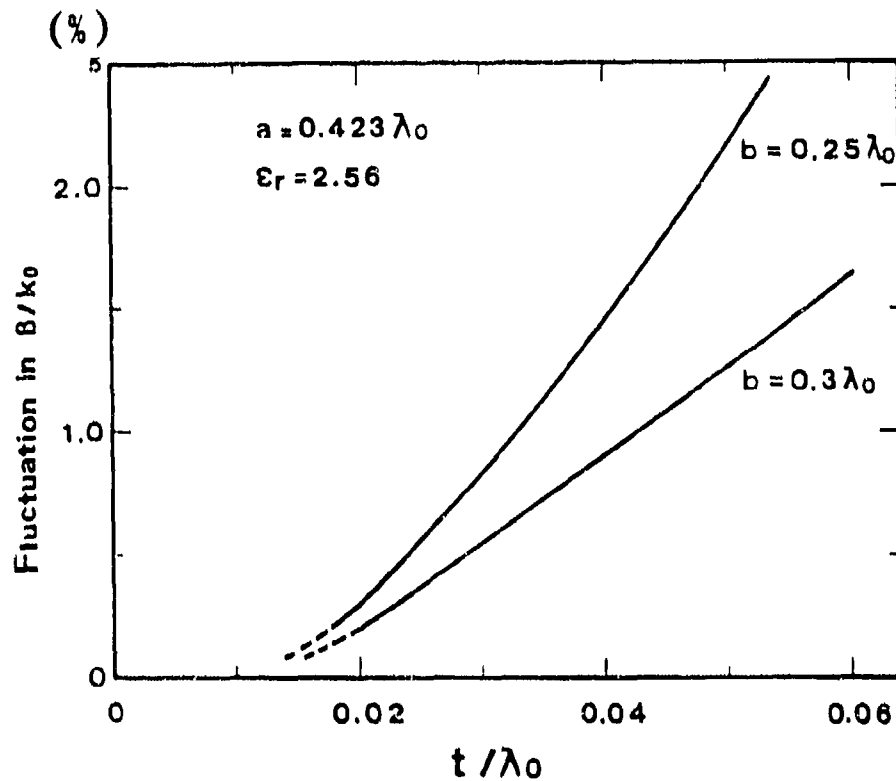


Fig. 3.20 The percentage fluctuation in β/k_0 as c/λ_0 is changed, as a function of t/λ_0 , for two different values of b/λ_0 . Note that the ordinate scale is enlarged.

value of α/k_0 and, to a lesser extent, on β/k_0 as well. But the values of α/k_0 vary as c/λ_0 changes. Let us take, therefore, the average values for α/k_0 , and also for β/k_0 when it varies, outside of the coupling regions in each of these figures. Then we employ the approximate but rather good rules of thumb summarized in Chap. II, Sec. D. From expressions (2.27) through (2.29) we obtain

$$\Delta\phi \approx \frac{285 \alpha/k_0}{\cos(\sin^{-1} \beta/k_0)} \text{ in degrees} \quad (3.10)$$

and from this expression we find, for our particular set of parameters:

c/λ_o	0.01	0.03	0.04	0.05
$\Delta\theta$	0.2°	1.3°	2.2°	4.3°

We therefore conclude that, by selecting length c to be no greater than necessary, we should be able to satisfactorily design NRD guide leaky-wave antennas that yield beam widths at least up to 4° or so, without any further considerations.

For beam widths greater than 4° or so, if the dispersion behavior is found to be *within* the coupling region, it is still easy to get around the coupling difficulties. It is then necessary to identify those regions of c/λ_o that correspond to the NRD guide leaky mode as opposed to the channel-guide leaky mode. For example, in Fig. 3.16 for the dashed curves, the flat region in the β/k_o plot has the properties of the NRD guide mode. The corresponding region of c/λ_o in the α/k_o plot is also of the NRD guide type; we may note that it appears as an approximate continuation of the periodic NRD guide solution. If our design then selects a value of c/λ_o that falls within one of those NRD guide regions, we will be assured of proper performance. Considerations of this type are examined in substantial detail in Chap. VII, Sec. D,2, in connection with the offset-groove-guide antenna.

IV.	SCANNABLE ARRAY OF NRD GUIDE LINE SOURCES	91
A.	DESCRIPTION AND OPERATION OF THE ARRAY	93
B.	ANALYSIS OF THE ARRAY	96
	1. Unit Cell Wavenumber Relations	96
	2. Transverse Equivalent Network of the Unit Cell	99
C.	PERFORMANCE FEATURES	104
	1. Behavior When the Cross-Plane Scan Angle is Zero	104
	2. Behavior as the Cross-Plane Scan Angle is Varied	104
	a. Coupling with Channel-Guide Leaky Modes	105
	b. Departure from Conical Scan	125
	c. Absence of Blindness Effects	128

IV. SCANNABLE ARRAY OF NRD GUIDE LINE SOURCES

(With: Prof. Xu Shanjia
University of Science and Technology of China,
Hefei, Anhui, China)

The nonradiative dielectric (NRD) guide leaky-wave line source employed in this array was described in Chap. III. The mechanism used to produce the leakage is asymmetry, and the line source radiates horizontal electric field polarization. When the frequency is changed or when the guide wavelength is changed electronically, the direction of the radiated beam is altered. The beam can therefore be *scanned in elevation* in the forward quadrant. The width of the beam in the elevation plane can be made narrow or broad, as one pleases, but the pattern in the cross plane is fan-shaped and broad.

If a *linear array* of such line sources is created, the radiation pattern in the cross plane is narrowed greatly, of course, and a pencil beam is produced. Then, if a phase shift is inserted between successive line sources, the array can be *scanned in the cross plane*, producing an antenna that radiates a pencil beam that can be scanned in two dimensions over a limited, but significant, sector of space. When the line sources are designed to radiate at a specific elevation angle, a variation in the phase shift between successive line sources causes the pencil beam to scan in an approximate conical fashion. The scan path is not strictly conical because the individual leaky-wave line sources are loaded a bit differently as the scan is performed in the cross plane, as we show later.

Although the concept of achieving a two-dimensional scan by employing leaky-wave scan in one plane and phase-shift scan in the other is not by itself novel, the *structure* employed here is novel and so is the *analysis* employed for it. In addition, the combination of performance advantages that are obtainable is notable; as we show below, the array radiation patterns have *no grating lobes*, *no blind spots*, and essentially *no cross polarization*. The antenna is also basically simple in structure, and therefore of potential interest for millimeter wavelengths.

In Sec. A, we present a description of the antenna configuration and its principle of operation. The method of analysis used is discussed in detail in Sec. B. It is based on the unit-cell approach described in Chap. II, and it leans heavily on material derived there.

Numerical results for the antenna's performance features are given in Sec. C. When the array is not scanned in the cross plane, and the pencil beam is at its central

position with respect to the azimuth plane, the unit cell reduces in such a way that the array performance in the elevation plane is identical to what is found in Sec. B of Chap. III, where the leakage occurs within the parallel-plate region. We are therefore able to apply directly to this special case for the array the numerical values obtained in that section of Chap. III. When the array is phased to scan in the cross plane, and the beam is shifted in both elevation and azimuth, the unit cell behavior becomes complicated, partly because the elevation scan behavior is influenced by the azimuth scan and partly because a set of channel-guide modes is excited. Coupling between the desired mode and the channel-guide modes occurs only for very large cross-plane scan angles and large plate heights. These features, and a demonstration that no blind spots are found, are included in Sec. C.

The principles underlying this novel array, and some of the results obtained from this study, were presented at a recent conference [16].

A. DESCRIPTION AND OPERATION OF THE ARRAY

The cross section of the linear phased array of leaky-wave NRD guide line sources is shown in Fig. 4.1. As seen, the individual line-source antennas are placed directly next to each other; the array period a is thus the same as the width of the individual line sources. Since a must be less than $\lambda_o/2$, as discussed in Chap. III, grating lobes are automatically avoided. This conclusion follows from expression (2.8) of Chap. II, since k_{xop}/k_o in that expression can never exceed unity, and $(k_z/k_o)^2$ is essentially positive real.

The propagation of power down the leaky-wave line sources in the array, perpendicular to the cross section shown in Fig. 4.1, is characterized by the phase constant β and the leakage constant α , as it is for the line sources when operated independently. The value of β/k_o yields the angle θ_m of the beam maximum in the principal plane of the leaky-wave line sources, and the value of α/k_o determines the width of that beam. The relevant relationships are given by (2.27) through (2.29) of Chap. II. The angle θ_m can be scanned in elevation by varying the frequency, thereby changing the ratio β/k_o , or by modifying β electronically.

Since the leaky-wave line sources in Fig. 4.1 are uniform longitudinally (except, of course, for any slow tapers for sidelobe control), the scan range can cover the *forward quadrant* only. This statement is also true for the printed-circuit array described in Chap. X, but not for the one in Chap. XI, which substitutes a periodic metal-strip grating for the uniform structures here and in Chap. X. In the case for which the line-source apertures are periodic, rather than uniform, the basic wave is made to be slow and thus nonradiating; the leakage is then furnished by the $n = -1$ space harmonic which can radiate into the full backward quadrant and part or all of the forward one, depending on the parameters involved.

To achieve *scanning in the cross plane*, and therefore in azimuth, as shown by the series of arrows in Fig. 4.1, we insert phase shifters at the feed end of each line source in the array and we introduce a phase shift between successive line sources. As in customary phased-array fashion, the sine of the angle of scan in the cross plane is then directly proportional to the phase shift introduced. When this phase shift is nonzero, the pencil beam points partly in elevation and partly in azimuth. As the phase shift between successive line sources is increased further, the beam traces out a path which is closely, but not exactly, *conical*. In any case, the beam eventually hits the ground, and the radiation stops. In Sec. B, we show that the value of β/k_o is changed slightly

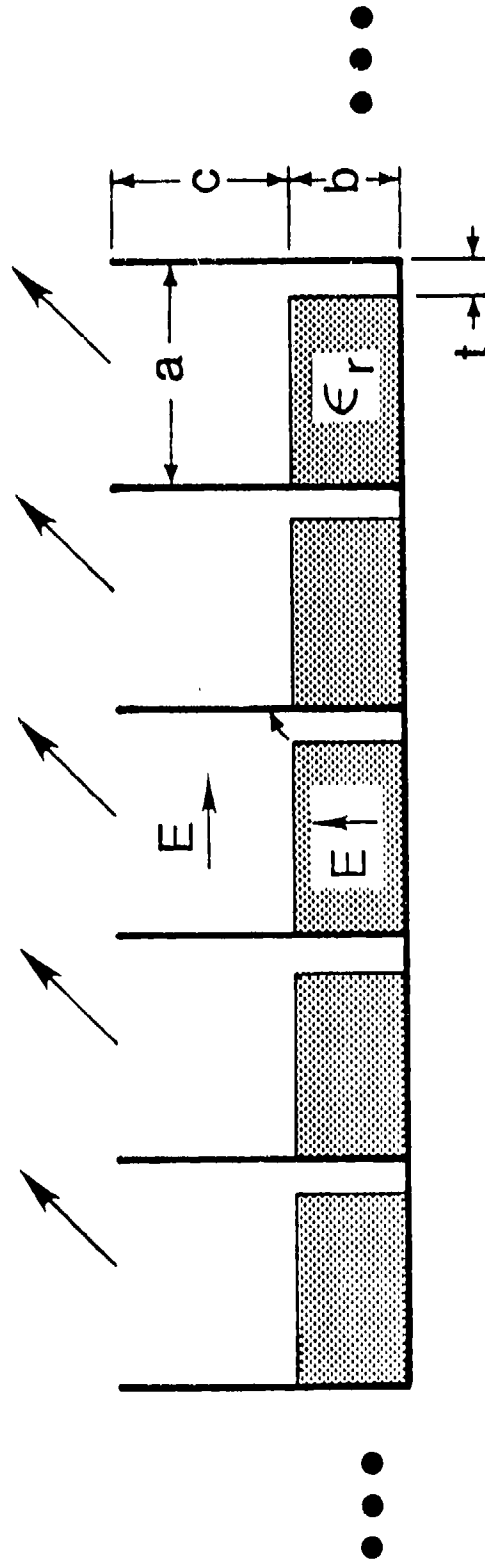


Fig. 4.1 Cross section of the linear phased array of asymmetric NRD guide leaky-wave line sources.

as this phase shift is increased; if it remained exactly the same, the scan path would be exactly conical.

The purpose of the *metal baffles* (or vertical plates) in the array in Fig. 4.1 is the same as it was for the individual NRD guide line sources discussed in Chap. III, namely, to eliminate the cross-polarized field component. As shown in the middle line source in Fig. 4.1, the mode that feeds the line sources is dominated by a vertical electric field component. The asymmetry, created by introducing an air gap on one side only, produces a net horizontal electric field component which corresponds to a TEM-like mode that propagates at an angle in the air-filled parallel-plate region, reaching the open upper end and radiating power at some elevation angle. The plate spacing a is such that the mode with the vertical electric field orientation is below cutoff. The length c of the metal baffles is then made large enough so that the power radiated in that polarization becomes negligible; a length equal to a half free-space wavelength is generally quite sufficient.

With the individual line sources, we found in Sec. C of Chap. III that, because length c is finite, an additional leaky-mode type becomes excited. In fact, a set of such modes, a modification of the channel-guide mode, is present, and these modes couple with the desired NRD guide mode when the leakage rate is high and when length c is large. We find with the *array* of such line sources that similar behavior can occur, but that the coupling effects are generally more subdued, and that they appear only for very large azimuth scans. The behavior is discussed quantitatively in Sec. C. Even when such coupling occurs, however, we can get around its effects, as we pointed out in Chap. III.

The numerical calculations indicate that *no blind spots* are found as the beam is scanned through all positions. It is quite possible, extrapolating from experience with phased arrays containing dielectric media, that blind spots could appear if the metal baffles were removed. But these baffles must be present anyway to eliminate the cross polarization.

The resulting array is basically simple in configuration, making it suitable for use at millimeter wavelengths, and it possesses the added virtues that the radiation patterns have no cross polarization, no blind spots and no grating lobes.

B. ANALYSIS OF THE ARRAY

1. Unit Cell Wavenumber Relations

We adopt the unit-cell approach for the analysis of the array, following the point of view outlined in Chap. II, and making use of the theoretical expressions presented there. In this approach, the array is replaced by a single unit cell, where the space above the array is treated as a periodic waveguide with phase-shift walls. The phase shift between the opposite walls of the periodic unit cell depends on the phase shift imposed between the successive line sources of the array. When the unit cell is properly characterized, all mutual coupling effects are automatically taken into account, and the array is represented rigorously. The analysis then proceeds by employing only waveguide techniques.

The unit cell representative of the array in Fig. 4.1 is shown on the left-hand side of Fig. 4.2. The lower waveguide portion of the unit cell, with metal outer walls, is the same as the corresponding portions of the individual line sources. The upper portion, with the phase-shift walls, is completely different.

In order to set up a transverse equivalent network for propagation down this unit cell, we examine the modes that can exist in the vertical (y) direction. In the lower, air-filled parallel-plate portion, which we shall call the "guide" region, the lowest mode is the TEM mode at an angle, which is therefore a TE_o mode with respect to the y direction. Its propagation wavenumber, k_{yog} , where subscripts o and g refer to "lowest mode" and "guide," respectively, is related to the free-space wavenumber k_o and the longitudinal (axial) wavenumber k_z by

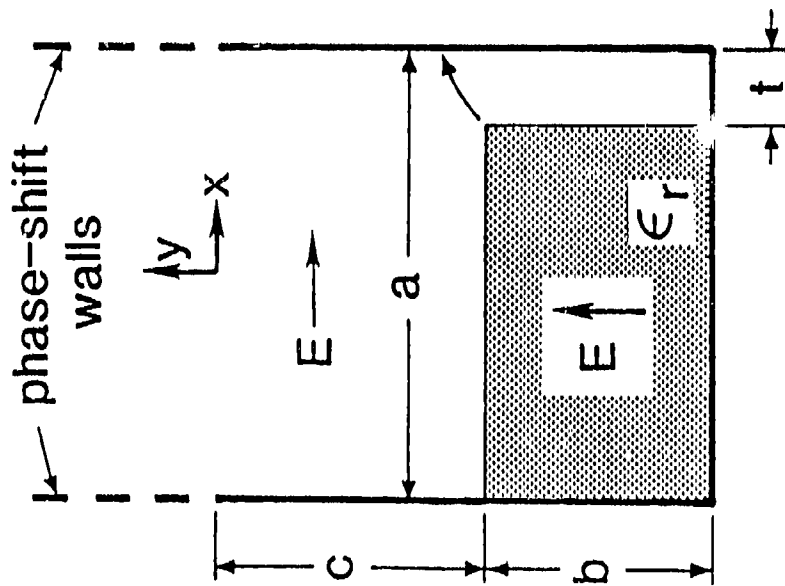
$$k_{yog}^2 = k_o^2 - k_z^2 \quad (4.1)$$

The longitudinal wavenumber $k_z (= \beta - j\alpha)$ is not known and is the ultimate goal of the analysis, because all the performance features of the array can be determined once β and α are known. An expression corresponding to (4.1) but for the higher modes is

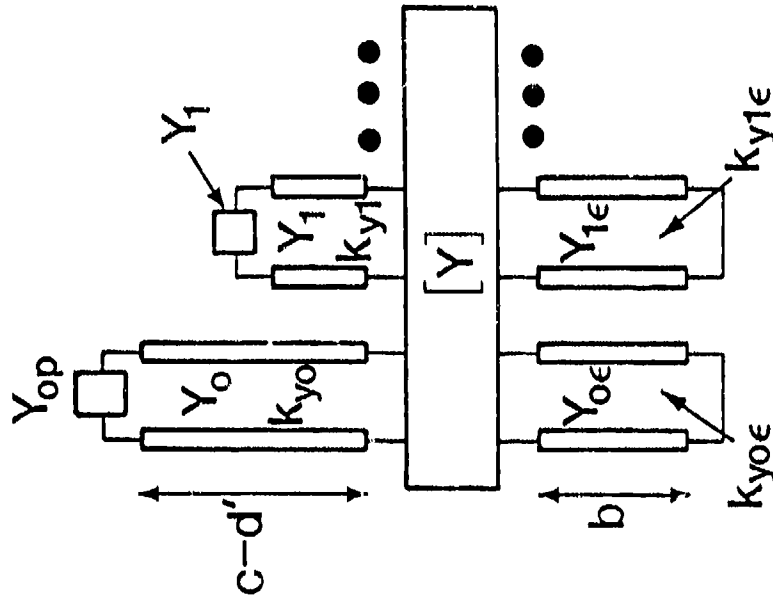
$$k_{ymg}^2 = k_o^2 - k_z^2 - (m\pi/a)^2 \quad (4.2)$$

where m is the mode number of the higher mode.

In the periodic (upper) region, represented in the unit cell in Fig. 4.2 by the guide portion with phase-shift walls, let k_{yop} be the wavenumber in the y direction of the lowest mode, where subscripts o and p represent "lowest mode" and "periodic region." The wavenumber k_{xop} in the x direction in that region has a value that is determined



UNIT CELL



TRANSVERSE
EQUIVALENT
NETWORK

Fig 4.2 Unit cell of the array shown in Fig. 4.1, and its transverse equivalent network. Because of space limitations, the subscript g was omitted in the wavenumber and characteristic admittance symbols in the transmission lines.

directly by the phase shifters between the successive line sources. In fact, the value of k_{xop} is *imposed* on the system and should be regarded as *given*. When all the line sources are fed in phase, $k_{xop} = 0$ and there is no scan in the cross plane. As a measure of the scan, we may take the ratio k_{xop}/k_o , which must be less than unity (see (2.9) of Chap. II), or $k_{xop}a$, which is the phase shift per unit cell, or θ_x , which is the angle whose sine is k_{xop}/k_o (see (2.1)) and which is measured from broadside and lies in the xy plane. In Sec. C of this chapter, we chose to use θ_x for this purpose. The angle in Fig. 4.1 between the arrows and the vertical direction is θ_x .

As explained in Sec. B of Chap. II, space harmonics are excited in the periodic region, with the n -th space harmonic wavenumber k_{xnp} related to k_{xop} by

$$k_{xnp} = k_{xop} + 2\pi n/a \quad (4.3)$$

The space harmonics in the x direction correspond directly to modes in the unit cell, where the transmission direction is vertical (in the y direction). The wavenumber k_{yop} for the lowest mode in the periodic region is then related to the other wavenumbers by

$$k_{yop}^2 = k_o^2 - k_{xop}^2 - k_z^2 \quad (4.4)$$

and the wavenumber k_{ynp} for the higher modes in the periodic region is given by

$$k_{ynp}^2 = k_o^2 - k_z^2 - (k_{xop} + 2\pi n/a)^2 \quad (4.5)$$

From (4.1) and (4.4), we have that

$$k_{yop}^2 = k_{yog}^2 - k_{xop}^2 \quad (4.6)$$

The polar coordinate system with its angles θ and ϕ are shown in Fig. 2.13 of Chap. II, and the relations between these angles and the wavenumbers are presented in (2.9). From that information we can see that when $k_{xop} = 0$, that is, when there is no imposed phase shift between successive line sources, $k_{yop} = k_{yog}$, and the beam in space is a direct continuation of the beam (or mode) in the parallel-plate guide region. As k_{xop} increases, however, the beam encounters some scan in azimuth (given by ϕ), and the angle in elevation increases, meaning that the beam is closer to the ground. The latter statement follows from (2.9) and from (4.6), from which it is seen that k_{yop} decreases. When k_{xop} is made to equal k_{yog} , the beam has hit the ground and all radiation ceases.

As mentioned above, the beam path executes conical scan to a good degree of accuracy as k_{xop} is varied. The angles at the two extremes of the conical scan range are related very simply, as discussed in Sec. B of Chap. II, and given by (2.16) or (2.17).

2. Transverse Equivalent Network of the Unit Cell

The transverse equivalent network of the unit cell is presented on the right-hand side of Fig. 4.2. Because of space limitations, the subscript g has been omitted from the wavenumber and transmission lines. The transmission direction in the network is the y direction, and in that direction there are three transmission regions with two discontinuity regions between them.

The lower discontinuity is that at the interface between the dielectric region with air gap below and the air-filled parallel-plate region above. At this discontinuity all the transverse modes are coupled. In the range of operation, three transverse modes are above cutoff in the dielectric region with the air gap, whereas only the TEM mode at an angle is above cutoff in the air region. The modes in the partially filled dielectric region that are above cutoff certainly "see" the short circuit at the base of the unit cell, and some of the below-cutoff modes will also, depending on their decay rates in the y direction and on the dielectric height b . In the air-filled parallel-plate region, the length c is deliberately made sufficiently long that all the higher modes will have decayed to negligible values at the radiating open end. Thus, all of the modal transmission lines except the one corresponding to the TEM mode at an angle are terminated in their (reactive) characteristic admittances. The termination on the remaining transmission line depends on the upper discontinuity and is discussed separately below.

The lower discontinuity discussed above is the same as the one in the individual NRD guide line-source antenna treated in Chap. III. As described there, a mode-matching procedure was used, with 15 TE and 15 TM modes taken in each of the two regions.

The upper discontinuity occurs at the junction between the air-filled parallel-plate region and the periodic waveguide with phase-shift walls. At that discontinuity, all the higher modes are excited in both the parallel-plate region and the periodic region. The problem is somewhat simplified by the fact that only one mode is above cutoff in each of these waveguiding regions. In the periodic region, the modes in the y direction correspond to the space harmonics in the z direction, so that the modes can

be readily tracked, and the mode functions are relatively simple. In fact, expressions for the mode functions for both the parallel-plate guide and the periodic waveguide with phase-shift walls are presented in Sec. C of Chap. II.

The difficulty that one encounters is that the mode functions for the periodic waveguide are a function of the imposed phase shift between successive line sources. To put it another way, the phase-shift walls are a function of the scan angle, so that the waveguide properties change with scan angle. As a result, the parameters of the junction discontinuity *change with scan angle*, or equivalently with the value of k_{xop} .

When the junction is a step junction of the type shown in Figs. 2.9 and 2.10, it is necessary to solve for the properties of the junction discontinuity, which is a nontrivial task. On the other hand, the junction discontinuity here is of the type shown in Fig. 2.11, for which, fortunately, a solution is available in the literature that requires only an analytic continuation.

The solution in question is the one given in Sec. 5.22 of the Waveguide Handbook [8], on pages 289-292; the structure and its equivalent network are presented here in Fig. 4.3 using the notation applicable here. The solution in the Waveguide Handbook applies to the case for which $k_z = 0$, that is, there is no longitudinal variation. We must be careful in adapting their result that the analytic continuation to finite (and complex) k_z is performed correctly.

The equivalent network for this junction discontinuity is phrased in a very elegant and simple form. The reactances associated with the stored higher modes are rephrased in terms of two transmission line shifts, one in the parallel-plate guide and the other in the periodic guide. Since for our application the periodic guide is terminated in its characteristic admittance, because the wave propagates into the far field, we actually need only one of those reference plane shifts, i.e., the one in the parallel-plate guide, permitting a further simplification in the equivalent network.

Let us first perform the translation in notation between our usage and that in the Waveguide Handbook:

Ours	a	d'	θ_x	Y_{op}	Y_{og}
WGH	b	d'	θ	Y_o	Y'_o

In addition, changes must be introduced because our application is to a *transverse* equivalent network.

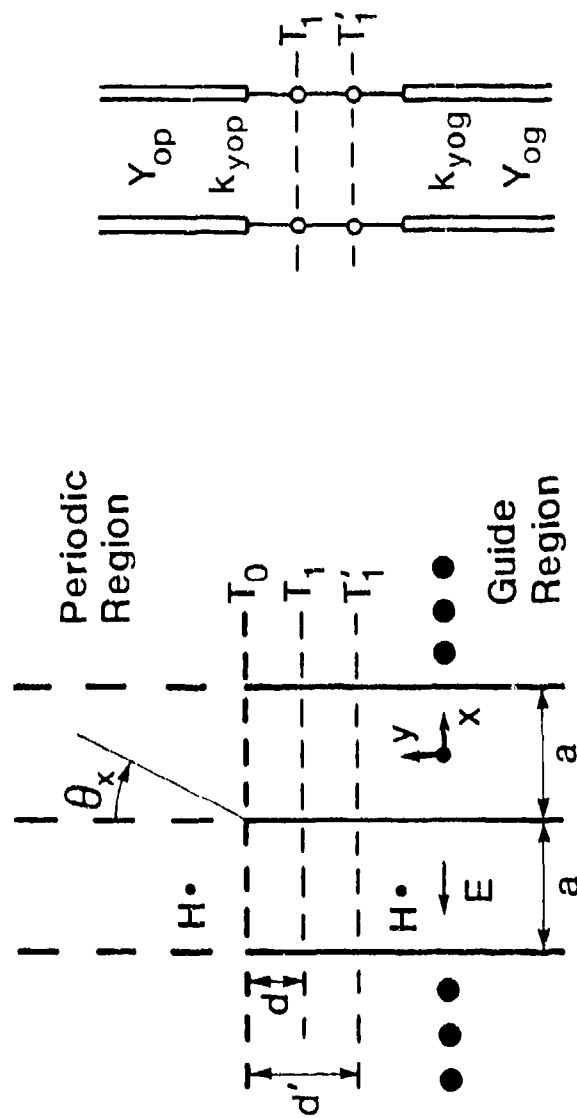


Fig. 4.3

Structure and equivalent network of the junction discontinuity occurring at the radiating open end. T_0 is the terminal plane located at the physical junction; d and d' are the reference plane shifts from T_0 to the output and input transmission line reference planes T_1 and T_1' . For our problem, we require only d' and T_1' .

Since the Waveguide Handbook results apply to the case for which $k_z = 0$, we should first adapt the results to the transverse equivalent network phrasing under that restriction. In our phase-shift application, the phase shifter imposes the wavenumber k_{xop} , so that k_{yop} becomes

$$k_{yop}^2 = k_o^2 - k_{xop}^2 \quad (4.7)$$

when $k_z = 0$. In the parallel-plate region,

$$k_{yog} = k_o \quad (4.8)$$

The modes, for $k_z = 0$, are all TM modes, with the lowest mode in the parallel-plate region being a TEM mode. We may therefore write for the characteristic admittance ratio

$$\frac{Y_{og}}{Y_{op}} = \frac{k_{yop}}{k_{yog}} = \frac{\sqrt{k_o^2 - k_{xop}^2}}{k_o} = \sqrt{1 - (k_{xop}/k_o)^2} \quad (4.9)$$

in view of (4.7) and (4.8). But

$$k_{xop} = k_o \sin \theta_x \quad (4.10)$$

so that

$$\frac{Y_{og}}{Y_{op}} = \cos \theta_x \quad (4.11)$$

in agreement with equation (1) on p. 289 of the Waveguide Handbook, after the appropriate changes in the notation.

On p. 290 of the Waveguide Handbook, we find the shorthand definitions

$$y = \frac{b}{\lambda} \sin \theta, \quad x' = \frac{b}{\lambda}$$

but λ is really $2\pi/k$, and in the transverse equivalent network k corresponds to k_{yog} . Also $k \sin \theta$ actually corresponds to k_{xop} . Making the additional notational change of b into a , we have that these shorthand definitions become, for our case,

$$y = \frac{ak_{xop}}{2\pi}, \quad x' = \frac{ak_{yog}}{2\pi} \quad (4.12)$$

Equation (3a) on p. 289 of the Waveguide Handbook begins with $2\pi d' / \lambda$, which we may now rewrite as $k_{yog} d'$, so that it represents the electrical length in the parallel-plate guide region of the physical length d' , which is one of the reference plane shifts indicated in Fig. 4.3.

Our next requirement is to generalize these expressions to the case $k_z \neq 0$. Since the geometric structure is *uniform along* the z direction, the generalization involves only the replacement of k_o by $\sqrt{k_o^2 - k_z^2}$ wherever it appears. Expressions (4.7) and (4.8) must now be replaced by (4.4) and (4.1), respectively.

The modes are more complicated now. They are no longer TM modes, but are now LSE or $H^{(z)}$ -type modes, with their characteristic admittances having the form given by (2.18) of Chap. II. The lowest mode in the parallel-plate guide region, which was a TEM mode when $k_z = 0$, is now a TE mode (actually the TEM mode at an angle), but also a limiting case of an H -type mode. Taking both modes to be $H^{(z)}$ -type modes, and the expression for their characteristic admittances from (2.18), we obtain

$$\frac{Y_{og}}{Y_{op}} = \frac{k_{yop}}{k_{yog}} = \sqrt{1 - (k_{xop}/k_{yog})^2} \quad (4.13)$$

using (4.1) and (4.4). Taking the lowest mode in the parallel-plate guide region to be a TE mode, we find

$$\frac{Y_{og}}{Y_{op}} = \frac{k_{yop} k_{yog}}{k_o^2 - k_z^2} = \frac{k_{yop}}{k_{yog}}$$

in agreement with (4.13), when (4.1) is used.

Expression (4.13) for the characteristic admittance ratio now replaces (4.11), and corresponds to equation (1) on p. 289 in the Waveguide Handbook. The expressions in (4.12) for the symbols y and x' are still valid, except that (4.1) must now be used for k_{yog} . Quantity k_{xop} is still assumed to be a given quantity, imposed by the phase shift per unit cell.

Expressions (2a) and (3a) on p. 289 of the Waveguide Handbook permit us to calculate the reference plane shifts d and d' (see Fig. 4.3). Since the periodic waveguide in our problem is infinitely long, we do not need d . We do need length d' , however, the expression for which becomes, in our notation,

$$k_{yog} d' = 2x' \ln 2 + \sin^{-1} 2x' - \sin^{-1} \frac{x'}{1+y} - \sin^{-1} \frac{x'}{1-y} \\ + S_2(2x'; 0, 0) - S_2(x'; 0, -y) - S_2(x'; 0, y) \quad (4.14)$$

where (4.12) is to be used to yield symbols x' and y , and where

$$S_2(x'; 0, b) = \sum_{n=2}^{\infty} \left[\sin^{-1} \frac{x'}{n-b} - \frac{x'}{n} \right] \quad (4.15)$$

Expression (4.14) has been obtained by the transform method and is rigorous in this range of parameters.

Returning to the transverse equivalent network in Fig. 4.2, we may now address the termination on the transmission line representing the lowest mode in the parallel-plate guide region. Since the transmission line representing the lowest mode in the periodic region is infinitely long, the input admittance to it is simply its characteristic admittance Y_{op} . In keeping with the equivalent network in Fig. 4.3, we therefore shorten the transmission line length c to $c - d'$, and place Y_{op} as the termination on that line.

As mentioned earlier, the subscript g was omitted in the wavenumber and characteristic admittance symbols in the transmission lines in Fig. 4.2 because of space limitations. In particular, in the transmission line of length $c - d'$, the wavenumber should read k_{yog} and characteristic admittance Y_{og} . The terminal admittance Y_{op} , normalized to Y_{og} , is then given by the reciprocal of the expression in (4.13).

In using this transverse equivalent network, we assume that k_{xop} is given, and that $k_z (= \beta - j\alpha)$ is the unknown quantity for which we are obtaining a solution. The reference plane shift d' is thus also complex and also unknown. It does not occur separately, however, but as $k_{yog} d'$, from (4.14), where both quantities are complex and unknown. We cannot separate out these quantities beforehand, therefore, but we determine their values simultaneously when we take the free resonance of the total transverse equivalent network.

C. PERFORMANCE FEATURES

When the scan in the cross plane is zero, the transverse equivalent network simplifies and the array behavior reduces exactly to the case we have already treated in detail, in Sec. B of Chap. III. Some comments are first made about this special case in subsection 1. below.

What is new in this chapter, therefore, is the antenna behavior as the scan in the cross plane is varied, that is, as k_{xop} is varied. Those new and interesting effects are considered in subsection 2. below. Included there are the influences due to the presence of the set of channel-guide leaky modes, the variation of β/k_o with cross-plane scan and its relation to strict conical scan, and two tests that verify the absence of blind spots.

1. Behavior When the Cross-Plane Scan Angle is Zero

When $k_{xop} = 0$, the phase shift between the successive line sources is zero and there is no scanning present in the cross plane (or in azimuth, therefore). The phase-shift walls in the unit cell in Fig. 4.2 then reduce to electric walls, or short-circuit walls, in view of the polarization of the electric field. As a result, the unit cell takes the form shown in Fig. 4.4. Since the unit cell in Fig. 4.4 possesses electric walls on its sides that proceed vertically to infinity, it is precisely the same as the structure that results in Chap. III when the parallel-plate walls in Fig. 3.1(b) are taken to be infinitely long. The behavior of the *array* when the cross-plane scan is zero is therefore *identical* with the behavior of the *individual line source* discussed in detail in Sec. B of Chap. III.

It is important to know the effects caused by changes in the geometric parameters and in ϵ_r , but these effects have already been discussed in some detail in Sec. B of Chap. III and illustrated numerically in Figs. 3.2 through 3.9. We will therefore not repeat any of the conclusions here, but instead refer the reader to the contents of the above-mentioned section.

2. Behavior as the Cross-Plane Scan Angle is Varied

The interesting new behavior now is due to the effects produced when $k_{xop} \neq 0$, that is, when scanning in the cross plane is present. We treat separately three basic considerations: coupling produced with a set of channel-guide modes, departures from conical scan, and the absence of blind spots.

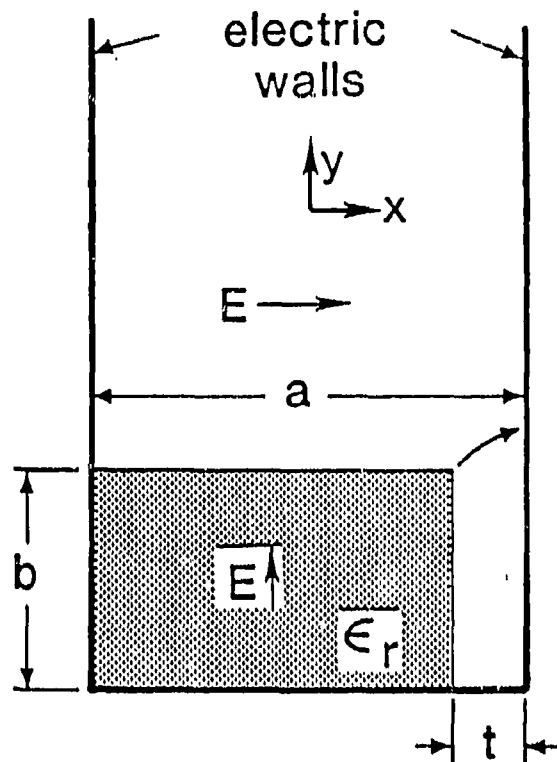


Fig. 4.4 Simplification of the unit cell when $k_{xop} = 0$, i.e., there is no scanning in the cross plane (or azimuth). The phase-shift walls reduce to electric walls (or short-circuit walls.)

a. Coupling with Channel-Guide Leaky Modes

When the scan in the cross plane is zero, the phase-shift walls become electric walls and the actual physical height c of the metal baffles in the array plays no role. When there is cross-plane scanning, however, the height c of those metal walls becomes very important. The key point is that when c is finite and $\theta_x \neq 0$ a discontinuity is produced between the parallel-plate metal baffles and the periodic unit cell waveguide above. That junction discontinuity is illustrated in Fig. 4.3 and represented by the equivalent network shown there; it is also discussed in detail in Sec. B,2 above. The discontinuity is a weak one for small cross-plane scan angles θ_x (or equivalently k_{xop}/k_o since these quantities are related by a sine function (see (4.10))).

For large scan angles, the discontinuity becomes quite strong.

This junction discontinuity introduces two very important effects. The *first effect* is that it produces a mild standing wave in the cross section between this junction discontinuity and the one corresponding to the air-dielectric interface. As a result, the values of β/k_o and α/k_o will undergo a periodic variation as a function of the height c/λ_o . We find, actually, that β/k_o varies only slightly, but that the variation in α/k_o is quite large. Of course, the amplitude of these variations will depend on the strength of the discontinuity, so that we should expect larger variations for larger scan angles θ_x . Also, we shall see below that, because of this effect, the *shape* of the dependence of β/k_o and α/k_o on θ_x will be influenced significantly by the choice of height c/λ_o .

The *second effect* is that the discontinuity permits the presence of an independent set of leaky modes, the so-called channel-guide modes, and that under appropriate conditions these channel-guide modes can *couple* to the NRD guide leaky mode with which we are concerned. The same type of coupling was encountered before in connection with the individual NRD guide line source, and was discussed in detail in Sec. C,2 of Chap. III.

Such coupling can occur only when the values of β and α of both mode types are equal. Since the values of α for the channel-guide modes are generally high, we would expect coupling to occur only for larger values of the air gap t (see Fig. 4.2) and for larger cross-plane scan angles θ_x .

These expectations are indeed borne out by a comprehensive set of numerical calculations. These calculations were made for two different values of cross-plane scan angle θ_x and for four different values of normalized air-gap thickness t/λ_o , and the results are obtained in each case for the normalized phase constant β/k_o and the normalized leakage constant α/k_o as a function of the normalized metal baffle height (or length) c/λ_o . The curves corresponding to these calculations are presented in Figs. 4.5 through 4.20. In each case, the geometrical parameters ($a/\lambda_o = 0.423$, $b/\lambda_o = 0.25$, and $\epsilon_r = 2.56$) are the same as those taken in Chap. III for the individual NRD guide line source.

The first set of curves, Figs. 4.5 through 4.12, corresponds to $\theta_x = 20^\circ$, which means a relatively small scan angle in the cross plane. The junction discontinuity at the radiating open end is therefore a relatively small one, and we find, as we would expect, that no coupling to the channel-guide modes occurs. It is nevertheless quite instructive to go through the set of curves.

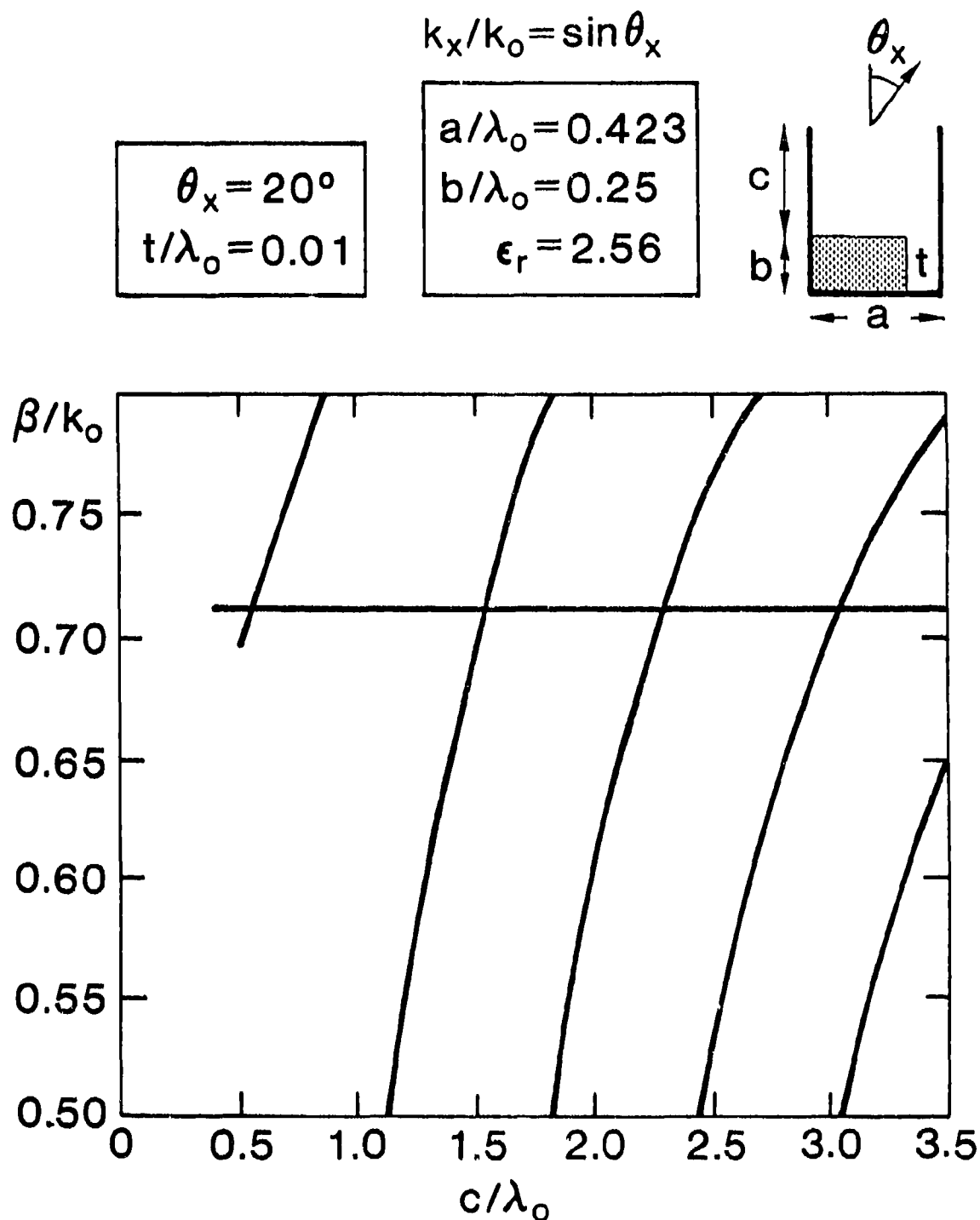


Fig. 4.5 Normalized phase constant β/k_o of NRD guide array as a function of normalized baffle height c/λ_o . The parameter values are given in the inset. The horizontal line represents the NRD guide leaky mode, and the remaining curves correspond to the channel-guide leaky modes. This figure is the first of a set for which the cross-plane scan angle $\theta_x = 20^\circ$, and in which the air-gap thickness t is varied. Here $t/\lambda_o = 0.01$, a very small gap.

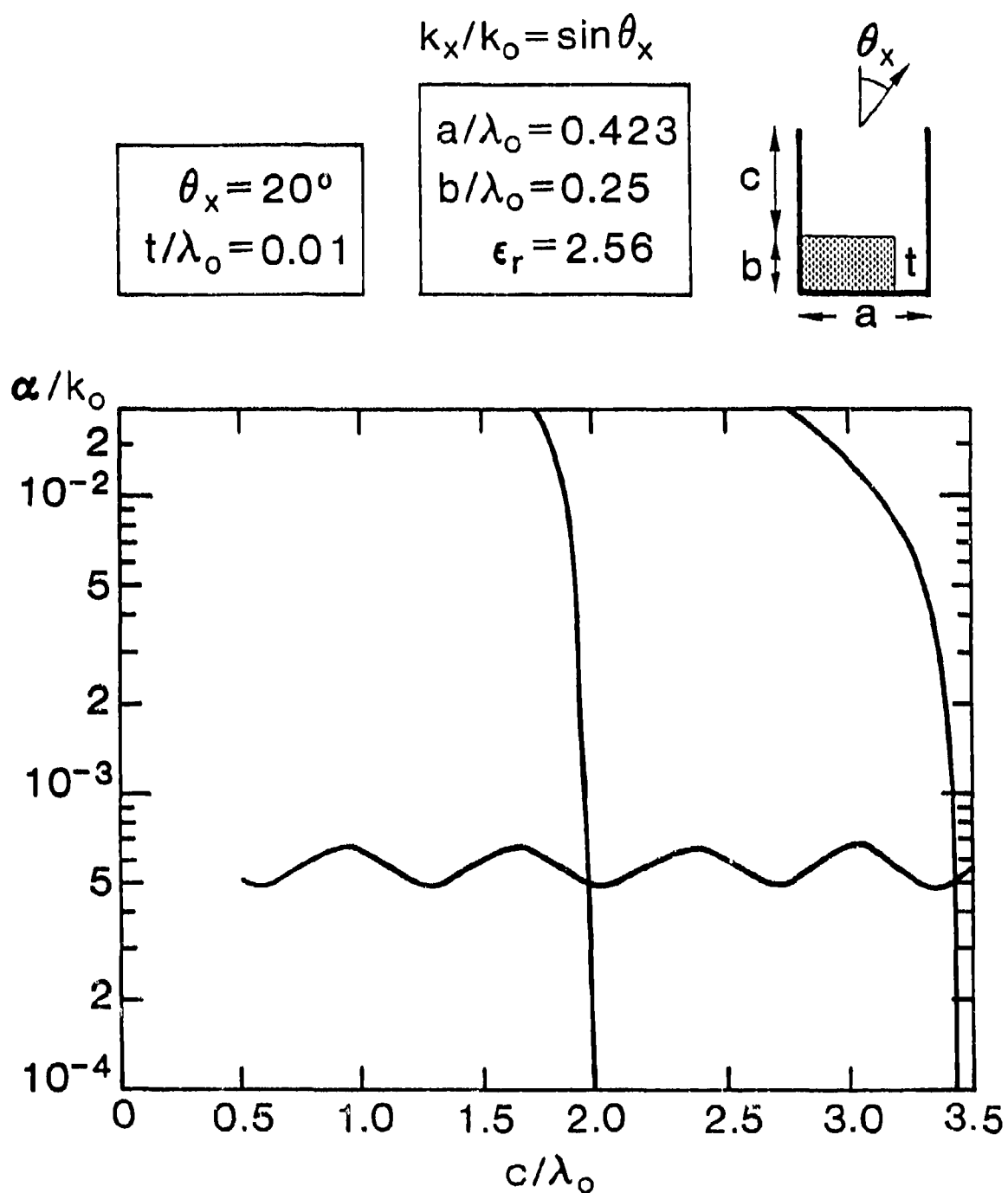


Fig. 4.6 Normalized leakage constant α/k_0 of NRD guide array as a function of normalized baffle height c/λ_0 . The remaining comments are the same as those for Fig. 4.5.

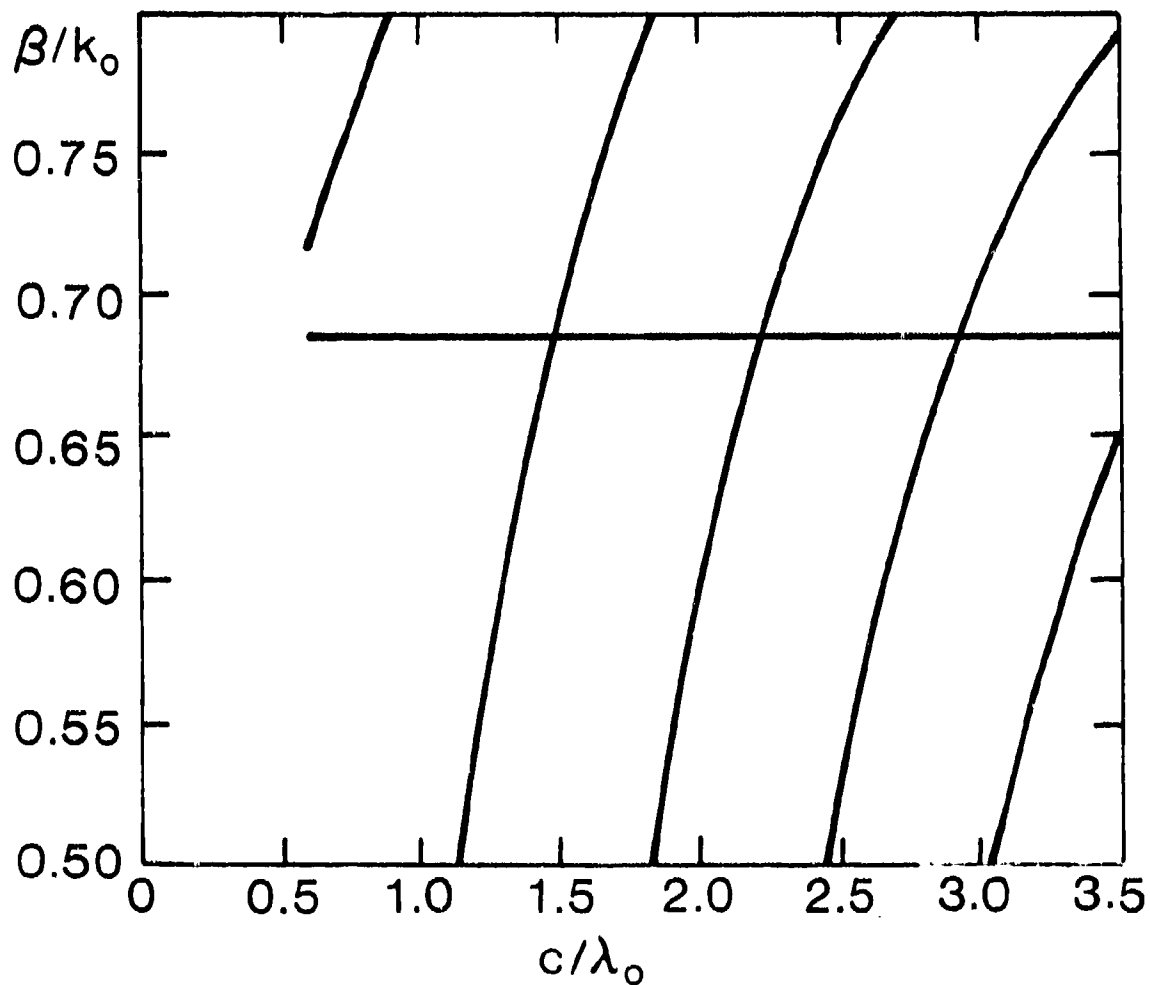
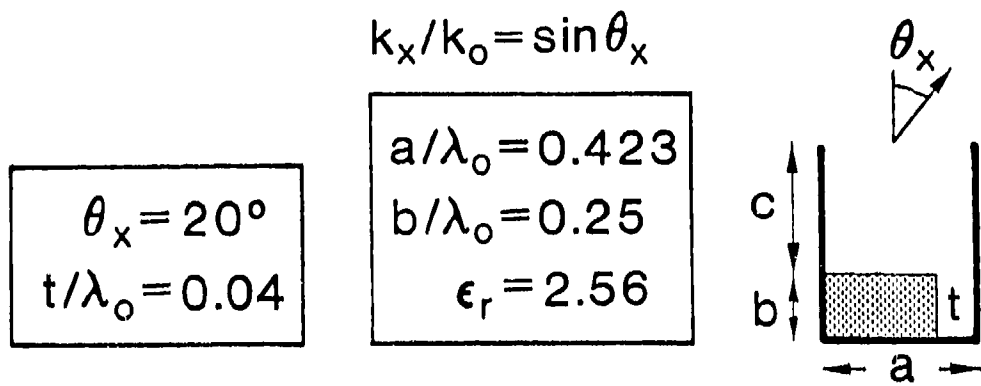


Fig. 4.7 Same as Fig. 4.5, except that $t/\lambda_o = 0.04$.

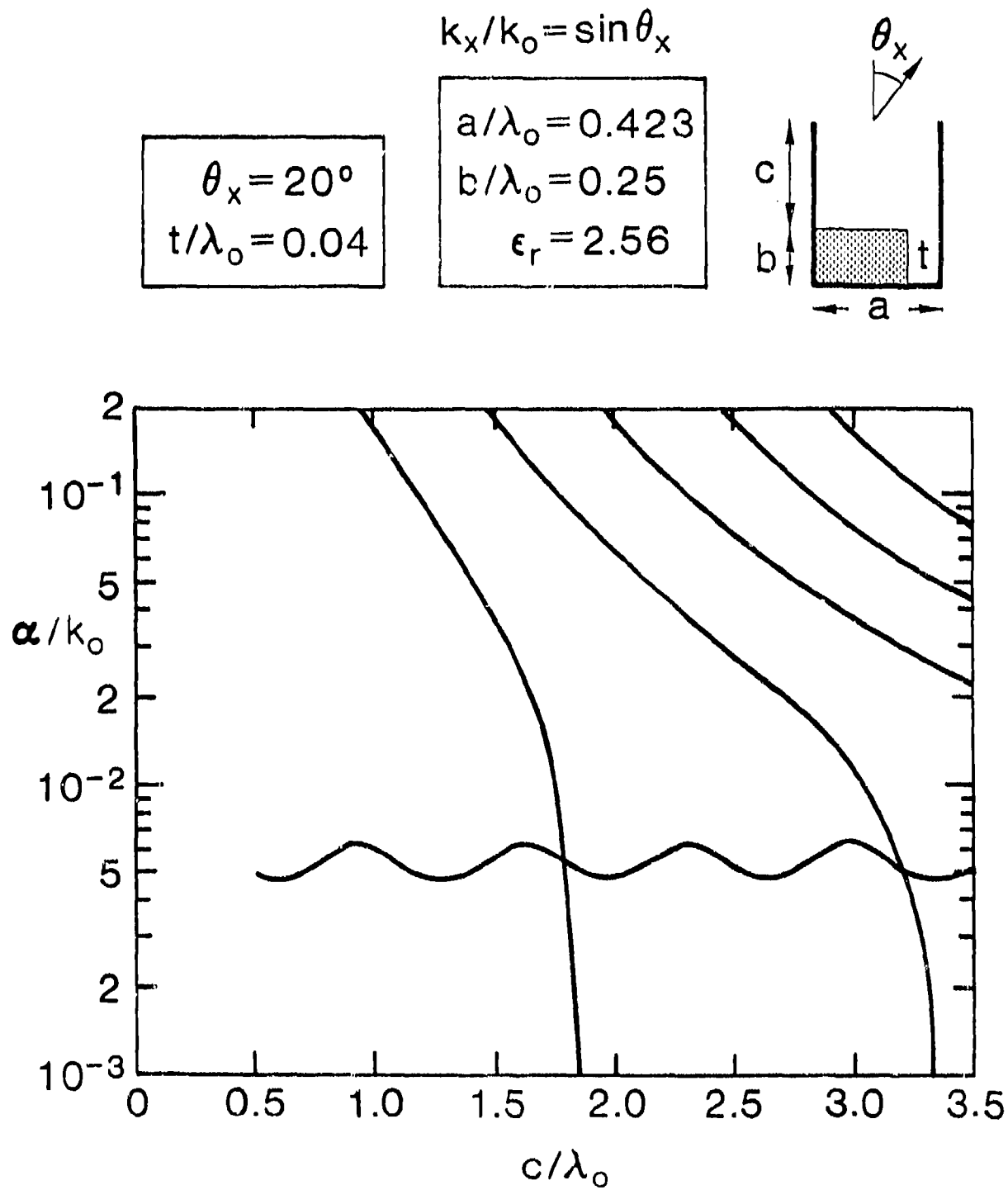


Fig. 4.8

Same as Fig. 4.6, except that $t/\lambda_0 = 0.04$.

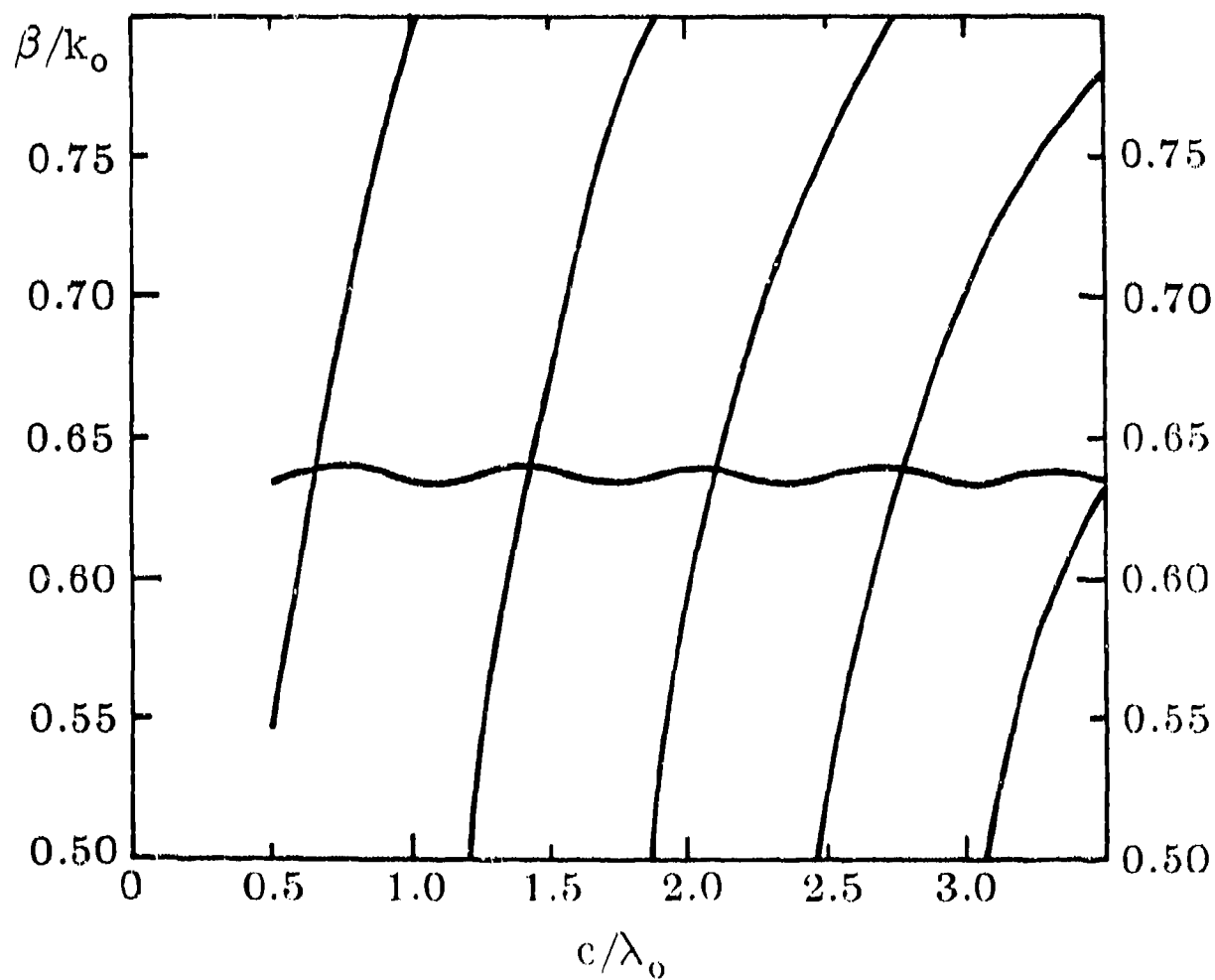
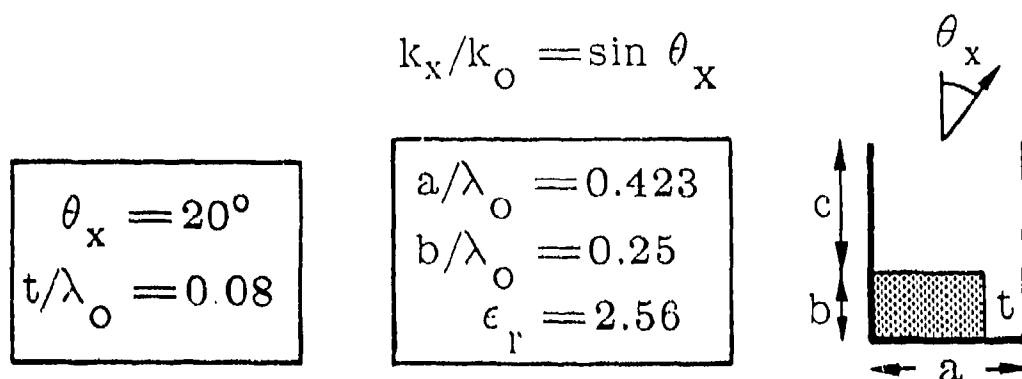


Fig. 4.9

Same as Fig. 4.5, except that $t/\lambda_o = 0.08$.

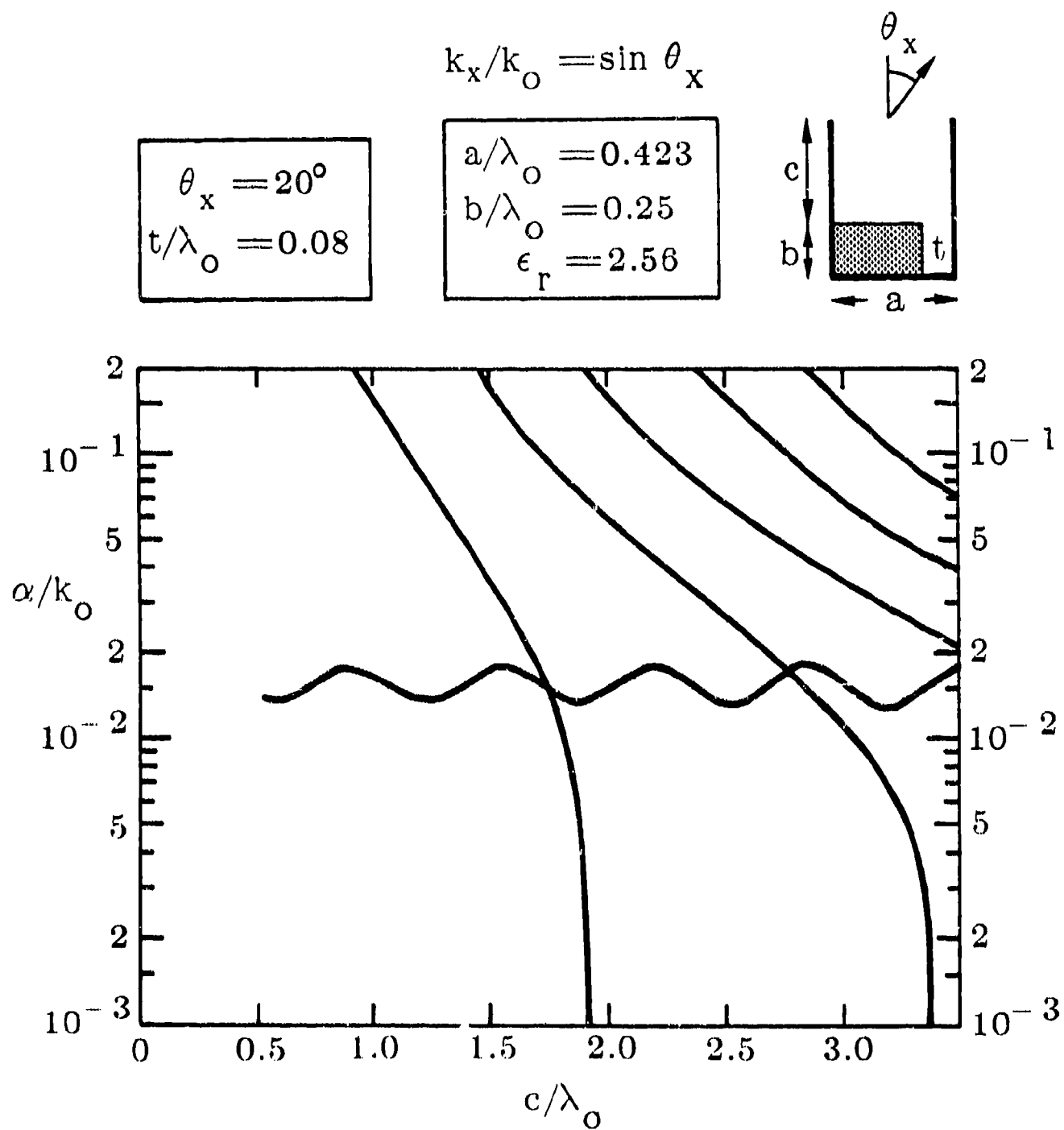


Fig. 4.10 Same as Fig. 4.6, except that $t/\lambda_o = 0.08$.

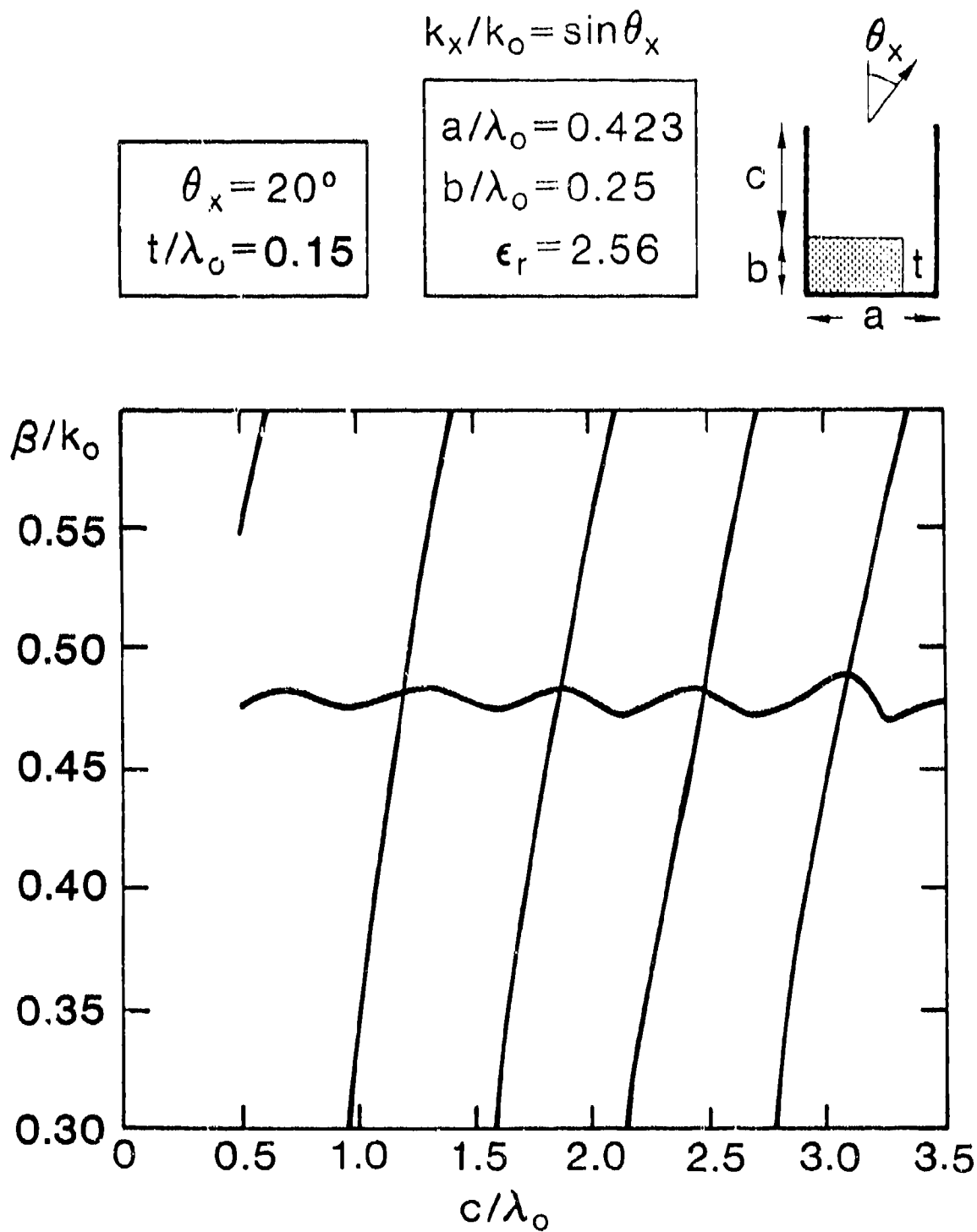


Fig. 4.11 Same as Fig. 4.5, except that $t/\lambda_0 = 0.15$, which is a very large air gap.

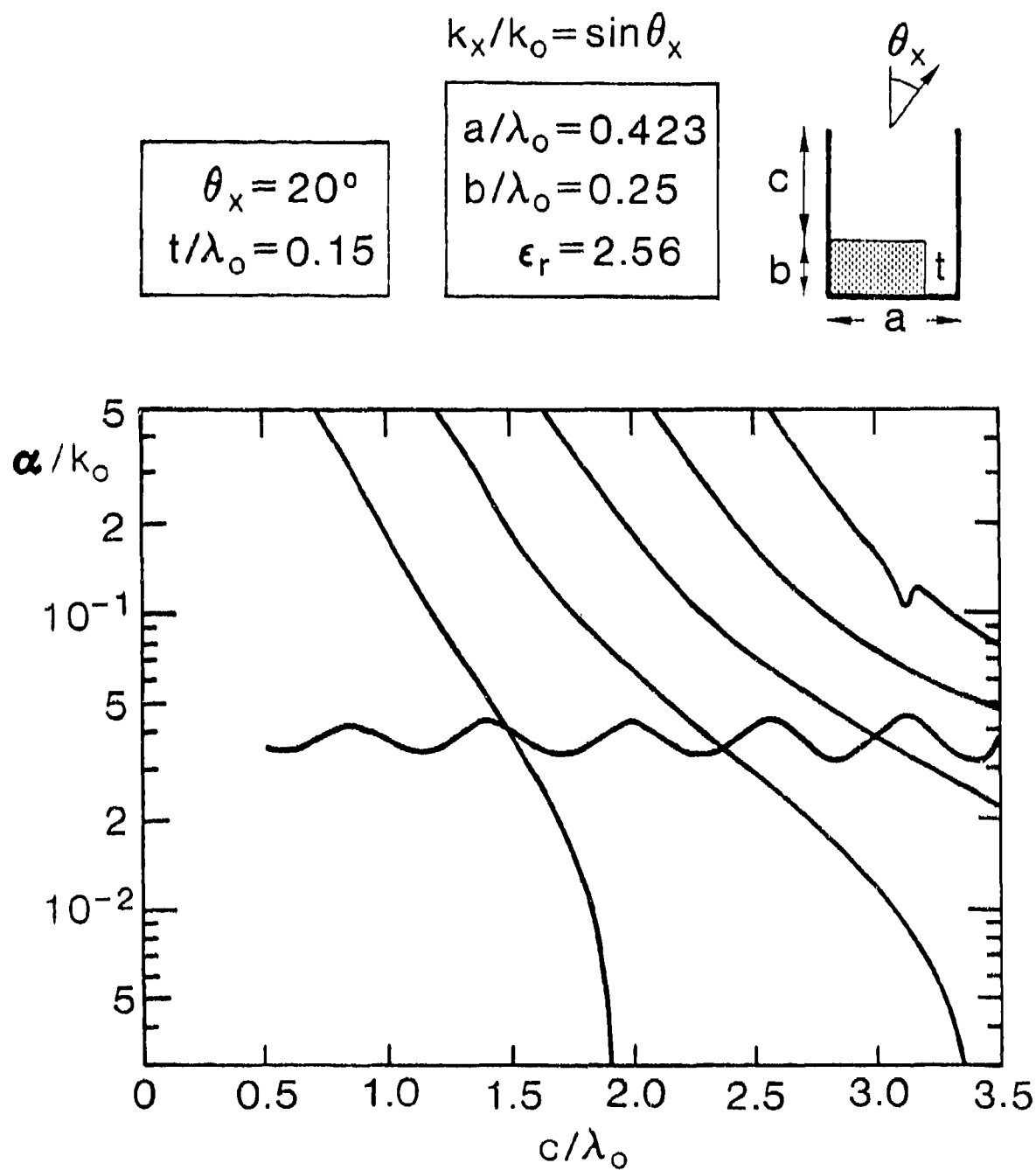


Fig. 4.12 Same as Fig. 4.6, except that $t/\lambda_o = 0.15$, which is a very large air gap.

The values of t/λ_o span a very wide range, from $t/\lambda_o = 0.01$ to 0.15, the latter being more than 1/3 of the guide width. The corresponding values of β/k_o decrease slowly as t/λ_o increases, taking its biggest jump in going from $t/\lambda_o = 0.08$ to 0.15. The corresponding variation in α/k_o is enormous, those values changing by two orders of magnitude. Those variations are in qualitative agreement with what was found in Figs. 3.2 and 3.3 of Chap. III for the individual line source when the height c is infinite (corresponding to $\theta_x = 0$ in the array). One should also note that, in contrast, the channel-guide modes change very little as t/λ_o is varied.

The first case, Figs. 4.5 and 4.6, holds for the smallest air gap value, $t/\lambda_o = 0.01$. The curve for β/k_o for the NRD guide mode is seen to be completely flat as c/λ_o is changed, whereas that for α/k_o in Fig. 4.6 does show a reasonable amplitude variation even though the magnitude of the leakage is very low. The next set, Figs. 4.7 and 4.8, for $t/\lambda_o = 0.04$, shows similar behavior, although the values of α/k_o have increased by an order of magnitude. For Figs. 4.9 and 4.10, which correspond to $t/\lambda_o = 0.08$, about 1/4 of the guide width, the curve of β/k_o now shows a small ripple as c/λ_o is varied, and that for α/k_o shows a *relative* variation in value as c/λ_o changes that is about the same as that found for the two previous cases, even though the average value is much higher. The final case for the set for $\theta_x = 20^\circ$, Figs. 4.11 and 4.12, corresponds to $t/\lambda_o = 0.15$ and shows a small change in behavior. For the larger values of c/λ_o , the ripple shapes change somewhat for both β/k_o and α/k_o ; the reason is that the fifth channel-guide mode is coming close to coupling with the NRD guide mode, as may be seen in Fig. 4.12 by the small dip in the α/k_o curve just above $c/\lambda_o = 3.0$.

Generalizing from the curves so far, we observe that, when the channel-guide modes and the NRD guide mode remain uncoupled, larger values of t/λ_o produce lower values of β/k_o , much higher values of α/k_o , a larger ripple in β/k_o vs. c/λ_o , and a relative variation in α/k_o vs. c/λ_o that remains about the same; finally, we also note that the curves for both α/k_o and β/k_o for the channel-guide modes are influenced very little by changes in t/λ_o .

The next set of curves, Figs. 4.13 through 4.20, are valid for a much larger cross-plane scan angle, $\theta_x = 40^\circ$, and therefore a much stronger discontinuity at the radiating open end. Several general observations may be made. The first is that, except for $t/\lambda_o = 0.01$, coupling now occurs between the two mode types. Another feature is that the curves for the channel-guide modes are now very different from

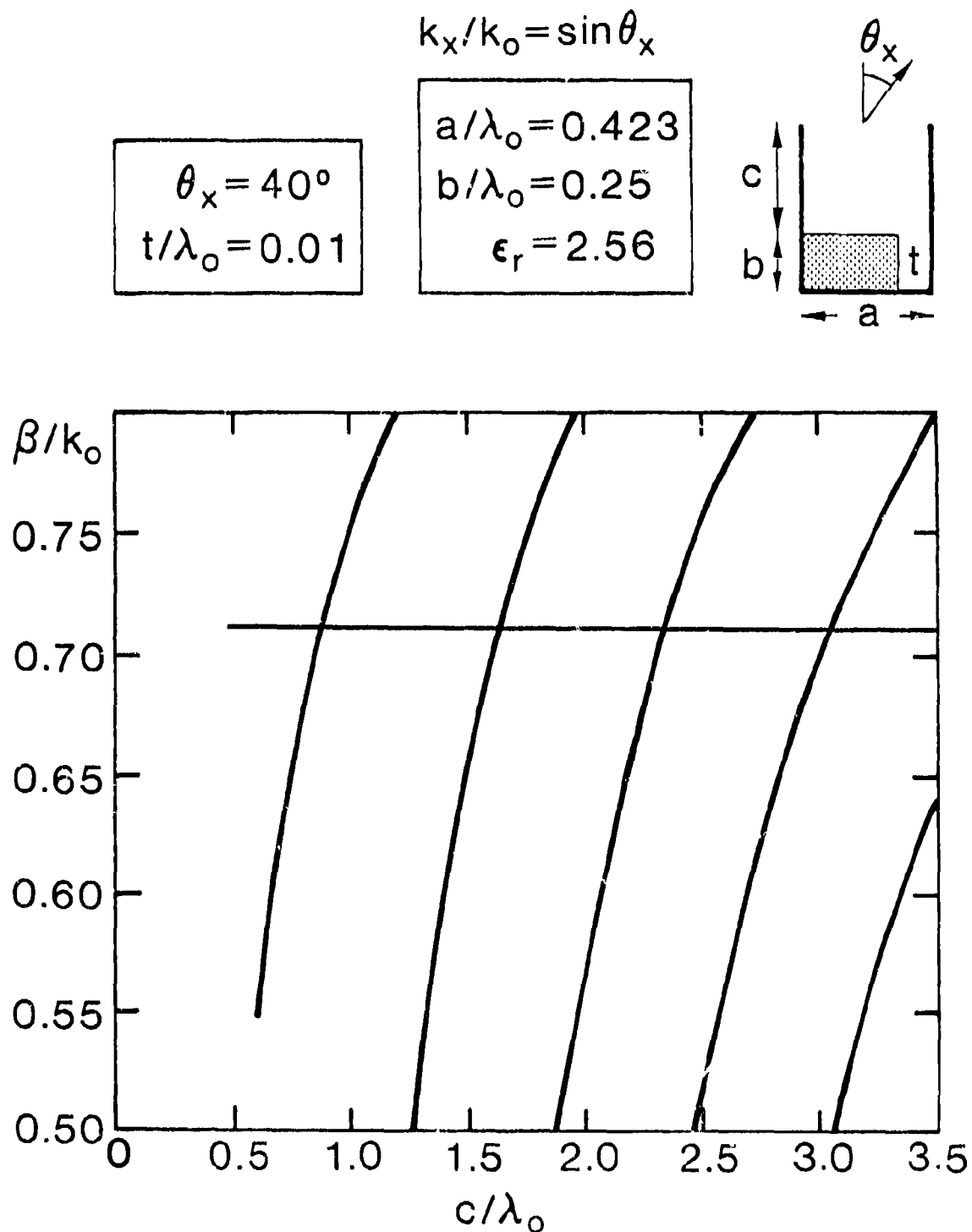


Fig. 4.13

Same as Fig. 4.5, except that this figure is the first of a set for which the cross-plane scan angle θ_x is 40° , rather than 20° , and in which t/λ_o is varied. Here $t/\lambda_o = 0.01$, a very small gap, and no coupling occurs.

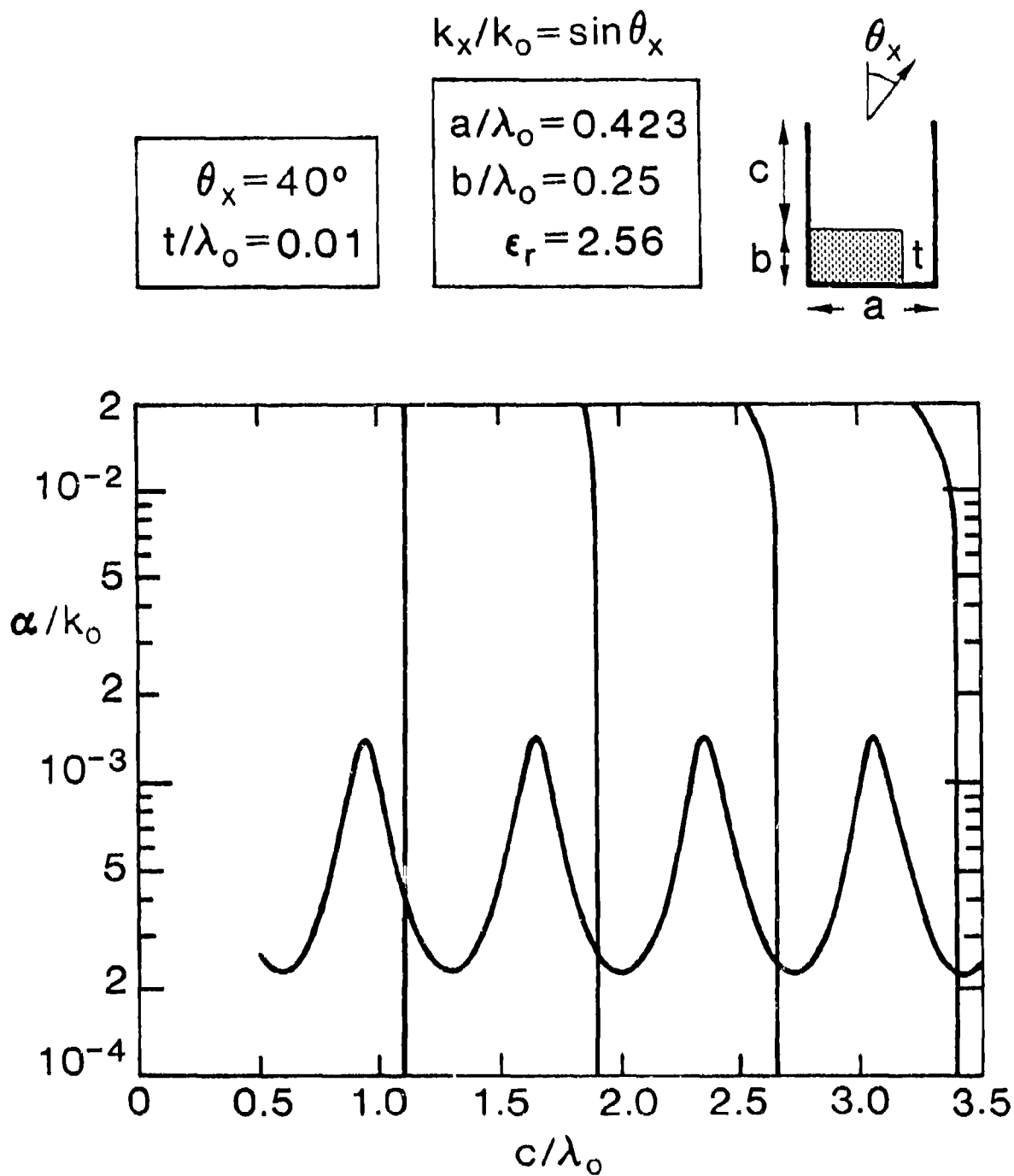


Fig. 4.14 Same as Fig. 4.6, except that here $\theta_x = 40^\circ$ and $t/\lambda_0 = 0.01$. The other comments for Fig. 4.13 apply here as well.

$$k_x/k_o = \sin \theta_x$$

$$\begin{aligned} \theta_x &= 40^\circ \\ t/\lambda_o &= 0.04 \end{aligned}$$

$$\begin{aligned} a/\lambda_o &= 0.423 \\ b/\lambda_o &= 0.25 \\ \epsilon_r &= 2.56 \end{aligned}$$

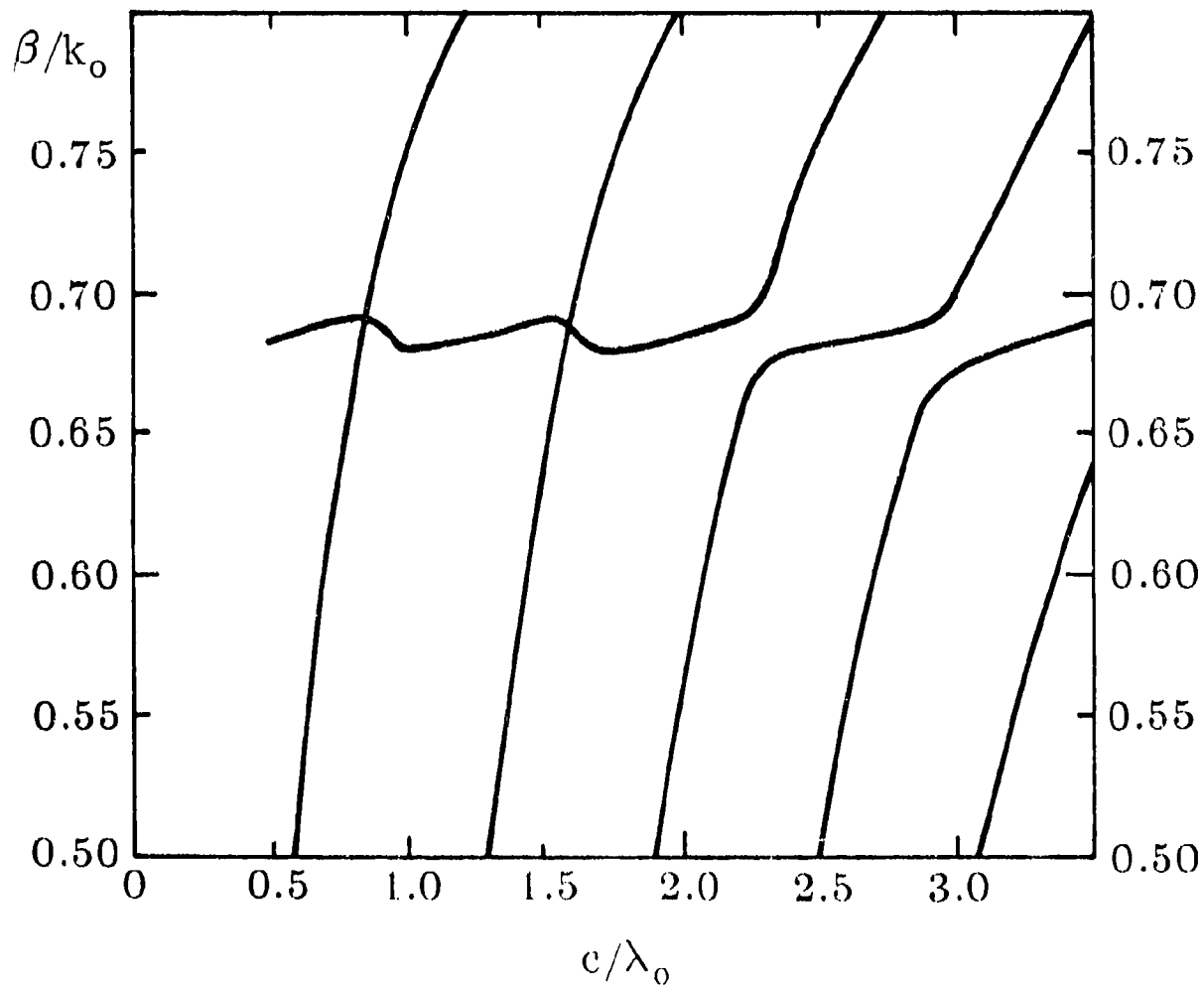
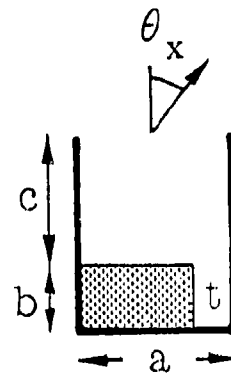


Fig. 4.15

Same as Fig. 4.13, except that $t/\lambda_o = 0.04$. We see that coupling occurs for the higher values of c/λ_o .

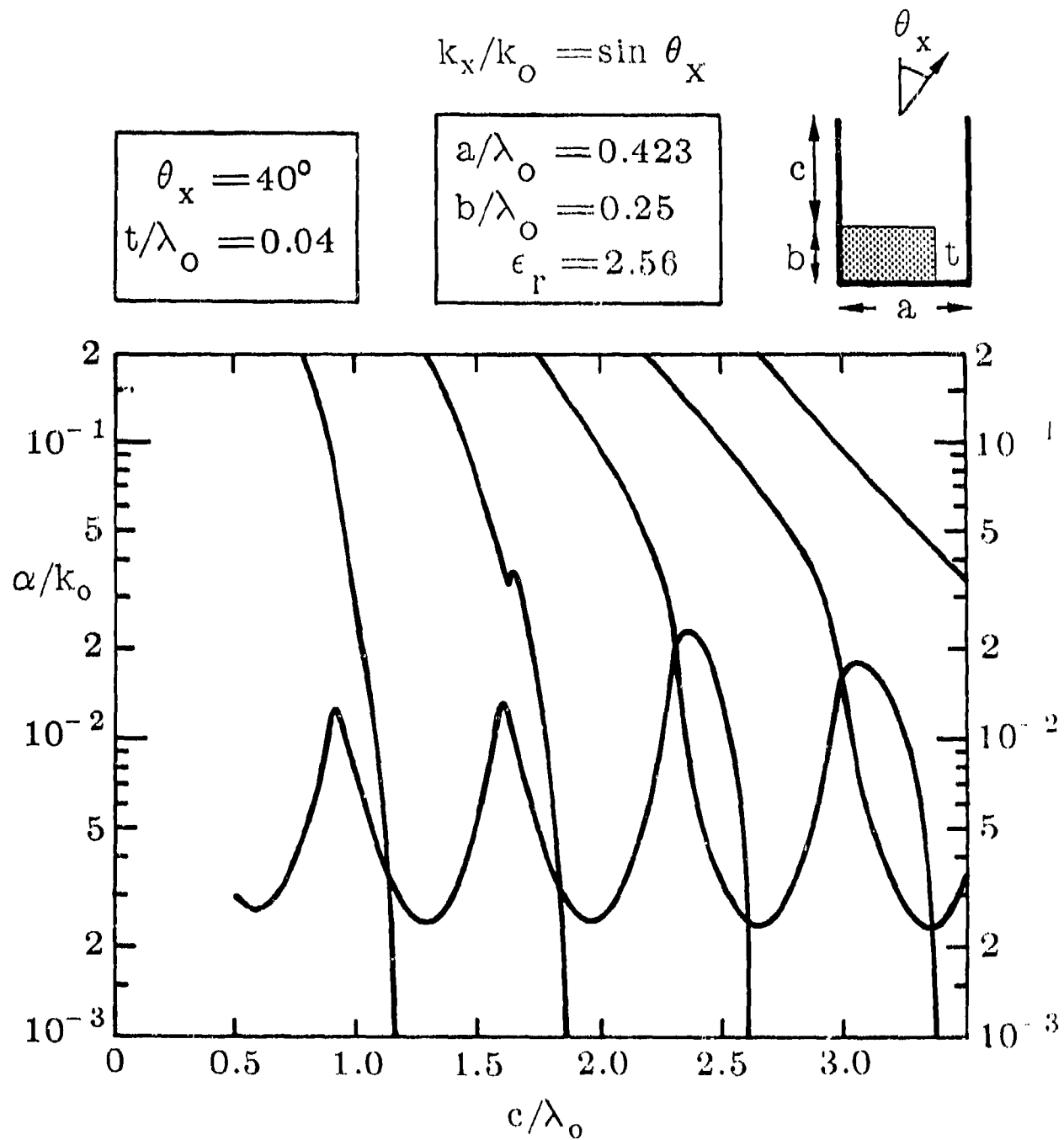


Fig. 4.16 Same as Fig. 4.14, except that $t/\lambda_o = 0.04$. We see that coupling occurs for the higher values of c/λ_o .

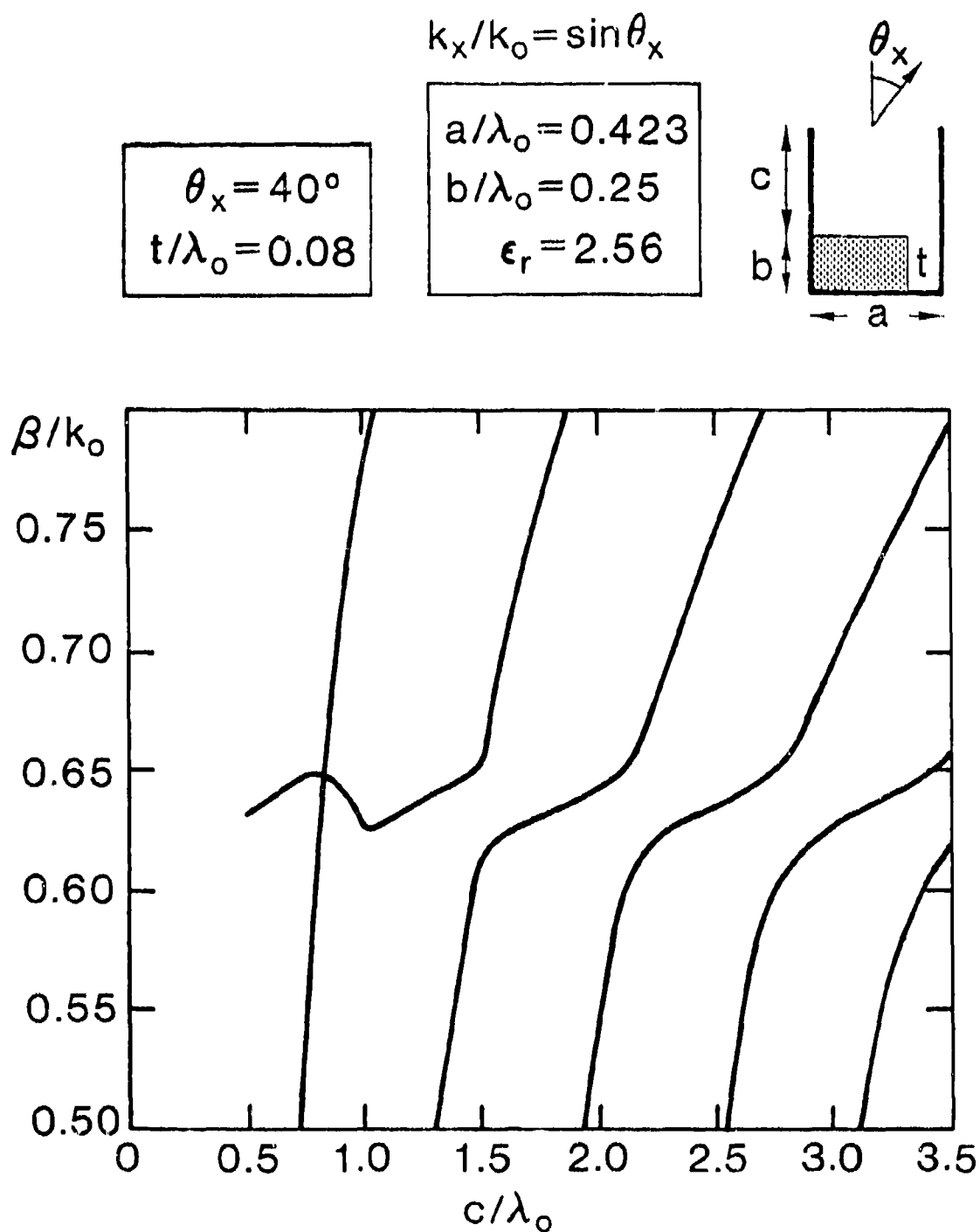


Fig. 4.17

Same as Fig. 4.13, except that $t/\lambda_0 = 0.08$. Coupling occurs with all the channel-guide modes but the lowest.

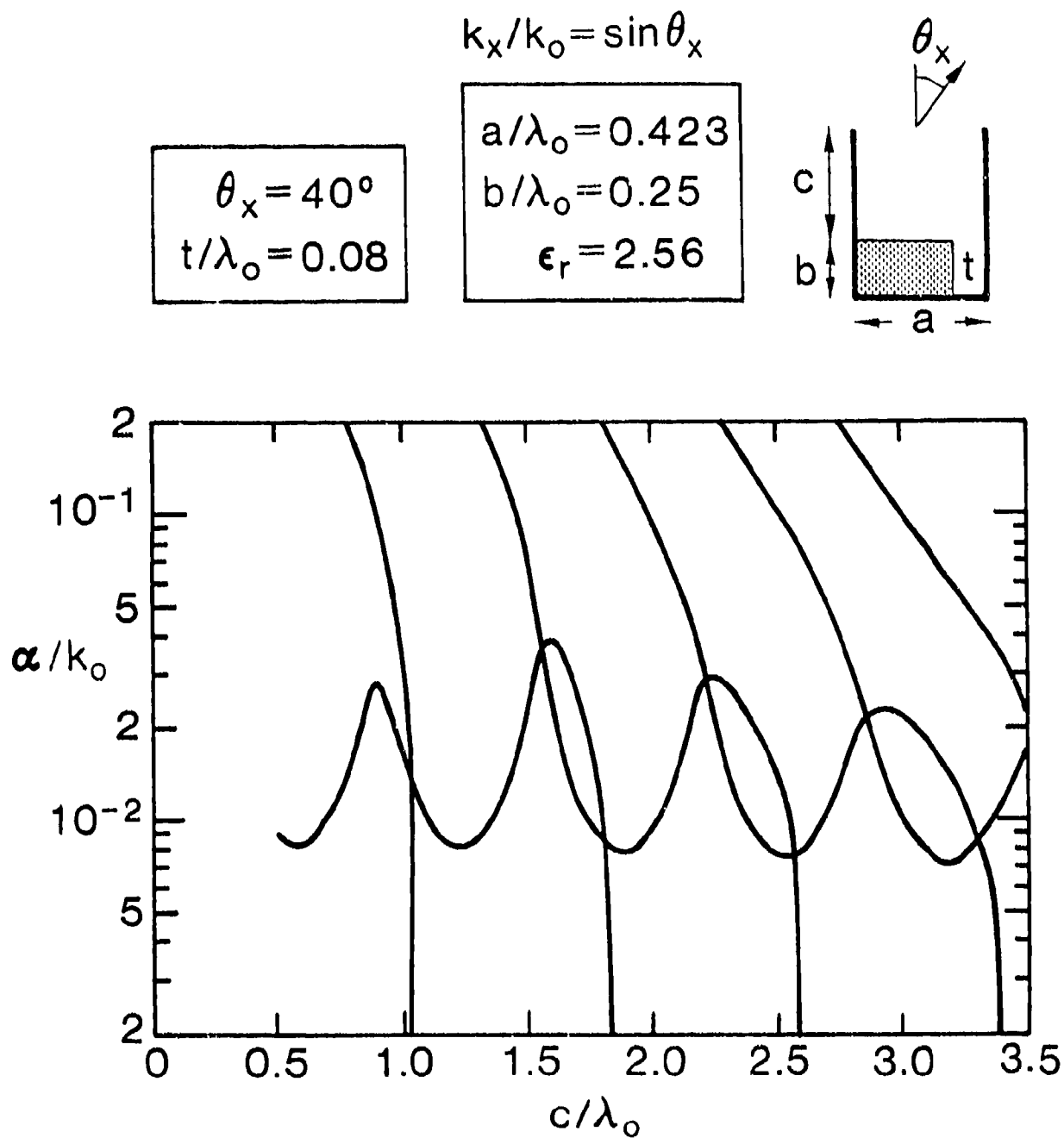


Fig. 4.18

Same as Fig. 4.14, except that $t/\lambda_0 = 0.08$. Coupling occurs with all the channel-guide modes but the lowest.

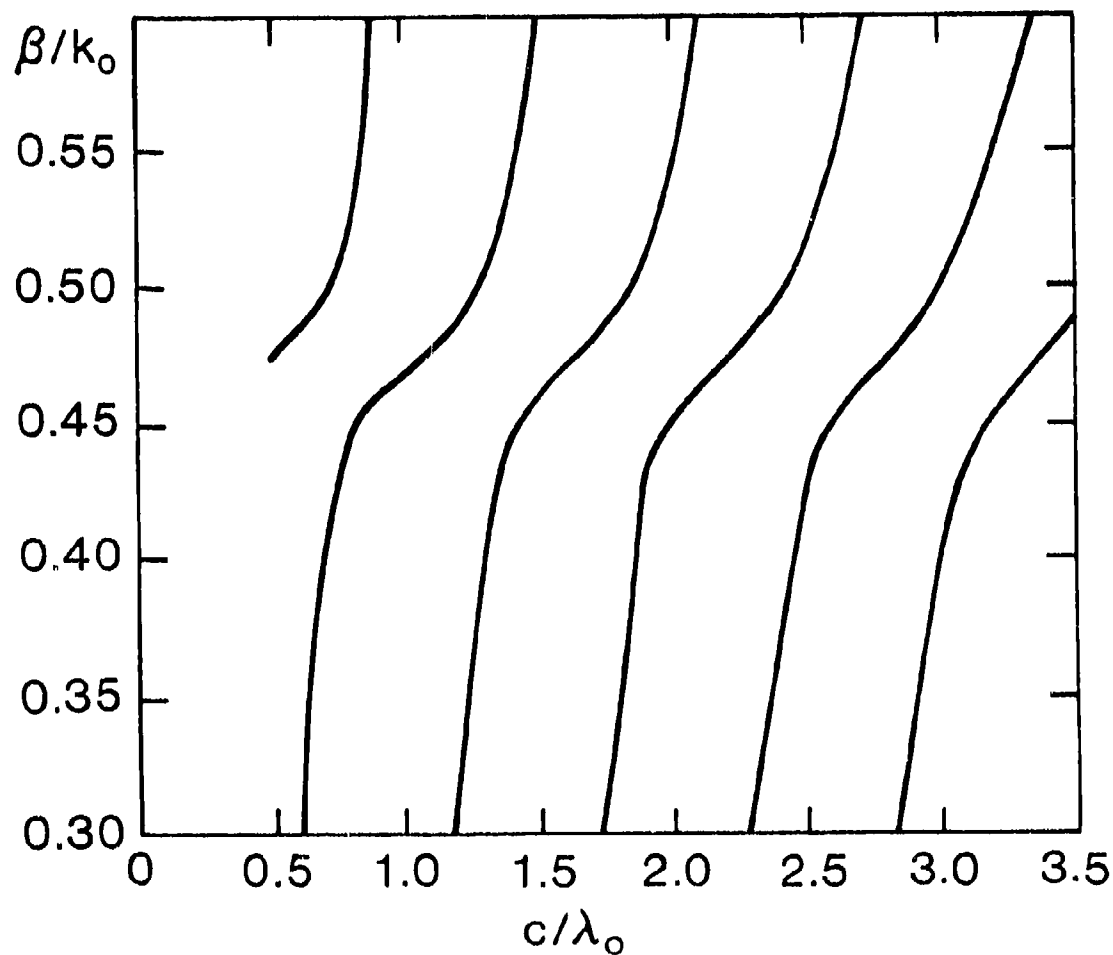
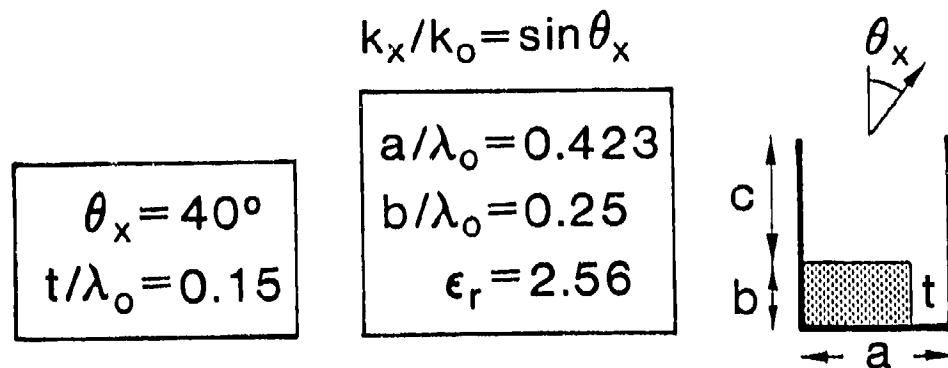


Fig. 4.19 Same as Fig. 4.13, except that $t/\lambda_0 = 0.15$. With this large value of air gap t and large scan angle θ_x , coupling occurs with all the modes.

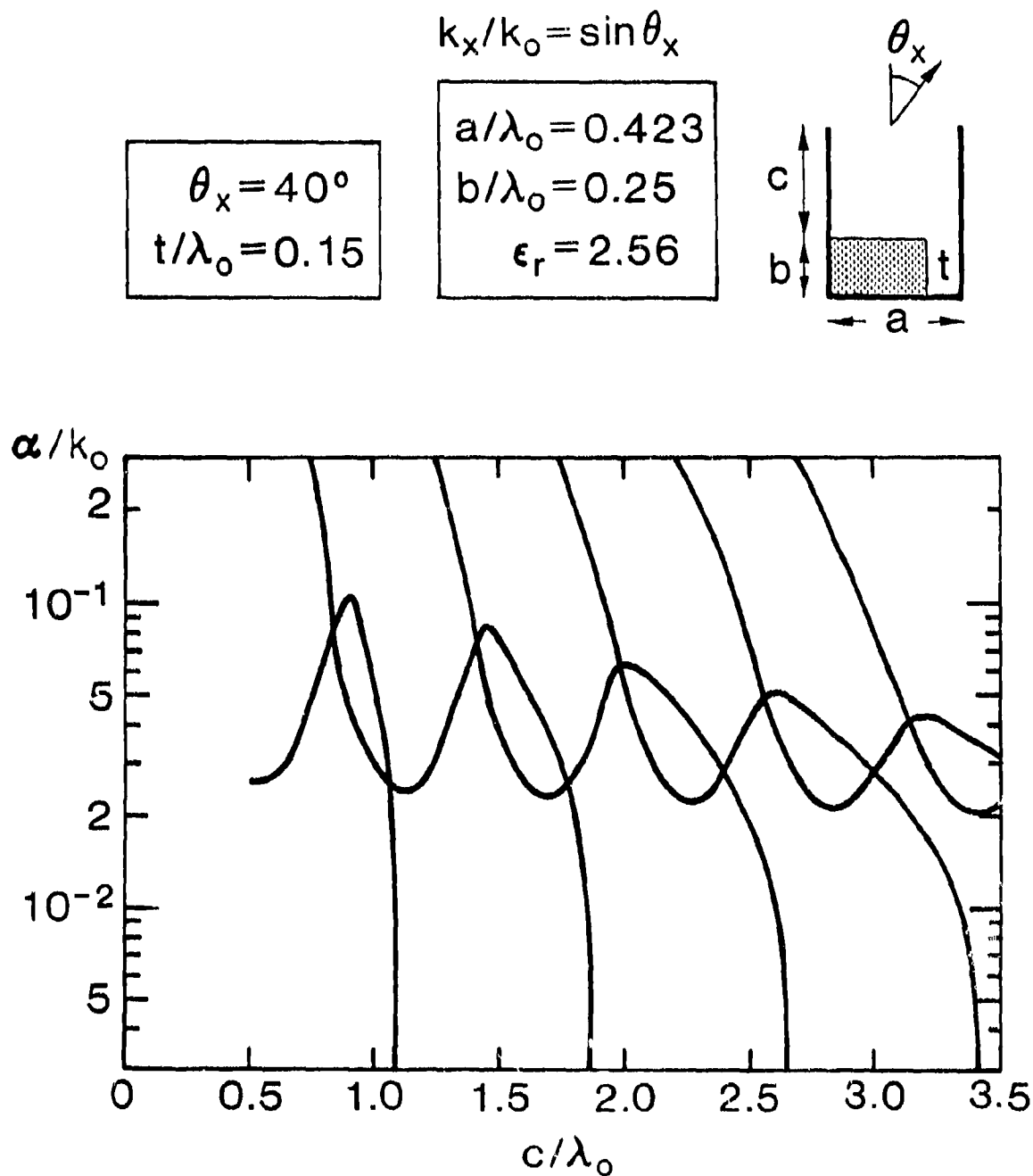


Fig. 4.20

Same as Fig. 4.14, except that $t/\lambda_o = 0.15$. With this large value of air gap t and large scan angle θ_x , coupling occurs with all the modes.

what they were for the $\theta_x = 20^\circ$ case; clearly, the channel-guide modes are affected little by changes in t/λ_o but are strongly influenced by alterations in θ_x . Another general observation is that the change in θ_x from 20° to 40° does not strongly modify the average values of β/k_o and α/k_o but greatly increases the amplitudes of the ripples in these quantities; the reason is that the stronger terminal discontinuity increases the amplitude of the standing wave produced between the radiating open end and the air-dielectric interface.

The first case in this second set, Figs. 4.13 and 4.14, which holds for the smallest air gap value, $t/\lambda_o = 0.01$, does not involve any coupling between the mode types because the value of α/k_o for the NRD guide mode is too small. The most interesting change from the $\theta_x = 20^\circ$ case is that the variation in the values of α/k_o as c/λ_o is changed is now very much greater. One can obtain a seven-fold change in the leakage rate just by altering one's selection of c/λ_o .

The next case, for $t/\lambda_o = 0.04$ and presented in Figs. 4.15 and 4.16, is particularly interesting because it shows the transition between the uncoupled and coupled regions. By observing the curves for β/k_o in Fig. 4.15 we may see most clearly that coupling occurs for larger values of c/λ_o . The reason that coupling now occurs is that the stronger discontinuity at the radiating open end has reduced the leakage rates for the channel-guide modes, bringing them down to the value possessed by the NRD guide mode; the higher maximum value for α/k_o of the NRD guide mode achieved now by the larger ripple amplitude may help, but not very importantly. The α/k_o plot in Fig. 4.16 has now become more complicated, but, as explained in detail in Sec. C,2 of Chap. III, the portions of the curve in the region of coupling that possess the properties of the NRD guide mode are those that resemble a continuation of the curve in the uncoupled portion. It is only those portions that are of interest in our array application.

The curves in Figs. 4.17 and 4.18, for $t/\lambda_o = 0.08$, and those in Figs. 4.19 and 4.20, for $t/\lambda_o = 0.15$, show behavior that is qualitatively similar to those just discussed, but the coupling is much stronger, making it more difficult to identify the portions of the curves that correspond to the NRD guide mode. The guidance above for Fig. 4.16 serves here as well.

b. Departure from Conical Scan

It was pointed out in Sec. B that the radiated beam traces out a conical scan as θ_x is increased from zero to its maximum value. Actually, the scan departs slightly from conical, especially for large azimuth scan angles, because of the discontinuity mentioned just above. That discontinuity, corresponding to the junction between the parallel-plate metal baffles and the periodic unit cell, was shown above to produce a standing wave in the parallel-plate region and to give rise to an additional set of leaky modes that can, under the right conditions, couple to the NRD guide leaky mode. Here, the discontinuity changes the value of β/k_o as θ_x is varied, in turn causing a mild departure from conical scan.

To understand the reason for the effect, let us reexamine the scan process. We first consider the limiting case for which $k_{xop} = 0$, so that $\theta_x = 0$. By reference to the polar coordinate diagram in Fig. 4.21, which is a more complicated version of Fig. 2.13

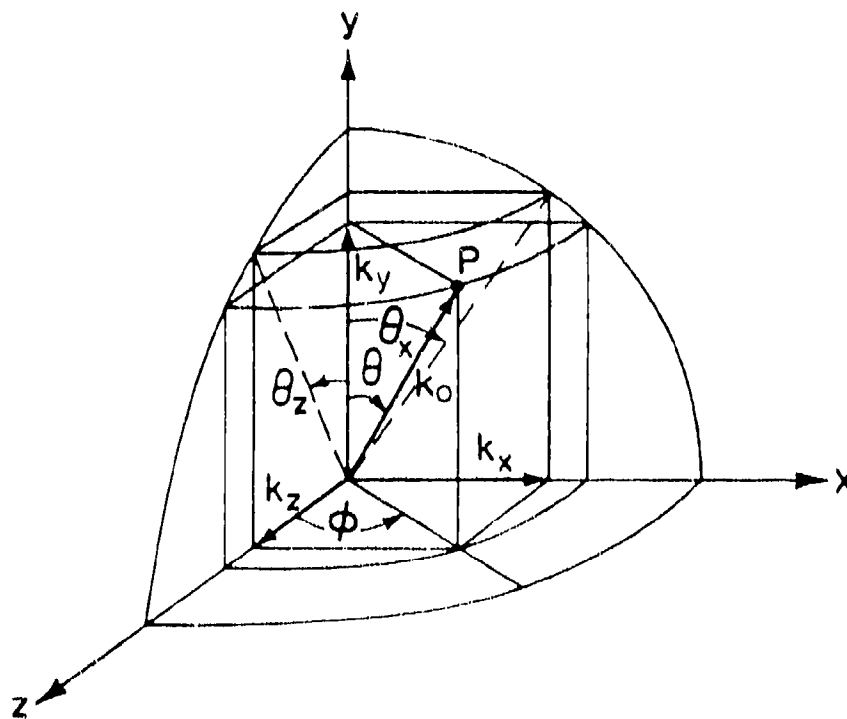


Fig. 4.21 Polar coordinate diagram, showing the various relevant angles and wavenumbers.

of Chap. II, this case is seen to correspond to azimuth angle $\phi = 0$. Angle θ is then in the yz plane, and the beam points in that plane. Let us call that angle θ_z , where

$$\sin \theta_z = \beta/k_o \quad (4.16)$$

since $k_z = \beta - j\alpha$, and we assume in these angle considerations that $\alpha \ll \beta$.

Then, as θ_x is increased, θ moves out of the yz plane and the beam begins to scan in azimuth ($\phi \neq 0$). From Fig. 4.21, which looks a bit like an Escher diagram but isn't, we can see that as ϕ becomes larger θ increases, meaning that point P gets closer to the ground (the xz plane). Eventually, as θ_x is increased sufficiently, the beam hits the ground, and all radiation ceases. At that point, $\theta = 90^\circ$ and, as shown in Chap. II as (2.16) and (2.17), we have

$$\phi_\theta = 90^\circ + \theta_\phi = 0 = 90^\circ \quad (4.17)$$

or

$$\phi_{k_y} = 0 + \theta_{k_x} = 0 = 90^\circ \quad (4.18)$$

If θ_z , or alternatively k_z , stays constant as θ_x (and therefore θ) increases, the trace of the scan will be exactly conical. However, the discontinuity at the radiating open end is a function of k_{xop} , and therefore θ_x (from (4.10)). From Fig. 4.3 and relations (4.12) through (4.14), we observe that both the terminating admittance and its reference plane location are functions of k_{xop} . Since the termination on the transmission line of length ($c - d'$) in the transverse equivalent network of the unit cell in Fig. 4.2 is thus a function of θ_x , we would expect that the value of β/k_o will change as θ_x is varied. To the extent that β/k_o changes, the scan path will depart from the ideal conical one.

The amount of change in β/k_o as the beam is scanned depends on the geometric parameter values, and particularly on the choice of c/λ_o . Let us first examine the behavior in Fig. 4.22, for $c/\lambda_o = 0.50$ and for three different values of air-gap thickness, $t/\lambda_o = 0.01, 0.08$ and 0.15 . The metal baffle height $c/\lambda_o = 0.50$ is a very likely choice in practice, being long enough to insure negligible cross polarization but not longer than necessary. The curve for the very small gap thickness, $t/\lambda_o = 0.01$, is very flat as θ_x is varied, as we would expect. But even for the larger gap thicknesses, $t/\lambda_o = 0.08$ and 0.15 , the change in β/k_o as θ_x increases is quite small. The scan path for these cases is therefore rather close to conical.

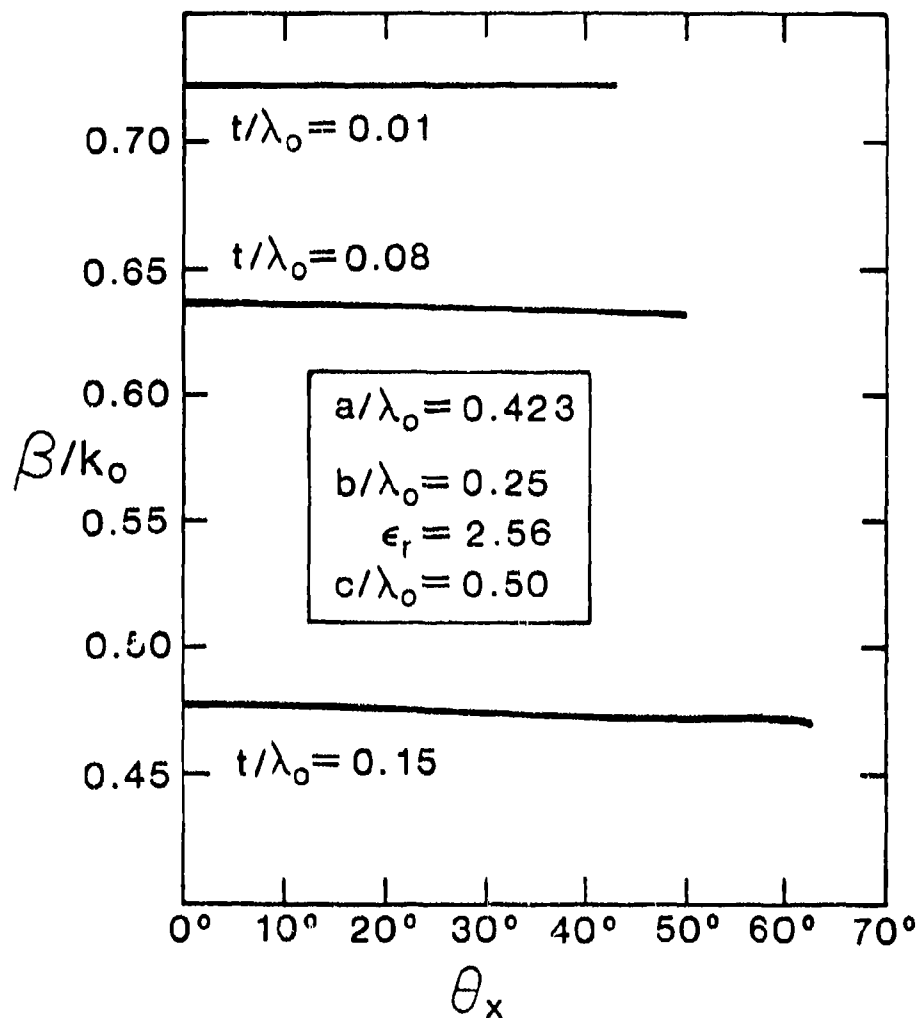


Fig. 4.22 Variation of normalized phase constant β/k_0 with cross-plane scan angle θ_x when $c/\lambda_0 = 0.50$, for three values of t/λ_0 : 0.01, 0.08 and 0.15. Each curve stops at the value of θ_x for which conical scan ends.

We next consider the behavior for much larger values of c/λ_o , in Fig. 4.23. The t/λ_o values are the same as in Fig. 4.22, but the changes in β/k_o are seen to be much greater here. The reason for the difference is readily understood by referring to the plots of β/k_o vs. c/λ_o , in Figs. 4.5, 4.9, 4.11, 4.13, 4.17 and 4.19, which correspond to the t/λ_o values covered here.

For the $t/\lambda_o = 0.01$ case, the β/k_o values remain flat as a function of c/λ_o in both Figs. 4.5 and 4.13 (for $\theta_x = 20^\circ$ and 40°), so that it is not surprising that the curve for $t/\lambda_o = 0.01$ in Fig. 4.23 is still quite flat. For the case $t/\lambda_o = 0.08$, however, it can be seen from Fig. 4.17, for $\theta_x = 40^\circ$, that the value of β/k_o when $c/\lambda_o = 1.60$ is near to the bottom of the portion of the curve that corresponds to the NRD guide mode. For $\theta_x = 20^\circ$, on the other hand, we see from Fig. 4.9 that the variation in β/k_o is much smaller; although $c/\lambda_o = 1.60$ is again close to the bottom of the ripple, its value is higher since the range of variation is much smaller. The value of β/k_o is therefore lower for $\theta_x = 40^\circ$ than it is for 20° , and the curve of β/k_o vs. θ_x in Fig. 4.23 slopes downwards. A corresponding inspection of Figs. 4.11 and 4.19 for $t/\lambda_o = 0.15$ leads to a similar conclusion.

On the other hand, if we chose $c/\lambda_o = 2.05$ rather than 1.60 for $t/\lambda_o = 0.08$ in Figs. 4.9 and 4.17, we would then find the trend going the other way. Inspection of the curves shows that we are now near to the tops of the curves and, since the variation is greater for the $\theta_x = 40^\circ$ curves, the value of β/k_o for $\theta_x = 40^\circ$ is now greater than it is for $\theta_x = 20^\circ$. As a result we would find that the curve of β/k_o vs. θ_x would *increase* slowly rather than decrease slowly, as in Fig. 4.23. The departure from conical scan can therefore go in either direction, depending on the parameter values, but even in the more severe cases the departure is not seen to be large.

c. Absence of Blindness Effects

Blindness effects occur when the array cannot radiate or receive power at some specific angle of scan. Such effects constitute a serious problem in phased array antennas; since the scanning in the cross plane (or in azimuth) is achieved by phase shifting, it is important that the behavior as a function of θ_x be checked to determine if any blindness effects are present. (We know from prior experience that blind spots do not occur when the array is scanned in elevation in leaky-wave fashion.)

In the discussion below, we use two separate tests for the presence of blind spots. In the first, we examine the variation of α/k_o vs. θ_x . In the second procedure, we

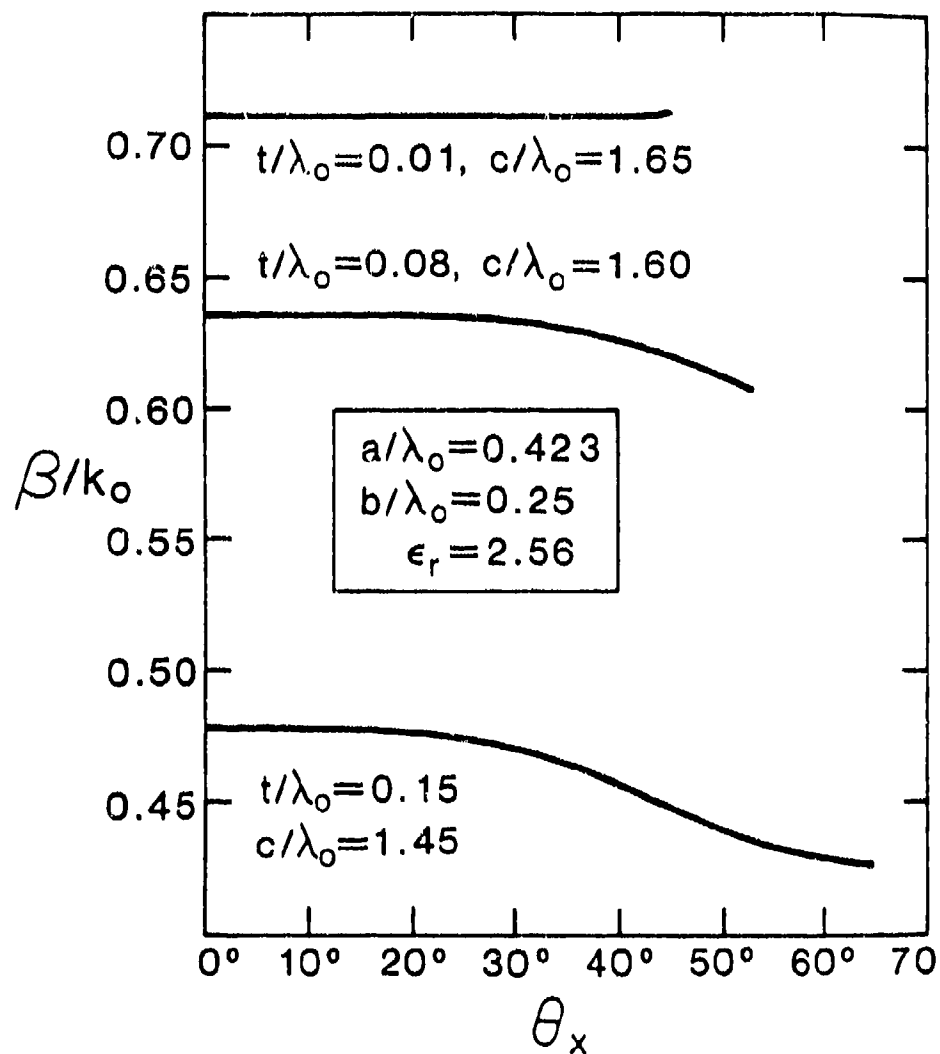


Fig. 4.23

Same as Fig. 4.22, except that the normalized metal baffle height c/λ_0 is much larger, being 1.65, 1.60 and 1.45 for $t/\lambda_0 = 0.01, 0.08$ and 0.15 , respectively.

determine the variation of the radiation conductance Y_{op}/Y_{og} at the end of the unit cell, or equivalently the periodic cell propagation wavenumber k_{yop} , as a function of θ_x . If the variations with θ_x in the two cases are smooth, and show no deep dips, then blindness effects are not present.

The quantity α/k_o is proportional to the rate of power leakage, and is also a direct measure of the beam width of the radiated beam in the elevation direction. If α goes to zero, there can be no power radiated. It is therefore important to examine the curve of α/k_o as a function of cross-plane scan angle θ_x ; if the value of α/k_o suffers a sharp dip anywhere within that scan range, then a blind spot is present.

In Fig. 4.24, the normalized leakage constant α/k_o is plotted as a function of θ_x for three different values of air-gap thickness, $t/\lambda_o = 0.01, 0.08$ and 0.15 . The leakage rates for each are quite different, of course, but the form of the variation with θ_x is pretty much the same. It is seen that the variation is smooth throughout the whole range of conical scan, with the leakage values decreasing only gradually until just before the end of the scan range, when the beam hits the ground. It is also clear that no deep dips occur, sharp or otherwise; we may feel secure that *no blind spots* are present.

The value of c/λ_o for which the data in Fig. 4.24 are valid is 0.50. For that case, we note that the curves *decrease* monotonically. For other values of c/λ_o , the curves may *increase* during the scan range before dropping off to zero at the end of the range. The shape of the variation may change but no blind spot dips have been found.

Examples of plots which exhibit *increases* during the scan range are shown in Fig. 4.25. As we found for the plots of β/k_o vs. θ_x in Figs. 4.22 and 4.23, the different behaviors become clear when we examine the curves as a function of c/λ_o . As an illustrative case, let us examine the plots in Figs. 4.6 and 4.13, for which $t/\lambda_o = 0.01$ and $\theta_x = 20^\circ$ and 40° , respectively. One sees that the ripples in the curves for the NRD guide mode are rather small for $\theta_x = 20^\circ$, in Fig. 4.6, but quite large when $\theta_x = 40^\circ$, in Fig. 4.13. For $c/\lambda_o = 0.50$, the curve for 40° is near its bottom, whereas for $c/\lambda_o = 1.65$ it is near to the top. As θ_x is increased from 20° to 40° , therefore, it is clear that α/k_o will decrease when $c/\lambda_o = 0.50$ but increase when it is 1.65.

The *second test* for the presence of blind spots involves the behavior of the radiation conductance during the scan process. That conductance is essentially the active input admittance to the periodic waveguide portion of the unit cell, and corresponds to the termination Y_{op} on the transmission line of length $(c - d')$ in the

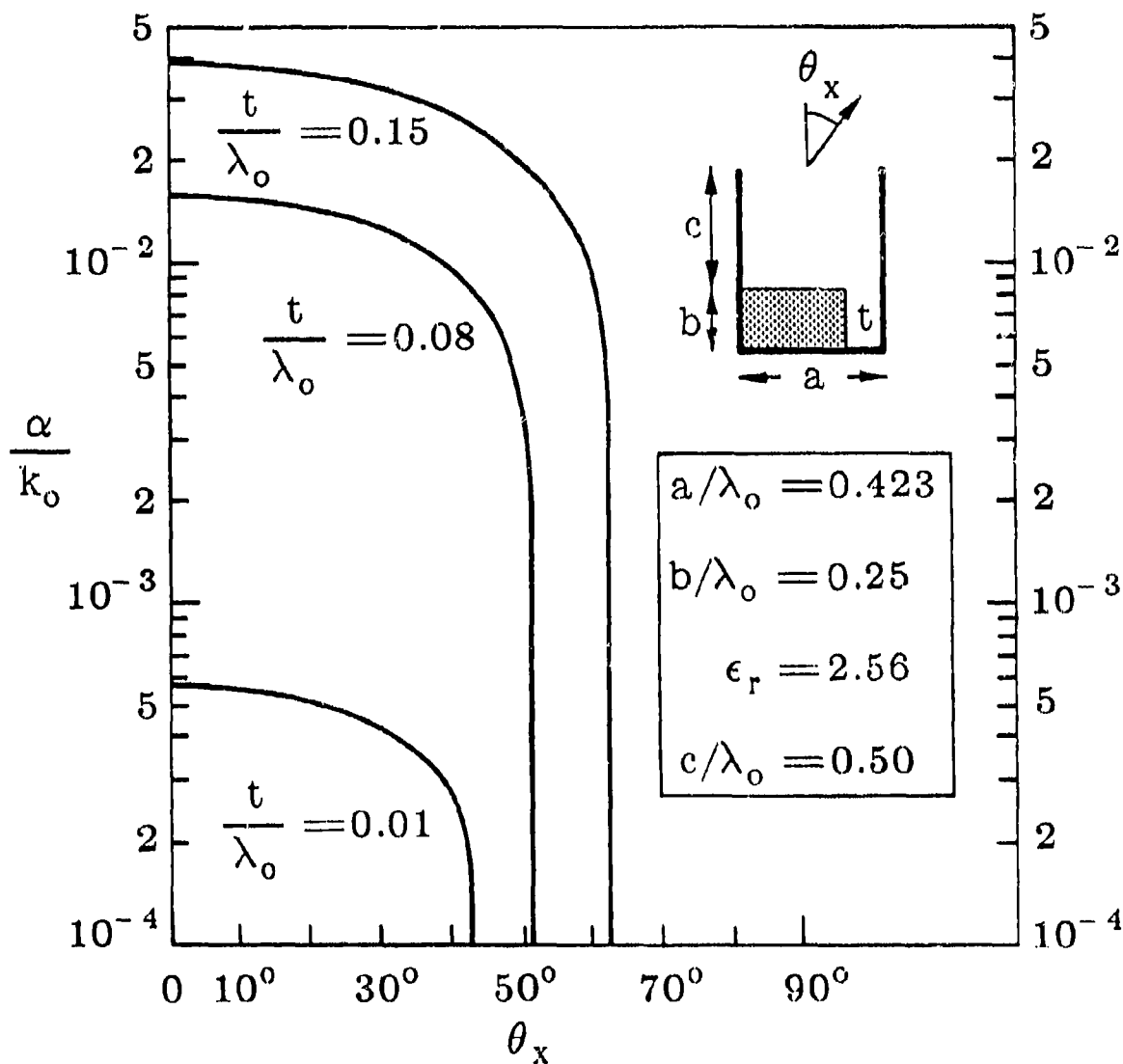


Fig. 4.24

Variation of normalized leakage constant α/k_0 with cross-plane scan angle θ_x when $c/\lambda_0 = 0.50$, for three values of t/λ_0 : 0.01, 0.08 and 0.15. The curves go to $\alpha/k_0 = 0$ at the end of the scan range.

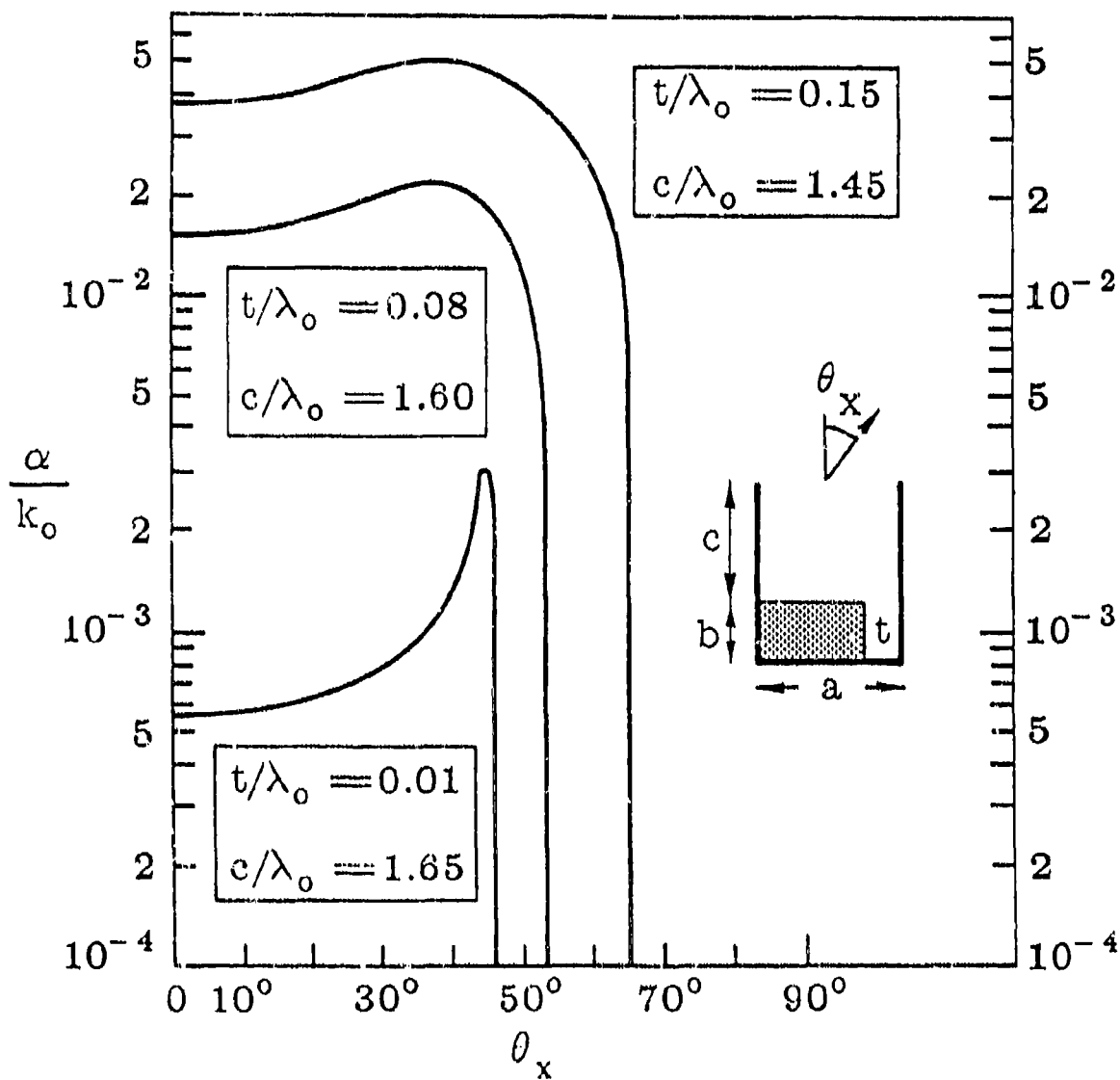


Fig. 4.25

Same as Fig. 4.24, but for larger values of c/λ_0 , namely, 1.65, 1.60 and 1.45 for $t/\lambda_0 = 0.01$, 0.08 and 0.15, respectively.

transverse equivalent network in Fig. 4.2. The normalized active input admittance to the periodic waveguide (which means to outside space) is Y_{op}/Y_{og} , which is related to the wavenumbers by (4.13). Equation (4.13) may be rephrased slightly as

$$\frac{Y_{op}}{Y_{og}} = \frac{k_{yog}}{k_{yop}} = \left[1 + \left(\frac{k_{xop}}{k_{yop}} \right)^2 \right]^{1/2} \quad (4.19)$$

on use of (4.6).

If a blind spot is present at some scan angle θ_x , or equivalently at some phase-shift wavenumber value k_{xop} , where $k_{xop} a$ is the phase shift per unit cell, then the radiated power must go to zero. That condition would be equivalent to having the array active admittance Y_{op} becoming zero or infinite. From (4.19) we see that it cannot become zero, but it could become infinite if wavenumber k_{yop} went to zero at some value of θ_x .

Wavenumber k_{yop} is actually complex, even though its imaginary part is very small. We shall first present accurate computations for both the real and imaginary parts of k_{yop} as a function of θ_x , and then interpret their physical meanings and interrelations with other wavenumbers by taking the approximation that the imaginary part is small. Curves of $\text{Re}(k_{yop}/k_o)$ vs. θ_x are shown in Fig. 4.26 for two different values of t/λ_o ; corresponding curves for $\text{Im}(k_{yop}/k_o)$ appear in Fig. 4.27. If k_{yop} were not complex, then the curves in Fig. 4.26 would be identically zero after the beam scan were completed (i.e., $\theta = 90^\circ$); also the curves in Fig. 4.27 would be identically zero during the scan range, but imaginary for θ_x greater than that value, since the periodic waveguide would then be below cutoff and the field there would be decaying in exponential fashion. Inspection of Figs. 4.26 and 4.27 shows that the behavior obtained is not too different from that described above, indicating that during the radiation process the imaginary part of k_{yop} is really quite small.

The important conclusion that one readily draws is that the curves of $\text{Re}(k_{yop}/k_o)$ behave very smoothly as θ_x is varied, and that they do not approach zero except at the end of the conical scan range. We therefore verify that *blind spots do not occur*.

When we assume that k_{yop} is essentially real during the radiation process and that its imaginary part is then very small, and we also write that $\alpha \ll \beta$ in k_z , then (4.4) reduces to

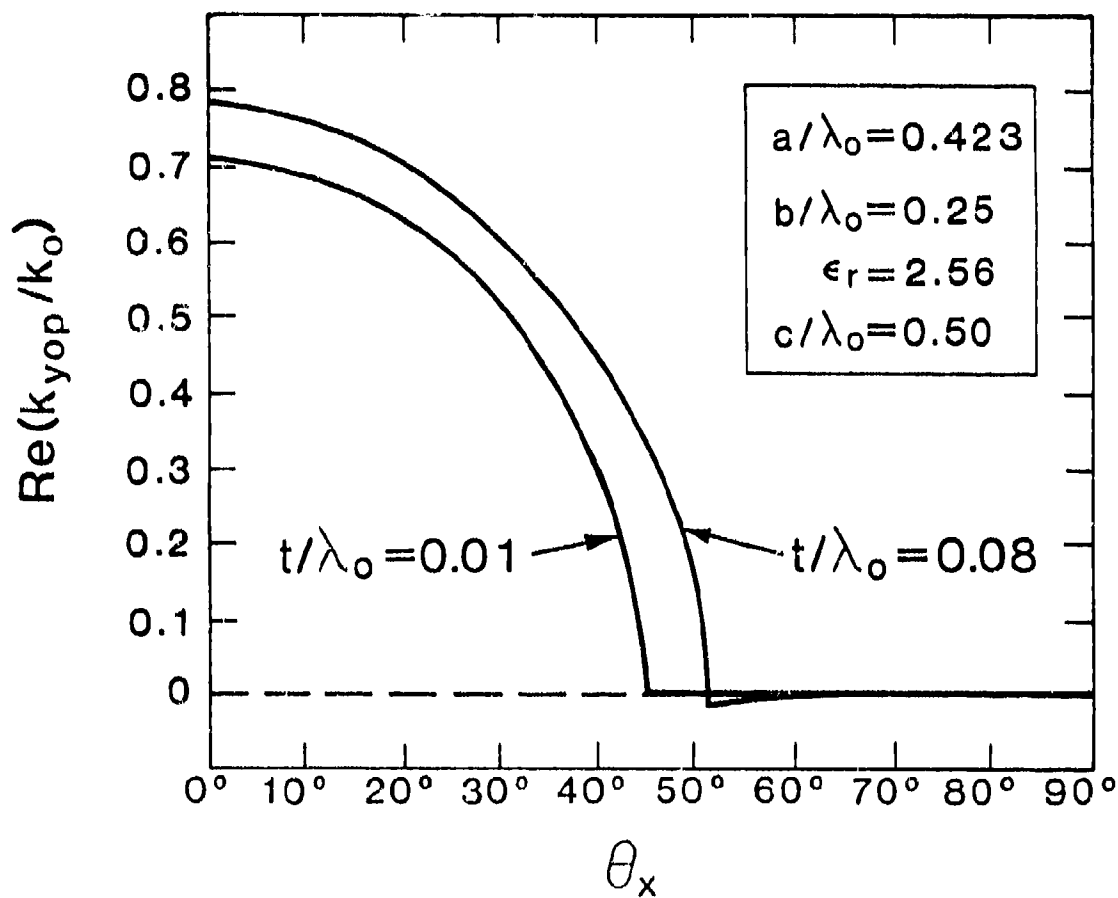


Fig. 4.26

Variation of $\text{Re}(k_{yop})$, the real part of the vertical propagation wavenumber of the lowest mode in the periodic unit cell, with cross-plane scan angle θ_x .

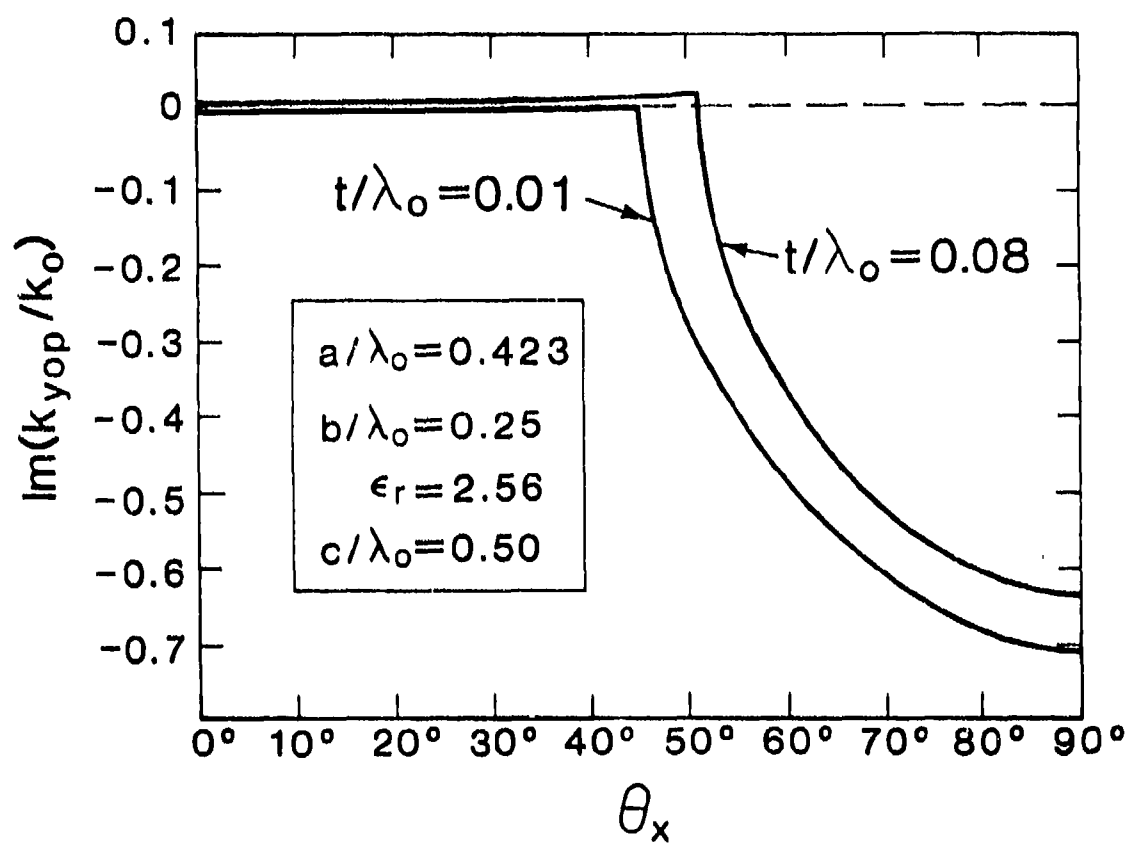


Fig. 4.27 Same as Fig. 4.26, except that the ordinate scale represents the imaginary part, $\text{Im}(k_{yop})$.

$$\operatorname{Re} \left(\frac{k_{yop}}{k_o} \right)^2 \approx 1 - \left(\frac{\beta}{k_o} \right)^2 - \left(\frac{k_{xop}}{k_o} \right)^2 \quad (4.20)$$

which offers us a simple approximate way to calculate values of $\operatorname{Re} (k_{yop}/k_o)$. Numerical values obtained in this fashion are found to agree quite well with the ones in Fig. 4.26.

We may also pursue this process to derive a simple approximate expression for $\operatorname{Im} (k_{yop}/k_o)$. By retaining the quantities in (4.1) as complex and then taking the imaginary parts of both sides, we obtain

$$\operatorname{Re} (k_{yog}/k_o) \operatorname{Im} (k_{yog}/k_o) = (\alpha/k_o) (\beta/k_o) \quad (4.21)$$

But, by taking the real parts of (4.1) and then setting

$$\alpha^2 \ll \beta^2 \quad \text{and} \quad \operatorname{Im}^2 (k_{yog}) \ll \operatorname{Re}^2 (k_{yog}),$$

we find

$$\operatorname{Re}^2 (k_{yog}/k_o) \approx 1 - (\beta/k_o)^2 \quad (4.22)$$

When (4.22) is employed in (4.21), the following approximate expression results

$$\operatorname{Im} \left(\frac{k_{yog}}{k_o} \right) \approx \frac{(\alpha/k_o) (\beta/k_o)}{\left[1 - (\beta/k_o)^2 \right]^{1/2}} \quad (4.23)$$

Treating (4.6) in the same fashion produces

$$\operatorname{Re} (k_{yop}/k_o) \operatorname{Im} (k_{yop}/k_o) = \operatorname{Re} (k_{yog}/k_o) \operatorname{Im} (k_{yog}/k_o) \quad (4.24)$$

when we equate the imaginary parts. When (4.20), (4.22) and (4.23) are employed in (4.24), we obtain finally

$$\text{Im} \left(\frac{k_{yop}}{k_o} \right) \approx \frac{(\alpha/k_o) (\beta/k_o)}{\left[1 - (\beta/k_o)^2 - (k_{xop}/k_o)^2 \right]^{1/2}} \quad (4.25)$$

Relation (4.25) can be utilized to compute in a simple way approximate values of $\text{Im} (k_{yop}/k_o)$, but it can also explain or predict the shape of the curve of $\text{Im} (k_{yop}/k_o)$ vs. θ_x . In Fig. 4.27 we note that the curve for $t/\lambda_o = 0.08$ is essentially flat with θ_x in the radiation region (the values in the curve for $t/\lambda_o = 0.01$ are too small). But this curve corresponds to $c/\lambda_o = 0.50$, and so do the curves in Figs. 4.26 and 4.24, for $\text{Re} (k_{yop}/k_o)$ and α/k_o vs. θ_x , respectively. From (4.20) we see that the denominator in (4.25) is equal to $\text{Re} (k_{yop}/k_o)$, and from Fig. 4.22 we determine that β/k_o remains almost constant with θ_x when $c/\lambda_o = 0.50$. The variation of the numerator in (4.25) with θ_x is thus described essentially in Fig. 4.24, and that of the denominator by Fig. 4.26. We observe that these variations are rather similar, with the curve for the denominator dropping a bit faster than the one for the numerator. We would thus predict that the shape of the curve in Fig. 4.27 would be rather flat with θ_x over most of the range but increasing slightly near the end of the scan range. Such behavior is precisely that found in Fig. 4.27.

If the value taken for c/λ_o were such that the curve for α/k_o vs. θ_x exhibited an increase during the scan range, as in Fig. 4.25, we would expect that the curve of $\text{Im} (k_{yop}/k_o)$ vs. θ_x would rise significantly rather than remain essentially flat. The curve shape can therefore vary somewhat, but it can in any case be determined to a decent approximation by the simple expression (4.25).

-139- 114/0

GROOVE GUIDE ANTENNAS

V.	A NEW EQUIVALENT NETWORK FOR THE CONSTITUENT E-PLANE TEE JUNCTION	143
A.	THE NEW EQUIVALENT NETWORK	144
B.	COMPARISONS WITH MEASUREMENTS	150
	1. Comparisons for a Slit-Coupled E-Plane Tee Junction	150
	2. Comparisons for a Slit That Couples Two Parallel Guides in E-Plane Fashion	154

V. A NEW EQUIVALENT NETWORK FOR THE CONSTITUENT E-PLANE TEE JUNCTION

(With: Prof. P. Lampariello, University of Rome "La Sapienza," Italy)

The analyses for the antennas discussed in Chapters VI, VII, VIII and X are all based on viewing the cross sections of these antennas in terms of an E-plane tee junction. The E-plane tee junction is thus a *key constituent* of the transverse equivalent networks for each of these antennas. Furthermore, since the parameters of the tee junction equivalent network turn out to be attainable in simple closed form, the corresponding dispersion relation for the phase constant β/k_0 and the leakage constant α/k_0 of each of the antennas is also in closed form. The numerical procedures for obtaining the complex $k_z (= \beta - j\alpha)$ values thus also become simpler.

Since we must take a resonance of the transverse equivalent network in order to obtain the dispersion relation for the longitudinal leaky mode on the antenna structure, we wish to have *analytical expressions* for the elements of the tee junction equivalent network. The problem is further complicated because the result we seek, namely k_z , is *complex*. We therefore must analytically continue into the complex plane the expressions as they occur in the dispersion relation.

As discussed below, the analytical expressions available in the Waveguide Handbook are valid only in the static limit, and were found to yield numerical values which were substantially in error in the frequency range applicable here. It was therefore necessary to develop a new equivalent network, with accurate expressions for the parameters of the network. This new network was adapted from the contents of an old Polytechnic report whose results were never published; the details are described below. In order to verify the accuracy of this new network, comparisons were made with available experimental results.

In the two sections that follow in this chapter, we present first the details of the new equivalent network and then the comparisons with measurements.

A. THE NEW EQUIVALENT NETWORK

The structure for which we require an accurate equivalent network is that shown in Fig. 5.1. It is an E-plane tee junction in a parallel-plate guide arrangement in which the propagation of the basic mode occurs in the x direction, and in which there exists a phase variation in the z direction, i.e., k_z is finite. (In our later applications of this structure, as a constituent of several different antenna cross sections, the network we seek becomes a portion of the transverse equivalent network for the antenna. In that context, terminations will be placed on the guides in the x or y direction, and propagation will occur in the z direction.)

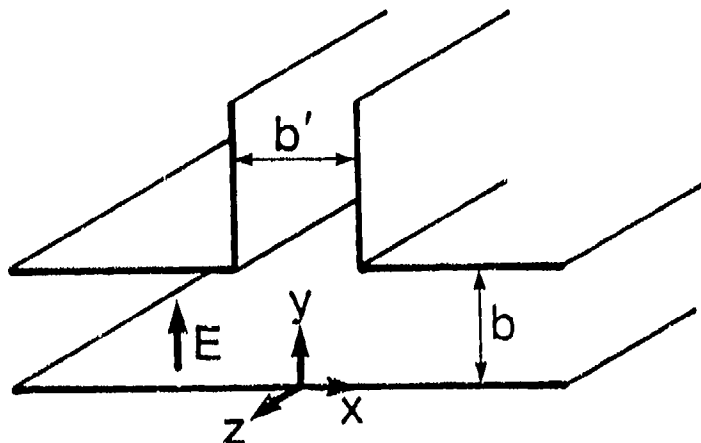


Fig. 5.1 E-plane tee junction in parallel-plate guide.

Since k_z is finite in the structure of Fig. 5.1, we may place side walls in the z direction so that the structure becomes an E-plane tee junction in *rectangular waveguide*, with $k_z = \pi/a$, where a is the guide width. We then tried to find available solutions in the literature for an accurate equivalent network for that structure.

The only solution we found is in the Waveguide Handbook [8], Sec. 6.1 on pp. 337-350. Many numerical curves are presented there for the various elements of the

network, with frequency as a parameter in the curves for each figure. Those numerical curves are deemed to be accurate. Unfortunately, however, the analytical expressions presented in that section are valid only in the static limit, $b/\lambda_g = 0$. Numerical values for some of the network elements computed from those expressions were found to be in substantial disagreement with the values on the curves in our frequency range of interest.

For example, for a typical case, for $2b/\lambda_g = 0.6$ and $b'/b = 1$, where b and b' are the main guide and stub guide widths, the curves on p. 341 show that B_b/Y_o , the most important network element, is 1.36, instead of 0.86 as one obtains from the analytical formulas, which are valid in the static limit only. For a narrower stub guide, say, $b'/b = 0.67$, the comparison is $B_b/Y_o = 0.84$ vs. 0.66, which is not as bad. For relatively narrow stub guides, therefore, the Waveguide Handbook expressions should yield results that are reasonably acceptable. On the other hand, the geometric aspect ratio is less interesting in that range, and we would be restricted to an undesirable extent.

It was therefore necessary to seek a new equivalent network. We were able to develop such a new network from results derived much earlier for a more complicated structure, and contained in a Polytechnic Institute of Brooklyn report [17], the contents of which were never published. This report, a comprehensive one on equivalent networks for slots in rectangular waveguide, contained the output of a group comprised of J. Blass, L.B. Felsen, H. Kurss, N. Marcuvitz and A.A. Oliner. The goals of that program and the approaches employed were furnished by N. Marcuvitz. The earlier work relevant to our current needs applied to an E-plane tee structure in rectangular waveguide in which a slot of finite dimensions in two directions was present at the stub junction plane. Expressions for the parameters of the equivalent network for that structure were derived by J. Blass and N. Marcuvitz, and are given on pp. 112-125 of that report [17]. By comparison with careful measurements, those expressions were found to be accurate for most of the range of slot dimensions when the ordinary (actually X band) rectangular waveguide aspect ratio was used.

For our case, the "slot" is wide open. However, the various guide dimensional ratios can be quite different in our applications; the ratio of stub guide to main guide widths can vary, and the rectangular guide "a" dimension is replaced by $2\pi/k_z$ of the leaky-wave antenna. Our final new equivalent network, only slightly modified from the one in [17], is presented in Fig. 5.3; Fig. 5.2 indicates the reference plane locations at which the network is valid.

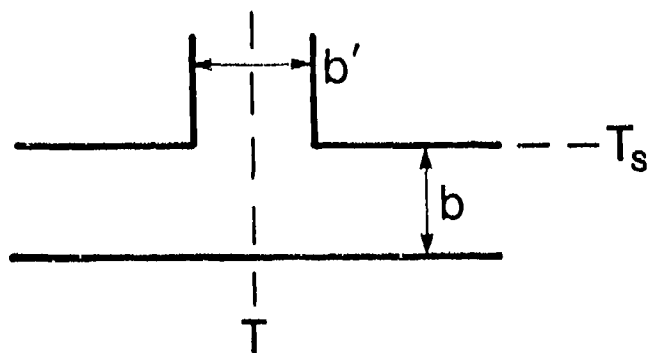


Fig. 5.2 Cross section of E-plane tee junction, showing the reference planes at which the equivalent network in Fig. 5.3 is valid.

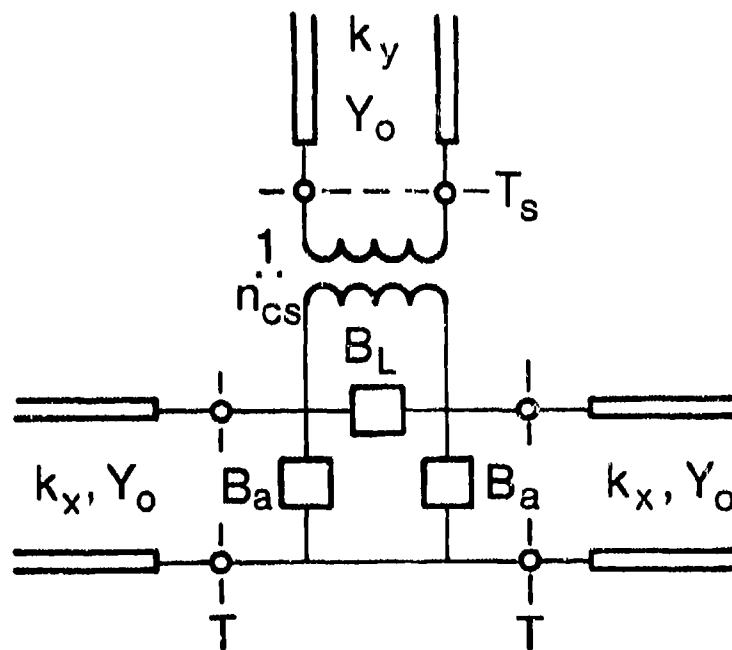


Fig. 5.3 New equivalent network for the E-plane tee junction shown in Fig. 5.1.

A symmetrical tee network requires four independent parameters for its rigorous characterization, but only three appear in Fig. 5.3. If one employs the transformer format shown, an additional series element should be present just above the transformer; however, we have found that the reactance of that series element is essentially zero, and that the element can be neglected. For our case, the expressions for the remaining three elements, B_L , B_a and n_{cs} , turn out to be in relatively simple closed form. The reduction from the original complicated slot solution to our wide-open slot case was unfortunately not quite straightforward, a situation that was complicated by the fact that several hitherto-unknown typographical mistakes were present in those original formulas.

An additional point of substantial importance is the following. An electric-wall, or short-circuit, bisection of the network, corresponding to a symmetric magnetic field excitation of the two main guides of the tee, reduces the three-port network to a two-port network, and involves the element combination $(2B_L + B_a)$. The theoretical derivation for this case yields this element combination, rather than B_L alone. (Element B_a is obtained independently from a magnetic-wall, or open-circuit, bisection, corresponding to a symmetric electric field excitation of the two main guides. Element n_{cs} is derived by taking the ratio of modal voltages in the stub and main guides.) The expression for $(2B_L + B_a)$ takes into account the stored power residing in the main guide region just under the stub junction. The original expression for the slot-coupled case was in the form of B_L , the susceptance of a transverse aperture coupling two waveguides, plus a correction term. The correction term accounts essentially for the presence of the bottom wall opposite the tee stub junction, and the absence of the side walls in the main guide region that would be present for an aperture in the junction plane. In the slot-coupled tees analyzed years ago, the correction term was usually small relative to the other terms. When the slot becomes wide open, as in our case, the "correction" term is all that remains. Because of this fact, we were concerned about the accuracy of the result, and we therefore made the comparisons with available measurements that are discussed in the next section.

We next present the final expressions for the elements of the equivalent network in Fig. 5.3, employing the notation in Fig. 5.1 for the guide dimensions. In our later applications of this network to various antennas, we shall modify the notation appropriately. The expressions are:

$$\frac{B_L}{Y_o} + \frac{1}{2} \frac{B_a}{Y_o} = \frac{1}{n_c^2} \left(\frac{2b}{\lambda_g} \right) \left[\ln \left(1.43 \frac{b}{b'} \right) + \frac{1}{2} \left(\frac{2b}{\lambda_g} \right)^2 \right] \quad (5.1)$$

where

$$n_c = \frac{\sin(\pi b' / \lambda_g)}{\pi b' / \lambda_g} \quad (5.2)$$

$$\frac{B_a}{Y_o} = - \frac{\pi^2}{16} \frac{b}{\lambda_g} \left(\frac{b'}{b} \right)^2 J_o^2 \left(\frac{\pi b'}{\lambda_g} \right) \quad (5.3)$$

where J_o is the Bessel function of zero order, and

$$n_{cs}^2 = n_c^2 (b' / b) \quad (5.4)$$

Element B_L can be expressed separately as

$$\begin{aligned} \frac{B_L}{Y_o} = & \frac{1}{n_c^2} \left(\frac{2b}{\lambda_g} \right) \left[\ln \left(1.43 \frac{b}{b'} \right) + \frac{1}{2} \left(\frac{2b}{\lambda_g} \right)^2 \right] \\ & + \frac{\pi^2}{32} \frac{b}{\lambda_g} \left(\frac{b'}{b} \right)^2 J_o^2 \left(\frac{\pi b'}{\lambda_g} \right) \end{aligned} \quad (5.5)$$

As indicated earlier, the network in Fig. 5.3, to which these expressions apply, is used in later chapters (VI, VII, VIII and X) as a constituent of the transverse equivalent networks of antennas. There, the structure of Fig. 5.1 forms a portion of the antenna cross section, and a guided wave propagates in the z direction with complex wavenumber k_z . Guide wavelength λ_g is then replaced by $2\pi/k_z$, and k_x is related to k_z by $k_z = \beta - j\alpha = (k_o^2 - k_x^2)^{1/2}$.

As seen, these expressions are in closed form and are rather simple. In order to satisfy our concerns about their accuracy, we present in the next section some comparisons with measured results. It should also be added that two other comparisons have been made in connection with an antenna for which this tee network is a constituent of the transverse equivalent network. The antenna is the offset-groove-guide antenna; in Chap. VII, comparison is made with numerical values obtained via another, totally different, theoretical approach, and in Chap. VIII comparison is made with measurements. In both cases, as is shown, the agreement is excellent.

B. COMPARISONS WITH MEASUREMENTS

1. Comparisons for a Slit-Coupled E-Plane Tee Junction

The first comparison will be made with measurements taken on a closely related structure, that of a slit-coupled E-plane tee in rectangular waveguide. The cross section of that structure is shown in Fig. 5.4. Measurements were taken for three different values of slit width b' .

To make possible such a comparison, we need first to modify the expressions for the elements in Fig. 5.3, to take into account the additional stored power present in the stub guide, due to the slit of width b' and residing just above the slit.

When the main guide of the tee structure in Fig. 5.4 is excited in symmetric magnetic field fashion, producing a short circuit at plane T, the relation between the susceptance and the stored powers may be written in variational form

$$j \frac{B_{sh}}{Y_o} = \frac{(S.P.)_{main} + (S.P.)_{stub}}{Y_o |V_{sh}|^2} \quad (5.6)$$

where the subscript sh in B_{sh} signifies "symmetric magnetic field," V_{sh} is the modal voltage across the slit due to this excitation, and $(S.P.)_{main}$ and $(S.P.)_{stub}$ are the stored powers (corresponding to the sum of the higher modes excited) in the main guide and the stub guide, respectively. For the structure in Fig. 5.1, it was assumed that all of the stored power exists only in the main guide, since the field in the stub guide junction plane is very similar to that in the dominant mode of the stub guide. Such an assumption is a good one in a variational expression such as the one in (5.6), which was employed in the derivation of expression (5.1). We may therefore write

$$j \left[\frac{B_L}{Y_o} + \frac{1}{2} \frac{B_a}{Y_o} \right] = \frac{(S.P.)_{main}}{Y_o |V_{sh}|^2} \quad (5.7)$$

To determine the manner in which we can account for $(S.P.)_{stub}$, let V_o be the modal voltage of the dominant mode in the stub guide. Then, the normalized susceptance B_t/Y_o of a transverse slit of width b' in the stub guide, shown in Fig. 5.5, may be written as

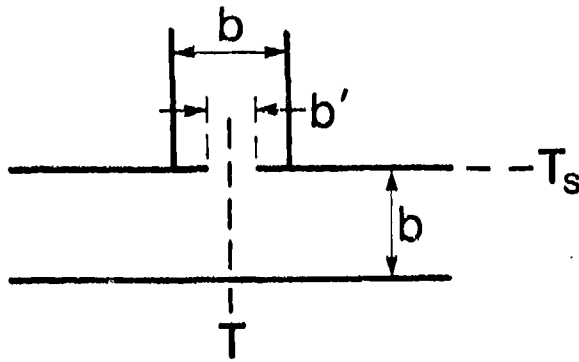


Fig. 5.4 Cross section of slit-coupled E-plane tee.

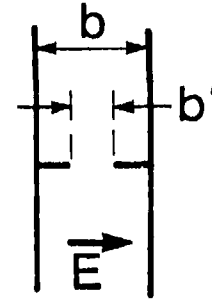


Fig. 5.5 Cross section of transverse slit, placed vertically.

$$\frac{B_t}{Y_o} = \frac{(S.P.)_t}{Y_o |V_o|^2} \quad (5.8)$$

By inspection, we observe from Figs. 5.4 and 5.5 that the $(S.P.)_{stub}$ in (5.6) is equal to one-half of the $(S.P.)_t$ in (5.8), assuming that the fields in each slit are the same, which is a good approximation. We may therefore obtain

$$\frac{(S.P.)_{stub}}{Y_o |V_{sh}|^2} = \frac{1}{2} \frac{(S.P.)_t}{Y_o |V_{sh}|^2} = \frac{1}{2} \frac{B_t}{Y_o} \frac{|V_o|^2}{|V_{sh}|^2} \quad (5.9)$$

Since

$$n_c = \frac{|V_{sh}|}{|V_o|} \quad (5.10)$$

we have finally that

$$\frac{(S.P.)_{stub}}{Y_o |V_{sh}|^2} = \frac{1}{2} \frac{1}{n_c^2} \frac{B_t}{Y_o} \quad (5.11)$$

When (5.7) and (5.11) are employed in (5.6), we obtain

$$\frac{B_{sh}}{Y_o} = \frac{B_L}{Y_o} + \frac{1}{2} \frac{B_a}{Y_o} + \frac{1}{2} \frac{1}{n_c^2} \frac{B_t}{Y_o} \quad (5.12)$$

Expression (5.12) was obtained from the excitation of the two main guides in symmetric magnetic field fashion. From the corresponding excitation in symmetric *electric* field fashion, resulting in an open-circuit bisection of the structure in Fig. 5.4, we find that the normalized input admittance to the tee junction as seen from the main guide is simply jB_a/Y_o , as it was for the structure in Fig. 5.1 and the network in Fig. 5.3. The higher modes excited by the slit for this excitation remain close to the region of the slit in Fig. 5.4, and are only weakly influenced by the side walls. In fact, expression (5.3) for B_a/Y_o was derived by taking the half-space Green's function on both sides of the slit. It can also be shown that (5.3) is equal to a small aperture result for this case, multiplied by the J_o term to account for larger slit sizes. In any case, it has been assumed that the stored power contribution to B_a/Y_o is the same on both sides of the slit, even when the slit is wide open, for which situation the approximation is less valid. Nevertheless, the approximation seems to yield reasonably accurate results. We thus conclude from this approach that the B_a/Y_o elements for the structures of Figs. 5.1 and 5.4 are the same.

When we put all these pieces together, we deduce that the equivalent network for the slit-coupled tee structure in Fig. 5.4 is that presented in Fig. 5.6. The turns ratio here is n_c , rather than n_{cs} , because the stub guide and main guide widths are equal in Fig. 5.4.

The expressions for the elements in the network in Fig. 5.6 are:

$$\frac{B_a}{Y_o} \text{ is given by (5.3)}$$

$$\frac{B_L}{Y_o} \text{ is given by (5.5)}$$

$$n_c \text{ is given by (5.2)}$$

$$\frac{B_t}{Y_o} = \frac{4b}{\lambda_g} \ln \csc \frac{\pi b'}{2b} \quad (5.13)$$

Expression (5.13) comes from the Waveguide Handbook [8], Sec. 5.1, and is the first term in expression (2a) on p. 218. Higher accuracy is obtainable by also employing the remaining terms in expression (2a) on p. 218, but the improvement is very slight for most cases and not worth the added complexity.

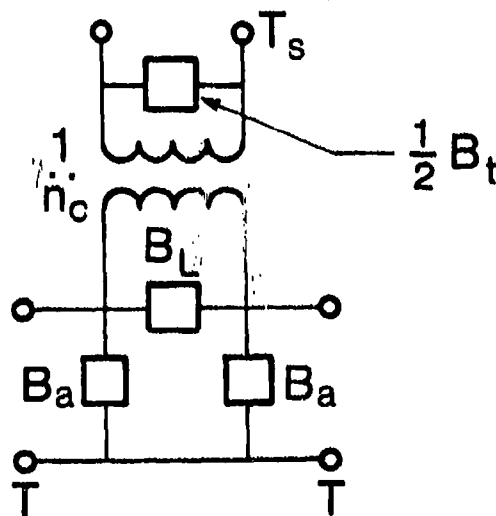


Fig. 5.6 Equivalent network for the slit-coupled E-plane tee shown in Fig. 5.4.

If the stub guide width were different from that of the main guide, and was equal to w , say, then n_c would be replaced by n_{cs} , where

$$n_{cs}^2 = n_c^2 \frac{w}{b} \quad (5.14)$$

and b in (5.13) would be replaced by w .

We are now in a position to compare our theoretical results with measured results on the slit-coupled tee junction of Fig. 5.4. The comparisons will be made for the

quantities B_{sh}/Y_o (see (5.12)) and B_a/Y_o , for three different values of b'/b . The measured values are taken from curves on pp. 173 and 175 of [17]. The comparisons are summarized in Table 5.1.

Table 5.1

Comparisons between theoretical and measured values
for the slit-coupled E-plane tee junction in Fig. 5.4

Quantity	$\frac{b'}{b}$	Measured	Computed
B_{sh}/Y_o	0.315	1.11	1.09
	0.64	0.54	0.52
	1.00	0.28	0.25
B_a/Y_o	0.30	-0.012	-0.012
	0.60	-0.045	-0.046
	1.00	-0.095	-0.109

It is seen that in general the agreement is very good. The worst case is that for B_a/Y_o for $b'/b = 1.00$, where the computed value is about 15% higher than the measured value. From the discussion above relating to symmetric electric field excitation, we would expect that the results for B_a/Y_o would be best for small values of b'/b , and worst when the slit is wide open. If we wanted to improve expression (5.3) by empirically multiplying it by 0.85, we could do so, but we are not sure that this factor still holds for narrower stub guides, and, in any case, the influence of B_a/Y_o on overall performance is generally secondary. We have therefore used expression (5.3) as is.

2. Comparisons for a Slit That Couples Two Parallel Guides in E-Plane Fashion

The cross section of the structure for which these next comparisons are made is shown in Fig. 5.7. By comparing the structure in Fig. 5.7 with those in Figs. 5.2 and 5.4, we observe that the bottom portions of all three are the same. Thus, on the assumption that the fields in the slit plane are about the same in each structure if the

excitations are similar, we can use the stored power approach discussed above to relate the elements in the equivalent network of one structure with those of the others. In particular, we can use expression (5.1) and (5.3) to obtain the equivalent network parameters that characterize the bottom half of the structure in Fig. 5.7.

Expressions for the network parameters for the structure in Fig. 5.7 are also given in the Waveguide Handbook [8], Sec. 7.1, pp. 373-375. These analytical expressions are very different in form from those in (5.1) and (5.3), however, and in fact B_a/Y_o is defined somewhat differently, so we must be careful in our comparisons. In addition, on p. 375 two *measured* values are presented against which we can compare our theoretical results. We have also found some misprint errors in the Waveguide Handbook and we will point them out as we proceed below.

We first detach the bottom portion of the structure in Fig. 5.7 by taking an open-circuit bisection horizontally, through the slit plane. The resulting structure and its equivalent network representation are given in Fig. 5.8; the original four-port network is thus reduced to a two-port network. When we perform a similar bisection of the four-port equivalent network in Fig. 7.1-1 on p. 374 of the Waveguide Handbook, we obtain a network form similar to that in Fig. 5.8, but B_a there is defined as the negative of our B_a , and their B_b is equal to twice our B_L . (An error appears in their Fig. 7.1-1 for B_b ; it is shown as an inductance but it is in fact a capacitance.)

An additional important difference is present in connection with B_a . For the tee junction, result (5.3) for B_a/Y_o includes the stored power (corresponding to an open-circuit bisection at reference plane T) in both the main guide *and* the stub guide, and assumes that they are equal, as mentioned above. For the network in Fig. 5.8, B_a/Y_o includes the stored power in the *lower portion only*, since there would be a separate B_a term in the equivalent network for the upper portion of the structure in Fig. 5.7. (This comment also applies to the B_a in the network in Fig. 7.1-1 in the Waveguide Handbook.) Thus, these two values of B_a/Y_o should differ by a factor of two.

From numerical comparisons, we find that the B_a/Y_o value for the tee junction network, for which twice the stored power is taken into account, is actually half of the B_a/Y_o value for the bisected four-port network. The reason for that is that the symmetric electric field excitation of the slit, that sets up an open circuit vertically at

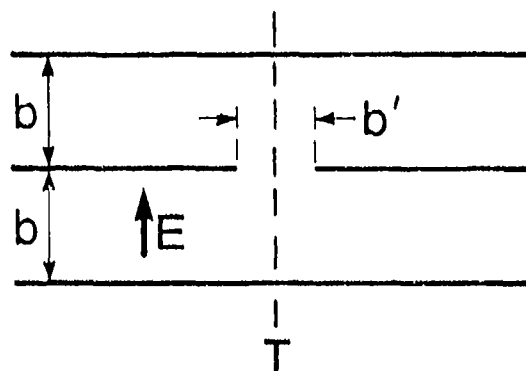


Fig. 5.7 Cross section of slit that couples two parallel guides, one above the other, in E-plane fashion.

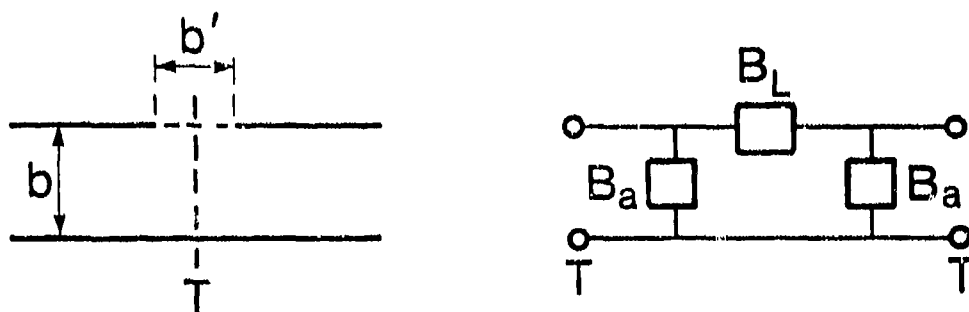


Fig. 5.8 Two-port structure and equivalent network that results when the four-port structure in Fig. 5.7 is bisected with a horizontal open circuit.

the mid-plane T, and that yields the expression for B_a/Y_o , actually relates X_a/Z_o to the stored powers. Thus, the contributions from the upper and lower portions of the tee junction are in series, in contrast to those for the symmetric magnetic field excitation, which are in parallel. We may therefore write

$$\left[\frac{B_a}{Y_o} \right]_{\substack{\text{bisected} \\ \text{4-port}}} = \left[\frac{B_a}{Y_o} \right]_{\text{WGH}} = 2 \left[\frac{B_a}{Y_o} \right]_{\substack{\text{tee} \\ \text{junction}}} \quad (5.15)$$

where WGH refers to the Waveguide Handbook notation.

We consider next the results of symmetric *magnetic* field excitation, which produces a short-circuit bisection at mid-plane T in the structures in Figs. 5.2 and 5.8. We wish to establish a relation between the relevant elements of the networks for these two structures. Since we have assumed earlier that no stored power is present in the stub guide in Fig. 5.2, we conclude that the stored power in the lower portion of the structure in Fig. 5.2 (and therefore in the whole structure) must be the same as that in the structure in Fig. 5.8, if the aperture fields are the same in each. We may therefore state that

$$\left[\frac{B_{sh}}{Y_o} \right]_{\substack{\text{tee} \\ \text{junction}}} = \left[\frac{B_L}{Y_o} + \frac{B_a}{2Y_o} \right]_{\substack{\text{bisected} \\ \text{4-port}}} = \left[\frac{1}{2} \left(\frac{B_b}{Y_o} + \frac{B_a}{Y_o} \right) \right]_{\text{WGH}} \quad (5.16)$$

where the "tee junction" and "bisected 4-port" refer to the networks in Figs. 5.3 and 5.8, and where WGH means the lower half of the Waveguide Handbook network, using their terminology. Since the various B_a/Y_o values are different, however, as seen from (5.15), the definitions for B_L are also different, but may be obtained via (5.15) and (5.16), if desired.

We now have all the background needed to make the comparisons mentioned earlier. First, we make use of the measurements quoted on p. 375 of the Waveguide Handbook [8]. Before presenting the comparisons, however, we should point out a misprint present in connection with these measurements, which were taken in X band rectangular waveguide at a wavelength $\lambda_o = 3.20$ cm. The slit width b' (called d there) is equal to 0.40 inch, so that $b'/b = 1.00$, but the misprint reads 0.04 inch.

Table 5.2

Comparisons between theoretical and measured values for the bisected four-port structure in Fig. 5.8

	Measured	Our Theory	WGH Theory
$2B_{sh}/Y_o$	0.58	0.50	0.36
B_a/Y_o	0.23	0.22	0.24

Table 5.3

A test of the validity of a modified Waveguide Handbook expression

	WGH Theory	Modified WGH Theory	Our Theory
b'/b	$\frac{B_b}{Y_o} - \frac{B_a}{Y_o}$	$\frac{B_b}{Y_o} - \frac{1}{2} \frac{B_a}{Y_o}$	$2 \frac{B_L}{Y_o} + \frac{B_a}{Y_o}$
1.00	0.36	0.48	0.50
0.64	0.78	0.83	0.88
0.32	1.39	1.41	1.47

The comparisons between the measurements, our theory, and the Waveguide Handbook theory are presented in Table 5.2. The definition for B_a/Y_o taken in the table is the one given in the Waveguide Handbook. It is seen that for parameter B_a/Y_o both theories agree well with the measured value, but that our theory for B_{sh}/Y_o is much better than that supplied in the Waveguide Handbook.

The poorer agreement with measurement for B_{sh}/Y_o found in the Waveguide Handbook, and reported there as well, is somewhat puzzling, leading to the supposition that some term is defined incorrectly there or that some term may be omitted. The expression for B_{sh}/Y_o in the Waveguide Handbook is written there as $(1/2)(B_b - B_a)/Y_o$, as stated in (5.16). In recognition of the fact that B_a/Y_o there is twice what we have for B_a/Y_o , as stated in (5.15), let us add $(1/2)B_a/Y_o$ from the Waveguide Handbook value for B_{sh}/Y_o . For the case covered in Table 5.2, we then find

$$2 \left[\frac{B_{sh}}{Y_o} \right]_{new} = \left[\frac{B_b}{Y_o} - \frac{B_a}{Y_o} \right] + \frac{1}{2} \frac{B_a}{Y_o} = 0.36 + 0.12 = 0.48$$

which is very close to the value of 0.50 obtained from our theoretical expression.

To check whether or not this greatly improved agreement is simply a coincidence for $b'/b = 1.00$, we repeated this test for two other values of b'/b , namely, 0.64 and 0.32. The results are summarized in Table 5.3, where it is seen that the improvement becomes less significant as b'/b is reduced. On the other hand, the WGH and our theoretical values grow closer together. The results are not conclusive, but we include them for completeness.

The important conclusion to be drawn from this section should be apparent from the comparisons with measurements given in Tables 5.1 and 5.2. Although these good agreements with measurement apply only to certain specific cases, they offer strong encouragement with respect to the validity and accuracy of the theoretical expressions presented in Sec. A.

VI.	THE L-SHAPED LEAKY-WAVE LINE SOURCE	163
A.	DOMINANT MODE AND HIGHER MODE PROPERTIES OF GROOVE GUIDE: A SUMMARY	164
	1. The Dominant Mode	164
	2. The Higher Modes, Which Are All Leaky	164
B.	THE L-SHAPED ANTENNA	169
	1. Theoretical Description	169
	2. Numerical Results	177

VI. THE L-SHAPED LEAKY-WAVE LINE SOURCE

(With: Prof. P. Lampariello, University of Rome "La Sapienza," Italy)

The leaky-wave line source to be described is the result of a search for the simplest leaky-wave structure based on the groove guide that we could devise consistent with our ability to analyze its behavior. The leakage mechanism is based on the fact that all higher modes on groove guide are leaky, but it could also be viewed as due to asymmetry. In any case, the simple structure of the antenna is the result of two successive bisections of the groove guide.

The resulting leaky-wave structure, which we have called the L-shaped antenna, has the virtue of simplicity, but it suffers from some performance limitations. In particular, it leaks quite strongly, so that it is suitable only for applications that require wider beam widths. It is also not easy to taper its effective aperture so as to control the sidelobe performance. In an attempt to overcome these limitations, we modified this L-shaped structure to create the very successful offset-groove-guide antenna described in Chaps. VII and VIII.

In the present chapter we first summarize the properties of the basic groove guide, with respect to both the dominant and the higher modes, and then we discuss the L-shaped antenna, and present both its theoretical description in terms of the E-plane tee junction equivalent network, discussed in Chap. V, and some numerical results regarding its leakage properties.

A. DOMINANT MODE AND HIGHER MODE PROPERTIES OF GROOVE GUIDE: A SUMMARY

1. The Dominant Mode

Groove guide was invented by T. Nakahara in the early 1960's as a way to overcome the dielectric loss in H guide without significantly affecting the metal losses. The waveguide is shown in Fig. 6.1, and is seen to consist only of metal. Instead of the dielectric in H guide, or NRD guide, the center region of groove guide is made wider than the upper and lower outer regions. The fields in the vertical direction then have a trigonometric dependence in the grooved region, but are exponentially decaying (evanescent) in the narrower regions above and below. The fields are therefore confined to the central grooved region in a manner similar to those in the central dielectric region of H guide or NRD guide.

A sketch of the electric field lines in the cross section of groove guide, and an approximate plot of the vertical component of the electric field, consistent with the discussion above, are shown in Figs. 6.2 (a) and (b).

The dominant mode in groove guide is seen from Fig. 6.1 to be an even closer relative to the TE_{10} mode in rectangular waveguide than the NRD guide is. The groove guide indeed looks like rectangular waveguide without most of its top and bottom walls; since the fields are evanescent above and below the central grooved region, we may say that the top and bottom metal walls have been replaced by reactive walls. The electric field is also primarily vertical for the groove guide, as sketched in Fig. 6.2(a), but the mode is not hybrid in the longitudinal direction as it is in NRD guide.

An improved solution for the properties of the dominant mode in groove guide was derived on the predecessor contract, and it has since been published [18]. This improved solution is notable in that it is compact, simple, accurate, has all its elements in closed form, and yields better agreement with measurements than any previous solution. The paper also contains a history of previous work on the groove guide dominant mode.

2. The Higher Modes, Which Are All Leaky

The dominant mode of groove guide is purely bound (nonradiating), but it turns out that all the higher modes are leaky. Nakahara and Kurauchi [19] had shown toward the end of an article many years ago that the *odd* higher modes were leaky. We extended their result to show that all higher *even* modes are also leaky.

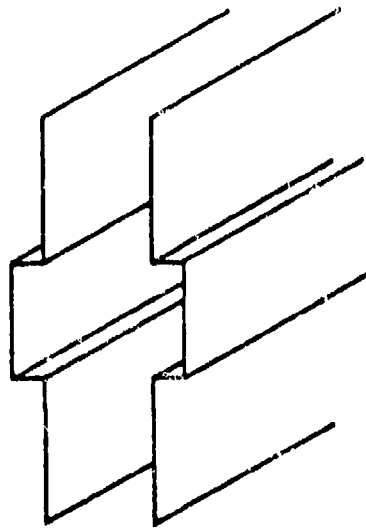


Fig. 6.1 The open groove guide, comprised of two parallel metal plates whose central regions are grooved outwards.

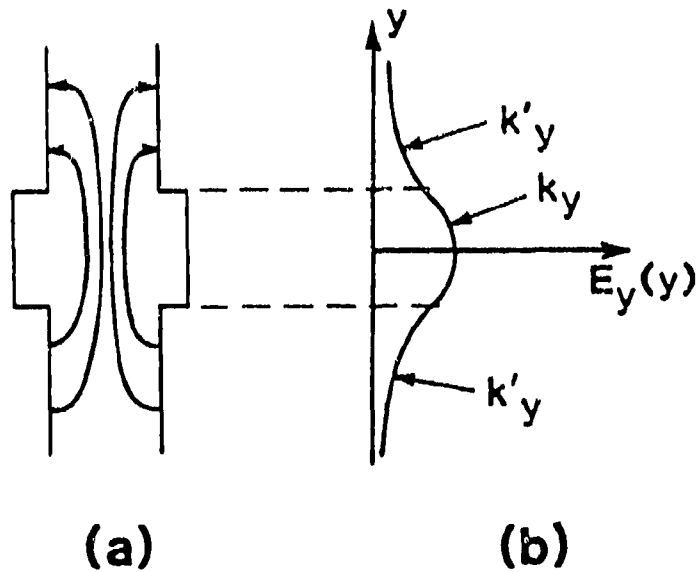


Fig. 6.2 The electric field of the dominant mode in open groove guide. (a) A sketch of the electric field lines in the cross section. (b) An approximate plot of the vertical component E_y as a function of vertical position y , showing that the guided mode is bound transversely to the central grooved region.

Since the latter result has not been published, we present its derivation now, together with a modified version of the original proof for odd higher modes given in [19]. The derivations also serve to illuminate some of the other properties of these higher modes.

We present first, following [19], the simple wavenumber considerations that indicate under what conditions the $n = 3$ mode (the first higher *odd* mode), is leaky.

When we excite the groove guide in the $n = 3$ mode, the field variation in the x direction, across the guide, possesses three half sine waves, so that $k_{x3} = 3\pi/a$ and $k'_{x3} = 3\pi/a'$. The primed and unprimed quantities refer to the regions of narrower width a' and greater width a , respectively. More precisely, we should say that the $i = 3$ *transverse* mode has these x variations. If the $n = 3$ longitudinal mode involved only the $i = 3$ transverse mode, then it would be purely bound, with k_{y3} real and k'_{y3} imaginary. Actually, if the groove guide cross section is excited in the $i = 3$ transverse mode, then, when this mode is incident vertically on the step junction between the sections of widths a and a' , an infinite number of odd transverse modes will be excited there, i.e., the $i = 1, 5, 7, 9 \dots$ modes.

Let us examine what happens to the $i = 1$ and $i = 3$ transverse mode constituents of the $n = 3$ longitudinal mode (the first higher odd mode) when that mode is above cutoff. We may write, for the $i = 3$ transverse mode,

$$k_o^2 = k_z^2 + \left(\frac{3\pi}{a}\right)^2 + k_{y3}^2 \quad (6.1)$$

$$k_o^2 = k_z^2 + \left(\frac{3\pi}{a'}\right)^2 + |k'_{y3}|^2 \quad (6.2)$$

since

$$k'_{y3} = -j |k'_{y3}| \quad (6.3)$$

and, for the $i = 1$ transverse mode,

$$k_o^2 = k_z^2 + \left(\frac{\pi}{a}\right)^2 + k_{y1}^2 = k_z^2 + \left(\frac{\pi}{a'}\right)^2 + (k'_{y1})^2 \quad (6.4)$$

but we do not yet know the nature of k_{y1} and k'_{y1} . However, from (6.1) and (6.4), we note that

$$k_{y1}^2 = k_{y3}^2 + \left(\frac{3\pi}{a}\right)^2 - \left(\frac{\pi}{a}\right)^2 = k_{y3}^2 + 2\left(\frac{2\pi}{a}\right)^2 \quad (6.5)$$

so that k_{y1} is real, and we also observe that

$$(k'_{y1})^2 = k_{y3}^2 + \left(\frac{3\pi}{a}\right)^2 - \left(\frac{\pi}{a'}\right)^2 \quad (6.6)$$

so that

$$(k'_{y1})^2 > k_{y3}^2 > 0 \quad (6.7)$$

if

$$\frac{a'}{a} > \frac{1}{3} \quad (6.8)$$

which is always true in any practical groove guide.

We therefore see that, if (6.8) is satisfied, both k_{y1} and k'_{y1} are real; the fact that k'_{y1} is real means that real power is carried away, and the *overall mode is leaky*. Furthermore, the power that leaks has the x dependence of the $i = 1$ mode, not the $i = 3$ mode.

The corresponding derivation for the first higher *even* mode, the $n = 2$ mode, is similar in approach to the one given above, but there are important differences which will become evident. Reference [19] did not consider the higher even modes.

In this derivation, we first note that the incident transverse mode is the $i = 2$ mode, and that it couples at the step junction to the $i = 0$ mode. All of the other even modes, $i = 4, 6, \dots$, are also excited, but they only contribute to the reactive content of the step junction. To understand what happens to the $i = 0$ transverse mode, i.e., whether or not it is above cutoff transversely, we first write

$$k_o^2 = k_z^2 + \left(\frac{2\pi}{a}\right)^2 + k_{y2}^2 \quad (6.9)$$

$$k_o^2 = k_z^2 + \left(\frac{2\pi}{a'}\right)^2 + |k'_{y2}|^2 \quad (6.10)$$

since

$$k'_{y2} = -j |k'_{y2}| \quad (6.11)$$

and

$$k_o^2 = k_z^2 + k_{yo}^2 = k_z^2 + (k'_{yo})^2 \quad (6.12)$$

because $k_{xo} = k'_{xo} = 0$. The $i = 0$ transverse mode is akin to a TEM mode traveling at an angle between parallel plates, so that there is no field variation across the plates. From (6.9) and (6.12) we observe that

$$(k'_{yo})^2 = k_{yo}^2 = k_{y2}^2 + \left(\frac{2\pi}{a}\right)^2 \quad (6.13)$$

From (6.13) we conclude that

$$k_{yo}^2 > k_{y2}^2 > 0 \quad (6.14)$$

and that

$$(k'_{yo})^2 > k_{y2}^2 > 0 \quad (6.15)$$

so that both k_{yo} and k'_{yo} are real. An interesting difference between the even and odd mode cases is that in the even mode case there is no restriction necessary, like (6.8) in the odd mode case.

Since k'_{yo} is always real no matter what the ratio a'/a is, the even modes will be leaky under all conditions. Furthermore, the power that leaks has no x dependence, and it propagates at an angle away from the groove region like a TEM mode.

It will be seen that this latter feature is of basic importance in the performance of leaky-wave antennas based on groove guide.

B. THE L-SHAPED ANTENNA

1. Theoretical Description

The first antenna based on the groove guide was proposed and analyzed under the predecessor contract, and the results of that study have been published [2,3]. That antenna is discussed briefly in Chap. I, Sec. B, and it is illustrated in Fig. 1.1. Leakage of radiation from the ordinarily bound dominant mode is produced by the mechanism of *asymmetry*, by introducing a continuous metal strip of narrow width on one side only, as seen from Fig. 1.1. The antenna possesses several desirable performance features, but it is a structure that would be difficult to build at millimeter wavelengths. From the fabrication standpoint, therefore, it became necessary to devise alternative structures that are *simpler* in configuration.

The simplest leaky-wave antenna that we could conceive, that was consistent with our ability to analyze its performance properties, is the L-shaped antenna to be described. A sketch of the antenna has been presented on the right-hand side of Fig. 1.5 and in Fig. 2.1. (As drawn, the structure resembles a backward L, but we could of course have drawn its mirror image; the performance would be identical.) As mentioned in Chap. I, the final L-shaped structure can be conceived in several different ways. Our original approach to it was based on the recognition that the first higher even mode (the $n = 2$ mode) in groove guide is leaky, as is proved in Sec. A of this chapter. This approach also provided the way to analyze the performance behavior of the antenna. The concept behind this antenna and some performance results for it were presented at a symposium [20].

The transition from the $n = 2$ mode in the full groove guide to the final L-shaped structure is illustrated in Fig. 6.3. On the left-hand side we see the full groove guide supporting the $n = 2$ mode, which we know leaks in the manner indicated by the arrows representing the electric field orientations. In the middle, we have the groove guide bisected vertically; the field distribution remains undisturbed by this bisection because the vertical mid-plane contains a null in the vertical electric field. A second bisection, horizontal this time, yields the final L-shaped structure on the right-hand side. Again, this bisection leaves the field undisturbed because the electric field is everywhere perpendicular to this bisection plane.

An alternative way to recognize that the bisected structure in the middle will leak is to note that it is asymmetrical and supports the groove guide dominant mode. The leakage mechanism is then similar to that first employed in the antenna shown in Fig. 1.1.

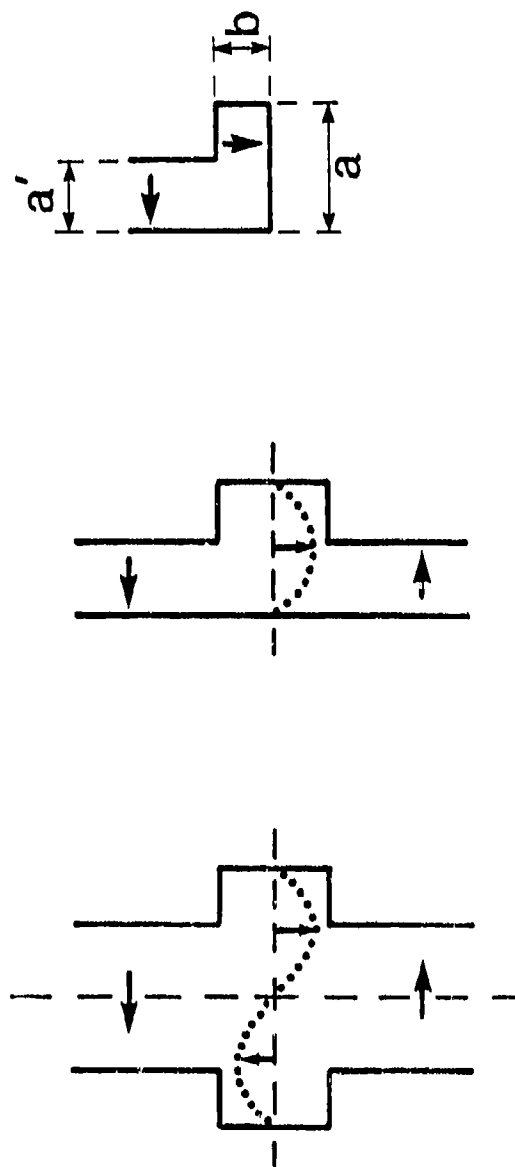


Fig. 6.3 Sketches showing the transition from the $n = 2$ mode in the full groove guide, on the left, to the L-shaped antenna structure on the right. The transition involves two successive bisections, neither of which disturbs the field distribution. The arrows represent electric field directions.

A third way to recognize that leakage must occur applies to the final L-shaped structure; it is seen that it resembles rectangular waveguide with a large off-center stub fed by its dominant mode. The easiest way to *feed* the L-shaped antenna is in fact by employing a rectangular waveguide.

Let us look again at the structure in the middle of Fig. 6.3 that results from a single bisection. We observe that it may be viewed as an *E-plane tee junction* in parallel-plate guide, placed on its side and with its stub guide short circuited some distance along it. This observation furnishes for us a novel method for analyzing the performance of this leaky structure, or, equivalently, that of the L-shaped antenna after the second bisection.

The bisected groove guide structure and the transverse equivalent network for it are presented in Fig. 6.4. The dimensional notation follows that given for the L-shaped structure in Fig. 6.3. The transverse equivalent network is based on the equivalent network for an E-plane tee junction shown in Fig. 5.3 and discussed in Chap. V, Sec. A. The theoretical expressions for the elements of the network in Fig. 6.4 are also taken from those in that same chapter.

In the parallel-plate regions in Fig. 6.4, only one mode is above cutoff and that mode is essentially a TEM mode propagating at an angle between the plates. The propagation wavenumbers k_x and k_y in the transmission lines in the transverse equivalent network are the same, as are the characteristic admittances Y_0 ; the dimensional differences between the main guide and the stub guide in the tee junction have been absorbed into the turns ratio n_{cs} .

When we adapt the expressions for the elements of the tee network from Chap. V we must be careful to switch the notation appropriately. First we employ the evident changes:

$$\begin{aligned} b' &\rightarrow 2b \\ b &\rightarrow a' \end{aligned}$$

Then we recall that the propagation in the main guide region in Chap. V was expressed in terms of λ_g ; here it is given by k_y . We therefore write

$$\lambda_g \rightarrow 2\pi/k_y$$

The expressions for the elements are then

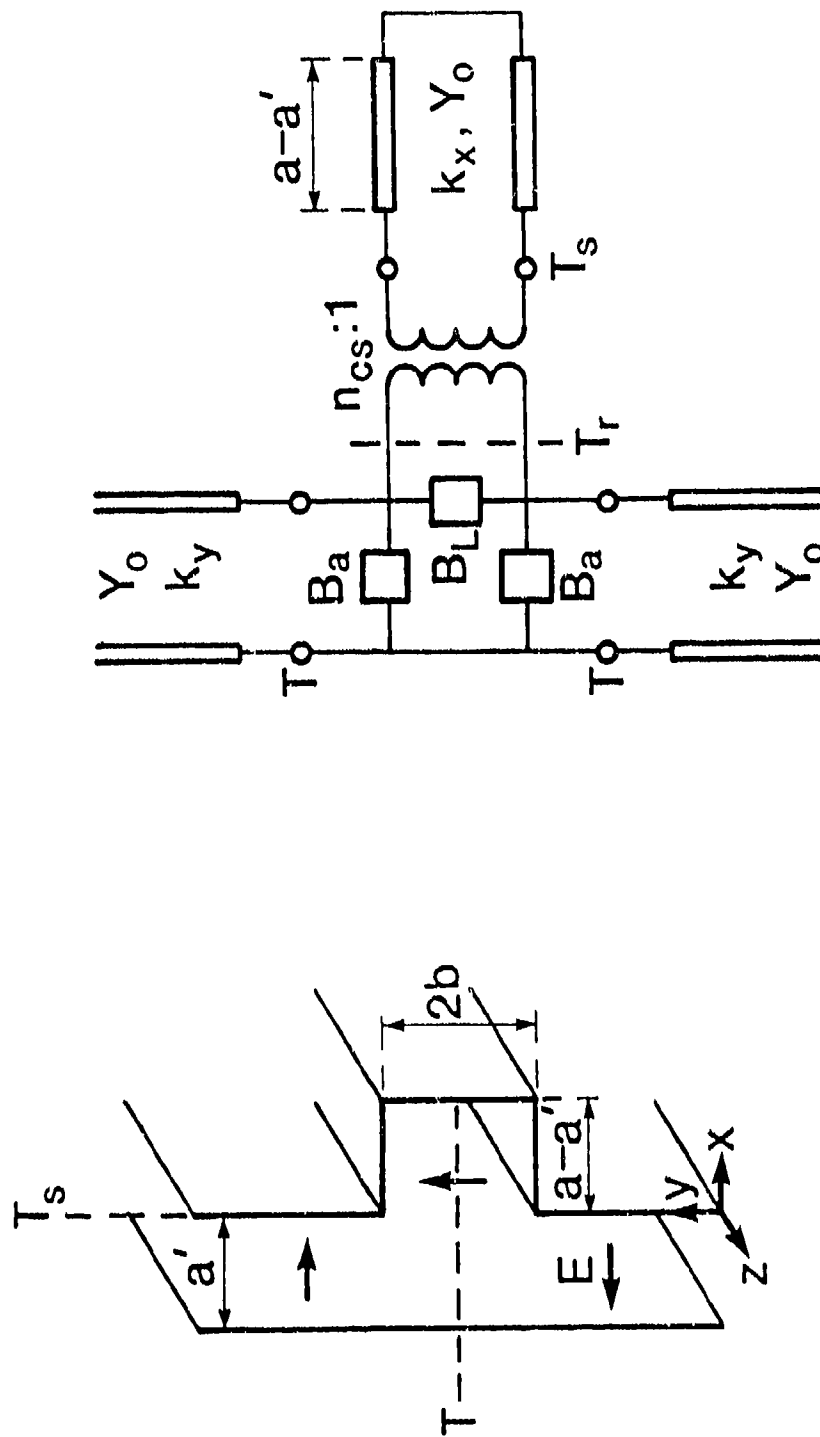


Fig. 6.4 Vertically bisected groove guide, and the transverse equivalent network for it that is based on the E-plane tee junction approach.

$$\frac{B_L}{Y_o} + \frac{1}{2} \frac{B_a}{Y_o} = \frac{1}{n_c^2} \frac{k_y a'}{\pi} \left[\ln \left(1.43 \frac{a'}{2b} \right) + \frac{1}{2} \left(\frac{k_y a'}{\pi} \right)^2 \right] \quad (6.16)$$

$$n_c = \frac{\sin(k_y b)}{k_y b} \quad (6.17)$$

$$n_{cs}^2 = n_c^2 \frac{2b}{a'} \quad (6.18)$$

$$\frac{B_a}{Y_o} = -\frac{\pi}{8} \frac{b}{a'} (k_y b) J_o^2(k_y b) \quad (6.19)$$

The *dispersion relation* is then obtained by choosing some reference plane T_r and summing to zero the admittances seen in both directions from this plane. The resulting transverse resonance relation, taken with respect to reference plane T_r in Fig. 6.4, is

$$j \left[\frac{B_L}{Y_o} + \frac{1}{2} \frac{B_a}{Y_o} \right] + \frac{1}{2} - j \frac{1}{n_{cs}^2} \left[\cot k_x (a - a') \right] = 0 \quad (6.20)$$

When we employ expressions (6.16) to (6.18) for the network elements, and recall that $k_x = k_y$, we obtain

$$\begin{aligned} & \frac{k_y a'}{\pi} \left[\ln \left(1.43 \frac{a'}{2b} \right) + \frac{1}{2} \left(\frac{k_y a'}{\pi} \right)^2 \right] \\ & - \frac{a'}{2b} \cot k_y (a - a') - j \frac{1}{2} \frac{\sin^2(k_y b)}{(k_y b)^2} = 0 \end{aligned} \quad (6.21)$$

where k_y is related to k_z , the quantity we actually seek, by

$$k_z = \beta - j\alpha = \sqrt{k_o^2 - k_y^2} \quad (6.22)$$

From dispersion relation (6.21) we see that k_y will be complex, so that β and α in (6.22) will yield the phase constant and the leakage constant of the L-shaped leaky-wave line source. From the relations presented in Chap. II, Sec. D, we may use the values of β and α to obtain the properties of the radiation pattern.

Dispersion relation (6.21) holds for the structures in Fig. 6.3, for which the open regions (corresponding to the main guide portions in Fig. 6.4) are effectively infinite in length. Although that arrangement yields a simpler dispersion relation, and offers a good approximation to a practical structure under most conditions, in reality those lengths must be *finite*. When such a finite length, equal to c , is imposed on the L-shaped antenna itself, the structure becomes that shown in Fig. 6.5, in which the corresponding transverse equivalent network is also presented.

The difference in the transverse equivalent network from the previous case of $c = \infty$ is that the matched load Y_o on the transmission line is replaced by the actual termination, which we call $G_R + jB_R$, where the subscript R signifies "radiating." This termination, at the end of line length c , will produce a standing wave in that line and will modify the values of β and α .

The physical discontinuity is that of a *radiating open end*. That discontinuity and our network representation for it in terms of G_R and B_R are given in Fig. 6.6. Fortunately, a rigorous expression for $G_R + jB_R$ is available in the Waveguide Handbook [8], Sec. 4.6a, pp. 179-183. We need, of course, to adapt those results to our notation. The following correspondences are required:

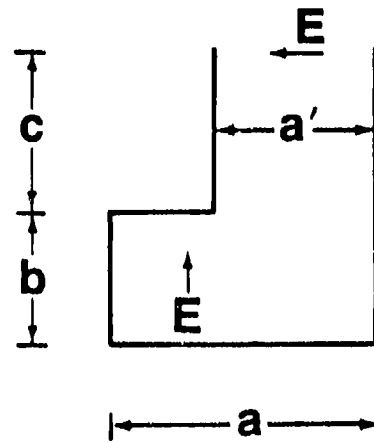
$$\begin{aligned} b \rightarrow a' & & x \rightarrow \frac{k_y a'}{2\pi} \\ \lambda' \rightarrow 2\pi/k_y & & \theta \rightarrow 2k_y d \end{aligned}$$

where

$$2k_y d = \frac{k_y a'}{\pi} \ln \left[\frac{e}{\gamma} \frac{4\pi}{k_y a'} \right] - 2S_1 \left(\frac{k_y a'}{2\pi}; 0,0 \right) \quad (6.23)$$

and where

Antenna Cross Section



Transverse Equivalent Network

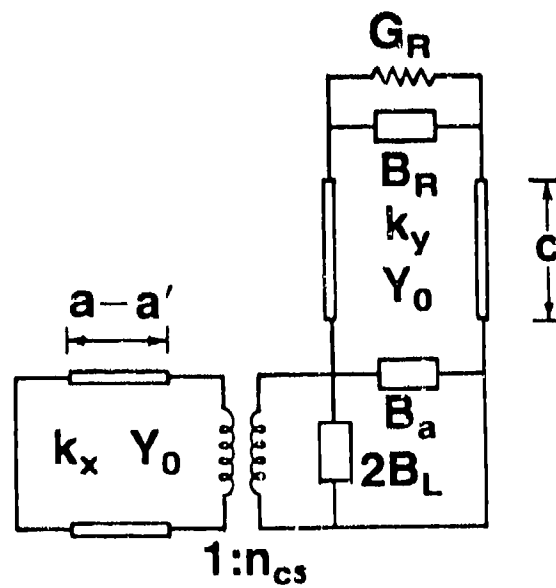


Fig. 6.5

L-shaped antenna structure when the radiating section is finite in length, and modified transverse equivalent network that includes the discontinuity at the radiating open end.

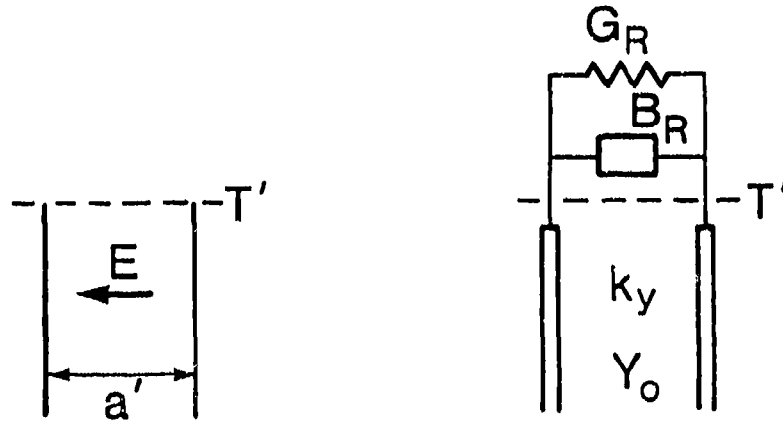


Fig. 6.6 The structure of the radiating open end, and its equivalent network.

$$S_1 \left(\frac{k_y a'}{2\pi} ; 0,0 \right) = \sum_{n=1}^{\infty} \left[\sin^{-1} \left(\frac{k_y a'}{2\pi} \frac{1}{n} \right) - \left(\frac{k_y a'}{2\pi} \frac{1}{n} \right) \right] \quad (6.24)$$

with $e = 2.718$ and $\gamma = 1.781$.

The normalized terminal admittance of the radiating open end at reference plane T' is then given by

$$\frac{Y_R}{Y_o} = \frac{G_R}{Y_o} + j \frac{B_R}{Y_o} = \frac{\sinh \frac{k_y a'}{2} + j \sin 2k_y d}{\cosh \frac{k_y a'}{2} + \cos 2k_y d} \quad (6.25)$$

where the expression for $2k_y d$ appears in (6.23) and (6.24).

The dispersion relation (6.21) also changes somewhat, and becomes modified to

$$\frac{k_y a'}{\pi} \left[\ln \left(1.43 \frac{a'}{2b} \right) + \frac{1}{2} \left(\frac{k_y a'}{\pi} \right)^2 \right] - \frac{a'}{2b} \cot k_y (a - a') - j \frac{Y_{iR}}{Y_o} \frac{\sin^2(k_y b)}{(k_y b)^2} = 0 \quad (6.26)$$

where

$$\frac{Y_{iR}}{Y_o} = \frac{j + \frac{Y_R}{Y_o} \cot(k_y (c + b))}{\cot(k_y (c + b)) + j \frac{Y_R}{Y_o}} \quad (6.27)$$

and Y_R/Y_o is given by (6.25). This modified dispersion relation thus takes into account the finite length c of the parallel-plate region associated with the radiating open end.

2. Numerical Results

The configuration of the L-shaped leaky-wave line-source antenna is indeed simple, and it can be easily fed when we view it as derived from a rectangular waveguide. To evaluate its behavior as an antenna, however, we must know what values of β/k_o and α/k_o can be achieved, and how these values will change as we vary the structural dimensions and the frequency. Such information is obtained directly by solving dispersion relation (6.21) together with (6.22) when length c is taken ideally to be infinite, and relations (6.26) and (6.27) together with (6.22) in the practical situation in which c is finite.

We first examine the situation in which c is infinite, and determine the variations in the normalized phase constant β/k_o and normalized leakage constant α/k_o as a function of aspect ratio b/a . Curves illustrating this behavior for a frequency of 50 GHz appear in Fig. 6.7. Ideally, we would wish that β/k_o would be flat with b/a ,

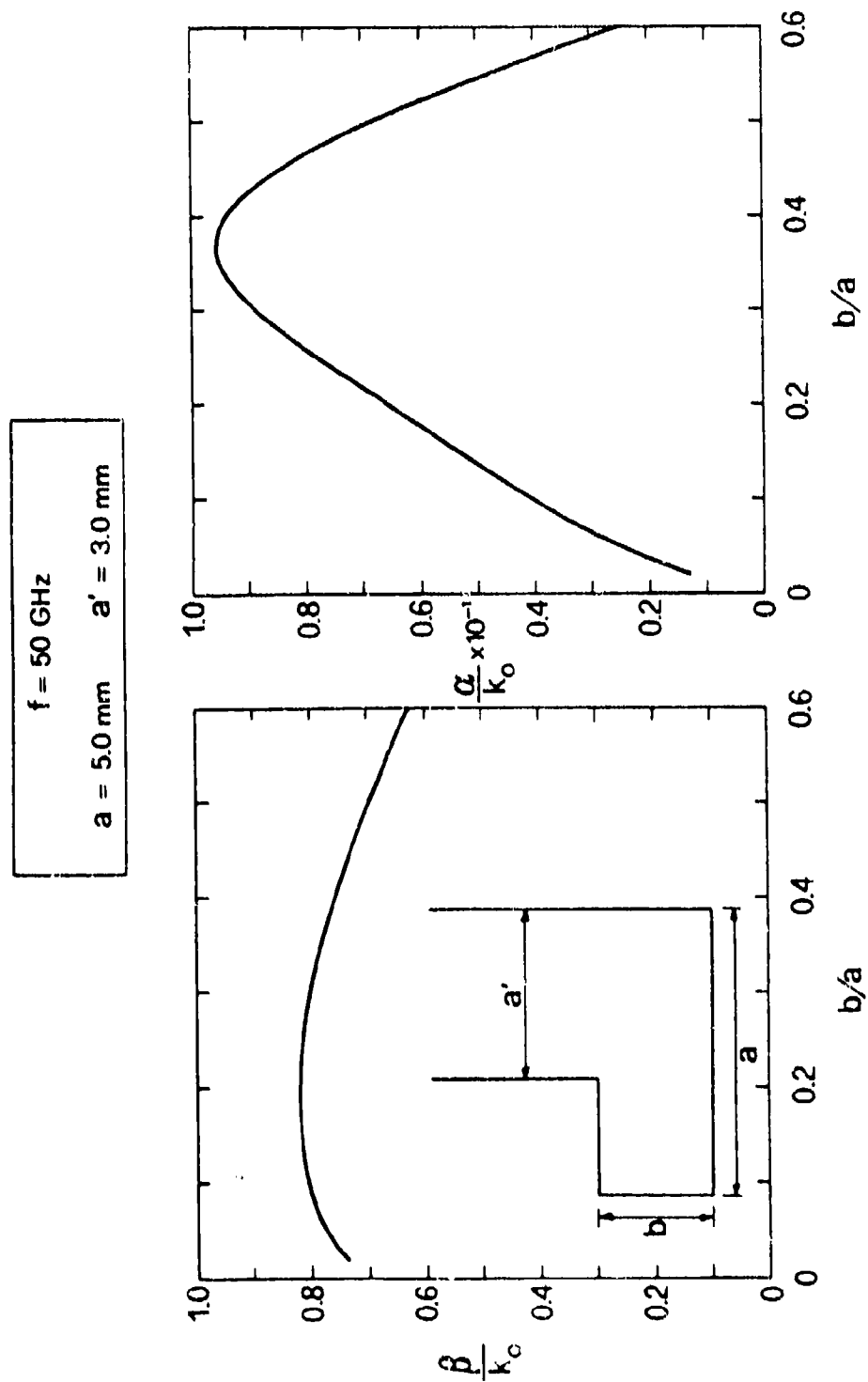


Fig. 6.7 Behavior of the normalized phase constant and the normalized leakage constant as a function of guide aspect ratio b/a , at a frequency of 50 GHz.

whereas α/k_o would vary strongly with it. Then, we could change the beam width (by varying α/k_o) while maintaining constant the angle of the beam maximum (which is given by β/k_o). What we find in Fig. 6.7 is that α/k_o can be changed significantly by varying b/a , but that β/k_o remains only roughly constant. The behavior is not ideal, but not that bad if we consider only a limited range. For example, from $b/a = 0.10$ to 0.30 , β/k_o has a maximum value of about 0.82 and a minimum value of 0.80 ; the corresponding beam angle varies from 55.1° to 53.1° , or only $\pm 1.0^\circ$. Over that same range of b/a , α/k_o more than doubles, from 4.0×10^{-2} to 8.9×10^{-2} .

The effect of changing frequency is shown in Fig. 6.8, where the same structure is taken but the frequency is increased to 64 GHz. The same qualitative behavior is found, but the leakage rate is cut roughly in half, and the beam maximum points further away from broadside.

An additional very important property that is common to both of these frequencies is that the leakage rate is rather large. The maximum value of α/k_o at 64 GHz and the median value at 50 GHz are roughly the same, equal to about 0.05 . From some simple relations presented in Chap. II, Sec. D, we may determine the approximate beam width corresponding to this value of leakage constant. Leaky-wave antennas are usually operated so that 90% or so of the power is radiated. Under that condition, relation (2.28) is valid; when it is inserted into expression (2.29) for the beam width $\Delta\theta$, and use is made of (2.27), we obtain the approximate relation

$$\Delta\theta \approx 285 \frac{\alpha/k_o}{\cos(\sin^{-1} \beta/k_o)} \quad \text{in degrees} \quad (6.28)$$

If we take $\beta/k_o \approx 0.7$ and $\alpha/k_o \approx 0.05$, we find that $\Delta\theta \approx 20^\circ$. For a smaller value of α/k_o , say 0.03 , $\Delta\theta$ becomes 12° . At $f = 50$ GHz one would need to work at the edges of the curve to obtain a narrower beam. We therefore conclude that the L-shaped antenna is useful only for applications that require a relatively large beam width.

It is possible that smaller values of α/k_o may be obtained by changing the a'/a ratio, but this possibility was not investigated. Instead, we next examined the influence of a finite value for c , the length of guide leading to the radiating open end. In Fig. 6.9 we observe the variations in β/k_o and α/k_o as length c is changed. The aspect ratio has been so chosen, however, that the value of α/k_o is reduced somewhat, in order to avoid the possible coupling to another leaky mode that caused problems in connection

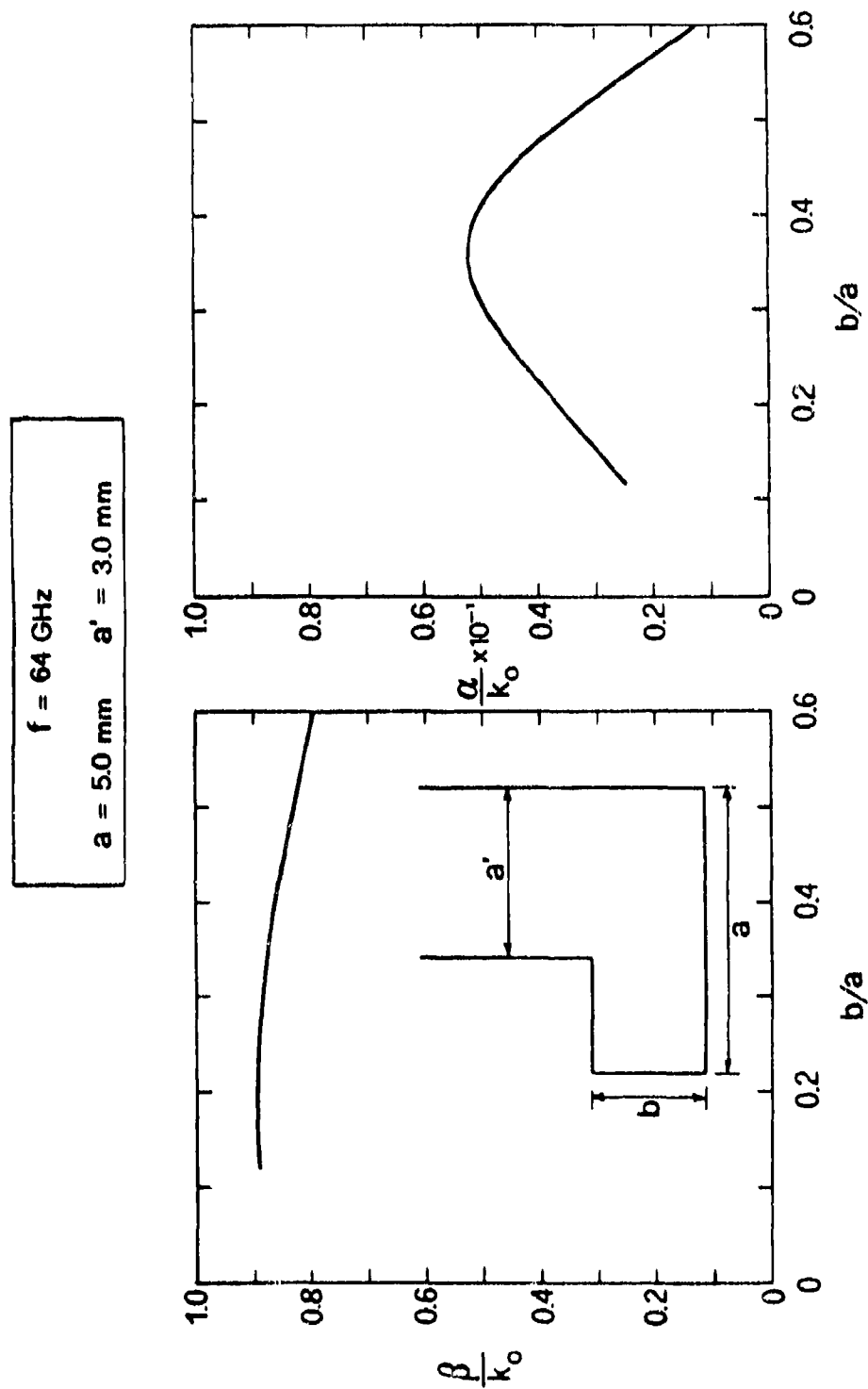


Fig. 6.8 Behavior corresponding to that in Fig. 6.7 but at $f = 64 \text{ GHz}$, indicating the effect of a higher frequency.

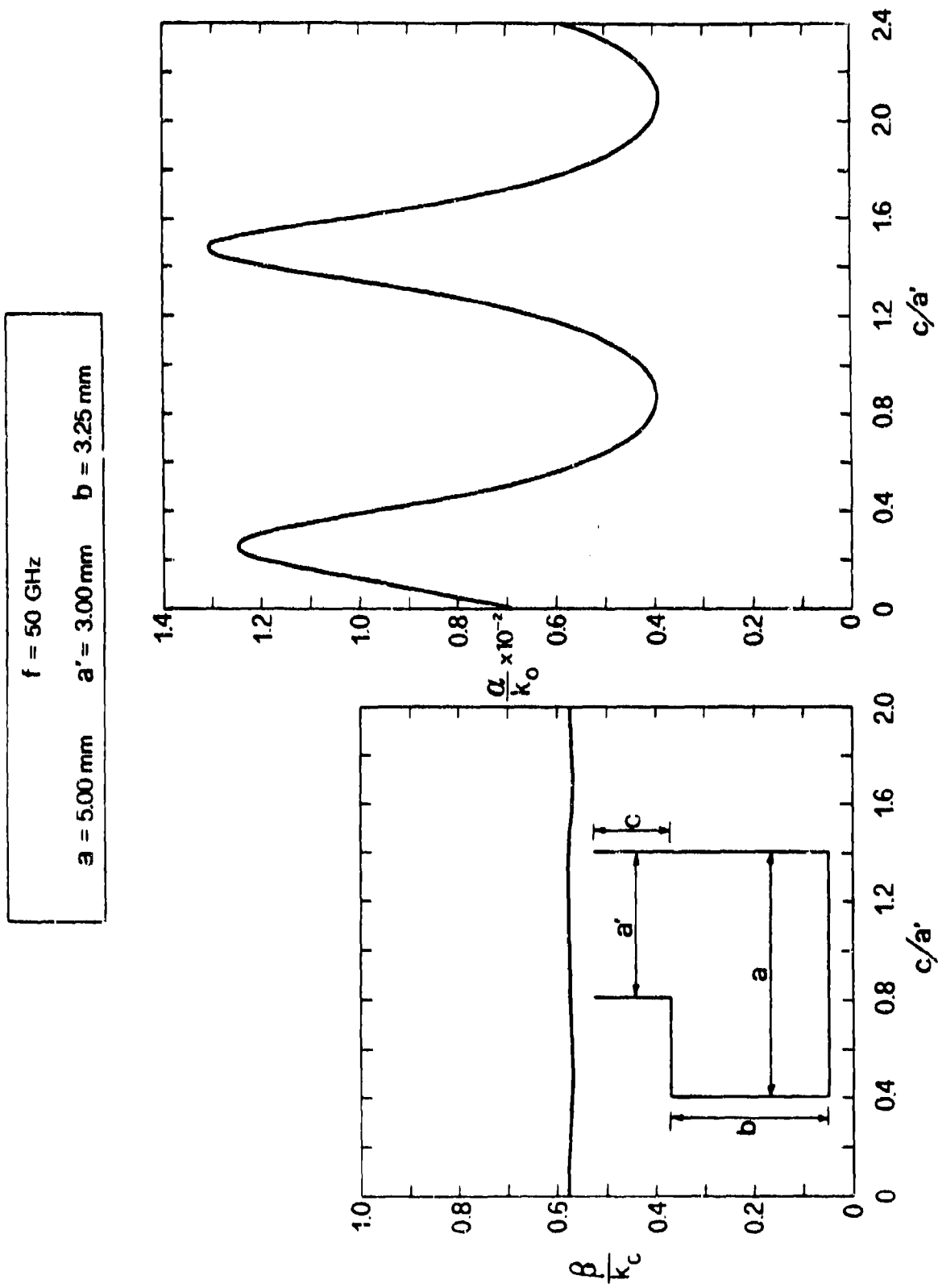


Fig. 6.9 The variations in the normalized phase and leakage constants as the length c is changed, where c is the finite length of the radiating section.

with the NRD guide line-source antenna (see Chap. III). We find in Fig. 6.9 that the effect of changing c is approximately periodic, showing that such coupling effects are avoided in this case. The value of β/k_o is seen to remain nearly constant, but that of α/k_o varies over a three to one range. If we wish to operate at a lower value of α/k_o , therefore, we can adjust the length c so as to be near one of the minima in the curve of α/k_o vs. c/a' .

In Figs. 6.10 and 6.11 we indicate the dependence of β/k_o and α/k_o on aspect ratio b/a for two different lengths c . We find the same qualitative behavior as that obtained when c was taken to be infinite, except that the maximum value obtained for α/k_o changes somewhat with the value of c . The basic characteristic of the L-shaped antenna is still that it leaks strongly, resulting in large beam widths. Instead of studying in a more thorough manner the properties of this antenna, we devised an alternative one that permits the flexibility in beam width that is absent here. That alternative structure is the offset-groove-guide antenna described in Chap VII; since it turned out to possess other desirable properties as well, we examined it in substantial detail, and even took measurements on it which are reported in Chap. VIII.

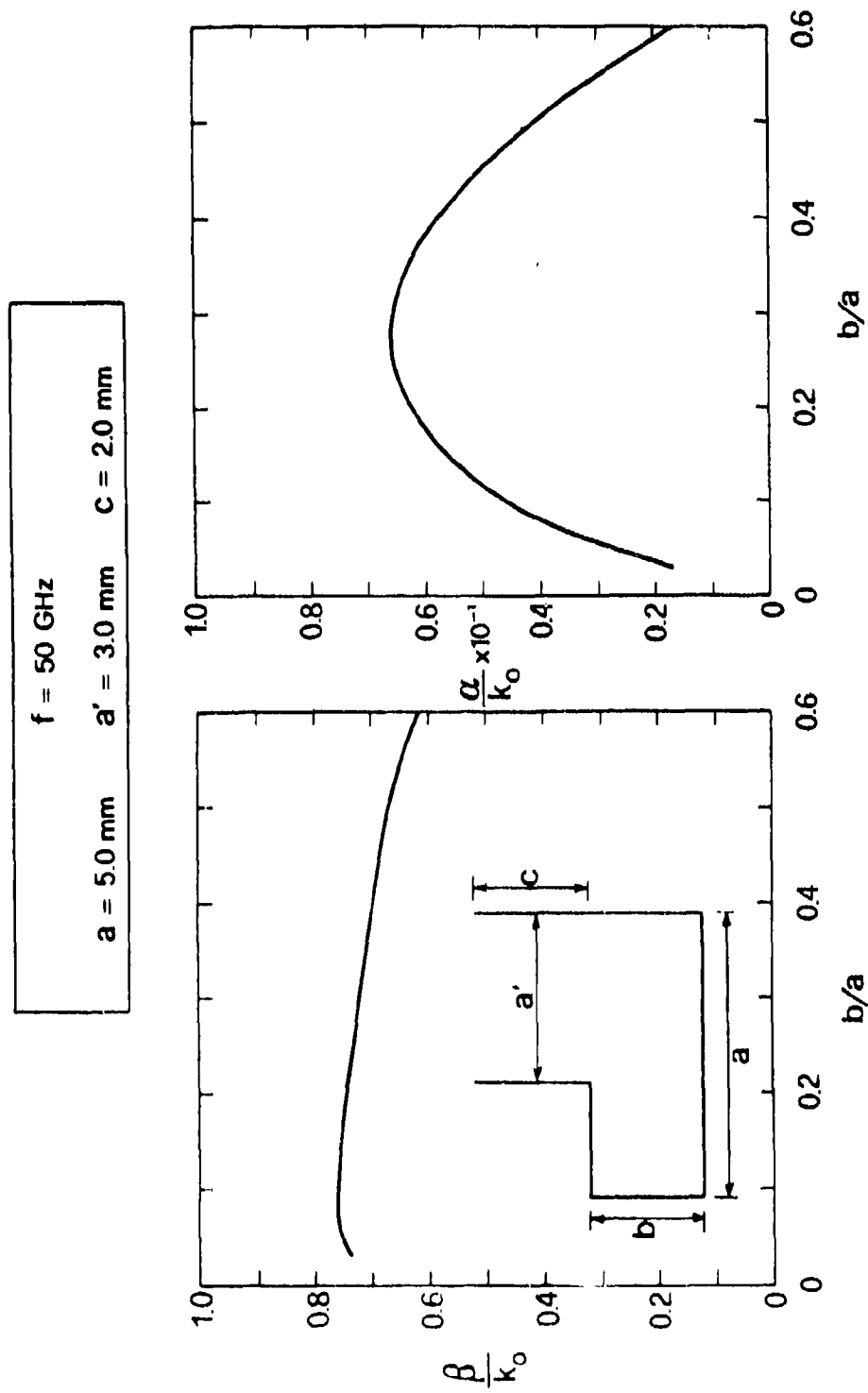


Fig. 6.10 Behavior of the normalized phase and leakage constants as a function of aspect ratio when length c is 2.0 mm.

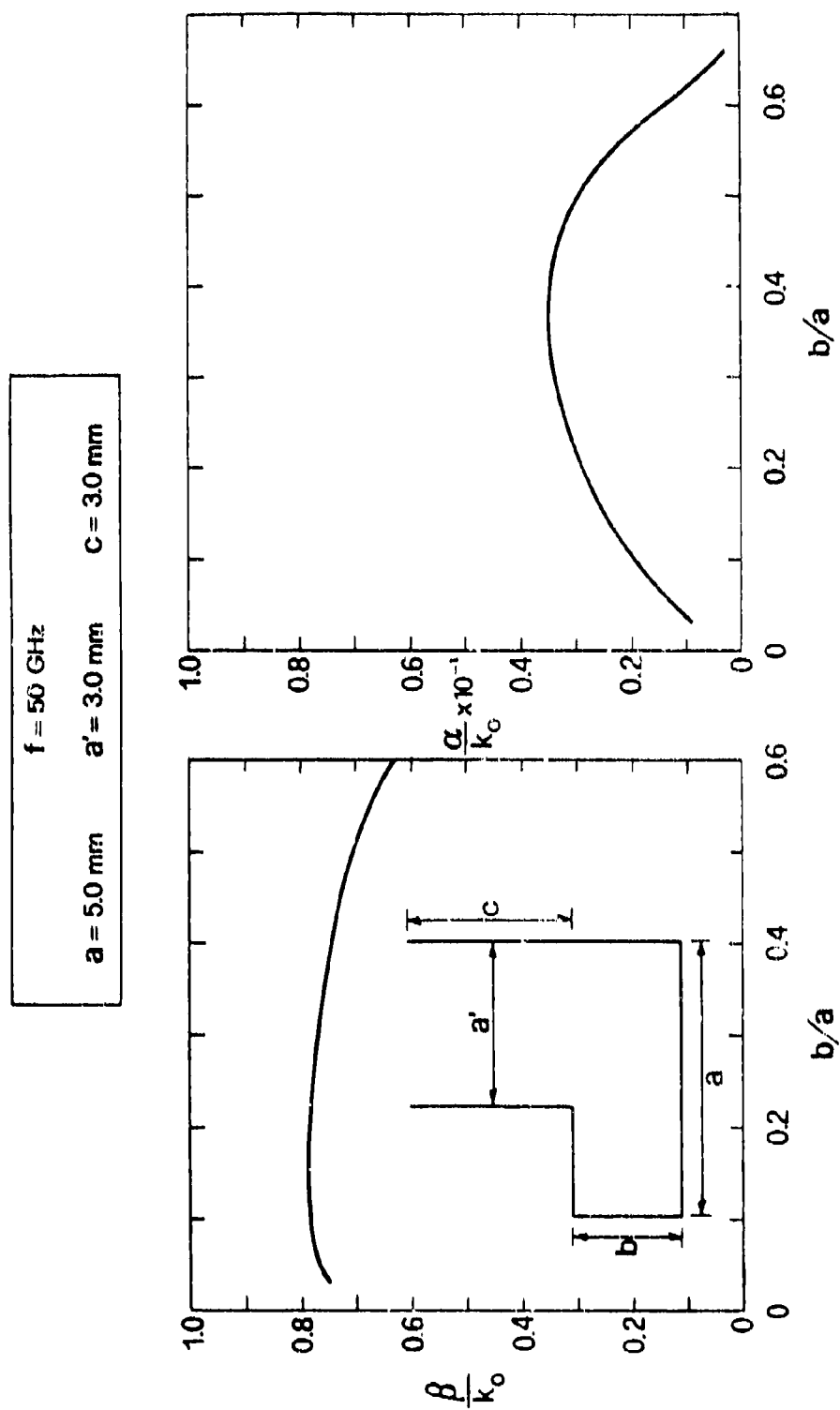


Fig. 6.11 Behavior corresponding to that in Fig. 6.10, but for length c equal to 3.0 mm.

VII.	THE OFFSET-GROOVE-GUIDE LEAKY-WAVE LINE SOURCE	187
A.	PRINCIPLES AND THEORETICAL DESCRIPTION	189
	1. Structure and Principle of Operation	189
	2. The Transverse Equivalent Network	192
	3. The Dispersion Relation	196
B.	NUMERICAL RESULTS FOR THE PROPAGATION BEHAVIOR	198
	1. Structures with a Flatter Aspect Ratio	198
	2. Aspect Ratio Equal to that of Rectangular Waveguide	204
	3. Variations with Frequency	208
C.	COMPARISON OF RESULTS WITH AN ALTERNATIVE THEORETICAL APPROACH	215
D.	EFFECTS DUE TO FINITE STUB LENGTH	220
	1. Modification of the Dispersion Relation	221
	2. Coupling with Another Leaky Mode	223
	a. Variations with Stub Length	224
	b. Variations with Stub Offset	229
	c. Variations with Frequency	235

VII. THE OFFSET-GROOVE-GUIDE LEAKY-WAVE LINE SOURCE

(With: Prof. P. Lampariello, Mr. F. Frezza
University of Rome "La Sapienza," Italy

and Prof. H. Shigesawa, Dr. M. Tsuji
Doshisha University, Kyoto, Japan)

The L-shaped leaky-wave antenna based on groove guide that is described in Chap. VI has the virtue of a very simple configuration, but it has limited flexibility in performance. In particular, it leaks strongly under most conditions, so that it is suitable primarily for applications that require wide radiated beams. In this chapter, we describe a *modification* of that structure that not only permits *great flexibility* in the range of achievable beam widths, but possesses other desirable performance features as well.

It is most easily viewed, and also analyzed, as an offset groove guide. In this chapter, we first describe the new leaky-wave structure and its principle of operation. Then we present an accurate theoretical description of the structure in terms of the new tee-junction equivalent network discussed in Chap. V, and with it derive the relevant dispersion relation for the propagation behavior of the new structure.

Numerical results for some performance characteristics are then presented to illustrate the virtues mentioned above. These numerical results are arranged in two groups, the first corresponding to a structure with a flat aspect ratio for the feed guide portion, and the second for a structure whose aspect ratio is equal to that of *rectangular waveguide*. The second structure was selected because the new antenna can most easily be fed from a rectangular waveguide. These curves are also relevant with respect to Chap. VIII, which presents *experimental* results for an offset-groove-guide antenna of the same size and shape as rectangular waveguide in that frequency range (centered about 50 GHz).

We next analyze some of the same performance properties by employing a *totally different* theoretical approach, that of a numerical mode-matching procedure, and we show that the numerical values for the propagation characteristics obtained by each method *agree very well* with each other. Such agreement justifies our confidence in the accuracy of our theoretical description.

Finally, we treat the effects introduced when the stub guide portion of the offset-groove-guide antenna is *finite*. The effects turn out to be very similar to those found in connection with the NRD guide leaky-wave antenna discussed in Chap. III. Although

the effects were first discovered and explained in connection with the NRD guide structure, we examined them here in much greater detail when we realized that in a qualitative sense the effects are universal to all leaky-wave structures with a finite stub length. The principal effect, which produces great complication in the performance properties but which we know how to get around, is that of an originally unexpected *coupling to another leaky mode*. The coupling effects are novel in that they involve the coupling between two leaky (complex) modes, and they represent a canonical type of interaction which we felt deserved careful attention and understanding in its own right.

It is interesting to note, from the author listing just under the title of this chapter, that the work encompassed within this chapter indicates a cooperative program involving three different areas of the world: Europe, Asia and North America.

A. PRINCIPLES AND THEORETICAL DESCRIPTION

1. Structure and Principle of Operation

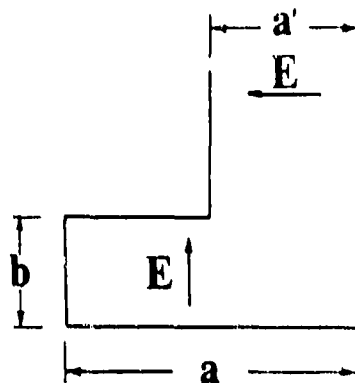
A leaky-wave line-source antenna is characterized by a complex propagation wavenumber $k_z = \beta - j\alpha$, where the phase constant β yields the angle of the maximum of the radiated beam and the leakage constant α determines the beam width. Simple approximate relations among these quantities are presented in Chap. II, Sec. D, as equations (2.27) to (2.29).

A desirable line source of this type for millimeter wave applications should possess the following properties. It should involve a simple structure, have low metal loss, radiate in a single polarization, possess flexibility in beam width (meaning that it should provide a wide range of α values), and permit one to change α without affecting β .

The L-shaped antenna discussed in Chap. VI does indeed possess several of these properties. It is particularly simple, has low loss and has pure single polarization, but α and β cannot be separated easily, and the antenna leaks so strongly that only wide beams can be obtained under most conditions. The L-shaped antenna appears in Figs. 6.3 and 6.5, but it is repeated in Fig. 7.1 for convenience. The objective in this portion of the study was to devise a *modification* in the structure of the L-shaped antenna that would retain much of the simplicity and its other desirable features, but would also provide the flexibility in beamwidth and the separability between α and β that the L-shaped structure lacks. The modified structure that satisfies these requirements is the *offset-groove-guide antenna* also shown in Fig. 7.1.

Its genesis from a nonradiating groove guide is illustrated in Fig. 7.2. On the left hand side we see the standard groove guide, for which the dominant mode is purely bound and is characterized by β only. Some electric field lines are shown, and they are intended to indicate that the field decays exponentially in the narrower regions at the top and bottom. (A further, short, description is given in Chap. VI, Sec. A,1.) The structure on the right has its top and bottom portions shifted over, or *offset*. The resulting structure is *asymmetrical*, so that some net horizontal electric field is created, forming a TEM mode that propagates power away at an angle, causing the overall mode to become leaky. To obtain the antenna in Fig. 7.1, we of course *bisect* the offset groove guide horizontally since the field is not affected thereby.

What is important is that the amount of leakage can be neatly *controlled* by the amount of offset. Since the beam width is linearly related to the value of α , the



It is simple, has low loss, has pure single polarization, but leaks so strongly that only wide beams can be obtained

Modified structure that also permits flexibility in beam width

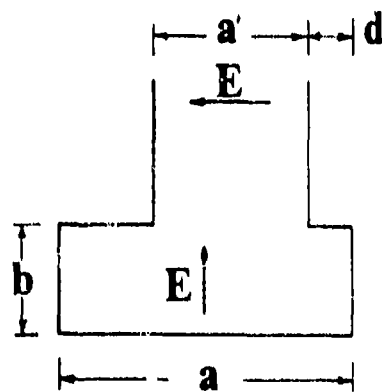
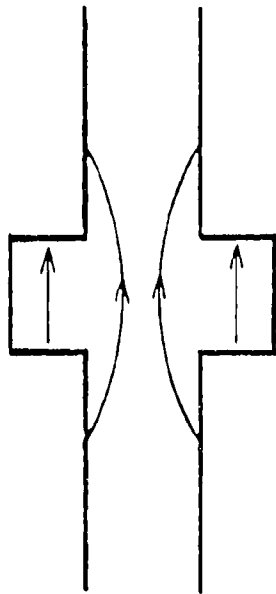


Fig. 7.1

The L-shaped antenna, shown at the top, and its modification, the bisected offset-groove-guide antenna, that overcomes its limitations.

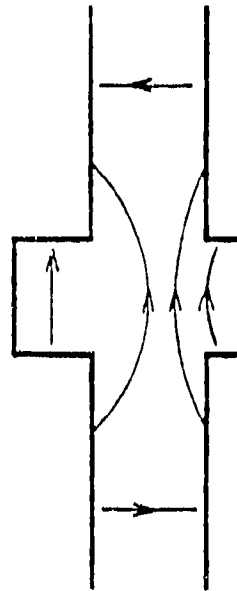
STANDARD GROOVE GUIDE



Dominant mode
is bound.

$$\beta$$

OFFSET GROOVE GUIDE



Dominant mode
becomes leaky.

$$\beta - j\alpha$$

Fig. 7.2

The transition from the nonradiating standard groove guide to the leaky offset groove guide.

leakage per unit length along the line-source antenna, we have a structure that is basically *simple*, yet yields a radiation pattern that is *flexible in beamwidth*. This variation in the leakage rate can also be seen from the limiting cases shown in Fig. 7.3. The zero radiation limit occurs when the stub is centered; one then has the original nonradiating groove guide. In the maximum radiation limit, the stub is located at one end (the length d shown in the figure becomes zero), and we obtain the L-shaped antenna that we found leaks strongly.

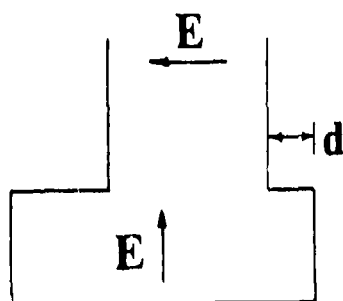
It is interesting that the bisected offset-groove-guide antenna resembles a *rectangular waveguide with an offset stub*. It could have been derived from rectangular waveguide, but that is not how it evolved. On the other hand, the resemblance to rectangular waveguide provides an excellent way to feed the structure. More is said about this feature in Sec. B,2 and also in Chap. VIII, where experimental results for this antenna type are presented.

The concept underlying this new antenna, together with some early numerical results with respect to its performance, was presented at an URSI meeting [21]. A more detailed presentation, including several of the results that appear in later sections of this chapter, such as the comparisons using an alternative theoretical approach and the effects due to the stub being of finite length, is contained in the Digest of the 1987 IEEE International Microwave Symposium [22].

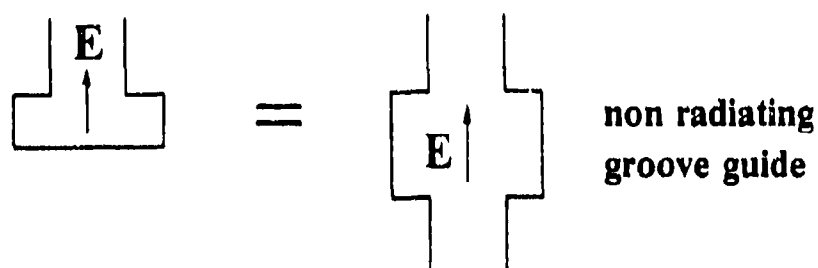
2. The Transverse Equivalent Network

A glance at the cross section of the offset-groove-guide antenna, shown in Fig. 7.1, makes clear that its central region resembles that of an E-plane tee junction. We may therefore employ the equivalent network presented and discussed in Chap. V for an E-plane tee junction as the central element in a transverse equivalent network representation of the offset-groove-guide antenna.

The same tee junction is the central element in the transverse equivalent network for the L-shaped antenna, but it is employed somewhat differently, and with different dimensional notations. There, as seen in Fig. 6.4, the tee junction is placed vertically in a structure that is doubled, i.e., what it was before a horizontal bisection; here, the tee junction is placed horizontally, and used directly in the cross section shown in Fig. 7.1. There the stub is short-circuited; here, the main guide ends are short-circuited. It is necessary, therefore, to present all the details again in this new context. Even the expressions for the elements of the tee-junction network are different, because the dimensions involved have changed their notation due to the 90° rotation of the tee junction.



Zero radiation limit (stub centered)



Maximum radiation limit ($d = 0$)

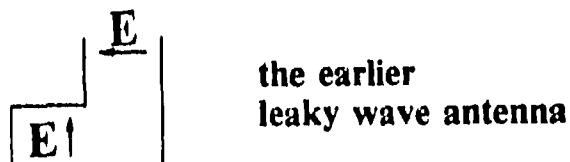


Fig. 7.3

The zero and maximum radiation limits for the (bisected) offset-groove-guide antenna. The zero radiation limit corresponds to the nonradiating groove guide, whereas the maximum radiation limit becomes the L-shaped antenna treated in Chap. VI.

We first adapt the expressions for the elements of the tee junction from Chap. V by changing the notation appropriately:

$$\begin{aligned} b' &\rightarrow a' \\ b &\rightarrow b \\ \lambda_g &\rightarrow 2\pi/k_x \end{aligned}$$

The expressions then become

$$\frac{B_a}{Y_o} = -\frac{\pi}{16} \frac{a'}{b} \frac{k_x a'}{2} J_o^2 \left(\frac{k_x a'}{2} \right) \quad (7.1)$$

where J_o is the Bessel function of zero order,

$$\frac{B_L}{Y_o} + \frac{1}{2} \frac{B_a}{Y_o} = \frac{1}{n_c^2} \left(\frac{k_x b}{\pi} \right) \left[\ln \left(1.43 \frac{b}{a'} \right) + \frac{1}{2} \left(\frac{k_x b}{\pi} \right)^2 \right] \quad (7.2)$$

$$n_c = \frac{\sin(k_x a'/2)}{k_x a'/2} \quad (7.3)$$

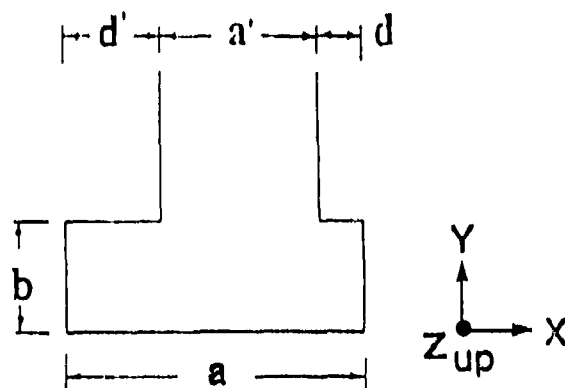
$$n_{cs}^2 = n_c^2 (a'/b) \quad (7.4)$$

$$\begin{aligned} \frac{B_L}{Y_o} &= \frac{1}{n_c^2} \left(\frac{k_x b}{\pi} \right) \left[\ln \left(1.43 \frac{b}{a'} \right) + \frac{1}{2} \left(\frac{k_x b}{\pi} \right)^2 \right] \\ &+ \frac{\pi}{32} \frac{a'}{b} \left(\frac{k_x a'}{2} \right) J_o^2 \left(\frac{k_x a'}{2} \right) \end{aligned} \quad (7.5)$$

These expressions correspond to the elements in the tee-junction equivalent network appearing in Fig. 5.3.

This tee-junction equivalent network is then made part of the complete transverse equivalent network shown in Fig. 7.4, which represents the antenna structure

CROSS SECTION



TRANSVERSE EQUIVALENT NETWORK

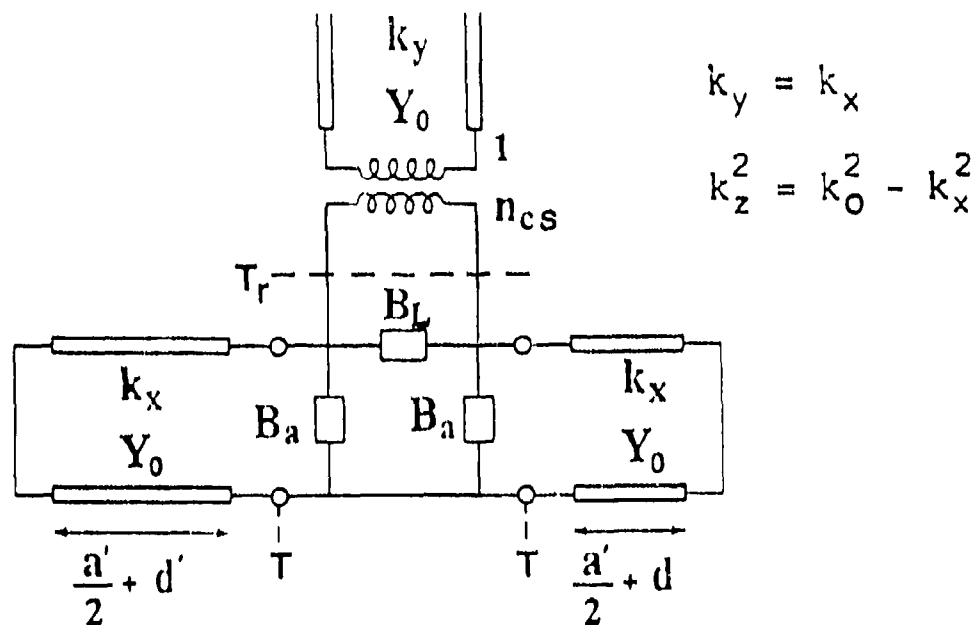


Fig. 7.4

The cross section of the offset-groove-guide antenna and its transverse equivalent network, which utilizes the new E-plane tee junction equivalent network discussed in Chap. V.

appearing on the bottom of Fig. 7.1 and repeated at the top of Fig. 7.4. It is seen that the *asymmetry* in the antenna structure due to the stub being offset reflects itself in the two unequal distances d and d' shown on the cross section. In turn, the asymmetry is accounted for in the transverse equivalent network by the unequal line lengths that represent the main guide arms. As in the case of the L-shaped antenna, only one mode is above cutoff in the main guide arms and in the stub guide, and that mode is essentially a TEM mode propagating at an angle between the parallel plates. Therefore, the wavenumbers k_x and k_y in the network transmission lines are equal, as are the characteristic admittances Y_o . The different widths b and a' of the parallel plate sections are absorbed into the turns ratio n_{cs} (see (7.4)).

The final important point in connection with the network in Fig. 7.4 is that the stub length is assumed to be infinite. In practice, of course, the stub length must be *finite*. In that case, the termination on the stub transmission line changes from a matched load to an admittance that represents a radiating open end. That modification was already applied to the transverse equivalent network for the L-shaped antenna, and discussed in detail in Chap. VI; the network modifications are shown in Figs. 6.5 and 6.6, and the relevant equations appear as (6.23) through (6.27). We will apply them to the offset-groove-guide antenna later in this chapter, in Sec. D, in the context of a full discussion of the various interesting and unexpected effects that can arise due to finite stub length. When those "interesting" effects are avoided (and we indicate there how they may be avoided), it turns out that the influence of finite stub length is relatively minor, and that the performance characteristics found for the case for which the stub length is infinite yield a very good indication of practical performance. Since the dispersion relation and the calculations are significantly simpler when the stub length is taken to be infinite, we will employ them for the earlier discussion, and then later, in Sec. D, examine in detail the various effects due to finite stub length.

3. The Dispersion Relation

The dispersion relation for the propagation behavior is obtained by taking the free resonance of the transverse equivalent network in Fig. 7.4. We choose a reference plane at T_r , just below the turns of the transformer, and sum to zero the admittances seen looking up and down from T_r . We then find

$$Y_{up} = \frac{1}{n_{cs}^2} Y_o \quad (7.6)$$

$$Y_{down} = jB_L + \frac{1}{1/(jB_a + Y_R) + 1/(jB_a + Y_L)} \quad (7.7)$$

where Y_R and Y_L are the main guide input admittances looking to the right of reference plane T on the right side of the network and to the left of T on the left side, namely,

$$Y_R = -j Y_o \cot k_x \left(\frac{a'}{2} + d \right) \quad (7.8)$$

$$Y_L = -j Y_o \cot k_x \left(\frac{a'}{2} + d' \right) \quad (7.9)$$

Setting

$$Y_{up} + Y_{down} = 0 \quad (7.10)$$

and normalizing to Y_o , we obtain

$$\frac{1}{n_{cs}^2} + j \frac{B_L}{Y_o} + j \frac{\left[\frac{B_a}{Y_o} - \cot k_x \left(\frac{a'}{2} + d \right) \right] \left[\frac{B_a}{Y_o} - \cot k_x \left(\frac{a'}{2} + d' \right) \right]}{2 \frac{B_a}{Y_o} - \left[\cot k_x \left(\frac{a'}{2} + d \right) + \cot k_x \left(\frac{a'}{2} + d' \right) \right]} = 0 \quad (7.11)$$

where the elements B_a/Y_o , n_{cs} and B_L/Y_o are given by expressions (7.1) through (7.5). Wavenumber k_x is related to k_z , the result we seek, by

$$k_z = \beta - j\alpha = \sqrt{k_o^2 - k_x^2} \quad (7.12)$$

We may observe that dispersion relation (7.11) is in *closed form* since all the elements of the transverse equivalent network are in closed form. This is an additional advantage of the network approach. From this dispersion relation, we see that k_x will be complex, so that β and α in (7.12) will yield the phase constant and leakage constant of the offset-groove-guide leaky-wave antenna. By employing the relations presented in Chap. II, Sec. D, these values of β and α yield information on the properties of the radiation pattern.

B. NUMERICAL RESULTS FOR THE PROPAGATION BEHAVIOR

1. Structures with a Flatter Aspect Ratio

Dispersion relation (7.11), together with (7.12), permit one to compute the variation of the phase constant β and the leakage constant α as a function of various geometric parameters. We first examine, in Fig. 7.5, the dependence of β/k_0 and α/k_0 , where k_0 is the free-space wavenumber, with respect to the *aspect ratio* b/a of the feed guide portion of the antenna. The other parameter values are shown on the figure. We note that the normalized leakage rate α/k_0 increases strongly as b/a is reduced, but that β/k_0 changes relatively little. The relative independence of β on height b is easily understandable. If the stub width a' is small, the value of β is determined almost entirely by the feed guide width a . For a wide stub guide, such as that taken for the data in Fig. 7.5, there is a small dependence on b . As b/a is changed from 0.3 to 0.5, though, the value of α/k_0 changes by roughly a factor of two. Thus, we can select an aspect ratio of 0.5, which corresponds to the cross section of rectangular waveguide at millimeter wavelengths, or we can flatten the cross section a bit to $b/a = 0.3$ and roughly double the value of α/k_0 . For either choice, the value of β/k_0 remains about the same, with the angle of the beam maximum going from 52° to 54° . For the next few curves, we choose $b/a = 0.3$ so that we can achieve a higher α/k_0 value; later, in Sec. 2, we select $b/a = 0.5$ to correspond to a simpler transition from rectangular waveguide, which would be used as the feed mechanism.

The variation of β/k_0 and α/k_0 with stub guide width a' is shown in Fig. 7.6. For these curves, the center of the stub guide is maintained constant, i.e., the offset position is constant. The two vertical dashed lines in the inset indicate the guide mid-plane and the stub mid-plane; it is seen that the shift between them is quite small, actually equal to $0.05a$, consistent with the maximum value of a'/a being 0.9. If we call the shift s , then

$$s = \frac{a}{2} - \frac{a'}{2} - d \quad (7.13)$$

We also note that as a' changes, d does also.

From Fig. 7.6 we observe that β/k_0 changes little with a'/a , particularly for wider stub guides. On the other hand, α/k_0 varies quite significantly. We would like to find an operating range over which β/k_0 remains constant while α/k_0 varies strongly, so that the beam width can be changed without shifting the angle of the beam maximum.

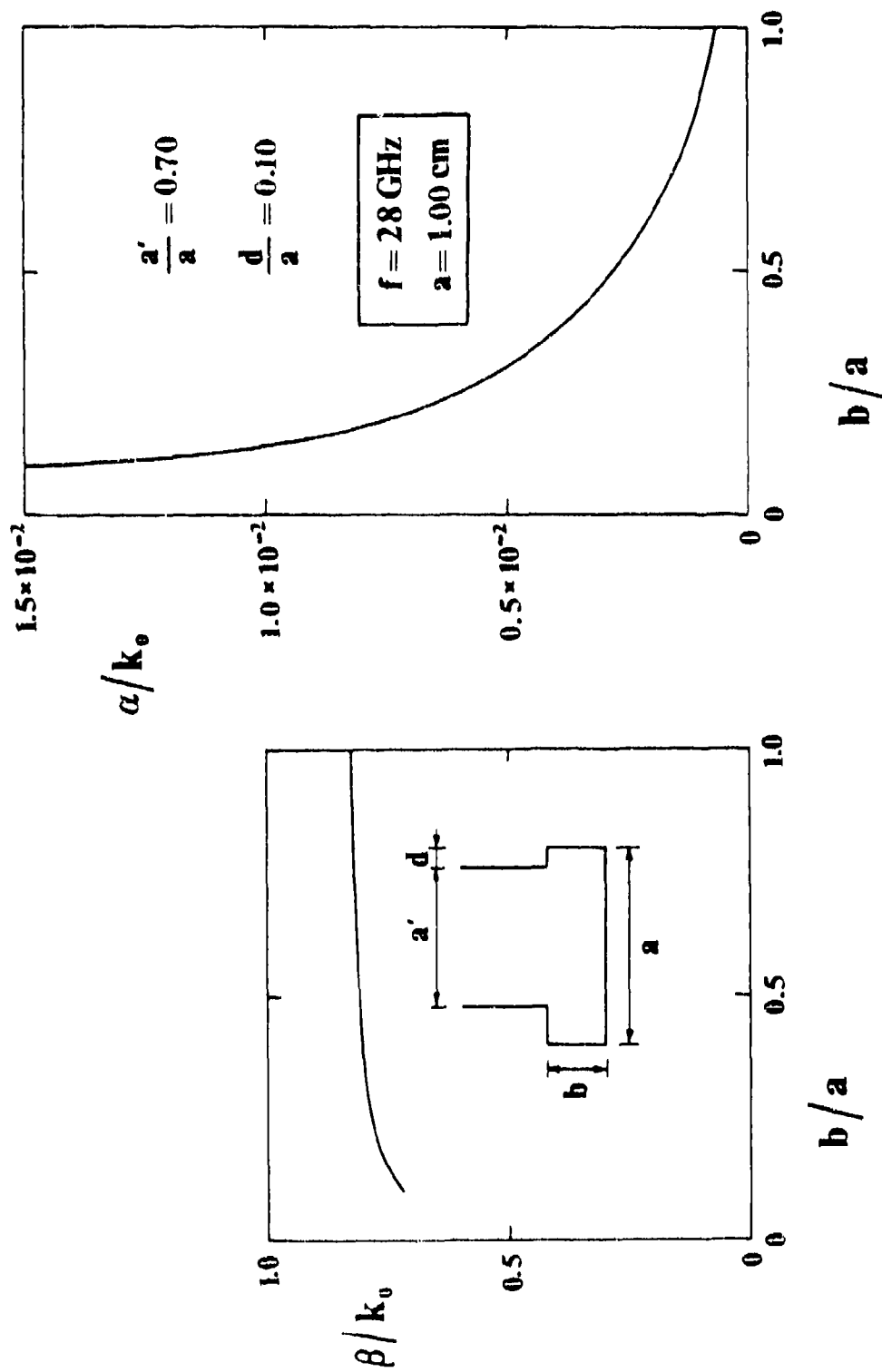


Fig. 7.5 Behavior of the normalized phase and leakage constants as a function of aspect ratio b/a .

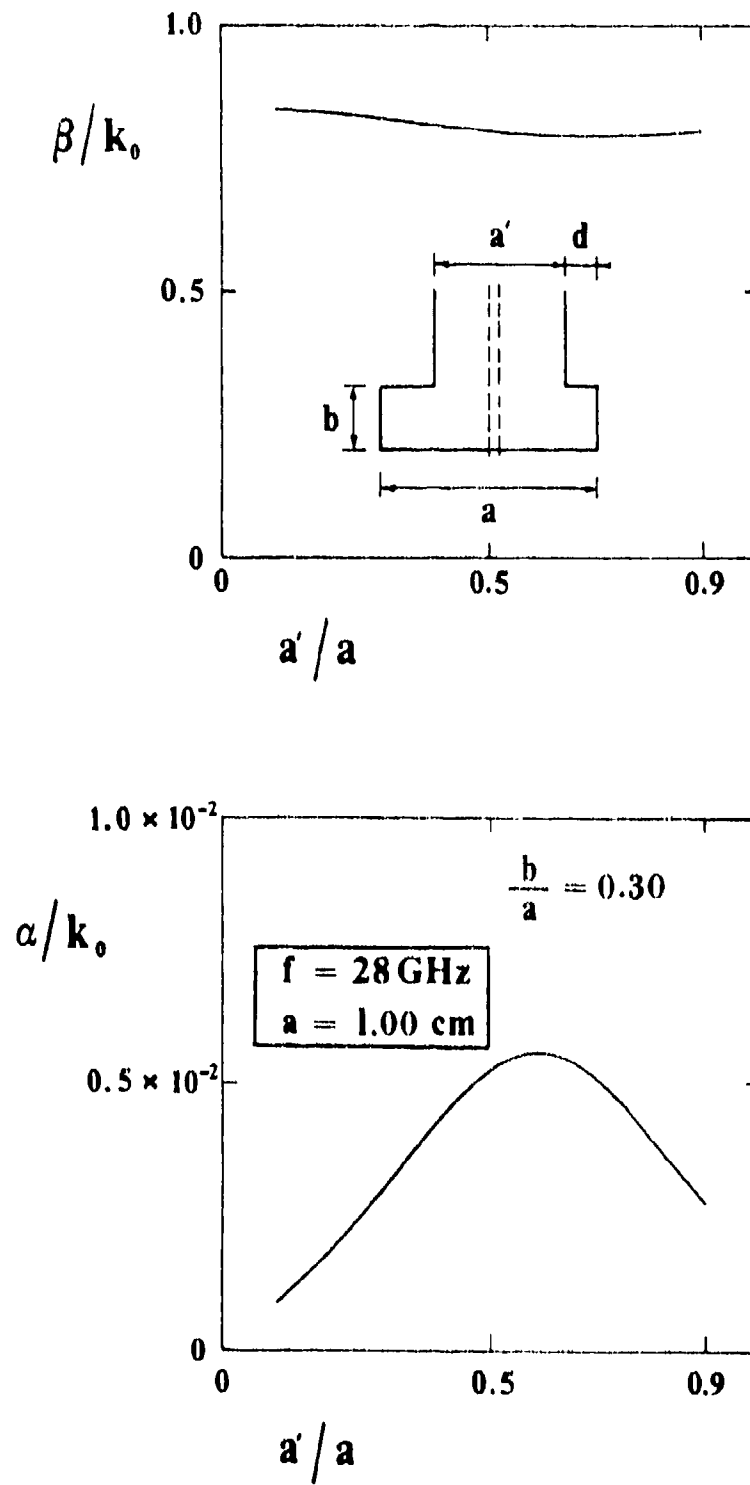


Fig. 7.6 Behavior of the normalized phase and leakage constants as a function of stub guide width a' .

Such a range can be identified here, with a'/a moving from about 0.55 to 0.85, over which β/k_o varies very little (less than 0.01, corresponding to less than a 1° shift in the beam angle) while α/k_o changes by almost 70%.

The remaining parameter to vary is d , while maintaining stub width a' constant. When $d = 0$, the stub is all the way to the end, and the leakage rate α is maximum (and very large); when the stub is centered, the structure becomes symmetrical and $\alpha = 0$. Thus we would expect α/k_o to vary over a very large range of values as we change d from one extreme to the other. We indeed find such behavior in both Figs. 7.7 and 7.8, for α/k_o vs. d ; Fig. 7.7 corresponds to a relatively wide stub ($a'/a = 0.7$), whereas Fig. 7.8 employs a narrower stub ($a'/a = 0.4$). The maximum values of α/k_o in these two figures are about 3.5×10^{-2} for the wider stub and about 8.7×10^{-2} for the narrower stub, corresponding to beam widths $\Delta\theta$ approximately equal to 17° and over 40° , respectively. However, one generally does not wish to have such wide beams, and beam widths ranging between those values and zero are readily achievable by simply choosing the appropriate value of d . One may note, in fact, that for the curve of α/k_o vs. b/a in Fig. 7.5, the parameters chosen were $a'/a = 0.70$ and $d/a = 0.10$. From Fig. 7.7 we see that $d/a = 0.10$ corresponds to a point rather far down on the curve (yielding a beam width of 2.3°). The maximum values for α/k_o would also be reduced if the frequency were raised somewhat.

We next examine the curves of β/k_o vs. d/a in Figs. 7.7 and 7.8 to determine how flat they are. If they remain relatively constant as d/a is changed, then the beam angle stays the same as the beam width is adjusted. In addition, the antenna's aperture distribution can be tapered to correspond to some desired side-lobe level. We note from these two figures that β/k_o changes very little, with most of the change occurring for the larger values of α/k_o . For Fig. 7.7, for the wider stub, the beam angle varies only from 52.0° to 52.7° as d/a is changed from 0.15 to 0.075. (This information comes from the computer printout, not from reading the curve.)

We thus find that the desirable property we seek, namely, that β/k_o can be maintained the same while α/k_o changes strongly, can be furnished in two ways: by varying a'/a or by changing d/a . One method will be superior to the other depending on the parameter values. It is also clear that by adjusting the value of d/a almost any desired value of beam width can be obtained.

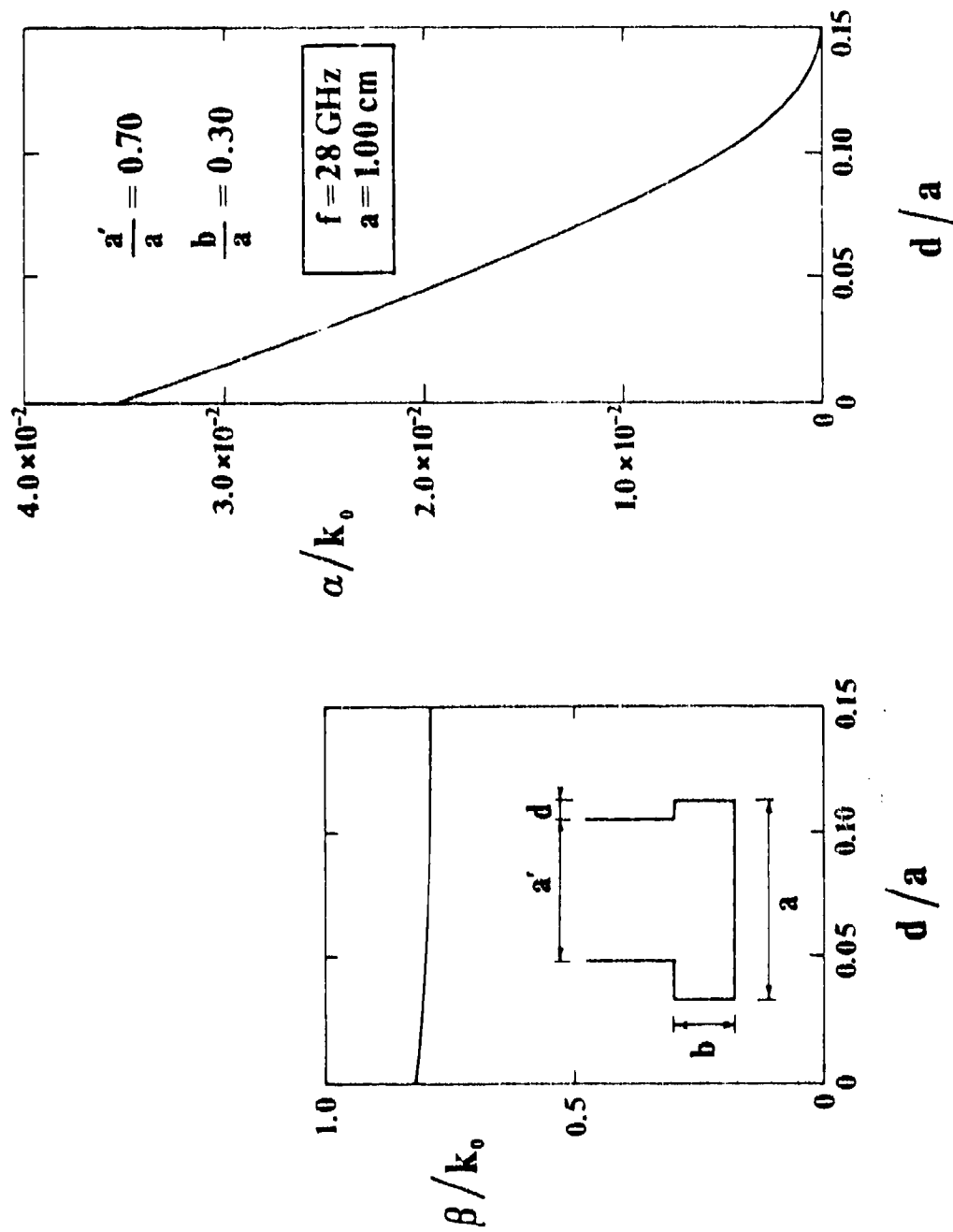


Fig. 7.7 Behavior of the normalized phase and leakage constants as a function of off-center shift of the stub guide, for a relatively wide stub guide ($a'/a = 0.70$), showing the wide range of α/k_0 that can be obtained.

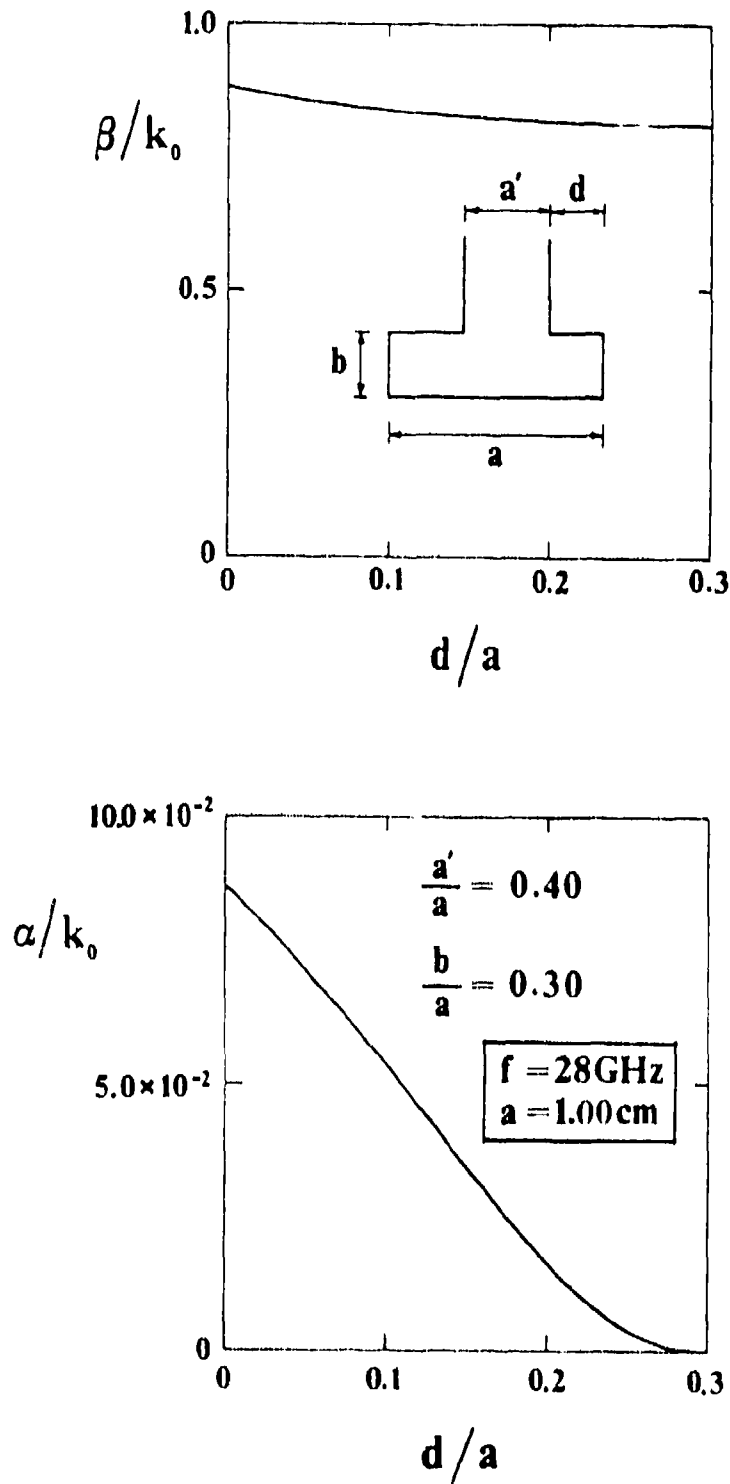


Fig. 7.8 Same as Fig. 7.7, except for a narrower stub guide ($a'/a = 0.40$).

2. Aspect Ratio Equal to That of Rectangular Waveguide

The offset-groove-guide antenna not only resembles rectangular waveguide with an offset open stub on top, but it turns out that rectangular waveguide offers a very effective and convenient way to feed the antenna. This method is used in the experiment described in Chap. VIII. Because of this practical feature, additional numerical results were obtained for a structure with an aspect ratio b/a equal to 0.5, at a frequency of 50 GHz.

The behavior of β/k_0 and α/k_0 as a function of stub offset, measured as d/a , is shown in Fig. 7.9 for a stub guide width equal to 0.50. The precise cross-section shape is indicated in the inset. As expected, the values of α/k_0 range from zero, when the stub is centered, to a maximum value when the stub is at one end. This maximum value for α/k_0 is about 0.077, which, for the value of $\beta/k_0 = 0.76$, corresponds to a radiation pattern beam width of about 33° , when the antenna length is taken to radiate 90% of the incident power, as is customary. As before, it is clear that beam widths can be readily achieved that range from this very large value (33°) down to widths that are as narrow as one pleases.

What is particularly interesting now is the behavior of β/k_0 . This quantity is now *much flatter* than we found earlier, in Figs. 7.7 or 7.8. In fact, for the range of d/a from 0.15 to 0.25 the value of β/k_0 is so flat that the corresponding beam angle, which is about 48° from broadside, is constant to within about 0.1° . The value of α/k_0 at $d/a = 0.15$ is 0.015, which corresponds to a beam width of 6.4° , so that the beam width can be varied over quite a large range while the beam angle stays very constant.

In order to achieve low sidelobes in the radiation pattern, it is necessary to *taper* the aperture distribution of the leaky-wave antenna, which means that the value of α/k_0 must be slowly varied in a specified way along the antenna length. At the same time, the value of β/k_0 must remain constant along the length so that all sections of the antenna radiate at the same angle. We find above from the behavior of β/k_0 and α/k_0 in Fig. 7.9 that their variation with d/a is precisely what we need in order to achieve whatever taper we require according to some desired sidelobe specification.

The variation with stub guide width a' is illustrated in Figs. 7.10 and 7.11 for two different values of d/a . The behavior is qualitatively similar to that seen in Fig. 7.6, but there are deviations in two ways. First, the offset (the quantity s in (7.13)) is larger here, so that the values of α/k_0 are much larger. Second, the values of β/k_0 are still fairly flat, but less so than we found in Fig. 7.6. For this set of parameters,

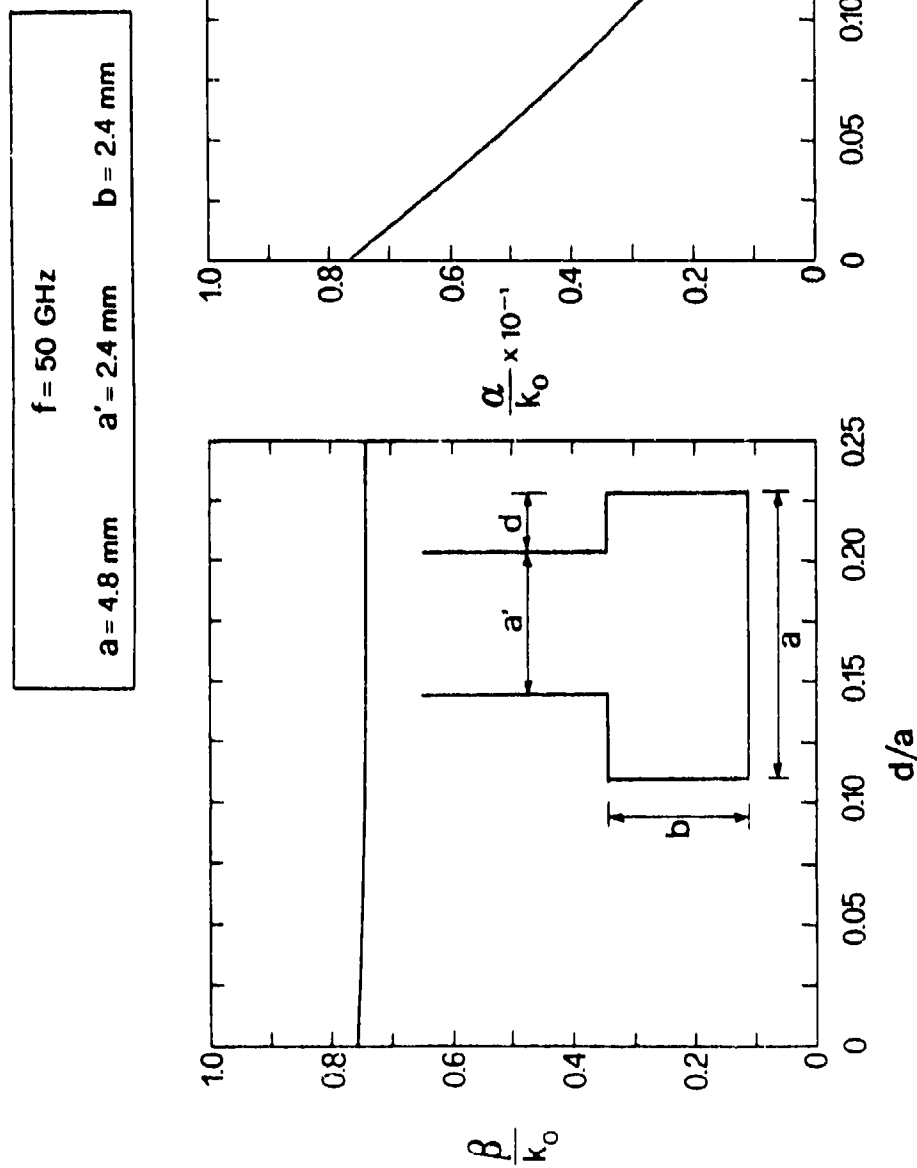


Fig. 7.9 Behavior of the normalized phase and leakage constants as a function of off-center shift of the stub guide, when the aspect ratio is that of rectangular waveguide. Note that very desirable characteristics are present, since β/k_0 remains very flat over most of the range, while α/k_0 varies greatly.

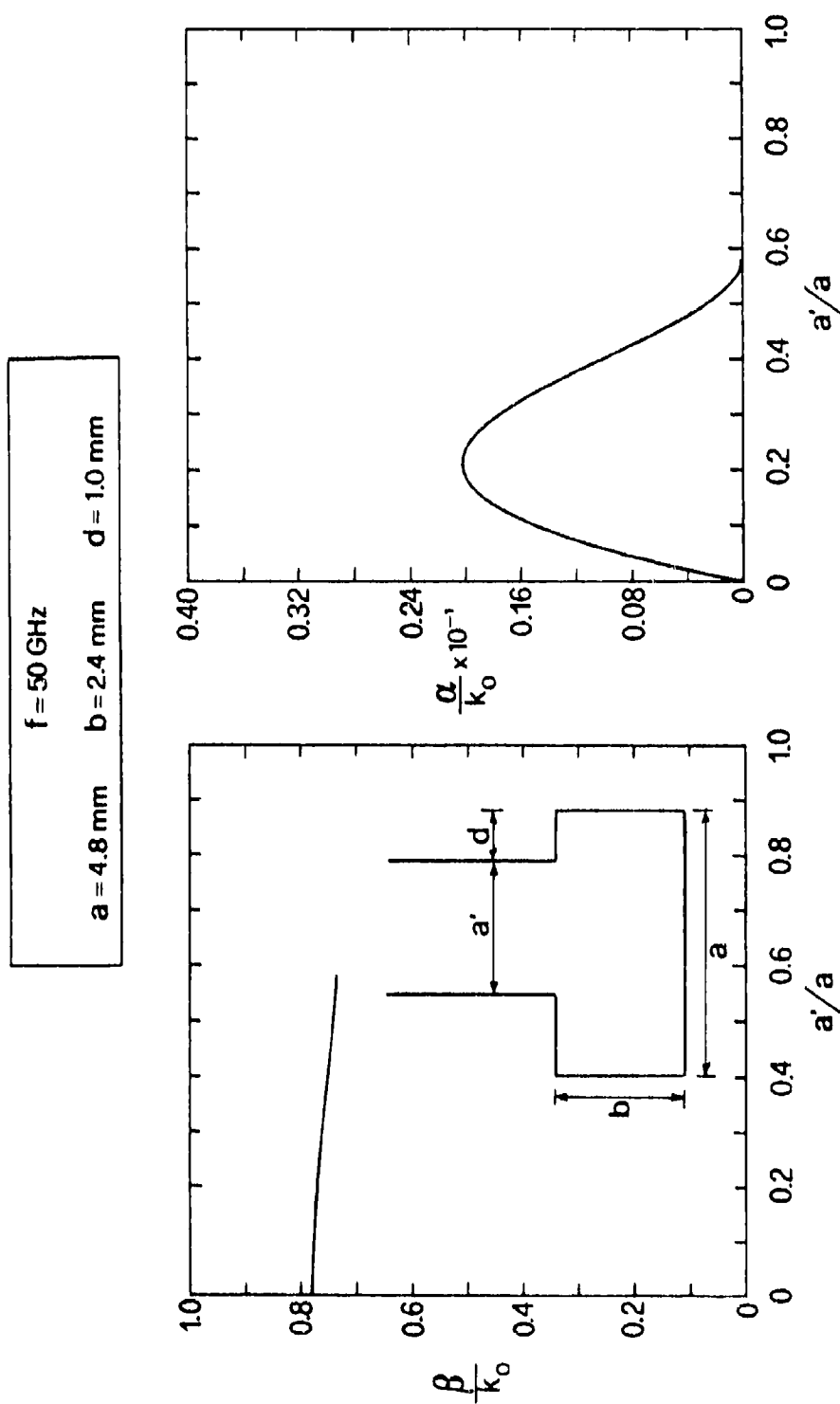


Fig. 7.10 Behavior of the normalized phase and leakage constants as a function of stub guide width a' when the aspect ratio is that of rectangular waveguide.

$f = 50 \text{ GHz}$
 $a = 4.8 \text{ mm}$ $b = 2.4 \text{ mm}$ $d = 0.8 \text{ mm}$

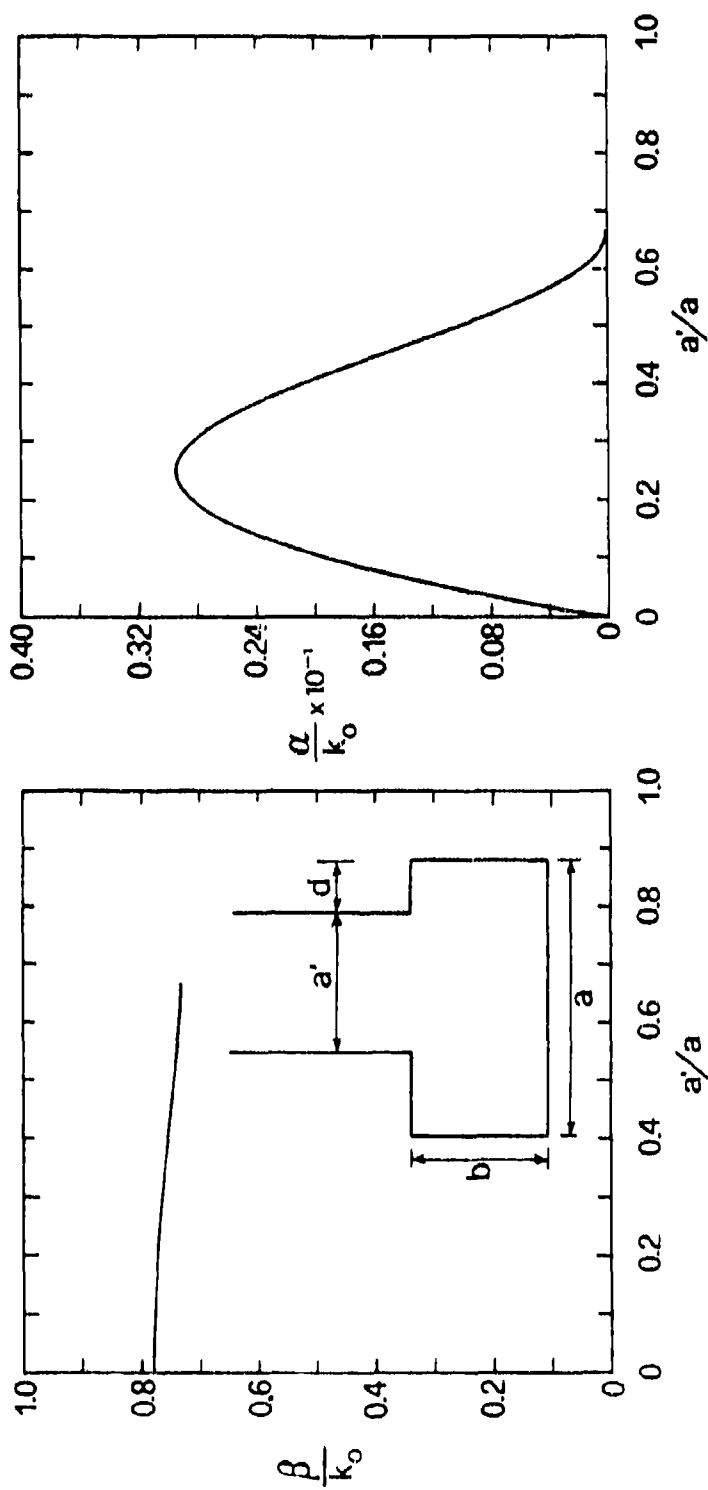


Fig. 7.1i Same as Fig. 7.10, except that the offset is somewhat larger here.

therefore, the variation with d/a is preferable to that with a'/a if one wishes to taper the antenna aperture distribution.

3. Variations with Frequency

For an offset-groove-guide antenna with an aspect ratio equal to that of rectangular waveguide, but with only a small offset so that the leakage rate is not very high, we present in Fig. 7.12 the behavior of β/k_o and α/k_o over a very wide range of frequencies. The explanation of the interesting behavior, particularly below cutoff, contains some novel features which, it is believed, are discussed here for the first time.

The curves for β/k_o and α/k_o are divided into two basic parts, for the region above cutoff and the one below cutoff. Above cutoff, which corresponds roughly to $f = 33$ GHz, the behavior is as expected, with β/k_o following a standard curve shape and with α/k_o decreasing monotonically with increasing frequency.

The transverse wavenumber k_t is equal to k_x in the main guide region, which in turn is equal to k_y in the stub guide region (see Fig. 7.4). If the stub guide were closed and the leakage were absent, k_x would be real and equal to π/a . In the actual offset-groove-guide antenna, k_t is *complex*, with a predominantly real part. For the parameter values given in Fig. 7.12, we calculate that

$$k_t = \text{Re } k_t + j \text{Im } k_t = 0.702 \text{ mm}^{-1} + j 3.00 \times 10^{-3} \text{ mm}^{-1} \quad (7.14)$$

and is *independent of frequency* since only one medium (air) is present. For comparison, $\pi/a = 0.654 \text{ mm}^{-1}$. The longitudinal wavenumber k_z is related to the transverse wavenumber k_t by (7.12), but we rewrite it here as

$$k_z^2 = (\beta - j\alpha)^2 = k_o^2 - k_t^2 \quad (7.15)$$

The variation of β/k_o with frequency above cutoff in Fig. 7.12 follows readily from (7.15) since α and $\text{Im } k_t$ are both relatively small.

The behavior *below* cutoff is not generally known. First of all, β/k_o does not approach zero or a constant as the frequency is reduced far below cutoff, as is generally believed. It turns up again, and in fact exceeds unity as the frequency becomes very low. If the leakage were stronger, the minimum value of β/k_o would be larger, the turn up faster, and the value unity would be reached at a higher frequency. (Similar behavior is shown for microstrip higher modes, which are leaky near cutoff and below it, in Chap. IX, in Figs. 9.19 and 9.21. The effects are much more dramatic there.)

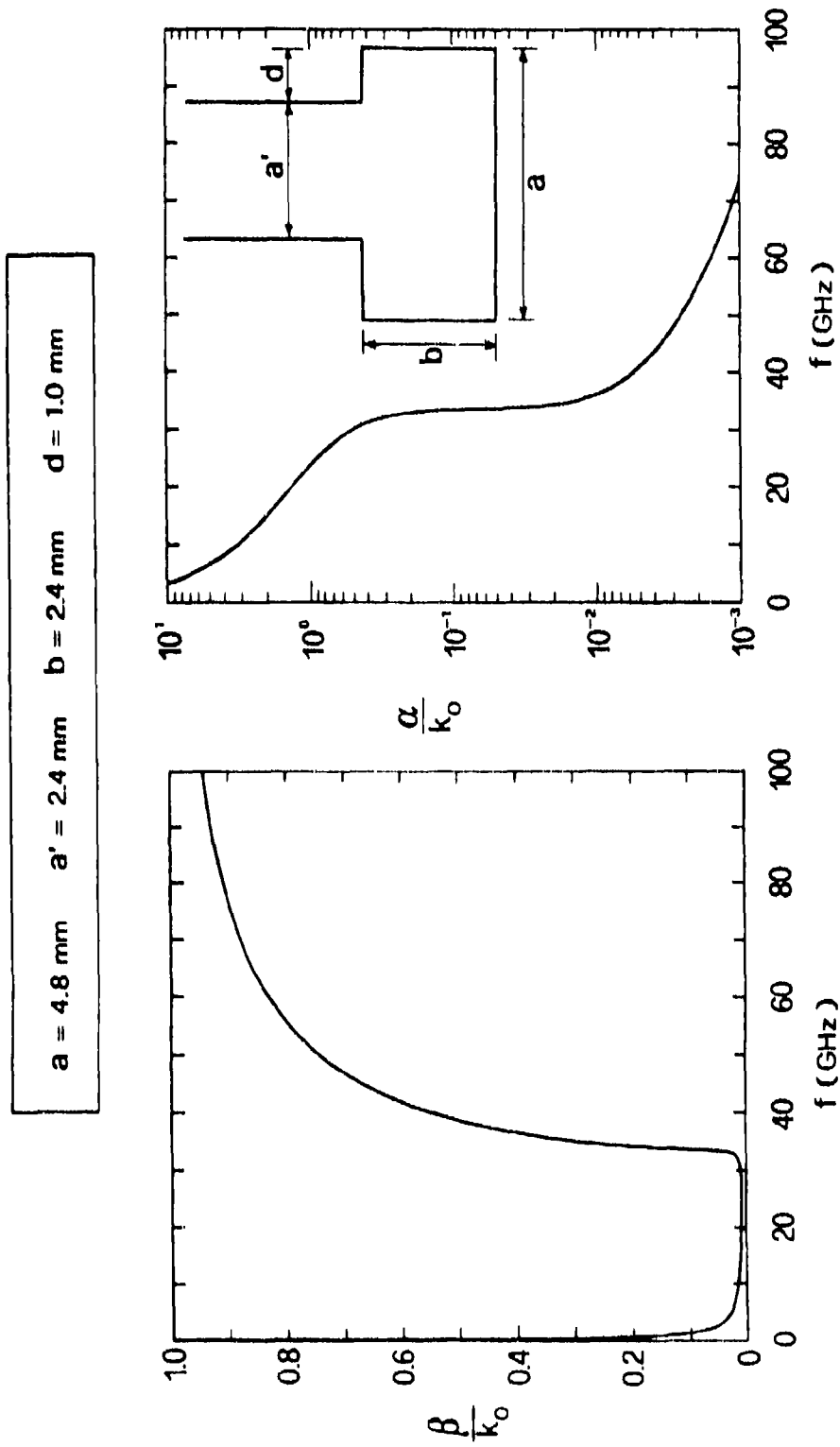


Fig. 7.12 The behavior of the normalized phase and leakage constants as a function of frequency, both above and below cutoff.

The explanation for the turn up in the value of β/k_o at low frequencies is that β itself approaches a constant as the frequency approaches zero, as shown in Fig. 7.13 (but not very clearly because the leakage is very low). Thus, if β approaches a constant, then β/k_o must increase without limit as the frequency goes to zero. The value of β/k_o will certainly exceed unity, therefore, but the solution has no meaning in that range. It is shown in Chap. IX, by employing the steepest-descent plane, that when $\beta/k_o > 1$ the pole representing the leaky wave solution is no longer captured by the deformation of the original path into the steepest-descent path. Physically, this means that the leaky wave is no longer a part of the total field for any angle of observation. For this reason, in Fig. 7.12 and in all other corresponding curves, we stop the solution at $\beta/k_o = 1$ and omit any values at lower frequencies.

The behavior of α/k_o in Figs. 7.12 and 7.13 is also different above cutoff and below it. Above cutoff, the value of α represents the leakage of power. Below cutoff, α represents primarily the *reactive decay* of the field, although some leakage of power also contributes a little to its value. Therefore, the value of α increases substantially once the leaky mode goes below cutoff. In addition, we see from Fig. 7.13 that α approaches a constant as the frequency approaches zero. The explanation for this feature readily follows from relation (7.15).

Expanding (7.15) into its real and imaginary parts, and using (7.14), we find

$$(\beta^2 - \alpha^2) = k_o^2 - [(\text{Re } k_l)^2 - (\text{Im } k_l)^2] \quad (7.16)$$

from the real parts, and

$$\alpha\beta = (\text{Re } k_l)(\text{Im } k_l) \quad (7.17)$$

from the imaginary parts. From (7.14) we see that $\text{Re } k_l \gg \text{Im } k_l$, so that (7.16) reduces slightly to

$$\beta^2 - \alpha^2 \approx k_o^2 - (\text{Re } k_l)^2 \quad (7.18)$$

Much below cutoff, it is clear that $\beta^2 \ll \alpha^2$, and (7.18) may be rewritten as

$$\alpha = [(\text{Re } k_l)^2 - k_o^2]^{1/2} \quad (7.19)$$

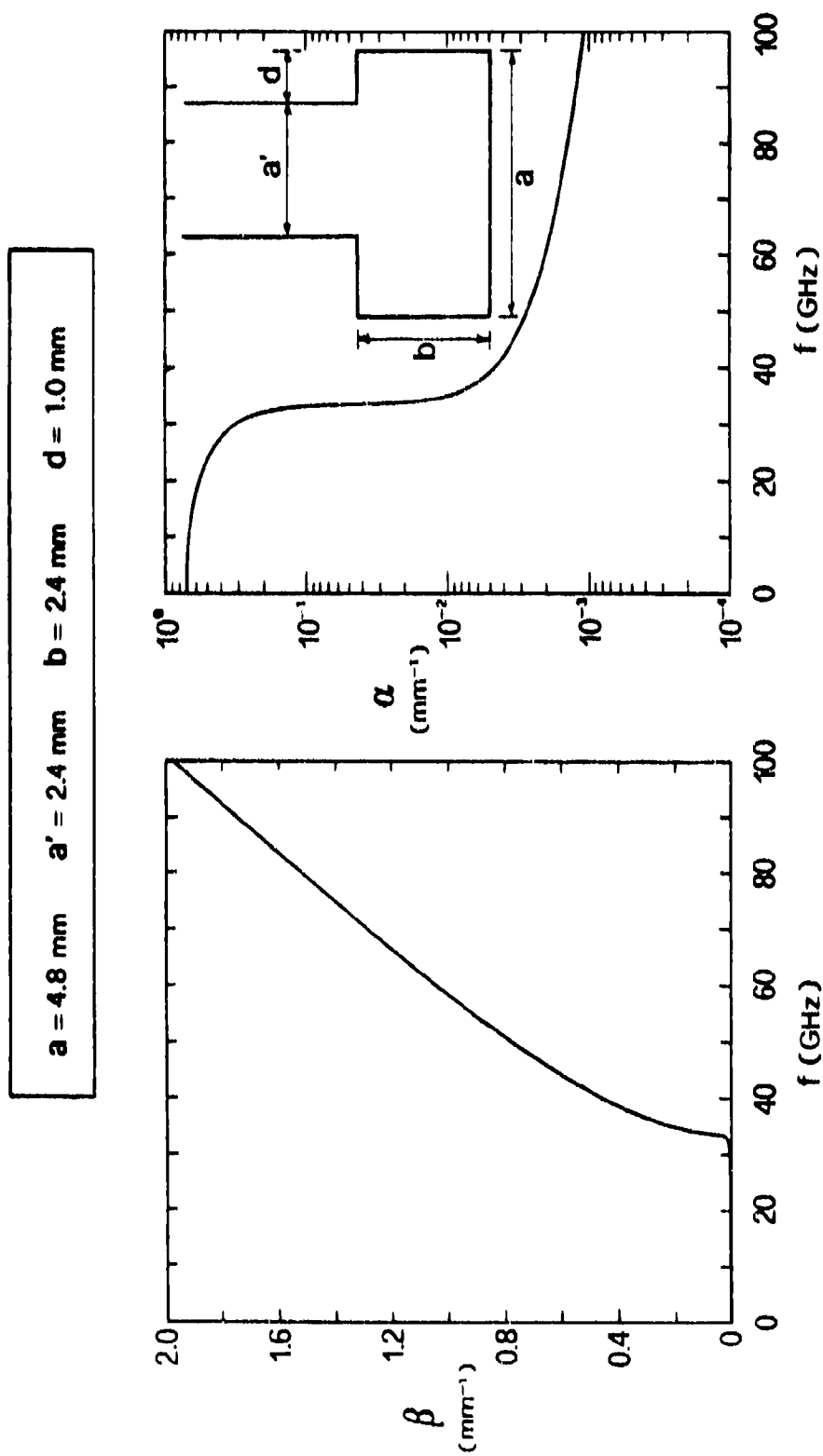


Fig. 7.13 The behavior of the phase constant β and leakage constant α vs. frequency, both above and below cutoff.

so that

$$\alpha \rightarrow \text{Re } k_t \quad (7.20)$$

as k_o approaches zero. We thus find that α does indeed approach a constant, and we determine from the curve for α in Fig. 7.13 that its value is 0.70, which agrees with the value of $\text{Re } k_t$ given in (7.14).

From (7.17), we can then assert immediately that β must also become a constant as the frequency approaches zero, consistent with the β curve in Fig. 7.13. We may also observe from (7.17) that the value of β in that limit is equal to that of $\text{Im } k_t$.

From the portions of the curves in Fig. 7.12 *above* cutoff, we may determine the behavior shown in Fig. 7.14. The curve of θ_m , the angle of the maximum of the radiated beam, measured in degrees from the broadside direction, follows directly from relation (2.27) of Chap. II, namely,

$$\sin \theta_m \approx \beta/k_o \quad (7.21)$$

The beam width $\Delta\theta$ is based on selecting a length for the antenna that corresponds to 90% of the power being radiated, and then taking the geometry to be longitudinally uniform (no taper) so that the aperture field is exponentially decaying. Under these conditions an approximate expression for $\Delta\theta$, taken from (2.28) and (2.29), is

$$\Delta\theta \approx \frac{52.1}{(L/\lambda_o) \cos \theta_m} \approx 285 \frac{\alpha/k_o}{\cos \theta_m} \quad (7.22)$$

in degrees.

When only one medium is present in the antenna cross section, the transverse wavenumber k_t is a constant independent of frequency, as in (7.14). It then turns out that when the beam angle θ_m is scanned by varying the frequency the value of beam width $\Delta\theta$ remains constant. This statement is easily proved. We take

$$\cos^2 \theta_m = 1 - \sin^2 \theta_m = 1 - (\beta/k_o)^2$$

from (7.21). Then, when $\alpha^2 \ll \beta^2$, we have from (7.16) that

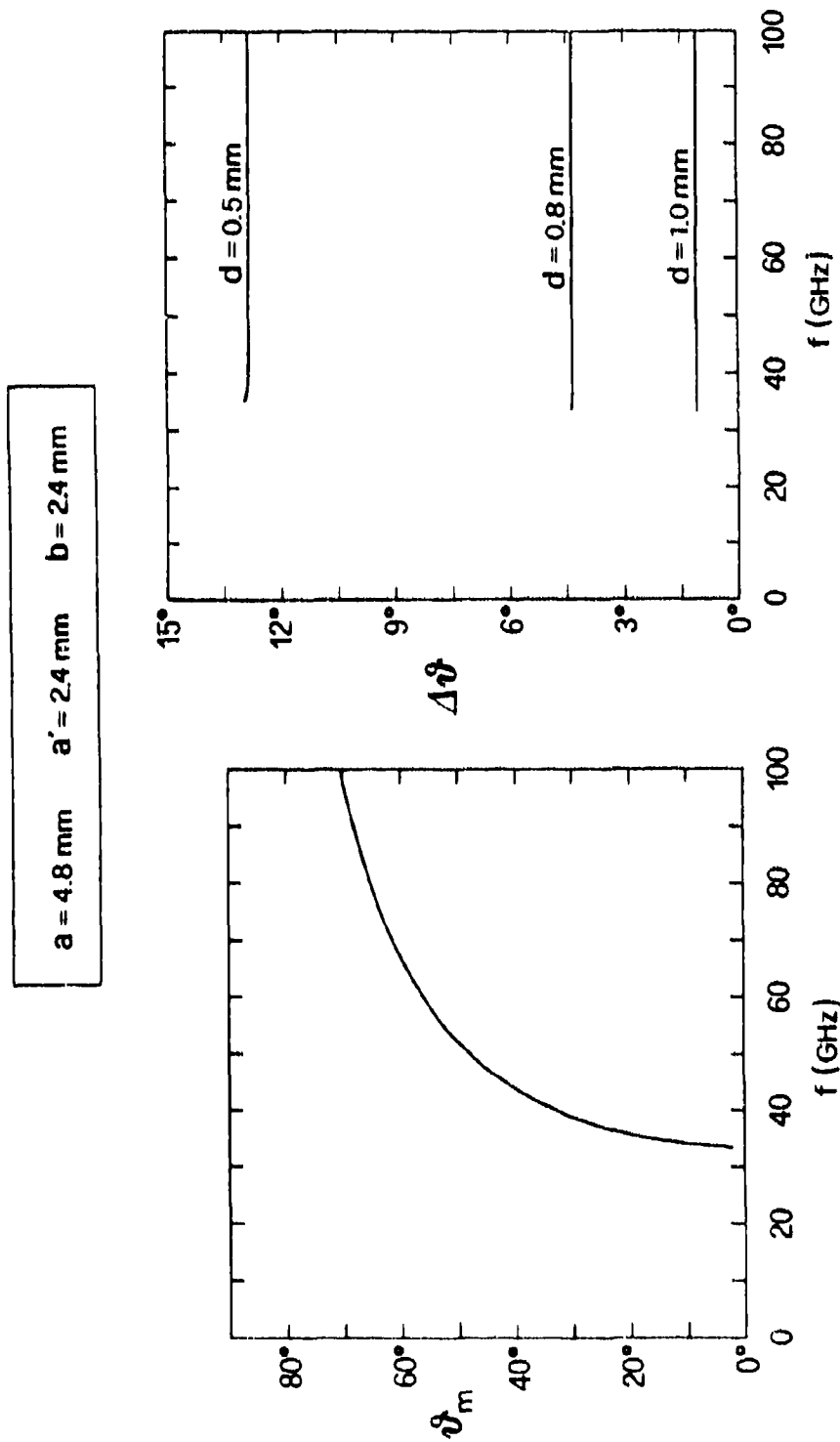


Fig. 7.14 The variations in beam angle θ_m and beam width $\Delta\theta$ of the radiation pattern as a function of frequency. Note the constancy of beam width with frequency scan.

$$1 - (\beta/k_o)^2 = 1 - (1 - (k_t/k_o)^2) = (k_t/k_o)^2$$

so that

$$\cos \theta_m = k_t/k_o \quad (7.23)$$

Substituting (7.23) into the first relation in (7.22) yields

$$\Delta\theta \approx \frac{327}{k_t L} \quad \text{in degrees} \quad (7.24)$$

which is independent of frequency.

The curve for θ_m in Fig. 7.14 is obtained directly from (7.21) and the curve for β/k_o above cutoff in Fig. 7.12. The curves for $\Delta\theta$ are obtained from (7.22) by taking accurate results for α/k_o and β/k_o , for three different values of offcenter shift. It is seen that the beam widths $\Delta\theta$ are *very constant* with frequency, in accordance with expectation from (7.24). This feature is an added advantage of the offset-groove-guide antenna.

C. COMPARISON OF RESULTS WITH AN ALTERNATIVE THEORETICAL APPROACH

In order to check the accuracy of the theoretical approach employed above, numerical calculations were made of some of the same performance properties by using a *totally different* theoretical method. This alternative method of computation is an accurate *mode-matching procedure*.

The mode matching is performed in the *vertical* direction in the offset-groove-guide structure shown at the bottom of Fig. 7.1 or the top of Fig. 7.4. In the upper (stub) waveguide, of narrower width a' , only the TEM mode is above cutoff; in the lower guide of width a , three modes are above cutoff, the TEM mode and the first TE and TM higher modes. The mode matching is set up rigorously, and for most points 100 TE and TM modes are included in the numerical computations. Convergence in the mean-square sense is employed.

We should note that this method is entirely different from the one based on the tee-junction equivalent network, not simply that the mode-matching procedure is basically numerical and the network one is basically analytical. In the network approach, the discontinuity involved is viewed as an E-plane tee; in the mode-matching procedure, it is treated as a transverse discontinuity, a change in guide width. Another major difference is that the network has closed-form expressions for its elements, and is therefore approximate; the mode-matching procedure is asymptotically rigorous.

Since the mode-matching procedure, to be accurate, must include many modes, it is computationally relatively costly. As a result, only three cases were selected with which comparisons were made with the numerical results obtained by means of the dispersion relation (7.11) together with (7.12). Two of these three cases involve the dependence on d/a ; numerical values obtained by the tee-junction transverse equivalent network approach (that is, using dispersion relation (7.11) plus (7.12)) were presented above as Figs. 7.7 and 7.8. The third case is concerned with variations with frequency; the numbers here are new, and they serve to supplement the discussion above on the frequency behavior.

The first comparison is shown in Fig. 7.15, for the behavior of β/k_0 and α/k_0 as a function of d/a , which is a measure of the offset of the stub guide. The dashed lines represent the numerical values that have already been presented in Fig. 7.7, corresponding to a wider stub ($a'/a = 0.7$). The solid lines correspond to numerical values obtained from the accurate mode-matching procedure. It is seen

$a'/a = 0.700$, $b/a = 0.300$, $a = 1.00$ cm, $f = 28.0$ GHz

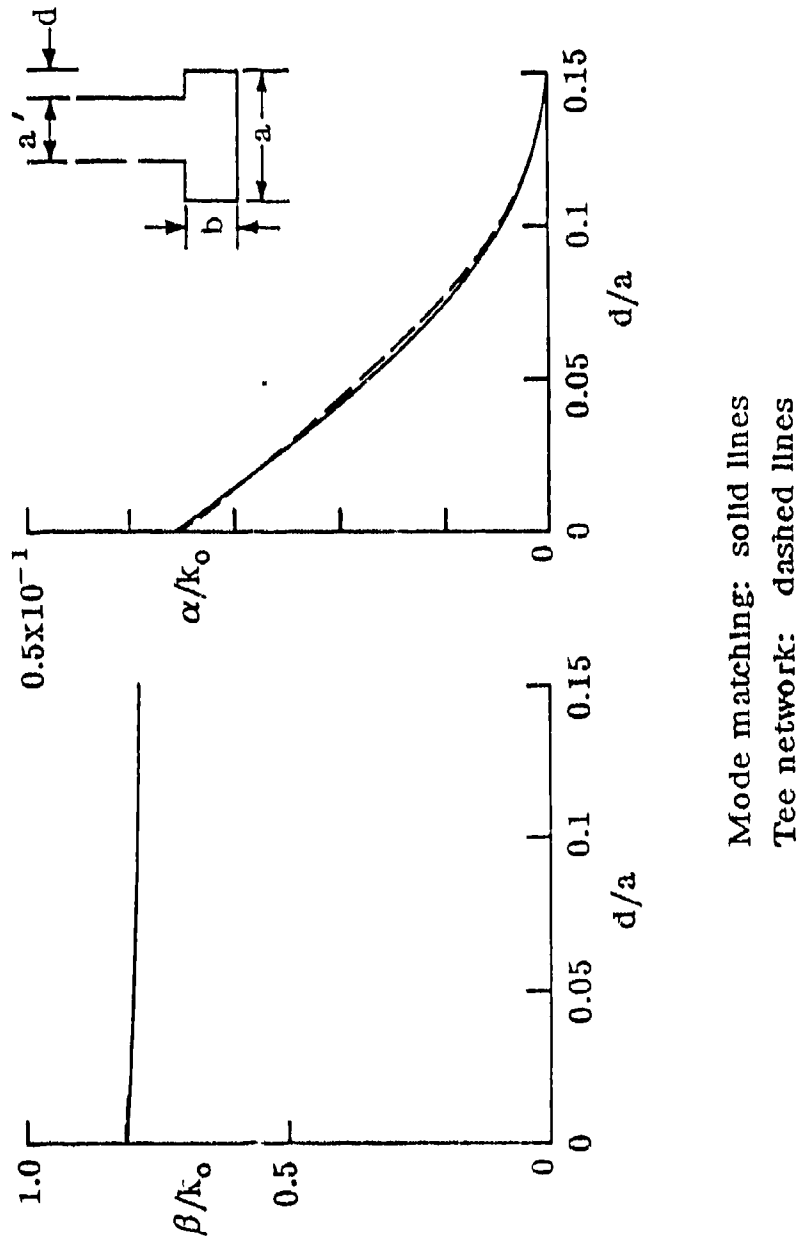


Fig. 7.15 Comparison of numerical results for β/k_0 and α/k_0 vs. d/a when $a'/a = 0.70$, obtained via two completely different theoretical methods. The dashed and solid lines correspond, respectively, to the tee-junction network approach and the mode-matching procedure.

that the agreement is really very good, over the complete range of d/a .

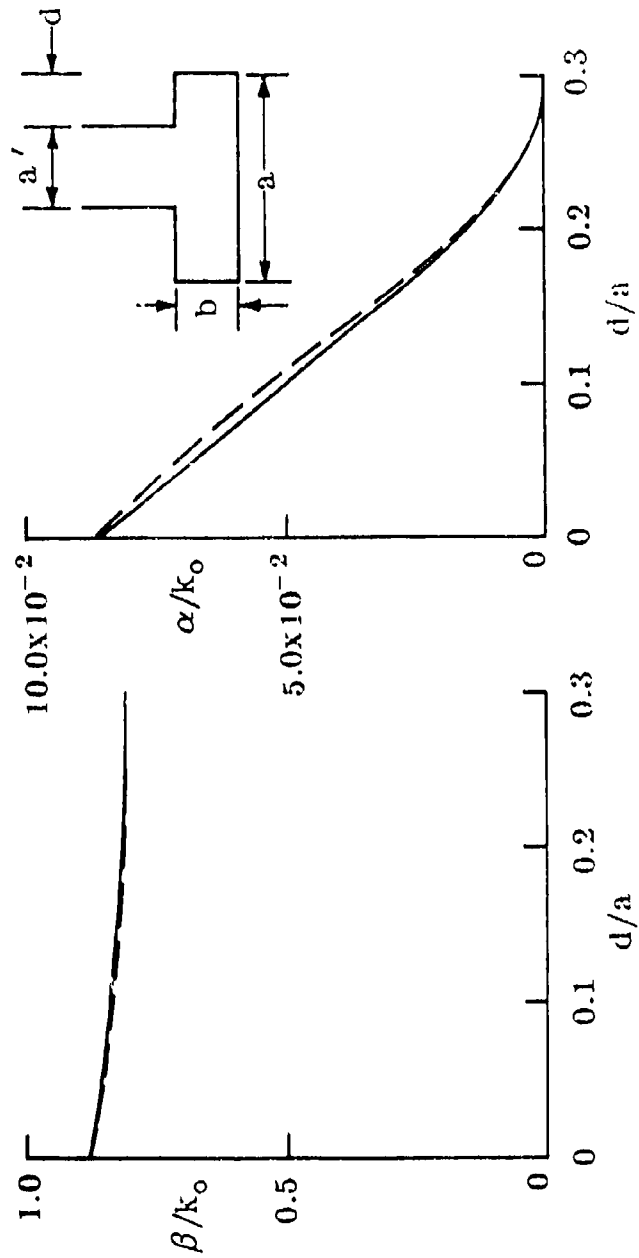
The second comparison, in Fig. 7.16, involves the data that already appear in Fig. 7.8, for a narrower stub guide ($a'/a = 0.4$). Again, the dashed and solid lines represent, respectively, the results computed by means of the tee-junction network and the mode-matching method. Again, the agreement between the respective curves is very close.

The third comparison, shown in Fig. 7.17, concerns the variations of β/k_o and α/k_o over the complete frequency range. These numbers have not been presented before, and the behavior itself will therefore be discussed in a moment. Let us first note the level of agreement between the two methods of calculation; as with the other figures, the dashed and solid lines represent the network and mode-matching approaches, respectively. Again, the agreement is very good over the very wide range of frequencies.

The dimensional values in Fig. 7.17 are different from the ones considered in Fig. 7.12; the aspect ratio is flatter and the guide width is greater here. In general, the leakage rate is significantly higher in Fig. 7.17. As a result, the value of β/k_o is much higher near cutoff and below it, and the turn up occurs sooner and is more pronounced. Although the cutoff occurs at a lower frequency, because dimension a is twice as large, the crossing of the $\beta/k_o = 1$ line at low frequencies occurs at a higher frequency. The larger leakage rate *above* cutoff thus affects in a significant way the behavior of β/k_o *below* cutoff. Such behavior is in agreement with the discussion surrounding relations (7.16) through (7.20).

The principal conclusion from these comparisons, however, is that in all three cases the agreement is very good, so that we may have confidence in the validity of our numerical results and in the reliability of both of the theoretical approaches.

$a'/a = 0.400$, $b/a = 0.300$, $a = 1.00$ cm, $f = 28.0$ GHz



Mode matching: solid lines
Tee network: dashed lines

Fig. 7.16 Same as Fig. 7.15, except that $a'/a = 0.4$.

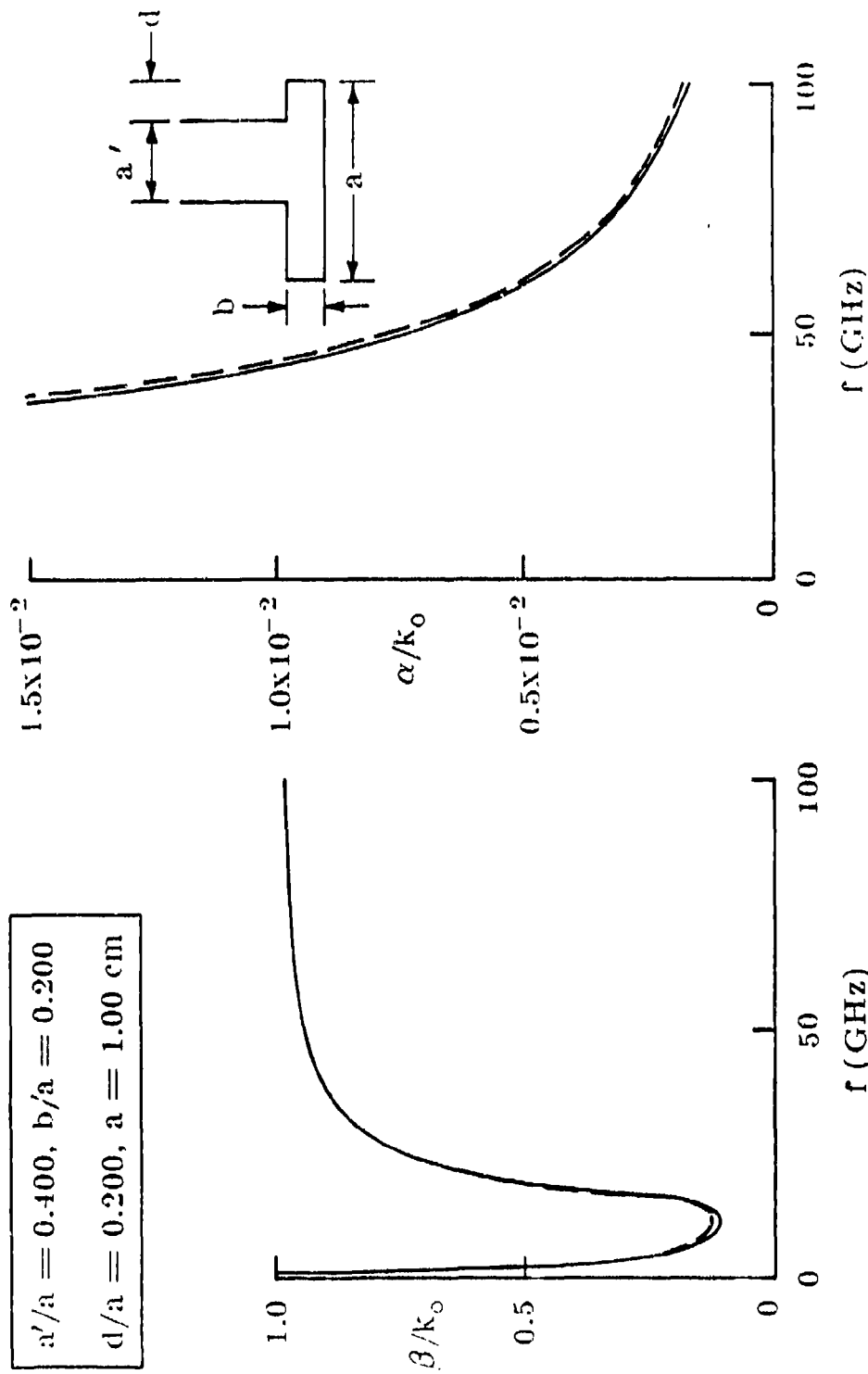


Fig. 7.17 Comparison of numerical results for β/k_0 and α/k_0 vs. frequency obtained via two completely different theoretical methods. The dashed and solid lines correspond, respectively, to the tee-junction network approach and the mode-matching procedure. The behavior for β/k_0 should be compared with that appearing in Fig. 7.12, where the leakage rate is lower.

D. EFFECTS DUE TO FINITE STUB LENGTH

A practical offset-groove-guide antenna structure must of course have a stub guide of finite length. The results above were computed for an infinite stub length because, in part, the computations are simpler for that case, but primarily because the basic performance behavior remains the same when the stub guide is of finite length, as long as one avoids the exotic interactions discussed below.

This section begins with the modifications in the transverse equivalent network that are necessary to take into account the finite, rather than infinite, length of the stub guide. The change in the dispersion relation is also derived. From the modified dispersion relation, we then present numerical results for the various new effects introduced by the finite stub length.

The first effect caused by the finite stub length is the mild *standing wave* that is produced because of the mismatch introduced by the radiating open end. The standing wave exists in the stub guide between the radiating open end and the junction between the stub guide and the main guide; therefore, as the stub guide length is varied, the values of β/k_0 and α/k_0 would be expected to undergo a periodic modification. That is precisely what is found when the leakage rate is low, with β/k_0 being affected very little if at all, and with α/k_0 enduring a cyclical variation in value. When we are careful (to be defined later) this effect is essentially all that we need to take into account, even for much larger values of leakage constant.

When the leakage rate is large, and for larger values of stub length, some exotic interactions are produced. They are due to *coupling* between the desired leaky mode and another leaky mode, which was initially unanticipated. That additional leaky mode is a modification of the "channel-guide" mode that was known about 30 years ago, and which does not exist when the stub length is infinite. The coupling between these two leaky modes occurs at the discontinuities arising at the radiating open end and the step junction between the stub and main guides. Furthermore, the coupling effects emerge automatically from our theoretical analyses, whether we employ the tee network approach or the mode-matching procedure (see Sec. C); in addition, the numerical values and all the qualitative effects computed via the two methods agree well with each other.

These effects were first discovered in connection with the asymmetric leaky-wave NRD guide antenna discussed in Chap. III, but we are now convinced that they are universal to all leaky-wave structures that possess a finite stub length. For this reason, we have studied these effects here in greater detail, as a model for what to expect in

other structures.

There is also a novel feature here in that the interactions involve the coupling between two *leaky (complex)* modes, so that the modes will not couple unless *both* their β and α values are the same. That requirement has probably served to make such coupling relatively rare. The manner in which the coupling manifests itself, particularly for the α/k_0 values, is therefore of interest in itself, and represents a canonical framework within which such coupling can be examined and understood.

In the material below, we describe the qualitative features of the coupling and also present detailed numerical results for several cases, including the variations of β/k_0 and α/k_0 as a function of stub length, stub offset, and frequency. Of particular importance is the interpretation of complicated data and the consequent identification of the desired mode. In addition, we draw conclusions with respect to how best to avoid these exotic coupling effects, or, if unavoidable, how to work around them.

1. Modification of the Dispersion Relation

As mentioned above, the transverse equivalent network in Fig. 7.4 and the dispersion relation (7.11) that follows from it have assumed that the stub length is infinite. When the stub length becomes finite, a *radiating open end* is produced for which we require an equivalent network representation. An exactly similar representation was required when the stub length was made finite in the case of the L-shaped antenna in Chap. VI. A sketch of the radiating open end, and an equivalent network representation for it, were given in Chap. VI as Fig. 6.6. Rigorous expressions for the elements G_R and B_R in this network, where the subscript R signifies "radiating," are available from the Waveguide Handbook [8], Sec. 4.6a, pp. 179-183, and are presented in relations (6.23), (6.24) and (6.25), after making the appropriate substitutions in notation.

The transverse equivalent network in Fig. 7.4 now needs to be modified to take into account the finite stub length c . We have only to make the length of the (vertical) transmission line representing the stub guide equal to c , and to terminate that line by the admittance $G_R + jB_R$. From this modified network we may readily obtain the appropriately modified dispersion relation. Relation (7.6) for Y_{up} now becomes

$$Y_{up} = \frac{1}{n_{cs}^2} Y_{iR} \quad (7.25)$$

where

$$\frac{Y_{iR}}{Y_o} = \frac{j + \left(\frac{G_R}{Y_o} + j \frac{B_R}{Y_o}\right) \cot k_y c}{\cot k_y c + j \left(\frac{G_R}{Y_o} + j \frac{B_R}{Y_o}\right)} \quad (7.26)$$

On use of (7.7) through (7.10), we find that dispersion relation (7.11) is now replaced by

$$\frac{1}{n_{cs}^2} \frac{Y_{iR}}{Y_o} + j \frac{B_L}{Y_o} + j \frac{\left[\frac{B_a}{Y_o} - \cot k_x \left(\frac{a'}{2} + d \right) \right] \left[\frac{B_a}{Y_o} - \cot k_x \left(\frac{a'}{2} + d' \right) \right]}{2 \frac{B_a}{Y_o} - \left[\cot k_x \left(\frac{a'}{2} + d \right) + \cot k_x \left(\frac{a'}{2} + d' \right) \right]} = 0 \quad (7.27)$$

where Y_{iR}/Y_o is given above by (7.26), and the elements B_a/Y_o , n_{cs} and B_L/Y_o are given by expressions (7.1) through (7.5). Both wavenumbers k_x and k_y now appear in (7.27), but we recognize that they are equal to each other, and that they are related to k_z ($= \beta - j\alpha$) by (7.12), as before.

Before we examine the numerical results, we should recall why we need the stub guide at all. It is to eliminate the vertically polarized electric field at the radiating open end, so that we are left with pure horizontal polarization in the radiated power. The vertical electric field arises from the mode configuration in the main guide of width a , which is above cutoff there but is below cutoff in the narrower stub guide of width a' . That modal field, associated with the $n = 1$ mode in the stub guide, decays exponentially away from the main guide; the amount of cross-polarized power thus depends on the decay rate of that mode and the length of the stub guide.

To determine the minimum length required in order to effectively, according to some criterion, eliminate the cross-polarized power, we first calculate the decay rate of the $n = 1$ mode in the stub guide. It is given by

$$k_{y1}^2 = k_o^2 - (\pi/a')^2 - k_z^2 \quad (7.28)$$

Taking $\alpha^2 \ll \beta^2$, (7.28) becomes

$$\frac{|k_{y1}|}{k_o} = \left[\left(\frac{\lambda_o}{2a'} \right)^2 + \left(\frac{\beta}{k_o} \right)^2 - 1 \right]^{1/2} \quad (7.29)$$

The power decay is then governed by

$$e^{-2|k_{y1}|c} = e^{-\frac{|k_{y1}|}{k_o} 4\pi \frac{c}{\lambda_o}} \quad (7.30)$$

For the frequency and the dimensions used in most of the curves below, we have $\lambda_o = 6.0$ mm, $a' = 2.4$ mm, and $\beta/k_o \approx 0.73$. Taking those values, (7.29) yields a decay rate $|k_{y1}|/k_o = 1.047$, which is reasonably large. To find the amount of cross-polarized power remaining at the radiating open end, expressed in dB down from its value at the junction between the main and stub guides (at $c = 0$), we take

$$8.686 \frac{|k_{y1}|}{k_o} 2\pi \frac{c}{\lambda_o} \quad (7.31)$$

and we find the following dB values corresponding to several lengths c/λ_o :

c/λ_o	0.3	0.4	0.5	0.7	1.0
dB down	17.1	22.9	28.6	40.0	57.1

From this short table we see that length c can certainly be less than a wavelength long. The length to choose depends on the criterion with respect to the level of cross polarization. For $c/\lambda_o = 0.4$, c would be equal to a' ; for many purposes, a reduction of 22.9 dB would be sufficient. It should also be realized that a narrower stub guide produces a faster decay rate and therefore a shorter stub length c .

2. Coupling with Another Leaky Mode

In the introduction to this section it was stated that exotic and initially unexpected interactions were found when the leakage rate was large and particularly when the stub length c was increased. These interactions, it said, were due to coupling between the desired leaky mode and another leaky mode, a modification of the channel-guide (CG) mode. We shall not repeat here the other remarks made in that introductory portion, but go directly to the nature of that leaky mode, and show how it relates to the desired mode, which we shall call the offset-groove-guide (OGG) leaky mode.

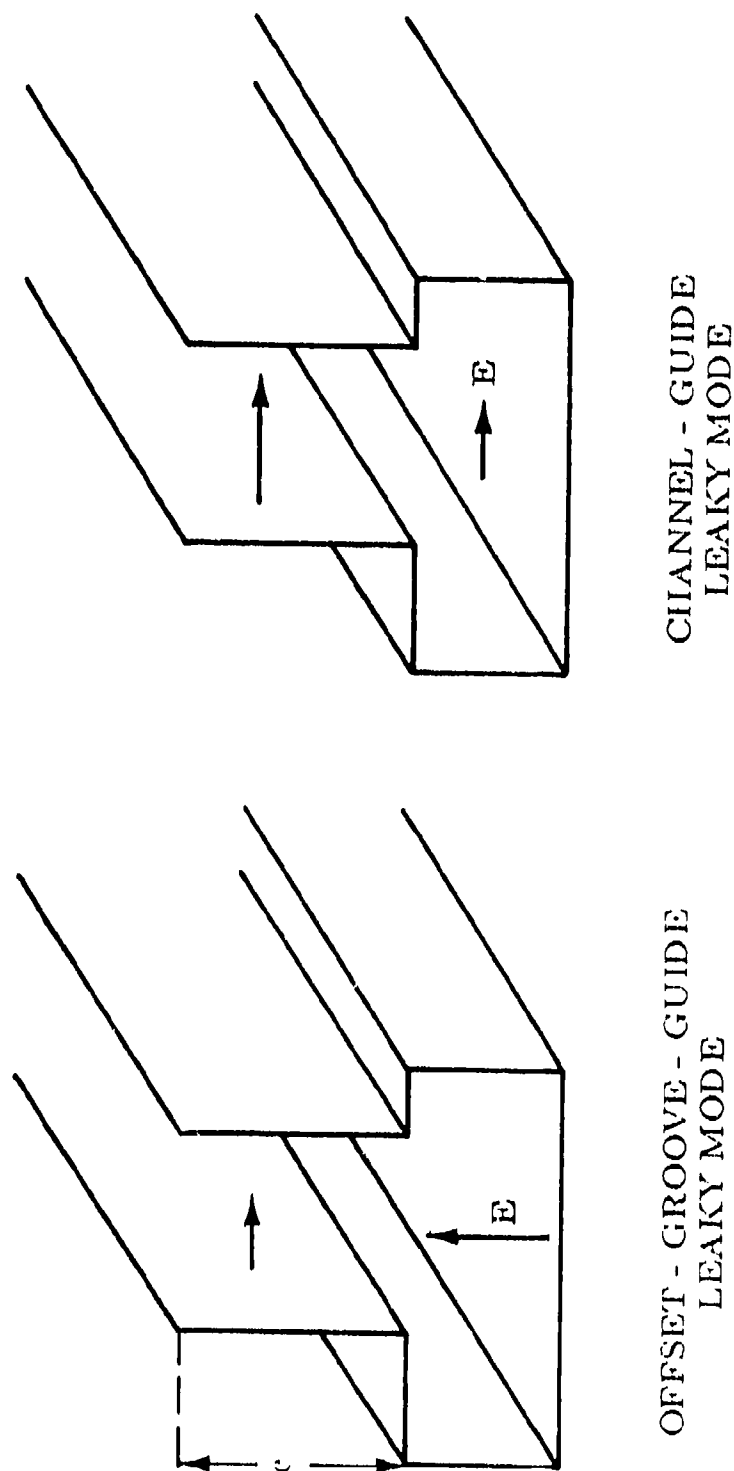
The electric field orientations in the offset-groove-guide antenna for each of these two leaky modes are shown in Fig. 7.18. For the offset-groove-guide, or OGG, leaky mode, most of the power resides in the main guide region with a vertical electric field polarization, and, by virtue of asymmetry, some power with a horizontal electric field polarization is produced in the stub guide region. In the channel-guide, or CG, leaky mode, most of the power is in the stub guide region, and the electric field polarization is basically horizontal everywhere. The length of the stub guide therefore has little influence, outside of a standing wave effect, on the OGG mode, but affects the CG mode critically. In fact, the number of CG modes present and above cutoff depends directly on the length c of the stub guide. We can also see that for the OGG mode the amount of power in the stub guide, and therefore the amount of leakage from the open end, depends strongly on the amount of stub guide offset. In contrast, the amount of stub guide offset should not significantly affect the behavior of the CG mode. Lastly, we know that the leakage rate of the OGG mode can vary from zero to a large value (depending on the amount of stub guide offset), but we would expect that the leakage rate for the CG mode will always be large. We will see from the numerical values discussed below that these expectations are indeed borne out.

a. Variations with Stub Length

If the CG leaky mode were not present, the variation of β/k_0 and α/k_0 with stub length c would be periodic, as a result of the mild standing wave produced by the mismatch from the radiating open end. Since the CG mode leaks strongly, it would not couple to an OGG mode with a very low leakage rate, since coupling would occur only if the α values (as well as the β values) were equal. Thus it is appropriate to first examine quantitatively the case of an OGG mode with a lower leakage rate. That first case is presented in Fig. 7.19, where the behavior of β/k_0 and α/k_0 are seen as a function of normalized stub length c/λ_0 .

Two sets of curves appear in Fig. 7.19 for both the β/k_0 and α/k_0 behaviors. The curves labeled $n = 0$, relatively flat for β/k_0 and relatively periodic for α/k_0 , represent the OGG mode. The other curves, which are seen to be very different in character, correspond to the set of CG modes. The number n of such modes increases as c/λ_0 increases because the CG modes are something like the modes that would be present in a rectangular waveguide of width c with an open side.

Since the β/k_0 values for the CG modes vary over a large range as c changes, it is evident that they cross the relatively flat curve corresponding to the OGG mode.



These modes will couple only when the α 's and the β 's of each are equal.

Fig. 7.i8 Electric field orientations in the offset-groove-guide antenna for the offset-groove-guide leaky mode and the modified channel-guide leaky mode, illustrating important differences between them.

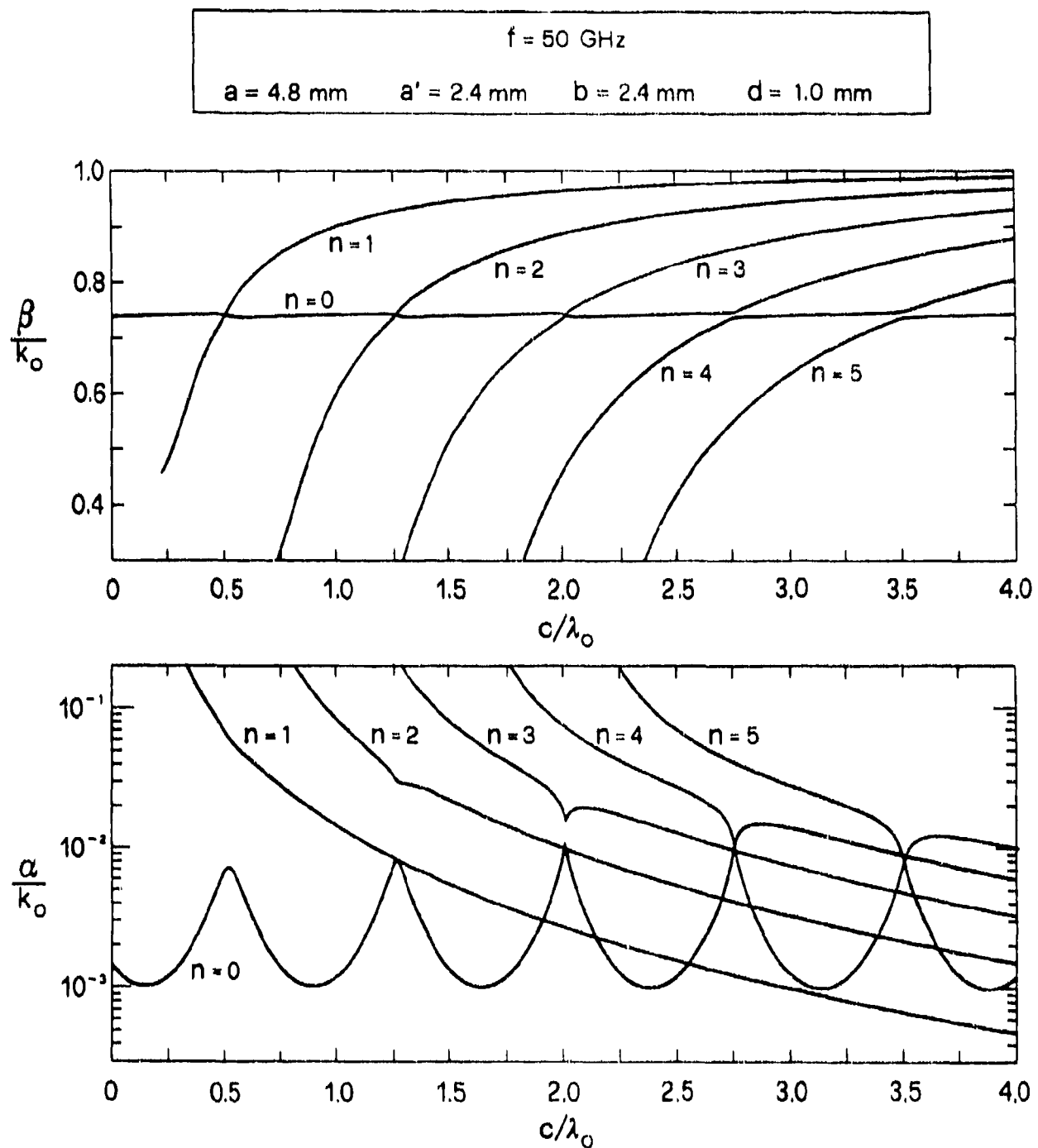


Fig. 7.19

Behavior of the normalized phase and leakage constants for the offset-groove-guide and channel-guide modes, for the case of small leakage, where coupling occurs only for large values of stub length.

However, coupling between the two mode types does not occur in Fig. 7.19 for small values of c/λ_o because the α/k_o values for the CG modes are too high. However, for the CG modes of higher n the value of α/k_o is smaller for the same value of β/k_o . As a result, coupling will eventually occur for a sufficiently long stub guide. This phenomenon is observed in Fig. 7.19, where for $n = 4$ the values of *both* α/k_o and β/k_o become equal for the two mode types. It is also interesting that the curves for α/k_o become affected by the two mode types and draw nearer to each other even though they do not cross (for the $n = 2$ and 3 CG modes).

In Fig. 7.20, the stub guide is offset somewhat more, and the leakage rate of the OGG mode is increased significantly. As a result, coupling occurs between the two mode types for all of the CG modes, with the first coupling region occurring at about $c/\lambda_o = 0.5$. The physics of what occurs in the coupling region is illustrated by the curve labeled $n = 1$, and shown partly dotted and partly dashed. Let us follow the $n = 1$ curve as c/λ_o increases. It is first in the dashed region, where it is clearly a CG mode. Then the curve reaches the first coupling region, where the character of the solution changes from that of the CG mode to that of the OGG mode; to reflect this change, the next portion of the curve is shown dotted. That changed character is retained until the next coupling region, at which a switch in character occurs back into the CG mode, shown dashed again.

If one knew nothing about the coupling process, and simply followed that solution from one end to the other, he would find for the α/k_o plot a curve that, as c/λ_o increased, dropped rapidly, reached a minimum, increased again, and after a maximum continued to decrease monotonically. He would not see any periodic character to the solution, and he would not know that in the dotted region the field distribution in the solution would be very different from that in the dashed region.

The coupling behavior in the β/k_o plot corresponds to what one would expect. What is new and interesting is what one finds for the α/k_o plot. If one concentrates on only those portions that correspond to the OGG mode, meaning those regions like the dotted one, the result is a continuous curve that is roughly periodic, though with decreasing amplitude, and is also something resembling the OGG mode curve in Fig. 7.19 before coupling occurs. For the β/k_o plot, the portions corresponding to the OGG mode are the flatter portions between the coupling regions, similar to the one shown dotted. It is therefore possible to identify the nature of the separate portions even though the plots are initially very confusing.

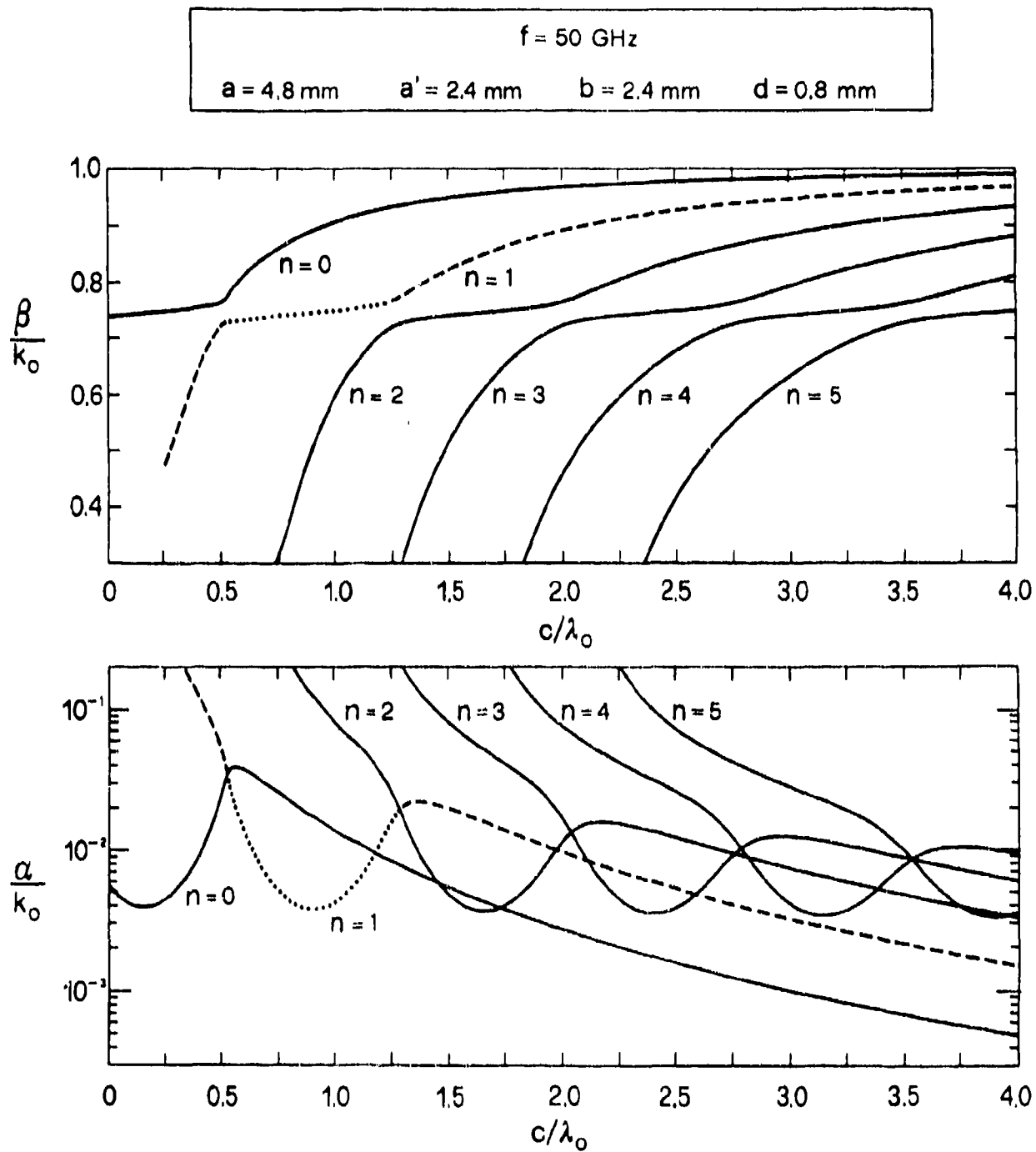


Fig. 7.20

Same as Fig. 7.19, except that the leakage rate for the offset-groove-guide mode is higher. The physical behavior associated with the coupling is illustrated by the dotted and dashed portions (see text).

In Fig. 7.21, the offset is made even greater, so that the leakage rate of the OGG mode becomes very large. The lessons learned from Fig. 7.20 still apply, and one can still identify the separate regions, but it has become more difficult to do so since the boundaries have become less sharp in the β/k_o plot.

It was shown in Sec. 1 above that the stub length c must be sufficiently long to prevent cross-polarized radiation, but that, for the dimensions employed in Figs. 7.19 to 7.21, the value of c/λ_o need not exceed 0.5 or so, depending on how much cross-polarized radiated power can be tolerated. The value 0.5 for c/λ_o corresponded to a reduction in the $n = 1$ (cross-polarized) mode of about 28 dB. If we view the curves in Figs. 7.19 to 7.21, we note that the first coupling region appears to occur for c/λ_o just over 0.5, so that the problems associated with the coupling can be avoided even when the leakage rate is high, by keeping the stub length only as long as is necessary and not any longer.

a. Variations with Stub Offset

In Fig. 7.22, we present the behavior of β/k_o and α/k_o as a function of stub guide offset, measured in terms of d/a , where $d/a = 0.25$ corresponds to the centered stub, for which there is no radiation. In this figure, c/λ_o , the normalized stub length, is the parameter. A set of values of c/λ_o have been chosen such that each value corresponds roughly to the middle of the offset-groove-guide (OGG) portion of the curves. This assertion may be verified by an inspection of Figs. 7.19 to 7.21.

The curves for β/k_o in Fig. 7.22 are seen to be relatively flat and independent of the value of c/λ_o . This feature is consistent with the flatness of the β/k_o curves in the OGG mode portions found in Figs. 7.19 to 7.21, and with the flatness with d/a for β/k_o noted in Fig. 7.9, for $c = \infty$.

For the curves of α/k_o in Fig. 7.22, we observe that the leakage rates are higher for smaller values of c/λ_o , a feature that is especially pronounced at the larger values of leakage. The reason for this behavior lies in fact that the curves of α/k_o vs. c/λ_o slope downwards when the leakage rates are higher, as seen in Fig. 7.21. (This feature would be clearer if the data were plotted on a linear scale.) It is also observed that all the curves go to zero when d/a is increased. We shall see in a moment that this behavior does not hold for the channel-guide (CG) leaky modes.

In Fig. 7.23, we again present the behavior of β/k_o and α/k_o as a function of d/a ,

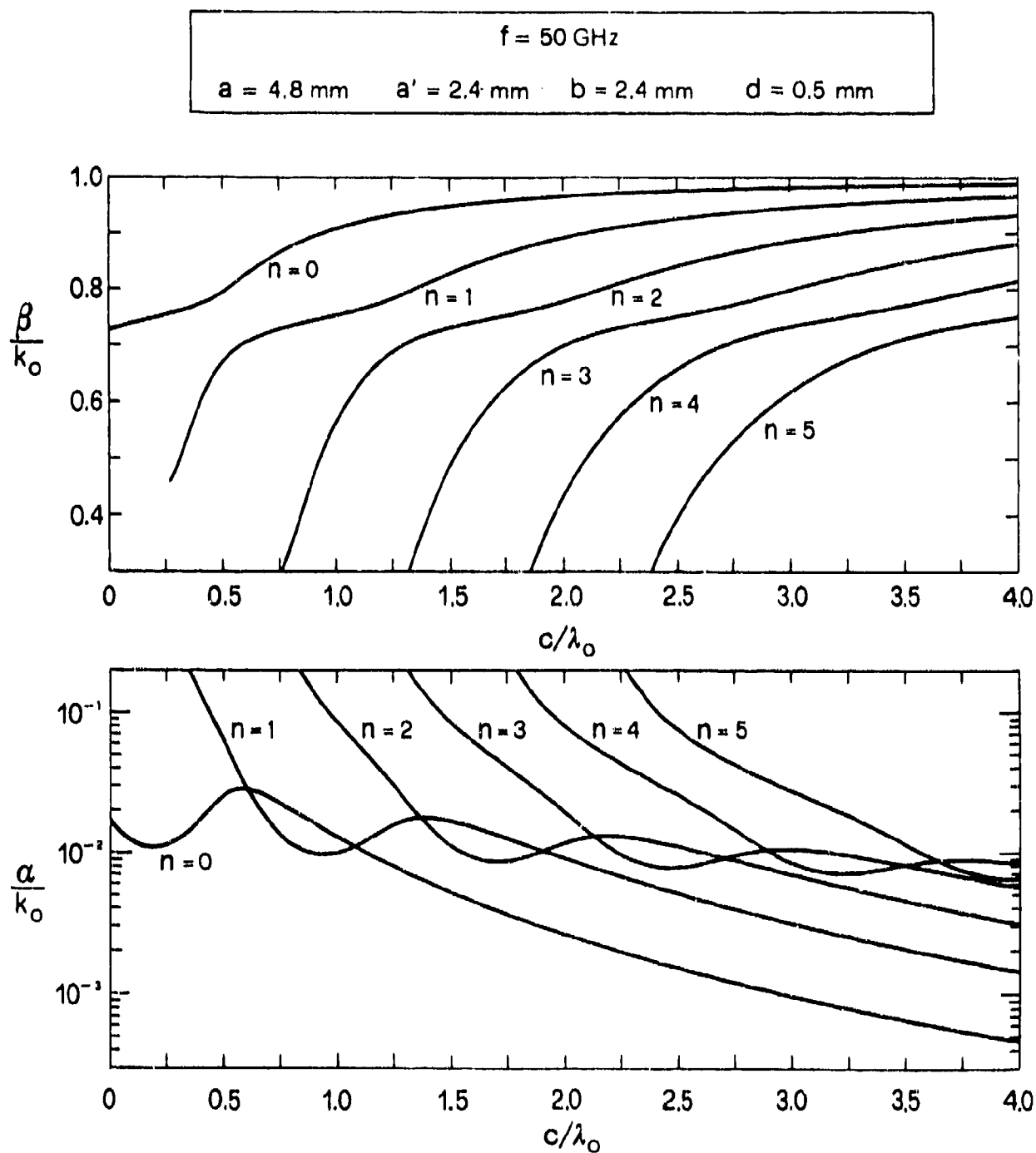


Fig. 7.21

Same as Fig. 7.19, except that the leakage rate is now much higher, making it more difficult to identify separate regions.

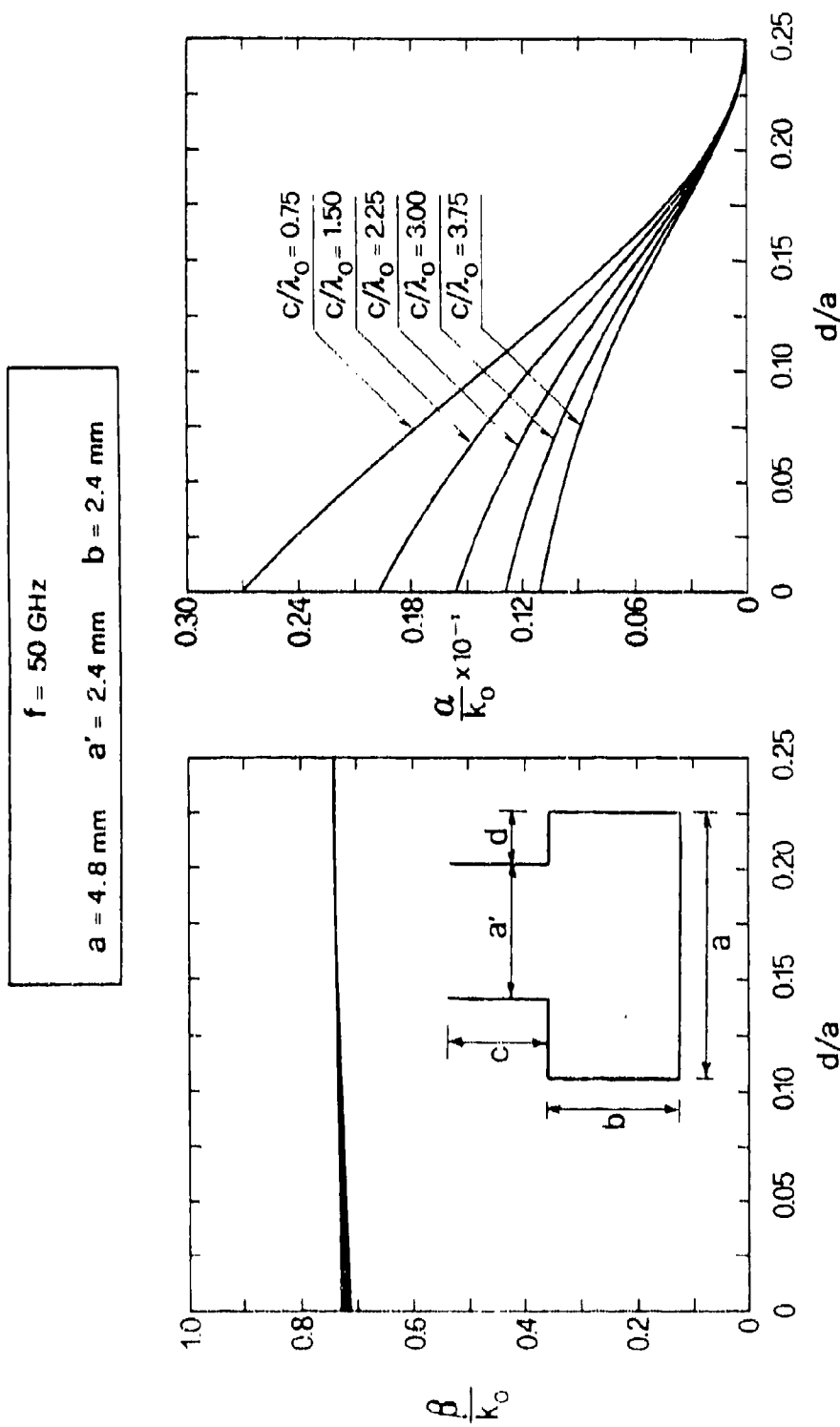


Fig. 7.22 Behavior of the normalized phase and leakage constants for the offset-groove-guide mode as a function of stub guide offset, for different values of stub length.

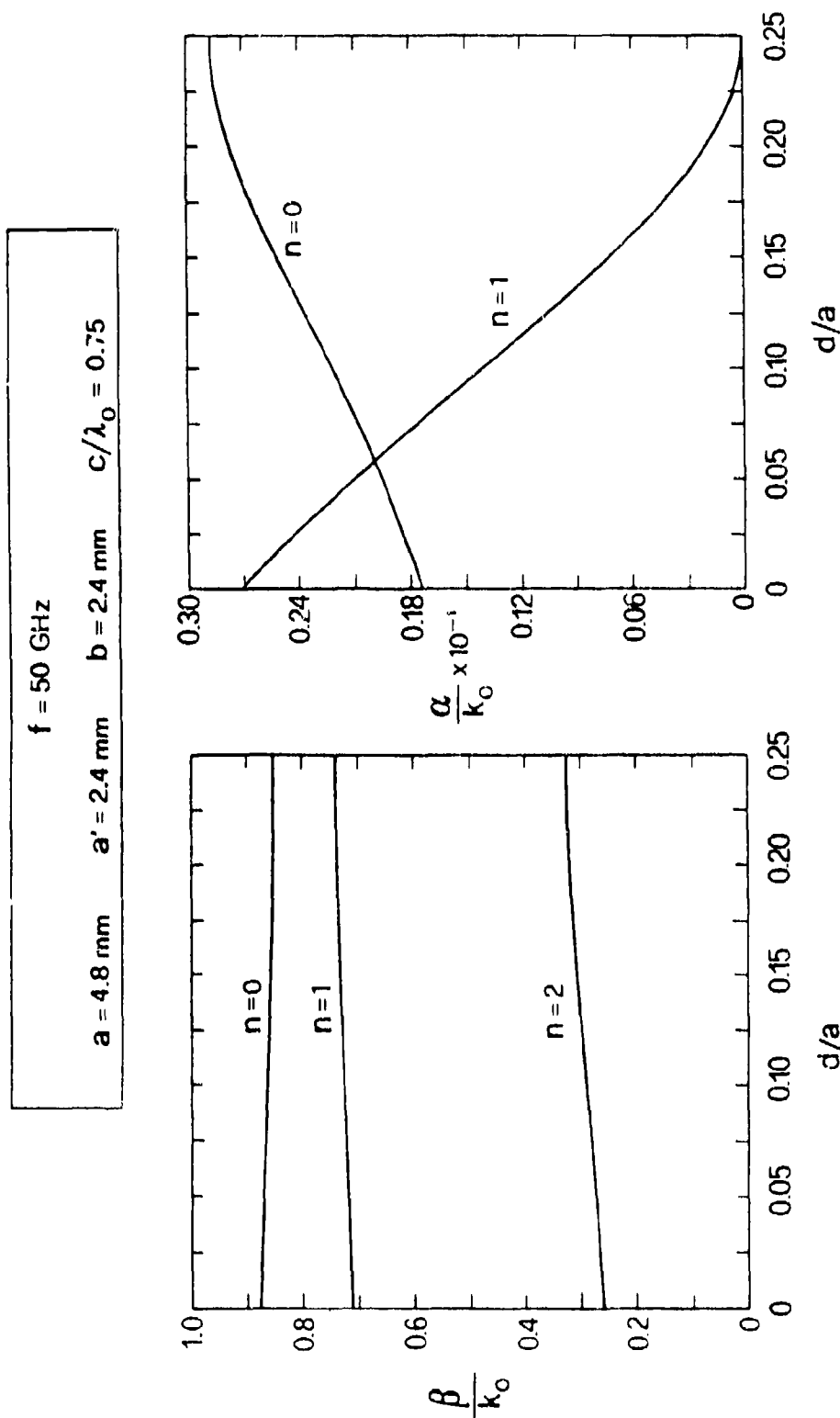


Fig. 7.23 Behavior of the normalized phase and leakage constants for both the offset-groove-guide and the channel-guide modes as a function of stub guide offset, for stub length $c/\lambda_0 = 0.75$. (The offset-groove-guide mode is $n = 1$.)

but for all the mode solutions that exist at the stub length value $c/\lambda_o = 0.75$. From Figs. 7.19 to 7.21 we note that three modes are present, the $n = 0$, $n = 1$ and $n = 2$ modes; the $n = 2$ mode is omitted from the α/k_o plot because its leakage rate is so large at this value of c/λ_o as to be off scale. Let us also note from Figs. 7.19 to 7.21 that the $n = 1$ mode for that value of c/λ_o possesses the character of the OGG mode (see the dotted lines in Fig. 7.20), whereas the $n = 0$ and $n = 2$ modes are clearly of the CG mode type.

(A comment should be made here regarding the mode number that characterizes the OGG mode. That mode number depends on when the coupling begins. If the coupling has not yet started for the value of c/λ_o , the mode number is still $n = 0$. If it started before that value of c/λ_o , n will be greater than zero. The $n = 1$ portion at $c/\lambda_o = 0.75$ for $d = 0.8$ mm (Fig. 7.20) is the same as that labeled $n = 0$ for $d = 1.0$ mm (Fig. 7.19). For labeling purposes in Fig. 7.23, however, the numbering used corresponds to that in Fig. 7.20.)

We may first see from Fig. 7.23 that for β/k_o all three modes are relatively flat as d/a is varied, showing that the behavior of β/k_o is not a good way of distinguishing between the two mode types. The behavior of α/k_o , on the other hand, is entirely different for the two mode types. The $n = 1$ mode, which for this value of c/λ_o has the nature of the OGG mode, has its α/k_o value go to zero as the stub becomes symmetrically located, as we would expect of this mode type. (In fact, it is the same curve as the one in Fig. 7.22 for $c/\lambda = 0.75$.) The $n = 0$ mode, however, which is of the CG mode type, does not go to zero, and in fact increases somewhat as the stub becomes centered. The CG modes are not strongly dependent on d/a because of their electric field orientation, as shown in Fig. 7.18.

A similar demonstration is made in Fig. 7.24, but for a much larger stub length, $c/\lambda_o = 3.0$, so that more modes are present simultaneously. There are actually 6 modes present, but only 5 are shown in the α/k_o plot because the values for the $n = 5$ mode are off scale. An inspection of Figs. 7.19 to 7.21 verifies that 6 modes are present, and that only one of them, the $n = 4$ mode, is an OGG mode and the rest are CG modes.

The β/k_o plot in Fig. 7.24 shows that all the modes are quite flat with d/a , as was found in Fig. 7.23. For the α/k_o plot, we see clearly that only the $n = 4$ curve, which is of OGG mode nature for this value of c/λ_o , goes to zero as the stub becomes centered. The CG modes are basically not affected when d/a changes. The behavior

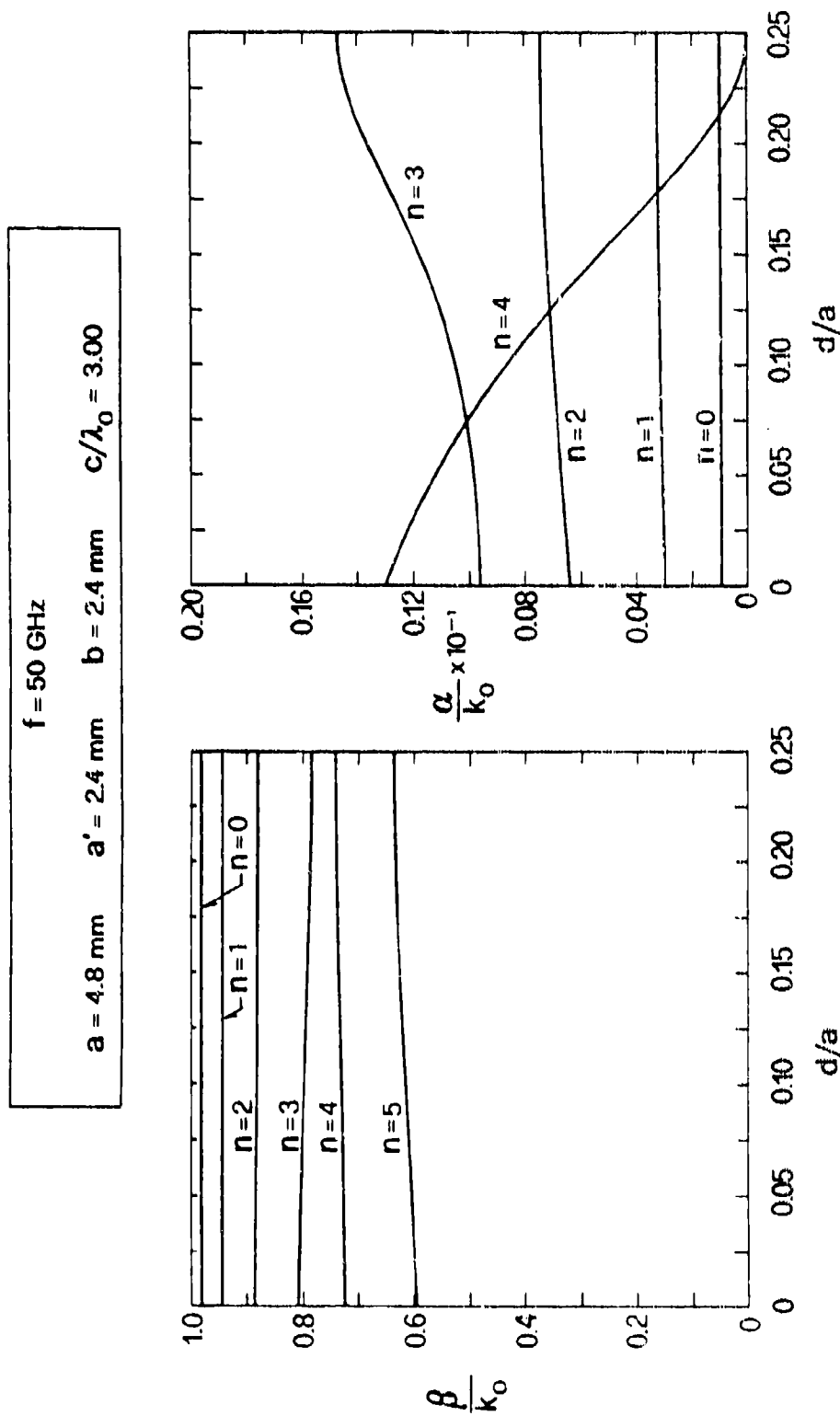


Fig. 7.24 Same as Fig. 7.23, except for a much larger stub length $c/\lambda_0 = 3.00$, so that more modes are present simultaneously. (The offset-groove-guide mode is $n = 4$.)

of α/k_o when the stub offset is altered is thus a sensitive test of the character of the mode in question.

b. Variations with Frequency

The curves in Figs. 7.19 through 7.24 above present data at the mid-range frequency of 50 GHz. We next examine what occurs when we vary the frequency over a wide range. We treat two different geometrical structures; both have a relatively short stub length ($c/\lambda_o = 0.75$), but one leaks weakly and the other leaks strongly.

We consider first the case for which there is a small leakage rate ($d = 1.0$ mm); results for β/k_o and α/k_o over a large frequency range are presented in Fig. 7.25. We note first that only three modes are present; that observation is consistent with the curves in Fig. 7.19 and the mode numbering used for the figure, since the dimensions correspond as well. In Fig. 7.19, the $n = 0$ mode is clearly the OGG mode, and the $n = 1$ and $n = 2$ modes are CG modes.

When we recall that the CG modes have a much higher leakage rate than the OGG mode, the behavior of the curves in Fig. 7.25 become clear. The $n = 1$ and $n = 2$ modes have much higher values of α/k_o in the region above cutoff, and the β/k_o behavior below cutoff shows that the CG modes have a much higher minimum and turn up much sooner. The β/k_o curve for $n = 0$ below cutoff does actually rise past unity as the frequency is lowered further, but it is not drawn here. That behavior is very similar to the one found in Fig. 7.12 for c infinite; the explanation for the behavior is given in the discussion relating to Fig. 7.12. A final point of interest is that in the α/k_o plot the $n = 0$ curve (for the OGG mode) drops very rapidly at cutoff, thereby crossing the curve for one of the CG modes.

The case involving the larger leakage rate ($d = 0.5$ mm, greater offset) is presented in Fig. 7.26. We again find three modes present for this stub length ($c/\lambda_o = 0.75$); by employing Fig. 7.21, we identify the $n = 1$ mode as the OGG mode and the other two modes as CG modes. The dependence on frequency here is similar to that seen in Fig. 7.25; the behavior of the CG modes is almost the same, but that for the OGG mode shows some differences. The differences are due to the higher leakage rate here; the curve for α/k_o above cutoff is certainly much higher here than in Fig. 7.25, and the curve of β/k_o below cutoff does not go down as far and turns up at a higher frequency. The crossing of curves for α/k_o in the neighborhood of cutoff noted in connection with Fig. 7.25 is seen to occur here as well.

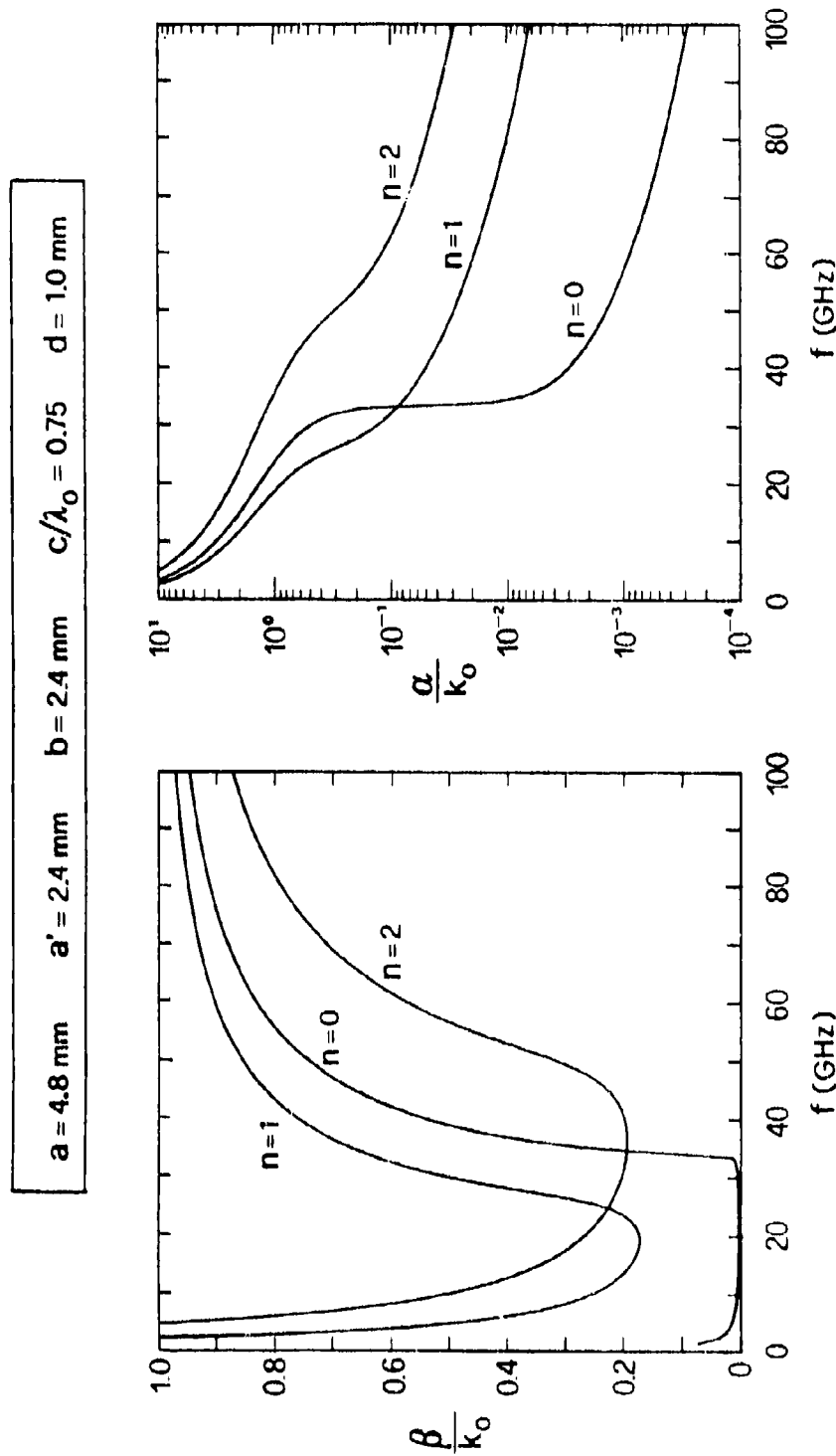


Fig. 7.25 Behavior of the normalized phase and leakage constants over a wide range of frequencies for the case of small leakage for both the offset-groove-guide and channel-guide modes. (The offset-groove-guide mode is $n = 0$).

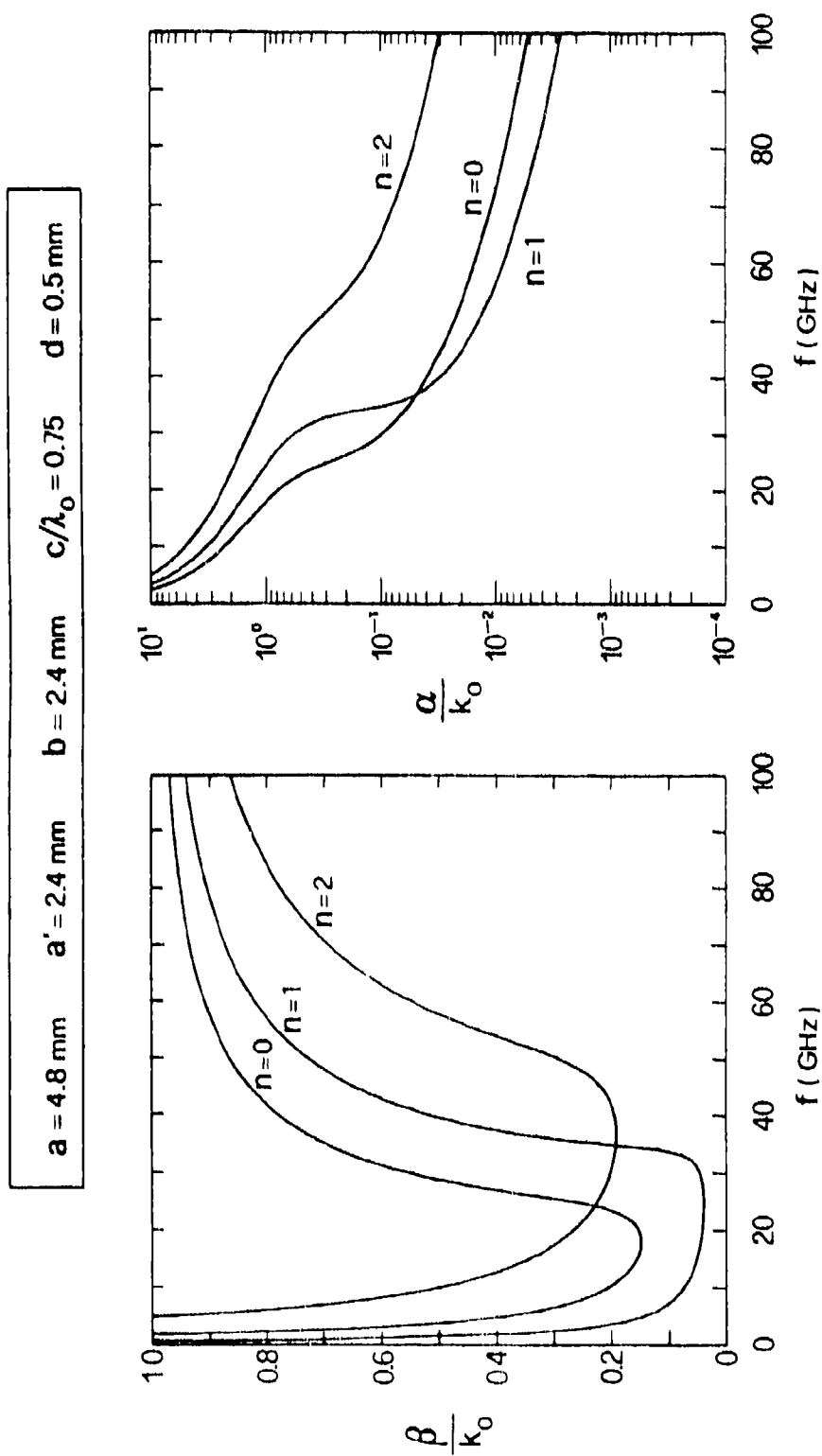


Fig. 7.26 Same as Fig. 7.25, except that the leakage rate is higher here. (The offset-groove-guide mode is $n = 1$.)

By employing relation (7.21), the curves for β/k_0 above cutoff in Figs. 7.25 and 7.26 may be used to provide the variation with frequency of θ_m , the angle from broadside of the maximum of the radiated beam. These curves, shown in Fig. 7.27, are similar to the one presented on the left hand side of Fig. 7.14, where c was taken to be infinite. In Fig. 7.27, we observe that the curves for the CG modes are quite similar in shape to those for the OGG modes ($n = 0$ and $n = 1$ in the upper and lower cases, respectively).

The concern thus arises as to whether or not the CG modes will provide additional but undesired radiated beams in the overall radiation pattern. The answer lies in how well they are excited. By referring to the field orientations shown in Fig. 7.18, we see that the OGG mode is excited by applying a vertical electric field in the main guide section. The CG mode is not excited directly. The horizontal electric field in the stub guide region is produced by virtue of asymmetry introduced by the off-center placement of the stub guide. However, this mode will not couple to the CG modes unless their β and α values are the same. Thus, the neighboring CG modes would be only very weakly excited by the initial feed power and they would not be coupled to the OGG mode except under special circumstances. We should therefore not expect any practical difficulty due to their presence, especially if the stub guide length is kept short.

$$a = 4.8 \text{ mm} \quad a' = 2.4 \text{ mm} \quad b = 2.4 \text{ mm} \quad c/\lambda_0 = 0.75$$

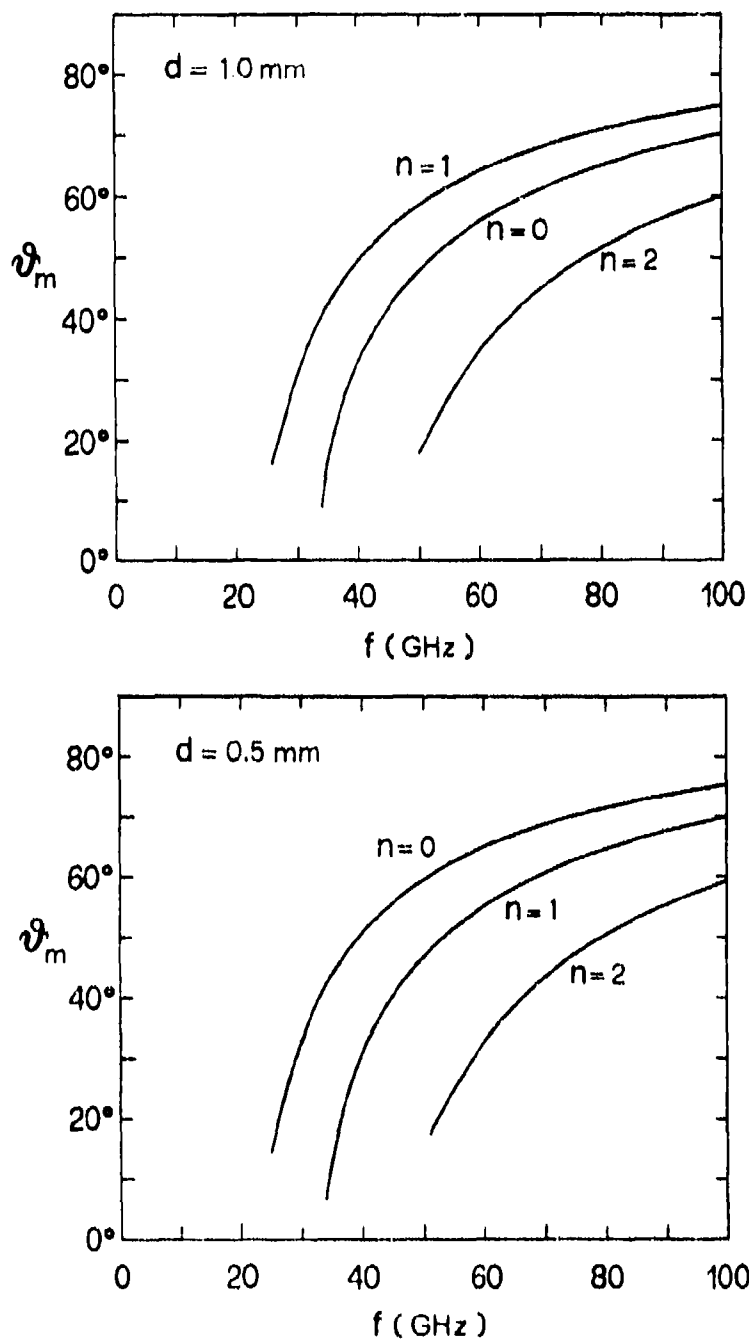


Fig. 7.27

Variation with frequency of the angle of the maximum of the radiated beam, when both the offset-groove-guide and the channel-guide modes are present. (The offset-groove-guide mode is $n=0$ and $n=1$ in the upper and lower boxes, respectively.)

VIII.	MEASUREMENTS AT MILLIMETER WAVE- LENGTHS ON THE OFFSET-GROOVE-GUIDE ANTENNA	243
A.	THE STRUCTURE UNDER MEASUREMENT	244
B.	MEASUREMENT METHODS	247
	1. Wavenumbers	247
	2. Radiation Patterns	247
C.	WAVENUMBER DATA	253
	1. Preliminary Theoretical Calculations	253
	2. Comparisons Between Theory and Measurements	256
	3. Design Considerations for Tapered Apertures for Sidelobe Control	258
	4. Vector Field Distributions	266
D.	RADIATION PATTERNS	270
	1. Calculations for the Near Field Patterns	270
	2. Comparisons Between Theory and Measurement	271

VIII. MEASUREMENTS AT MILLIMETER WAVELENGTHS ON THE OFFSET-GROOVE-GUIDE ANTENNA

(With: Prof. H. Shigesawa and Dr. M. Tsuji,
Doshisha University, Kyoto, Japan)

The performance characteristics found for the offset-groove-guide leaky-wave line source in Chap. VII were so desirable and attractive that we wanted to take some measurements on a typical example of that antenna at millimeter wavelengths. We wished to answer two questions:

(a) How accurate is our theory? That is, how well do the measurements agree with the theoretical results?

(b) Do any unexpected problems arise when we try to build and operate this antenna at millimeter wavelengths? In other words, does the antenna still work as expected despite the fabrication difficulties related to its small size? The frequency range is 40 GHz to 60 GHz, so that the smallest wavelength is only 5 mm.

The structure of the antenna that was fabricated and measured is discussed in Sec. A, and photographs of it are presented there. The structure differs slightly from the one in Chap. VII in that a flange is now present at the radiating aperture, whereas we did not previously consider a flange. In Sec. C we show how the theory should be modified to take this small change into account, and all comparisons between theory and measurement employ this modified theory.

Measurements were made of the wavenumbers β and α and of radiation patterns. The measurement procedures employed are described in Sec. B.

Comparisons between measurements and theory for the wavenumbers are presented in Sec. C, and those for the radiation patterns in Sec. D. In all cases, for all the quantities considered, very good agreement was obtained.

Some of the material contained in this chapter, including comparisons between measurements and theory, was presented at the IEEE International Symposium on Antennas and Propagation in 1987, and appears in their Digest [23].

A. THE STRUCTURE UNDER MEASUREMENT

A cross-section sketch of the offset-groove-guide antenna structure that was measured appears in Fig. 8.1. It differs from the structure that was analyzed in Chap. VII only in that *flanges* are present here at the radiating open end. The radiating discontinuity is thus slightly different, so that the numerical values for β and α turn out to be slightly different, but the principle of operation and all the performance features are identical to those of the antenna described and discussed in Chap. VII.

The antenna that was built and measured was designed to operate at a mid-frequency of 50 GHz; it has the dimensions shown in Fig. 8.1. A photograph of the cross section of the structure is given in Fig. 8.2, in which it is seen that the guiding portion is channeled out of a solid block of brass. A 10 yen Japanese coin (23 mm in diameter) is shown for size comparison.

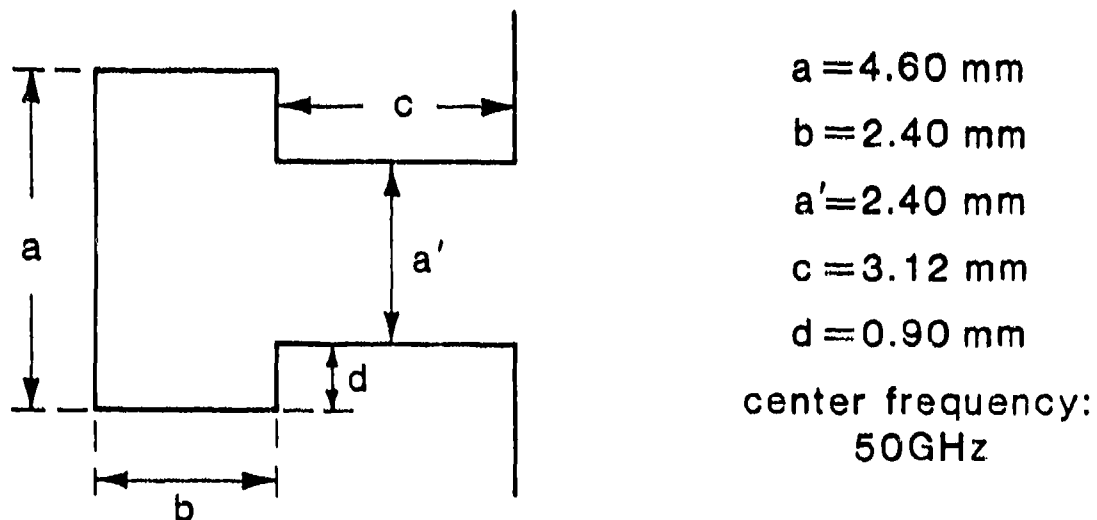


Fig. 8.1 Cross section of the offset-groove-guide antenna that was measured. The dimensions shown are exactly ten times the actual ones.

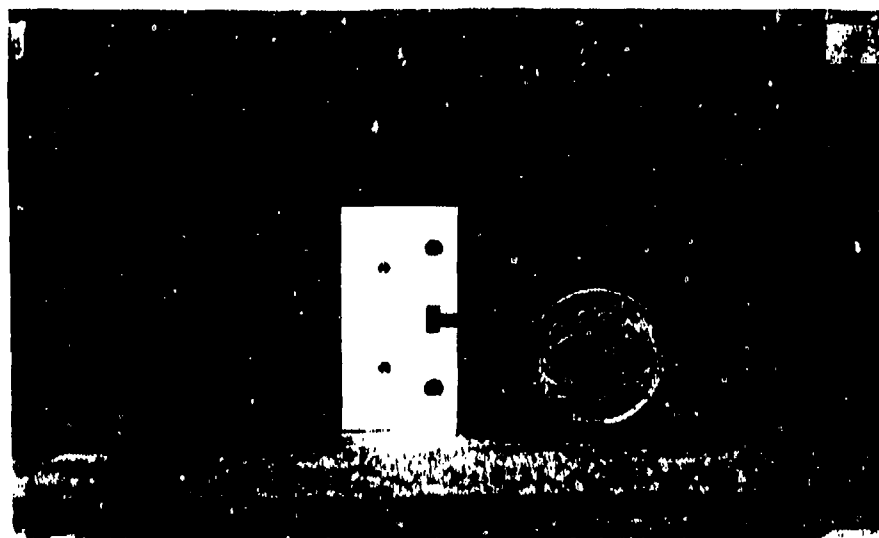


Fig. 8.2 Photograph of the cross section of the actual antenna that was measured. A 10 yen Japanese coin (23 mm in diameter) is shown for size comparison.

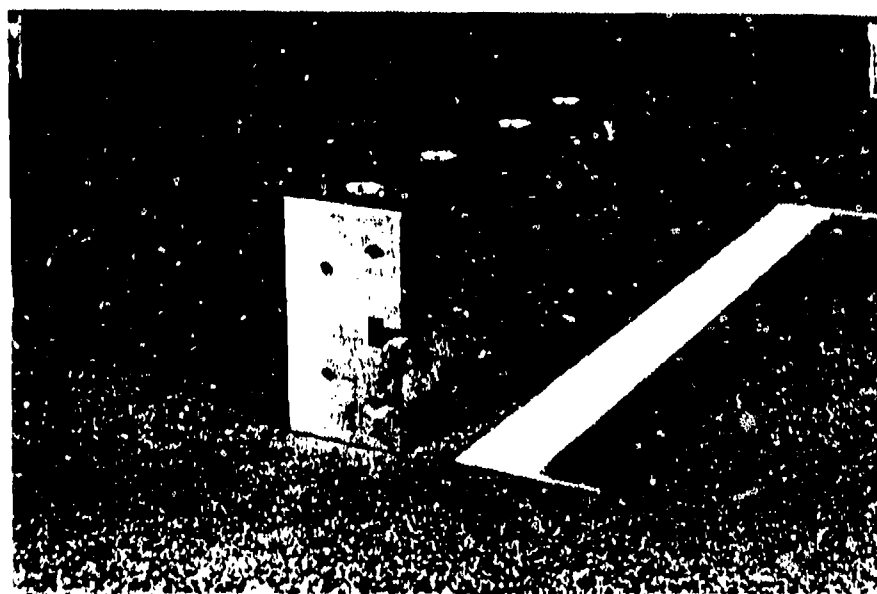


Fig. 8.3 Photograph with a three-dimensional view of the antenna, showing that the antenna aperture is 10 cm long. The projection appearing part way down the guide is a moveable short circuit.

From Fig. 8.2 (and Fig. 8.1) we see that the stub guide length c is equal to 3.12 mm, which turns out to be roughly a half free-space wavelength at the mid-frequency, 50 GHz. That length is reasonably short so that we should avoid the peculiar coupling problems to another leaky mode that we discussed in detail in Chap. VII, Sec. D. In Sec. C, below, we demonstrate that such problems are indeed avoided here.

The photograph with the three-dimensional view in Fig. 8.3 indicates that the length of the antenna aperture is 10.0 cm. Note that a projection appears part way down the guide. It is a moveable short-circuit plunger that has the same cross-section dimensions as the antenna itself; it was used to obtain the values of α and β by measuring the variation in reflected power produced by changing the distance between the input plane and the moveable short. The details of the measurement procedure are presented in the next section.

The antenna was fed from a rectangular waveguide of almost the same dimensions as the main guide section of the antenna. The feed waveguide is WR 19, with nominal cross-section dimensions 4.775 mm by 2.388 mm; the antenna's cross-section dimensions are 4.60 mm by 2.40 mm. The mismatch at the junction between the two structures was found to be very small.

The feed waveguide's cutoff frequency is 31.4 GHz, and its recommended operating range is 39.3 GHz to 59.7 GHz. We took measurements from 40 to 60 GHz of both the wavenumbers β and α and the radiation patterns. The wavenumber results are discussed in Sec. C and the radiation patterns in Sec. D.

B. MEASUREMENT METHODS

Measurements were made of two different quantities: wavenumbers β and α , and radiation patterns. The measurement set-ups and the measurement procedures are quite different for each, and they are therefore discussed separately below.

1. Wavenumbers

The wavenumbers β and α were measured by employing the moveable short shown in Fig. 8.3, and measuring the reflected power as a function of the distance of the moveable short from the junction between the feed waveguide and the antenna structure. A schematic diagram of the measurement system is given in Fig. 8.4, where the reflections from the offset-groove-guide antenna structure are monitored and measured using the network analyzer.

A typical plot is presented in Fig. 8.5 of the measured relative reflected power plotted on a logarithmic scale as a function of the distance of the moveable short from the junction mentioned above. The total antenna aperture length is 100 mm. The oscillation in the reflected power is due to the interference between the reflected wave from the moveable short and the wave reflected back from the small discontinuity present at the junction between the feed guide and the antenna. One can apply Deschamps' reflection coefficient procedure [24] to determine accurately the scattering-matrix parameters that characterize that small discontinuity, and then subtract out its effect at each point to determine the true reflection coefficient at each distance z in Fig. 8.5. When that step is performed, one obtains the solid straight line shown roughly midway between the two dashed straight lines. However, a result that is almost the same is achieved by simply taking the average of the slopes indicated by the two dashed lines, a step that is valid if the reflection from the feed discontinuity is sufficiently small.

The value of the attenuation constant α in dB/mm is determined by taking one-half of the slope of the solid line mentioned above. To find α/k_o , the above value for α is divided by 8.686 times the appropriate value of k_o . The distance between neighboring maxima or minima is equal to $\lambda_g/2$; a measurement of this distance thus yields π/β , with β in units of mm^{-1} .

2. Radiation Patterns

A schematic diagram of the experimental system that was used to measure the radiation patterns in the 50 GHz range is shown in Fig. 8.6. A receiving pick-up horn was used to sample the radiated field, and the horn was located on a boom that swung

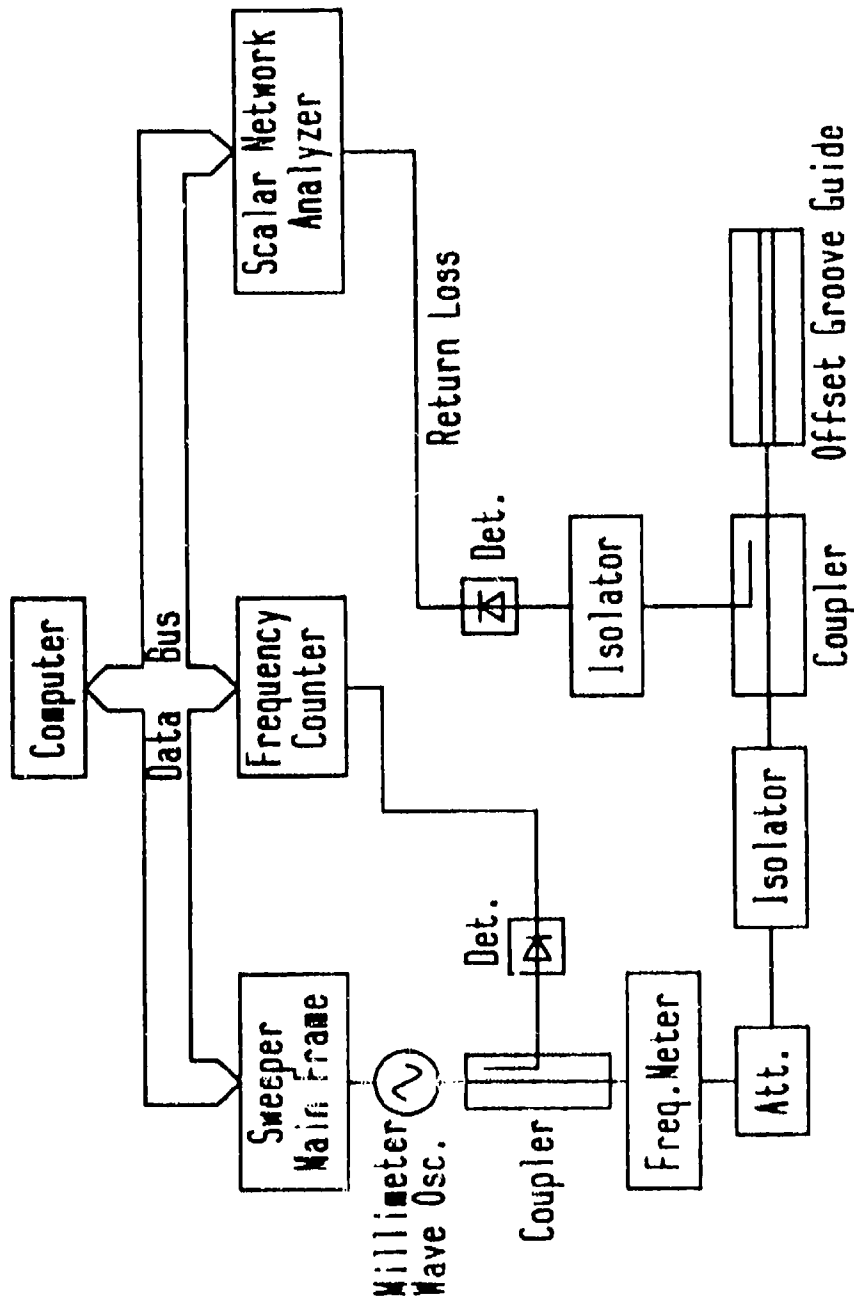


Fig. 8.4 Schematic diagram of the experimental set-up for the measurement of phase constant β and attenuation constant α in the 50 GHz range.

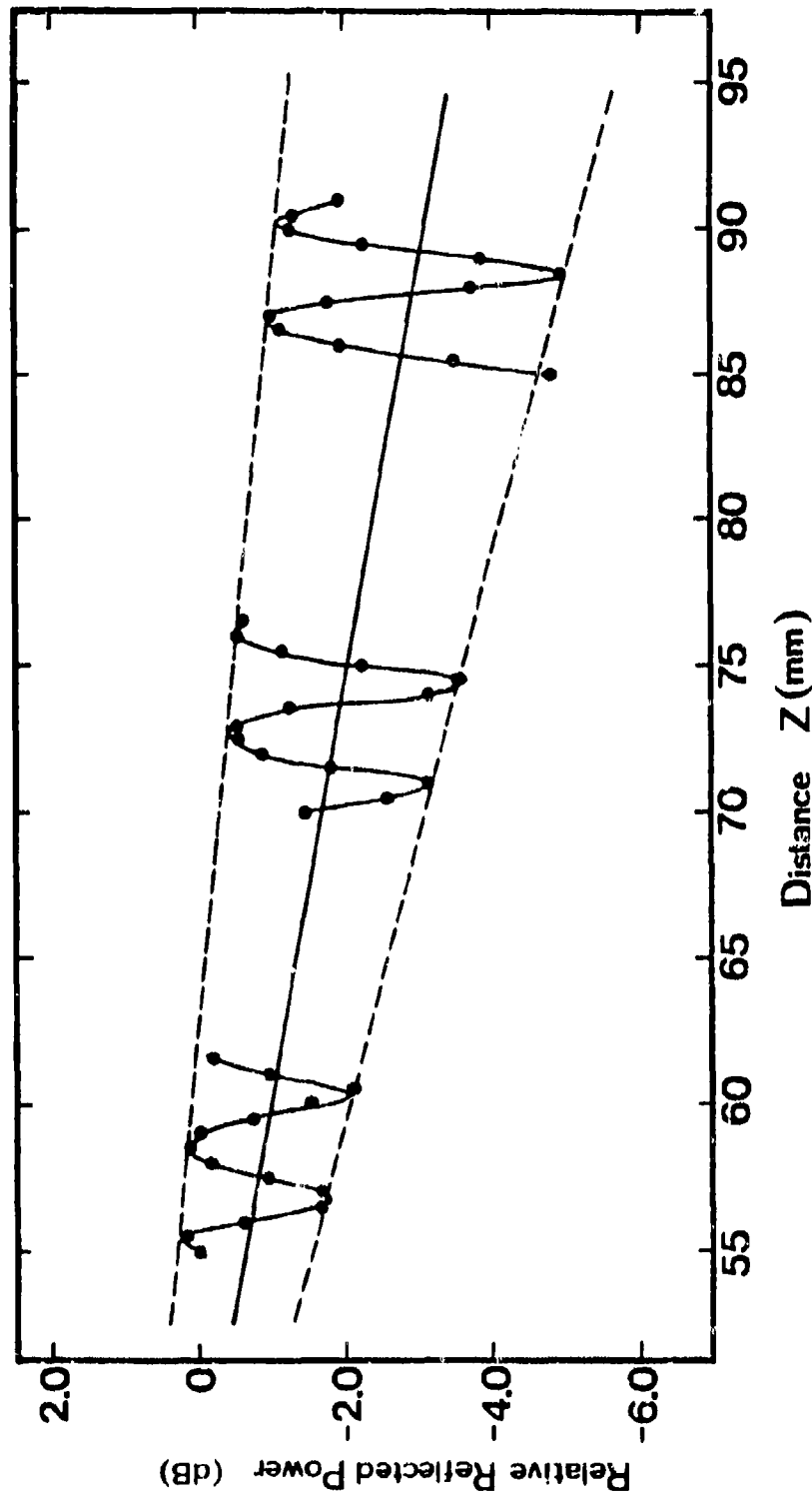


Fig. 8.5 Typical plot of the measured relative reflected power in dB at 54.8 GHz as a function of the distance of the moveable short to the junction between the antenna and the feed guide. The dimensions of the antenna are those indicated in Fig. 8.1.

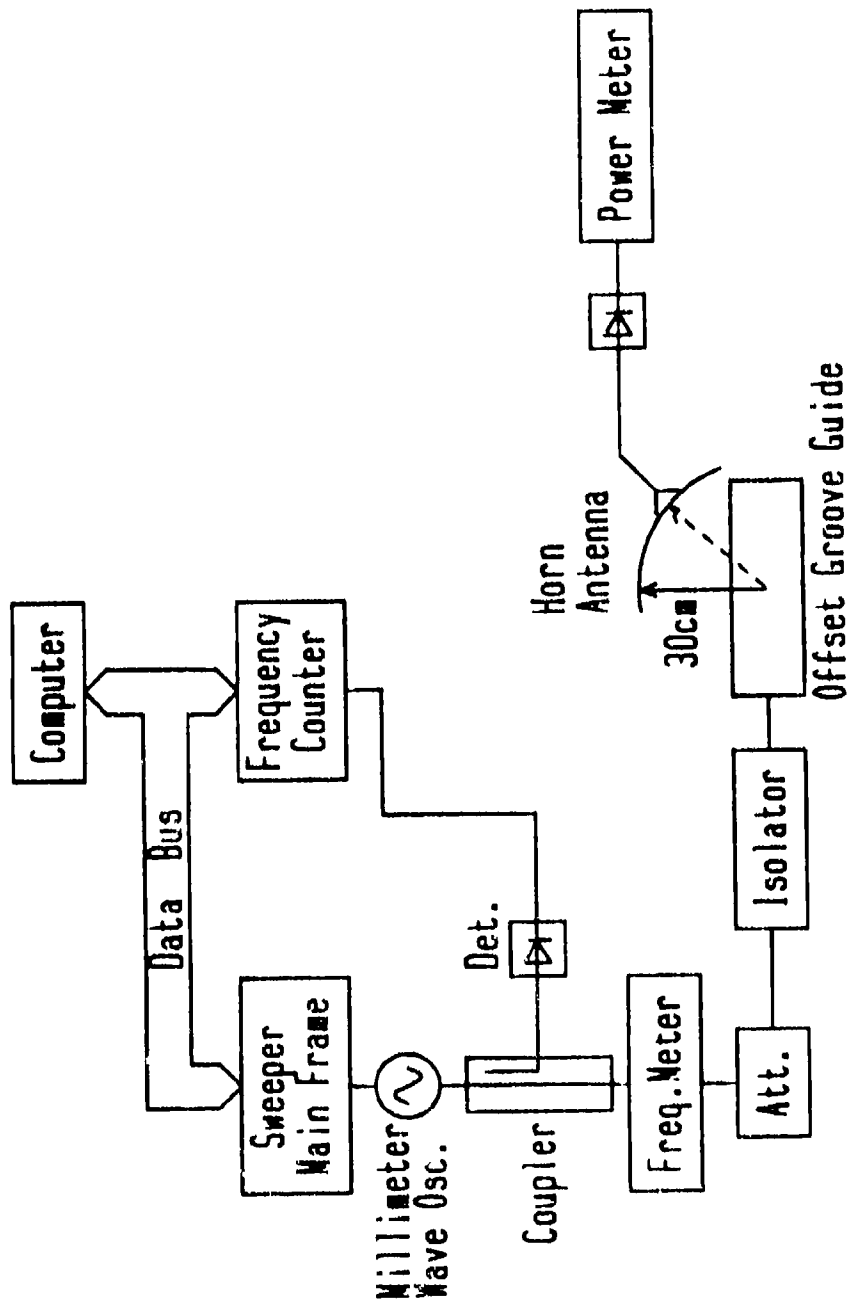


Fig. 8.6 Schematic diagram of the experimental system that was used to measure radiation patterns in the 50 GHz range.

through the required range of angles. The surrounding area was covered with absorbing material. These features are illustrated in the photograph in Fig. 8.7.

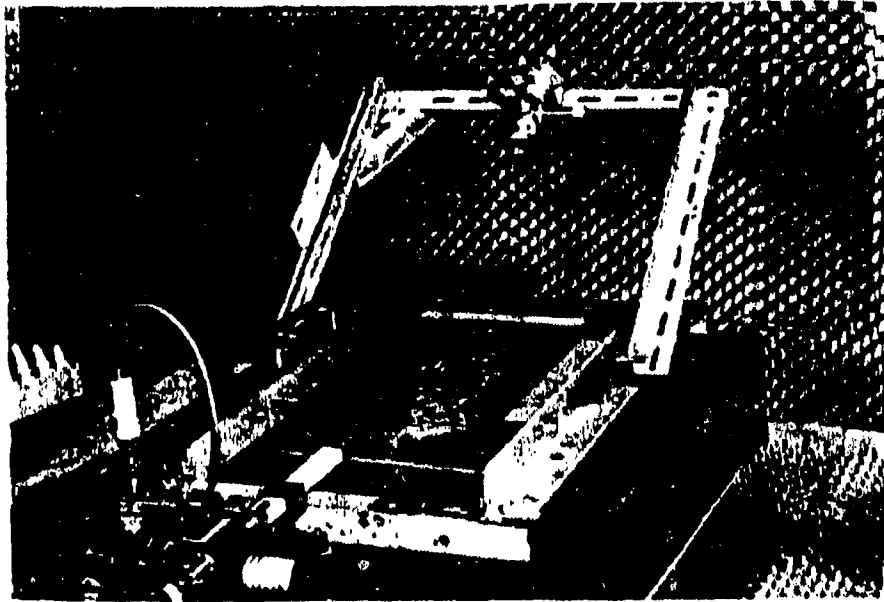


Fig. 8.7 Photograph of the experimental set-up for the measurement of near field patterns, showing the pick-up horn on its boom, the structure being measured and its feed arrangement, and the absorbing material in back.

For these radiation measurements, the offset-groove-guide antenna was fed at one end by the rectangular waveguide arrangement mentioned above, and shown (not so clearly) in Fig. 8.7. At the other end of the antenna a matched load is placed, but that cannot be seen.

A key problem that arose in connection with these measurements is that the boom holding the receiving horn antenna was too short to permit far-field measurements. The measurements had to be taken in the *near field*, where the patterns are not as simple or pretty, but near field pattern calculations were made that showed very good agreement with the measured data. These comparisons and further details are presented in Sec. D.

The measurements were all taken at a distance of 30 cm from the center of the antenna aperture, as indicated in Fig. 8.6. Using the far field criterion, $R \approx 2L^2/\lambda_o$, where R is the distance in question, $L = 10$ cm is the antenna aperture length, and $\lambda_o = 6$ mm is the wavelength at the mid-range frequency 50 GHz, we find $R = 333$ cm, so that the pick-up horn should be located at least that distance away to be at the beginning of the far field. We note that the minimum distance for far field measurements would be about ten times the distance available to us for these measurements. We therefore had to be careful regarding both the measurements and the calculations with which they are compared in Sec. D.

C. WAVENUMBER DATA

1. Preliminary Theoretical Calculations

In the actual offset-groove-guide leaky-wave antenna, where the stub guide is of finite length c (see Fig. 8.1), it is possible to excite another leaky mode in addition to or instead of the desired offset-groove-guide leaky mode, and it is possible to couple these two modes together. The explanation for these effects is presented in detail in Chap. VII, Sec. D. The proper design of the antenna thus requires some preliminary theoretical calculations to assure us that, first, the leaky mode we are measuring is indeed the offset-groove-guide leaky mode, and second, the two leaky modes are not coupled together.

Such early theoretical calculations for the antenna to be measured are presented in Figs. 8.8 and 8.9. They correspond to the behavior of β/k_o and α/k_o as a function of the stub length c at three different frequencies (40 GHz, the low end; 50 GHz, the mid-range frequency; and 60 GHz, the high end). It is seen, first of all, that the two leaky modes (the "other" leaky mode is the channel-guide leaky mode -- see Fig. 7.18) do *not* couple for this set of parameters. Second, the general behaviors of both β/k_o and α/k_o are quite the same as the ones observed in Chap. VII (and Chaps. III and IV) for smaller values of leakage rate.

The choice of stub length $c = 3.12$ mm is seen in Fig. 8.9 to yield values of α/k_o that are near to the top of their "periodic" variation, so that wider beams will result. Alternatively, a value of c nearer to 4.5 or 5.7 could have been chosen to achieve narrower beam widths.

The other consideration affecting the choice of stub length is that it should be long enough to effectively reduce to negligible values the power in the cross-polarized field component. That consideration was treated in detail in Chap. VII, Sec. D,1, in the discussion surrounding relations (7.29) to (7.31). For the present antenna dimensions, for the mid-range frequency 50 GHz, we find from (7.29) and (7.31), with the value of β/k_o taken from Fig. 8.8, that the choice $c = 3.12$ mm results in a value of 29.5 dB for the amount of cross-polarized power remaining at the radiating open end, down from its value at the junction between the main and stub guides. That result should be very satisfactory.

The modifications in the values of β/k_o and α/k_o as the frequency is changed are also of interest. We see from Fig. 8.8 that the beam angle will move away from broadside as the frequency is increased. We cannot, however, draw any conclusions

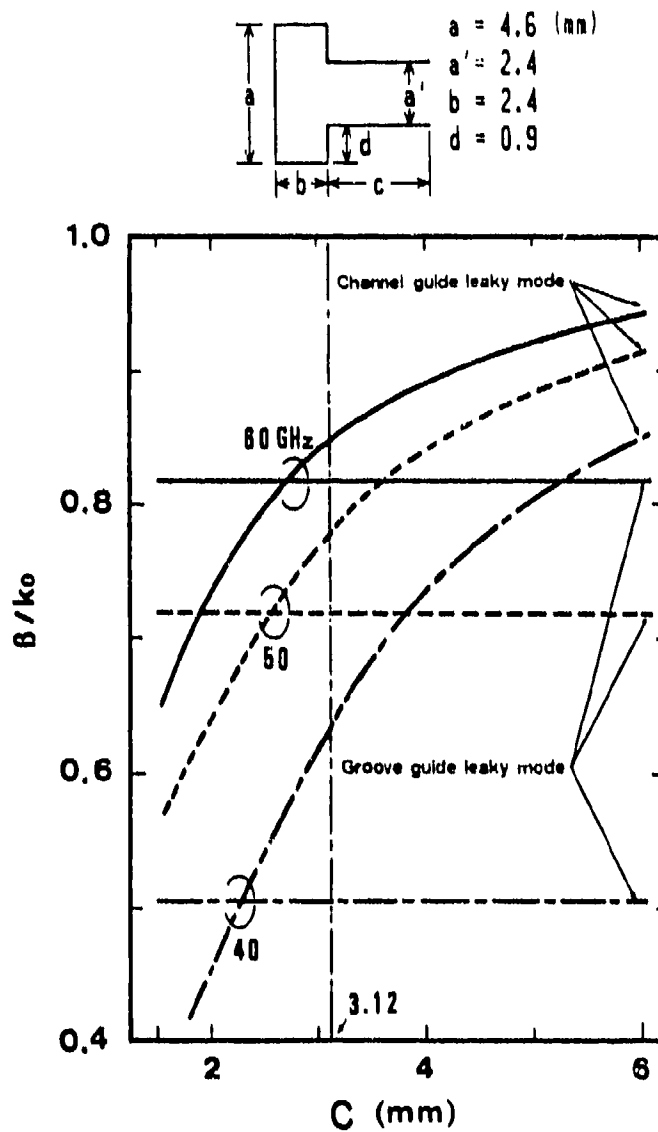


Fig. 8.8

Preliminary theoretical calculations of the normalized phase constant as a function of stub guide length for both the offset-groove-guide and channel-guide leaky modes, for three different frequencies.

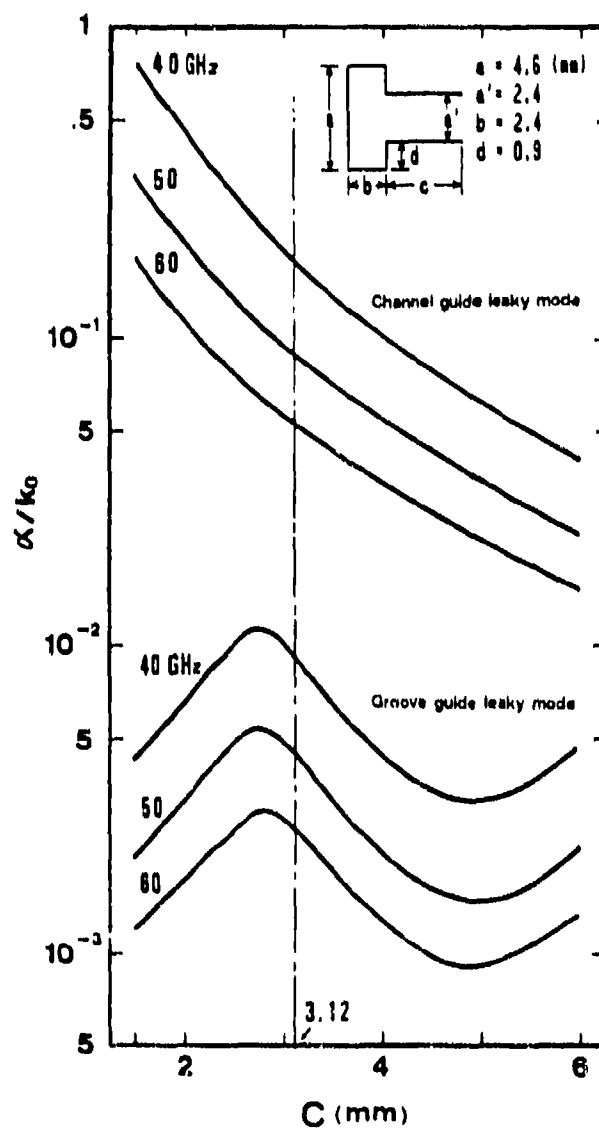


Fig. 8.9 Same as for Fig. 8.8, but for the normalized leakage constant.

regarding the beam widths from the α/k_o values alone. The changes in leakage constant are compensated by the modifications in the phase constant so as to yield a beam width that remains essentially constant with frequency, as is shown below and as we found in Chap. VII for this antenna type. We can assert from Fig. 8.9, however, that the percentage of power radiated from an antenna of fixed length will decrease as the frequency is increased, since both α/k_o and α itself decrease with increasing frequency.

2. Comparisons Between Theory and Measurements

The preliminary theoretical calculations presented in Figs. 8.8 and 8.9 were based on the structure appearing in Fig. 7.18 rather than the one in Fig. 8.1; that is, the structure did not have a flange at the radiating open end. Since those theoretical values were obtained to serve as a guide to design, the precise values were not as important as the behavior trends. Now, however, we wish to make careful comparisons between theoretical values and measured results, so that it becomes necessary to take into account the presence of the *flange*, which alters the numerical values for the wavenumbers by a small amount.

To calculate the values of β/k_o and α/k_o , we may wish to employ the dispersion relation (7.27), together with (7.25) and (7.26). Those relations remain valid, since the only change from the case without a flange to the case with one is that the terms representing G_R/Y_o and B_R/Y_o in (7.26) must be replaced. Those terms relate to the *radiating open end*. When the flange is *absent*, the sketch appropriate to that radiating open end, and the equivalent network representation for it, were given in Fig. 6.6. Rigorous expressions for the elements G_R and B_R in that network are taken from the Waveguide Handbook [8], Sec. 4.6a, pp. 179-183, and are presented in this report in Chap. VI as (6.23) to (6.25), after making the appropriate substitutions in notation.

When the flange is present, new expressions must be sought for G_R/Y_o and B_R/Y_o , and we are fortunate in that they may be found in the Waveguide Handbook, in Sec. 4.7a, on pp. 183-185. The expressions are approximate but accurate, and two sets are given. The more accurate set, corresponding to their equations (1a) and (2a), is

$$\frac{G_R}{Y_o} = \int_0^{k_y a'} J_o(x) dx - J_1(k_y a') \quad (8.1)$$

$$\frac{B_R}{Y_o} = - \int_0^{k_y a'} N_o(x) dx + N_1(k_y a') + \frac{2}{\pi} \frac{1}{k_y a'} \quad (8.2)$$

where the J and N quantities are Bessel's functions of the first and second kinds, and where the following changes in notation were made

$$\begin{aligned} k &\rightarrow k_y \\ b &\rightarrow a' \end{aligned}$$

It should be added that the minus sign appearing before the integral in the expression (8.2) for B_R/Y_o is missing in the Waveguide Handbook due to a typesetter's error.

The simpler set, which is very accurate for $k_y a' < 1$, corresponds to equations (1b) and (2b) there, and becomes

$$\frac{G_R}{Y_o} = \frac{k_y a'}{2} \quad (8.3)$$

$$\frac{B_R}{Y_o} = k_y \frac{a'}{\pi} \ln \left[\frac{e}{\gamma} \frac{\pi}{k_y a'} \right] \quad (8.4)$$

where $e = 2.718$ and $\gamma = 1.781$, after the appropriate substitutions in notation are made. For the values appropriate to our antenna, numbers obtained from (8.3) and (8.4) differ from those from (8.1) and (8.2) by about 10% and 8%, respectively. Expression (8.3) can readily be improved by taking the next set of terms in the small-argument expansions of J_o and J_1 ; it then becomes

$$\frac{G_R}{Y_o} = k_y \frac{a'}{2} - \frac{(k_y a')^3}{48} \quad (8.5)$$

The added cubic term in (8.5) reduces the above-mentioned 10% to 2%, which is a dramatic improvement in our case for such a small correction. Corresponding expansions for the N_0 and N_1 terms are more slowly convergent; taking the cubic terms into account reduces the 8% mentioned above to 6%, which is only a small improvement, and probably not worth the added effort.

Expressions (8.1) and (8.2) or (8.5) and (8.4) may be employed for G_R/Y_0 and B_R/Y_0 in (7.26) and then substituted into dispersion relation (7.27) if one adopts the tee-junction network theoretical approach. Alternatively, one may utilize the mode-matching procedure, which was described in Chap. VII, Sec. C, and shown there to yield numerical values that agreed very well with those obtained using the tee-junction approach. For this alternative approach, these expressions may also represent the radiating open end when it is incorporated into the procedure to yield results for the wavenumbers. The calculations made for comparison with the measured data on the antenna in Fig. 8.1 in fact used the mode-matching procedure.

Measurements of β/k_0 and α/k_0 as a function of frequency were taken using the sliding short technique described in Sec. B. The frequency range was 40 GHz to 60 GHz, and the measured data are shown in Fig. 8.10 as the dark dots. The solid and dashed curves in that figure represent the theoretical calculations, incorporating the modifications above to take the flange into account, for both the desired offset-groove-guide leaky mode and the channel-guide leaky mode.

The first point to note is that the mode that is excited in the antenna is without question the offset-groove-guide mode. We next observe that *very good agreement* has been obtained between the measured and the theoretical values for both β/k_0 and α/k_0 .

3. Design Considerations for Tapered Apertures for Sidelobe Control

It is well known that the sidelobe level and distribution of a leaky-wave antenna can be controlled by appropriately specifying the antenna's aperture distribution. The resulting design customarily requires that the antenna cross-section dimensions be slowly tapered along the antenna's length. The taper in the dimensions corresponds to some specified variation in leakage constant α along the length while simultaneously maintaining the phase constant β the same.

We are not concerned here with the relation between the desired sidelobe configuration and the resultant required taper in α because there are many possible sidelobe requirements and various ways to achieve the tapers in α , and such relations

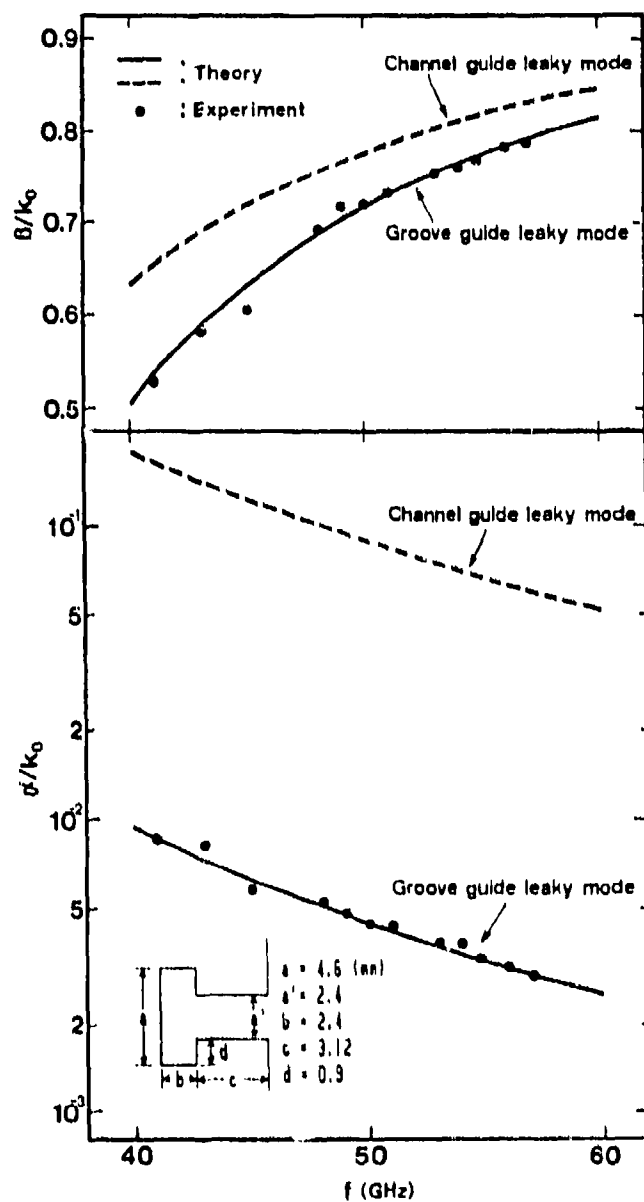


Fig. 8.10

Comparisons of theoretical and measured values for the normalized phase and leakage constants of the offset-groove-guide antenna as a function of frequency from about 40 GHz to 60 GHz.

have been treated in the literature. Our concern here is with the relation between the taper in α and the geometry of the antenna. In particular, the common and customary problem that arises is that when α is varied β changes also, instead of staying the same. We wish to present one way of overcoming this difficulty for the offset-groove-guide leaky-wave antenna.

When the leaky waveguide's cross section is maintained constant along the aperture length (i.e., along the length of the radiating open end, if viewed transversely, or side, if viewed longitudinally), the leakage constant α and the phase constant β are both maintained constant along this length, and the antenna's aperture has exponential amplitude decay and uniform phase progression. For an antenna of finite length, the radiation pattern possesses a high sidelobe level, somewhat akin to that for a uniform amplitude aperture distribution. In order to achieve a much lower sidelobe level, and to shape the sidelobe distribution according to some desired specification, it is necessary to taper the antenna aperture's amplitude distribution, while maintaining its phase progression uniform. The relation between the specified sidelobe performance and the required aperture amplitude distribution is independent of the particular structure of the leaky-wave antenna.

The specific structure of the antenna becomes essential when we apply these considerations to a given type of leaky-wave antenna. Then, we first seek a "best" geometrical parameter to alter in order to vary the value of α in a required way while simultaneously not disturbing β . Usually, however, β also varies a little bit. It then becomes necessary to compensate the small change in β by adjusting some other dimensional parameter, while simultaneously hoping that the α variation is not altered. For a good structure, such as the offset-groove-guide antenna, one iteration is usually sufficient. For some other structures, such as the ultra-simple uniform strip microstrip leaky-wave antenna discussed in Chap. IX, such compensation seems not even possible to achieve because only the strip width is easily accessible, and changing the strip width alters both α and β strongly. Even a good structure can be made *better*, however, if we can design the geometry so that changing some dimension will vary α but not disturb β at all. We show below a design method to do just that for the offset-groove-guide antenna.

If we return to Fig. 7.9 in Chap. VII, we observe that, for an offset-groove-guide antenna of nearly the same cross-section dimensions as the antenna being measured here, the value of α/k_0 can be varied neatly over a very wide range by changing d/a (the amount by which the stub guide is placed off center) but that the value of β/k_0 varies very little. Parameter d is thus the "best" parameter for this purpose. However,

those numbers corresponded to a structure with an infinite stub length. When a corresponding calculation is made for the actual structure in Fig. 8.1, with a finite stub length and a flange at the radiating open end, the resulting curves are shown in Fig. 8.11 for the mid-range frequency of 50 GHz, and in Figs. 8.12 and 8.13 for 40 GHz and 60 GHz.

We note that the behaviors for α/k_o and β/k_o in these figures are qualitatively similar to each other and to those in Fig. 7.9. Also, the distinctions between the behaviors for the offset-groove-guide mode and the channel-guide mode are very similar to those seen in Fig. 7.23 of Chap. VII. The precise numerical values are different because the stub lengths are different for each. For the offset-groove-guide mode, the curves in Fig. 8.11 correspond to a point near the top of the "periodic" variation with stub length, whereas those in Fig. 7.23 correspond to a point near the bottom of that variation. For the channel-guide mode, the different stub lengths seriously affect the numerical values because the curves vary strongly as the stub length c changes (see Figs. 8.8 and 8.9). In addition, dimension a is not quite the same for each structure, and the radiating open ends are somewhat different, the present one with a flange and the earlier one without.

When comparing the curves for β/k_o in Fig. 8.11 and in Fig. 7.9, we see that the one in Fig. 8.11 is less flat, which was initially disappointing. However, the load exerted by the stub guide is different for each, and it becomes clear that the flatness desired in β/k_o can be adjusted by changing other geometrical parameters. With this in mind, we next examined the possibility of obtaining the desired flatness by finding an optimum aspect ratio b/a .

We calculated the variation of β/k_o with b for $d = 0$ (the maximum leakage offset) and for $d = 1.1$ mm (the offset for zero leakage). The results are plotted in Fig. 8.14 for the mid-range frequency of 50 GHz. Since $d = 1.1$ mm corresponds to $d/a = 0.24$, we note that the two extreme values of d for which the computations in Fig. 8.14 are made are the same as the two ends of the abscissa scale in Fig. 8.11. We see in Fig. 8.14 that the two curves cross at the value $b = 4.25$ mm, indicating that if b is set equal to that value the two end points in the β/k_o vs. d/a plot will be identical.

Calculations for that value of b are presented in Fig. 8.15 as the solid lines; the dashed lines correspond to the value of b used in Fig. 8.11. It is seen that β/k_o now appears to be *perfectly flat* when d/a is changed, as we desire. In fact, its value of 0.7395 is constant across the range of d/a to the fourth significant figure. For this set of parameters, therefore, α can be varied gradually as a function of position along the

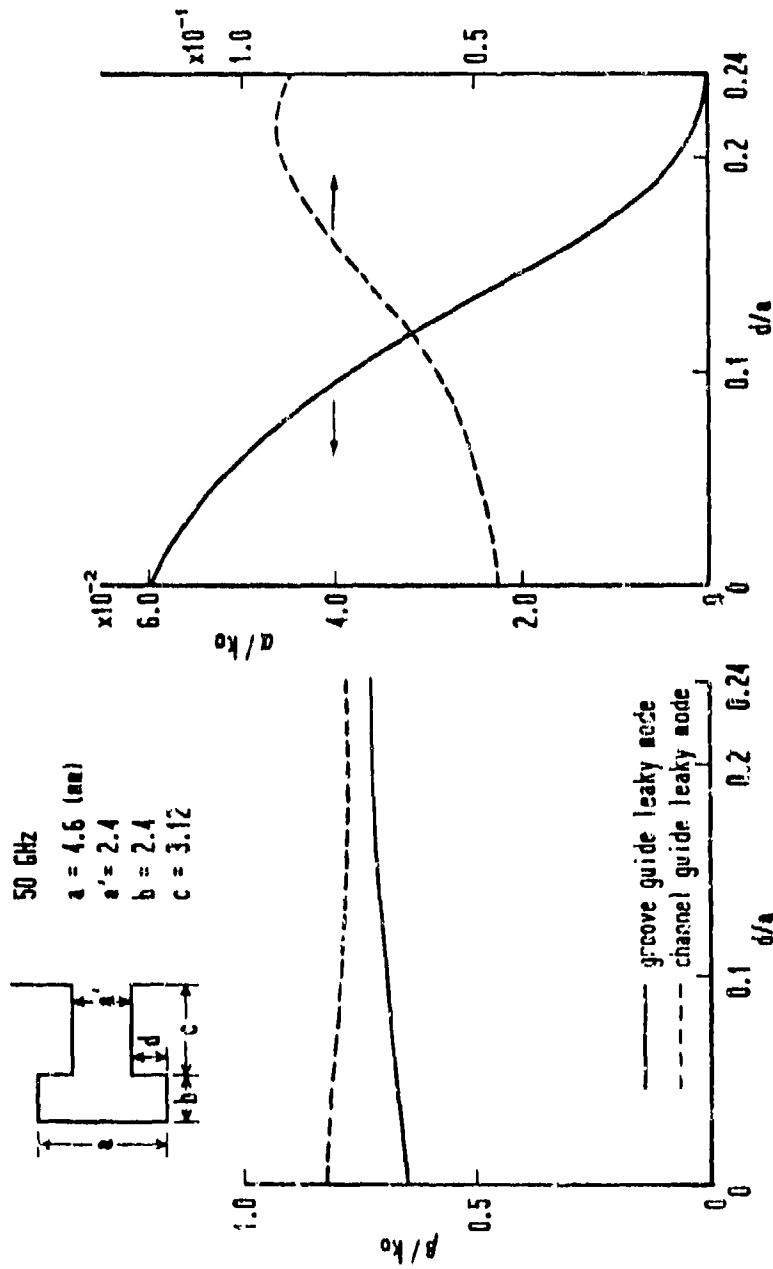


Fig. 8.11 Behavior of the normalized phase and leakage constants as a function of offset stub location at the mid-range frequency of 50 GHz.

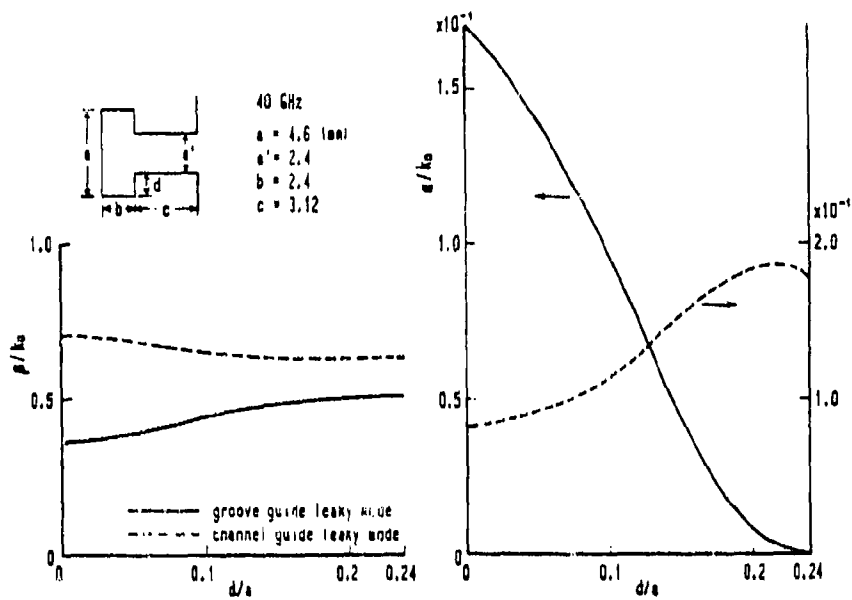


Fig. 8.12 Same as for Fig. 8.11, but at 40 GHz.

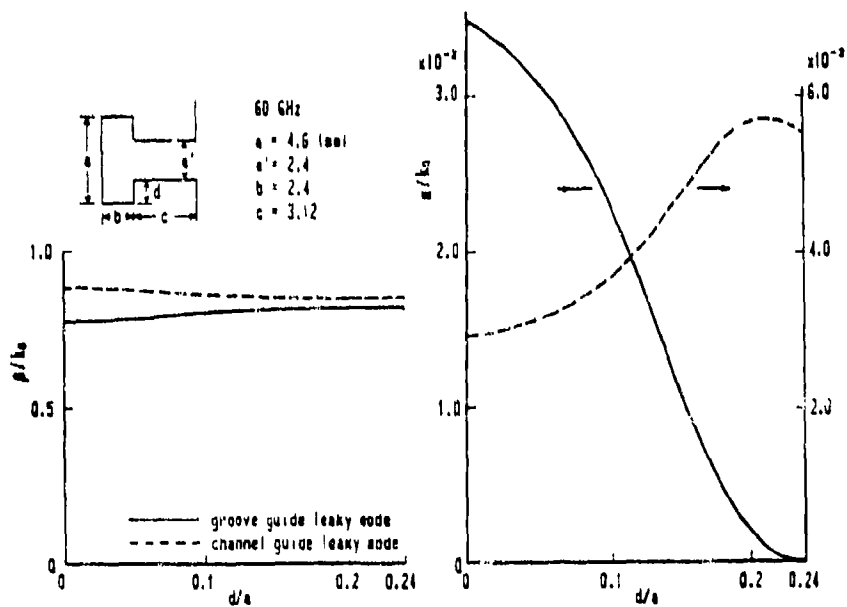


Fig. 8.13 Same as for Fig. 8.11, but at 60 GHz.

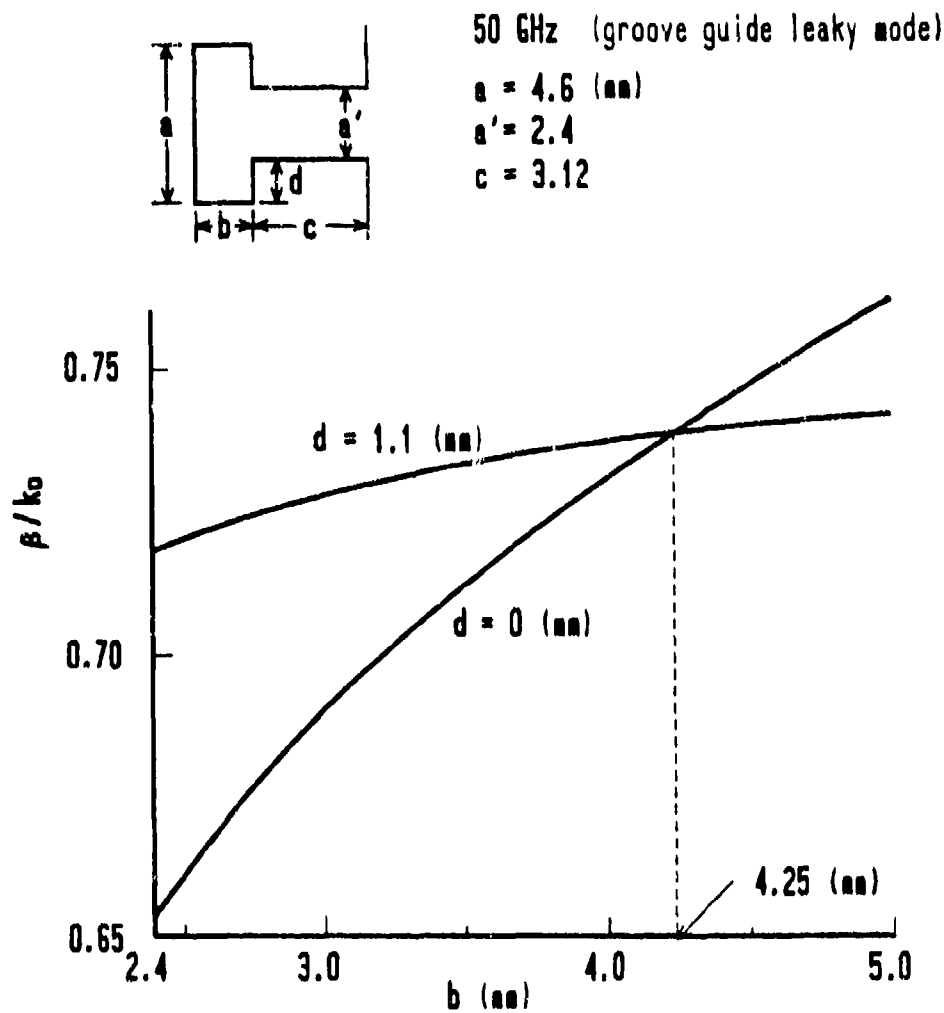


Fig. 8.14 Plots of normalized phase constant as a function of height b of the main guide at 50 GHz for two different stub guide offset positions: $d = 1.1$ mm (no leakage) and $d = 0$ (maximum leakage).

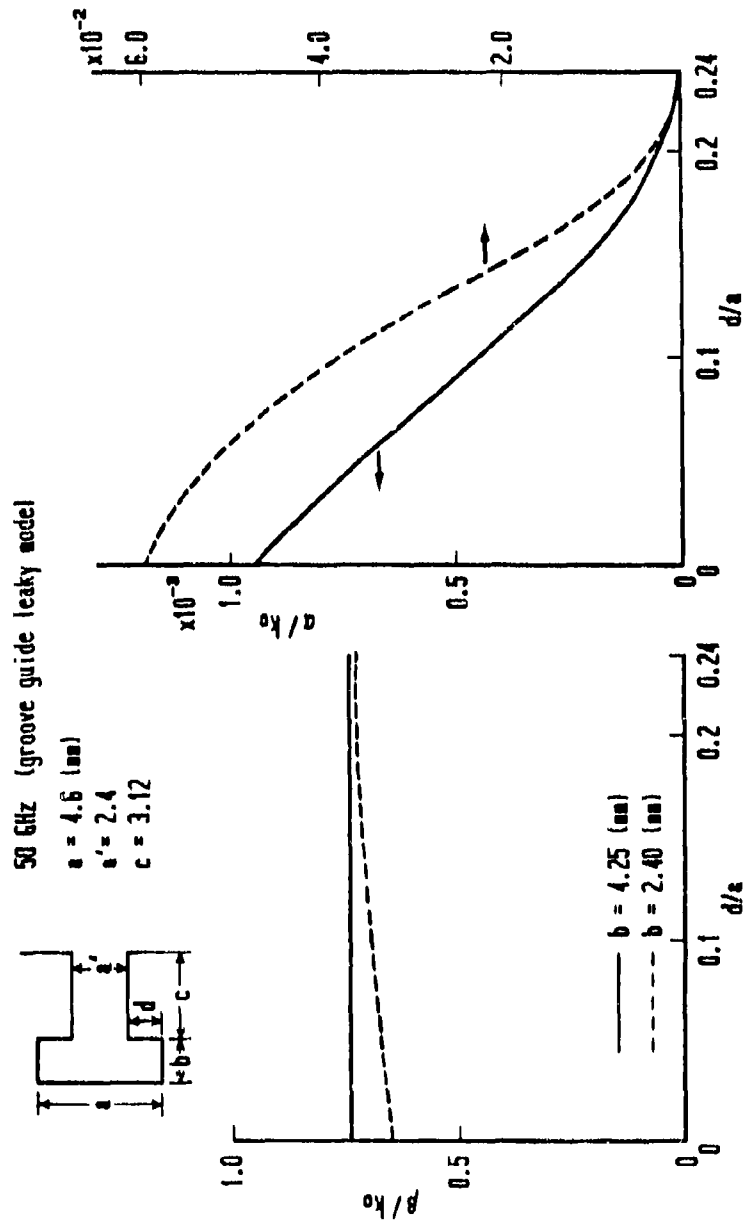


Fig. 8.15 Behavior of normalized phase and leakage constants as a function of offset stub location at 50 GHz, for two different values of main guide height b , showing that for one of them ($b = 4.25 \text{ mm}$, derived from Fig. 8.14) the curve of β/k_0 vs. d/a is perfectly flat.

antenna length in accordance with the design, and β will remain exactly the same, so that no iterations will be required. (Of course, attention must be paid to the transition (perhaps a taper) between the new antenna and the rectangular feed guide.)

Because b/a is fairly large, however, the value of α/k_o is reduced significantly, as one can predict from Fig. 7.5. As a result, this particular design will yield a very narrow beam, about 0.5° at the 3 dB level, if the antenna aperture length is chosen so that 90% of the power is radiated. Alternatively, if the antenna length is maintained at 10 cm, the beam width will remain almost the same as it was before b was increased, but the antenna efficiency will be much lower.

It is highly likely, however, that if some manipulation of the various dimensional parameters is attempted, it will be possible to obtain a similar flat response for β/k_o , but with a larger corresponding value of α/k_o . We have not had any interest in such an optimization, and we have therefore not tried to obtain one. The material above is presented to illustrate the principle, and to imply that the process may indeed be a practical one for a large class of such leaky-wave antennas.

4. Vector Field Distributions

As a byproduct of the mode-matching calculation procedure, we are able to obtain information regarding the electric field strengths and their directions at any interior point in the guiding structure. We therefore prepared a grid with many points, and determined the vector electric field strengths at each of those grid points. The resulting computer-plotted patterns within the leaky waveguide cross section are presented in Figs. 8.16 and 8.17, for the offset-groove-guide leaky mode and the channel-guide leaky mode, respectively, at a frequency of 40 GHz.

It is interesting to see the influence of asymmetry in both of the cases. In Fig. 8.16, for the offset-groove-guide mode, the field distribution in the main guide is clearly similar to what we would expect for the lowest mode in rectangular waveguide; the asymmetric stub guide is seen to produce a small amount of oppositely polarized field which then maintains itself as one moves along the stub guide, while the original polarization content steadily decreases. The leakage rate is small here, however, so that the details of the field at the radiating open end are not very clear. In Fig. 8.17, the channel-guide leaky mode is seen to be very different, with predominantly the opposite polarization, and with a phase reversal in the stub guide. The electric field in the aperture is also quite strong, consistent with the fact that its leakage constant is more than an order of magnitude higher than that for the offset-groove-guide mode. Also, the fields in the vicinity of the junction between the main and stub guides

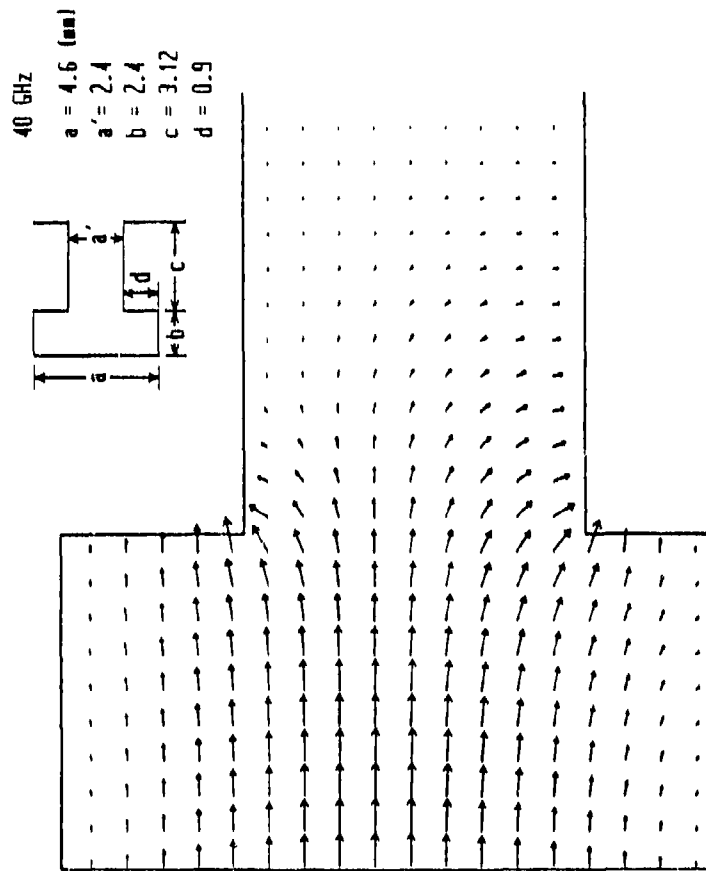


Fig. 8.16 Vector electric field plot for the offset-groove-guide leaky mode, showing the field strengths and the field directions at each point in a grid of many points.

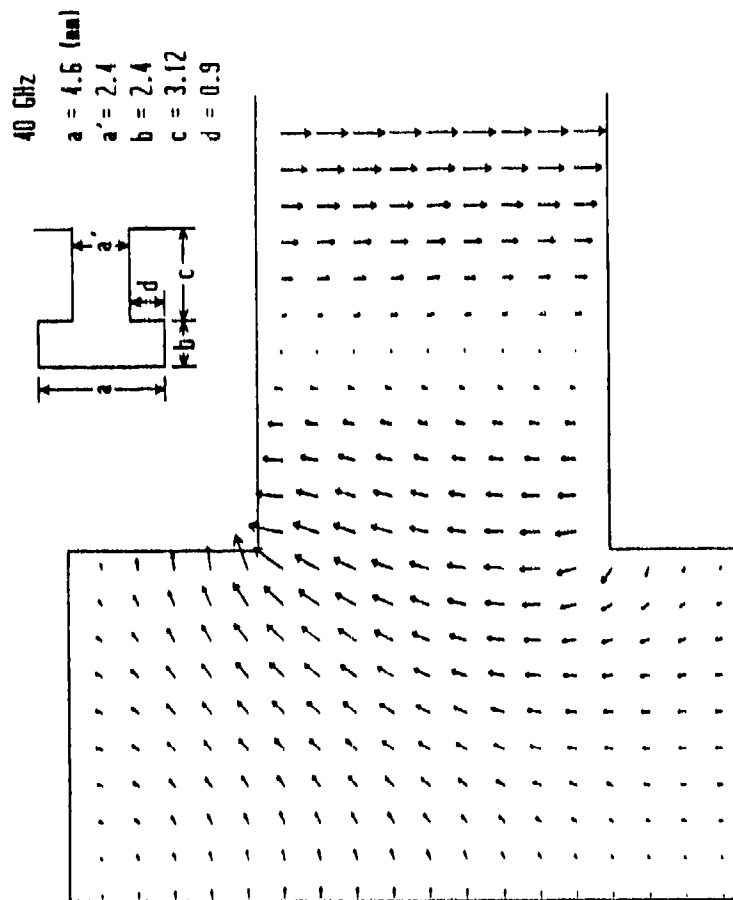


Fig. 8.17 Same as for Fig. 8.16, but for the channel-guide leaky mode.

resemble what one would expect for the dominant mode in parallel-plate guide incident on a transverse change in height. The field lines are disturbed only a little in the stub guide, and the bulk of the field line curvature occurs in the main guide portion.

D. RADIATION PATTERNS

1. Calculations for the Near Field Patterns

It was explained in Sec. B,2 that the experimental set-up available did not permit far-field radiation patterns to be taken, and that it was necessary instead to perform such measurements in the *near field*. The far field was estimated there to be further away than about 300 cm, but that the boom holding the pick-up horn could be placed no further than 30 cm away from the center of the antenna aperture. The 30 cm distance is indicated on the block diagram in Fig. 8.6, and should be clear from the photograph in Fig. 8.7. Before being able to compare measured with theoretical results, we must therefore compute the field patterns one should expect to find in the near field as compared to those in the far field.

For the measurements of the field patterns, we placed a matched load at the end of the antenna aperture. The aperture field distribution along the propagation direction z is thus of the form

$$e^{-j(\beta - j\alpha)z} \quad (8.6)$$

The near field pattern in the principal plane is then given approximately by

$$F(R, \theta) \approx \left| \int_{-L/2}^{L/2} e^{-j(\beta - j\alpha)z} \frac{e^{-jk_0 r}}{r} dz \right|^2 \quad (8.7)$$

where

$$r^2 = R^2 + z^2 - 2Rz \sin \theta \quad (8.8)$$

and the various symbols are defined in the sketch in Fig. 8.18. In the integration, we do not approximate (8.8) for r . From (8.7) and (8.8) we see that the pattern shape should be a function of distance R .

Calculated near field power patterns at 50 GHz as a function of angle θ at several distances R are presented in Figs. 8.19 through 8.22. The various distances R are 30 cm, 50 cm, 70 cm, 100 cm and 200 cm. On each plot there also appears a fine line curve, which represents the *far* field pattern. It is seen that in the near field the sidelobes are higher, the dips fill differently, and the beam width increases a bit. When $R = 200$ cm, in Fig. 8.22, one sees that the differences between the near and far field patterns become greatly reduced, a result that is consistent with our earlier calculation (in Sec. B) that the far field begins at R somewhat greater than 300 cm.

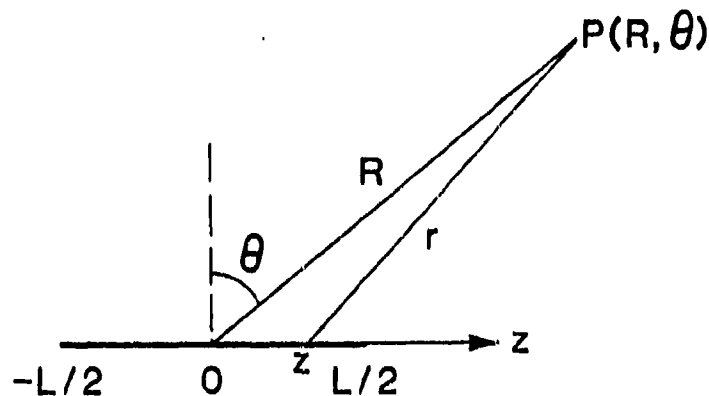


Fig. 8.18 Sketch defining the symbols used in connection with the near field pattern calculations.

2. Comparisons Between Theory and Measurement

Polar plots of the near field patterns at $R = 30$ cm are presented in Figs. 8.23 through 8.27 for a set of different frequencies: 41 GHz, 45 GHz, 50 GHz, 55 GHz and 58 GHz, respectively. The solid lines on these plots represent the theoretical near field calculations based on (8.7) and (8.8); the points correspond to measured results obtained by using the set-up discussed in Sec. B. Also, on the polar plot for 50 GHz in Fig. 8.25 we have included a fine line drawing that corresponds to the far field calculation at that frequency.

Inspection of the plots in Figs. 8.23 through 8.27 reveals that the points agree very well with the theoretical curves. Although both the measured and the theoretical results hold for the near field at the distance $R = 30$ cm, their good agreement suggests that the far field calculations, employing the appropriate α and β values, should also be accurate. These near field plots are also somewhat ugly and it should be clear that the far field patterns are smooth and clean, as one would expect. This statement is borne out by the fine line far field plot appearing in Fig. 8.25.

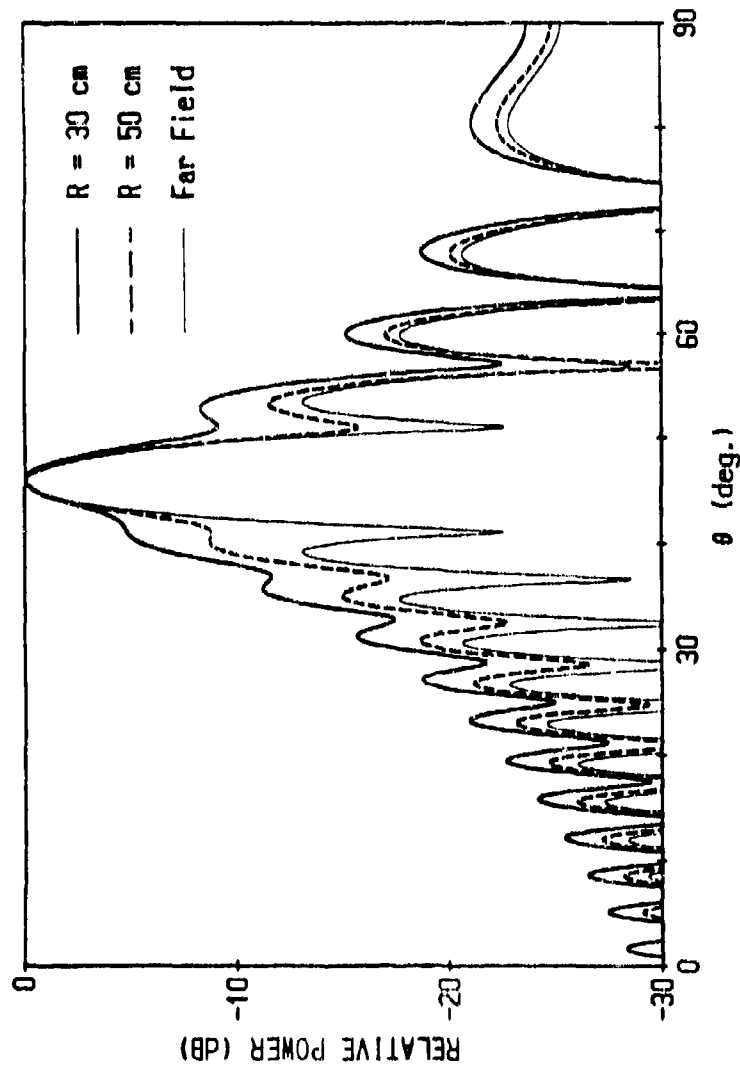


Fig. 8.19 Calculated near field power patterns at the mid-range frequency 50 GHz for several distances R from the antenna. The distances here are 30 cm and 50 cm, and the patterns for them are compared with the far field pattern.

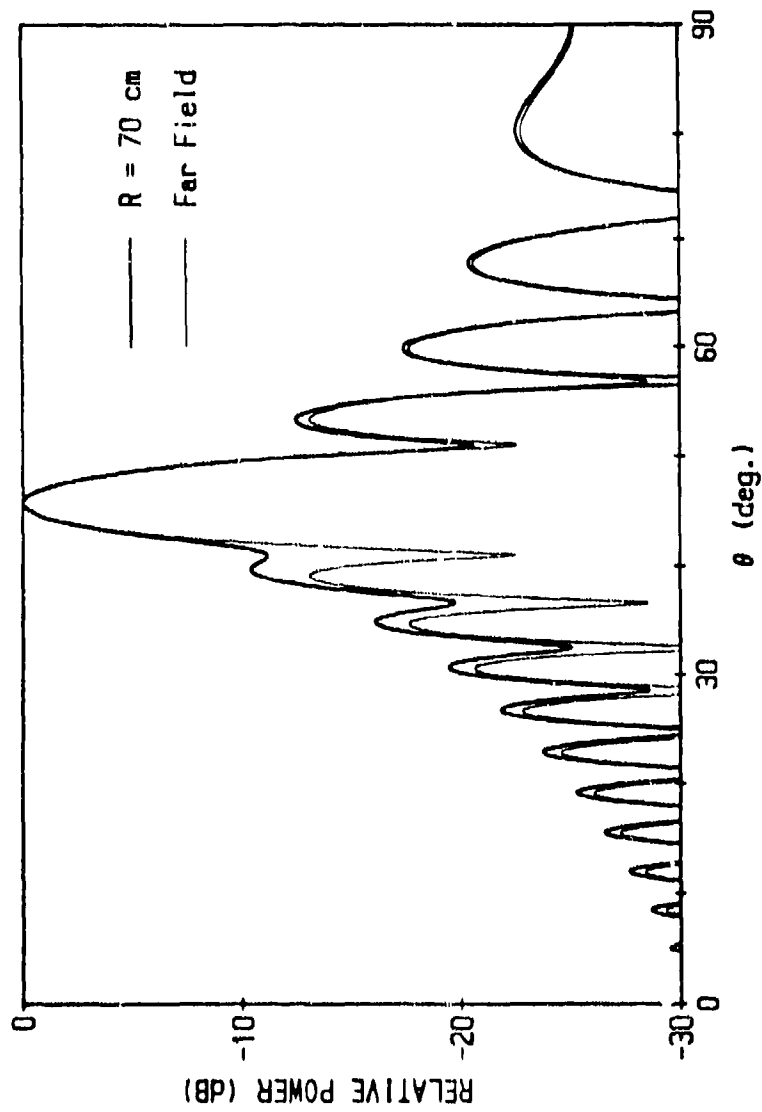


Fig. 8.20 Same as for Fig. 8.19, but for a distance from the antenna equal to 70 cm.

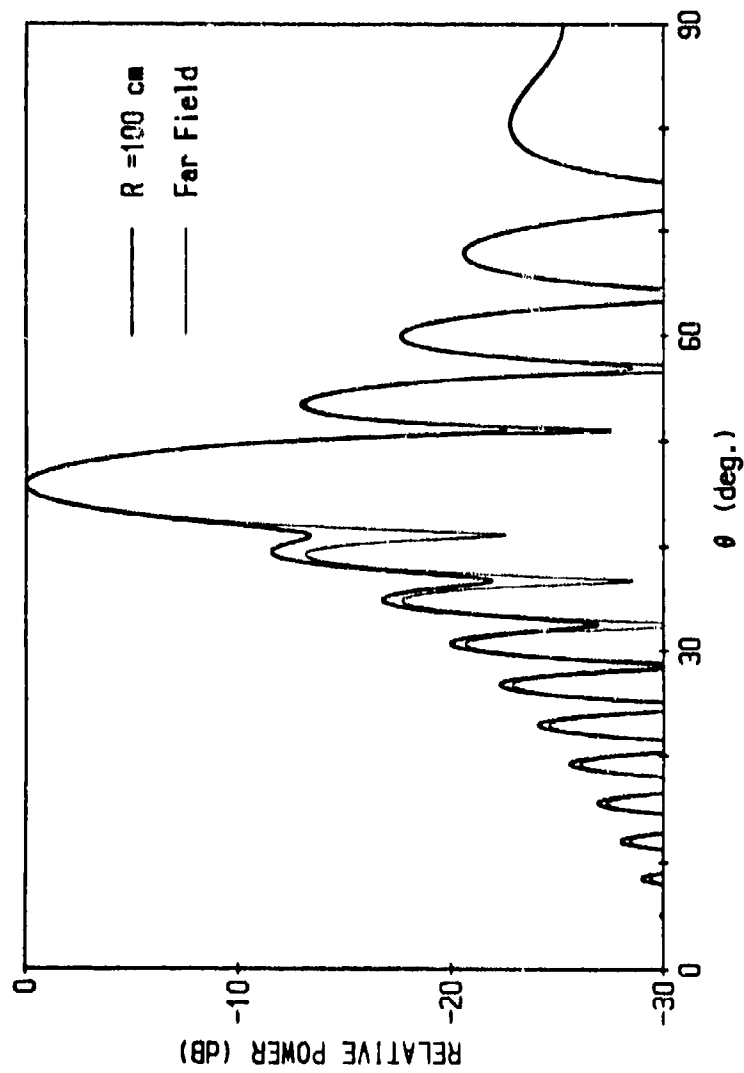


Fig 8.21 Same as for Fig. 8.19, but for a distance from the antenna equal to 100 cm.

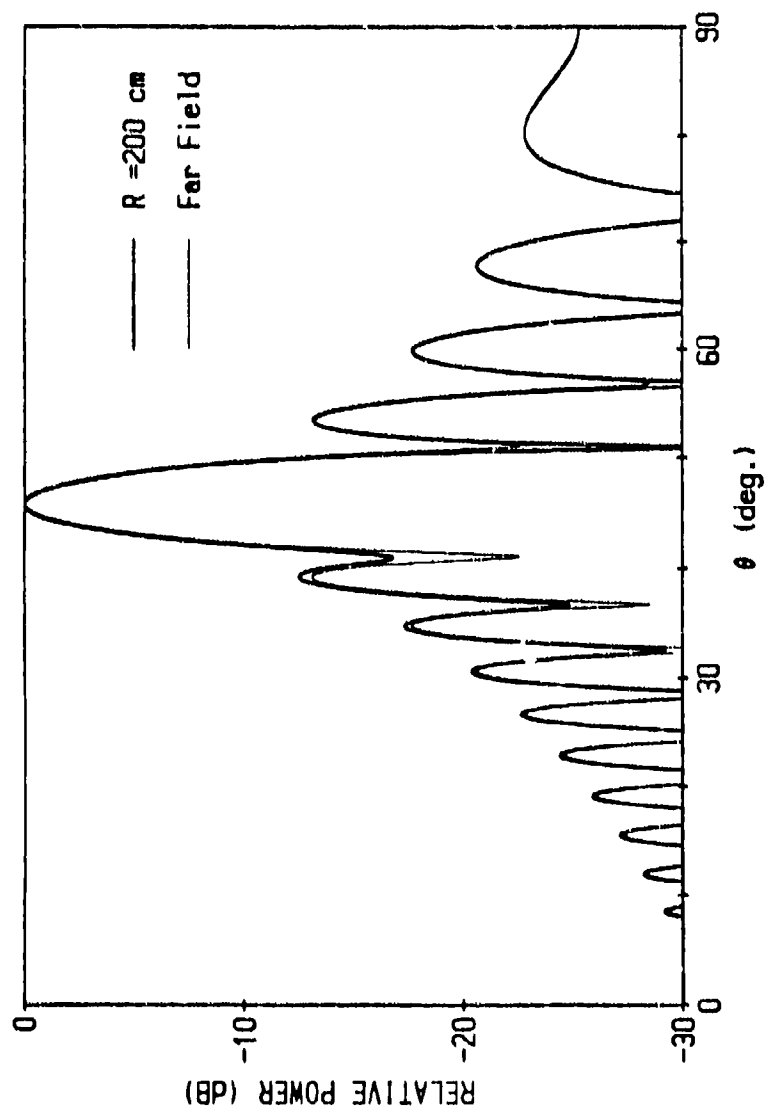


Fig. 8.22 Same as for Fig. 8.19, but for a distance from the antenna equal to 200 cm, approaching the beginning of the far field, which is somewhat over 300 cm.

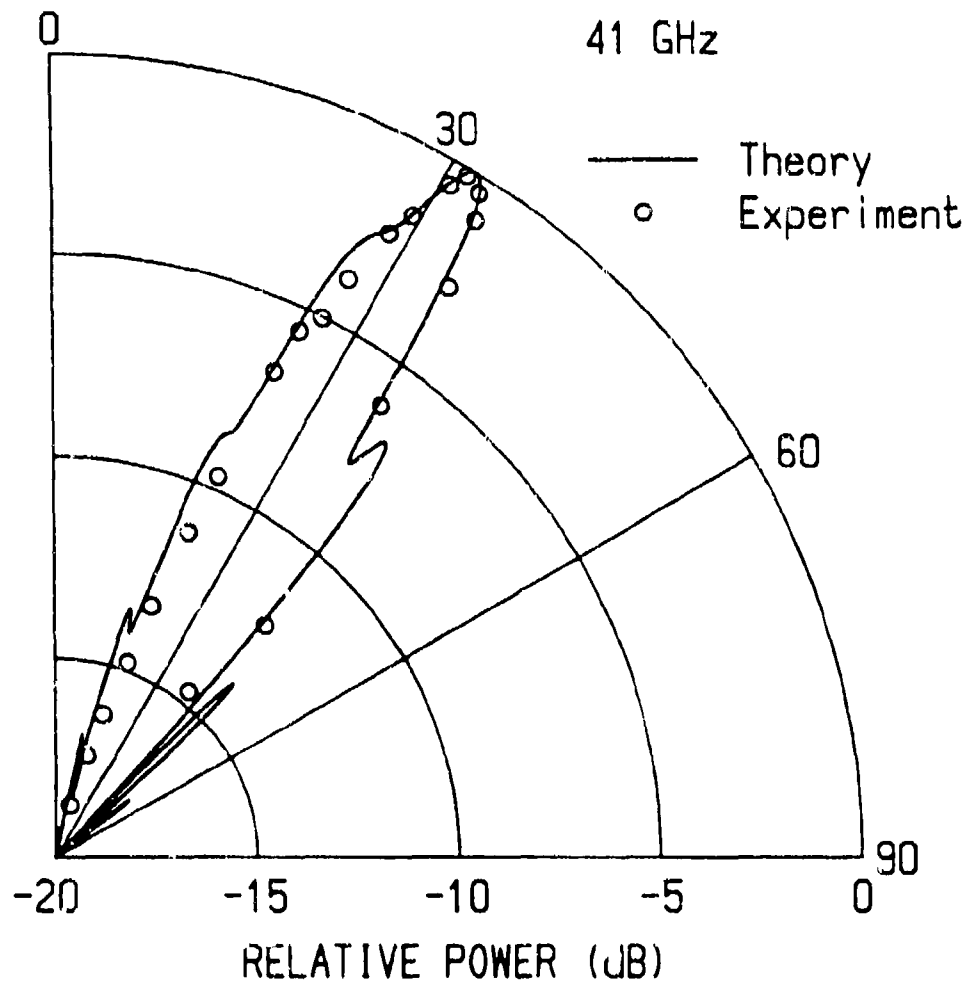


Fig. 8.23

Comparison at 41 GHz between the theoretical near field pattern (solid curve) and measured values (hollow points) employing a polar power plot. The distance from the antenna is 30 cm.

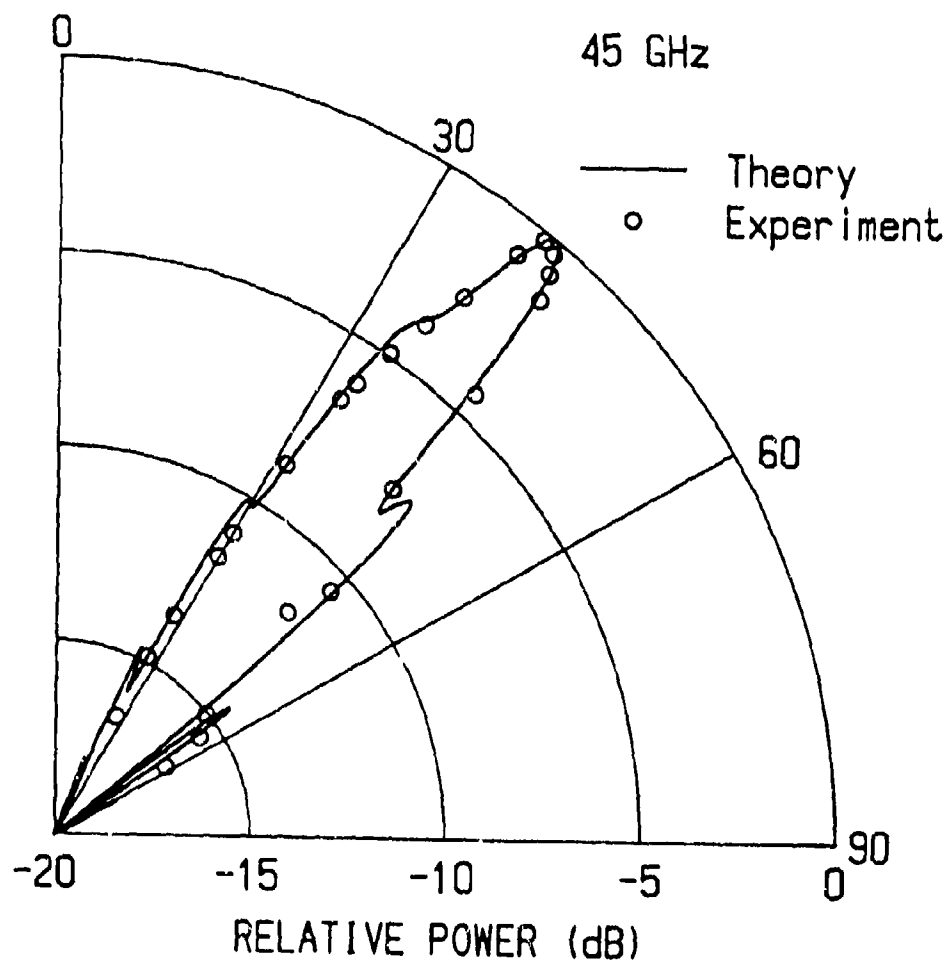


Fig. 8.24 Same as for Fig. 8.23, but for a frequency of 45 GHz.

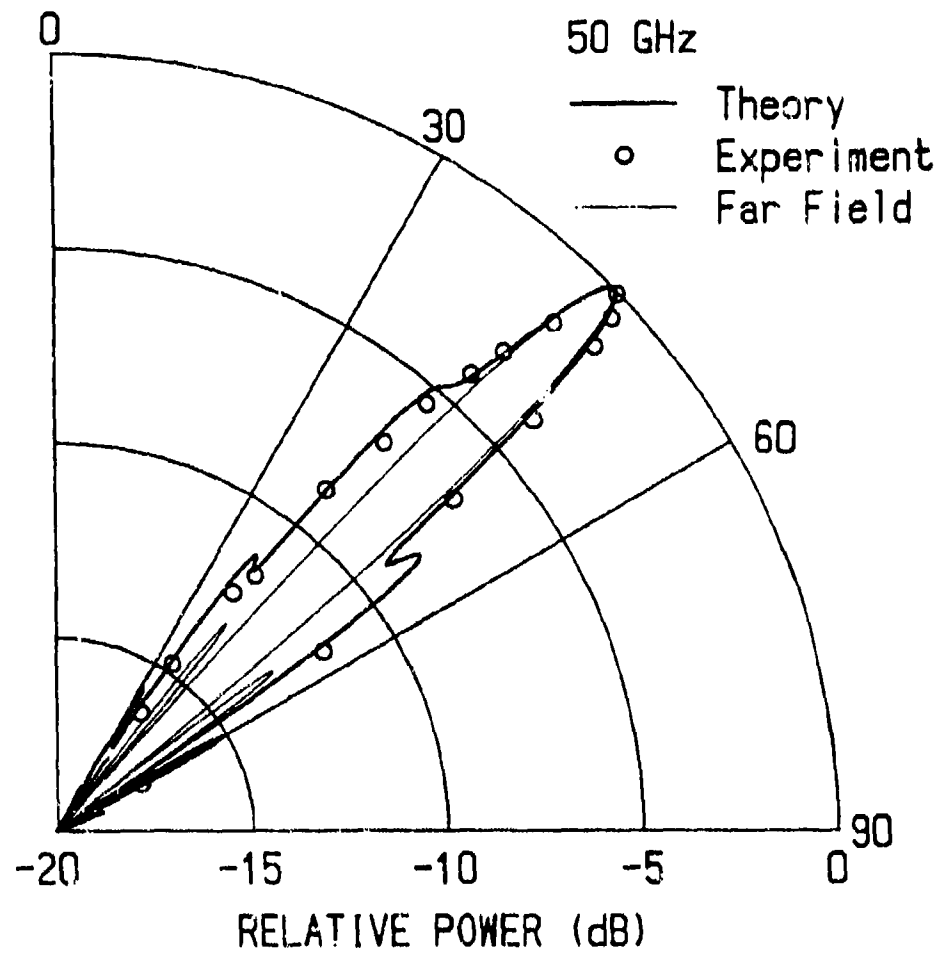


Fig. 8.25

Same as for Fig. 8.23, but for 50 GHz. A fine line curve representing the far field pattern is added here.

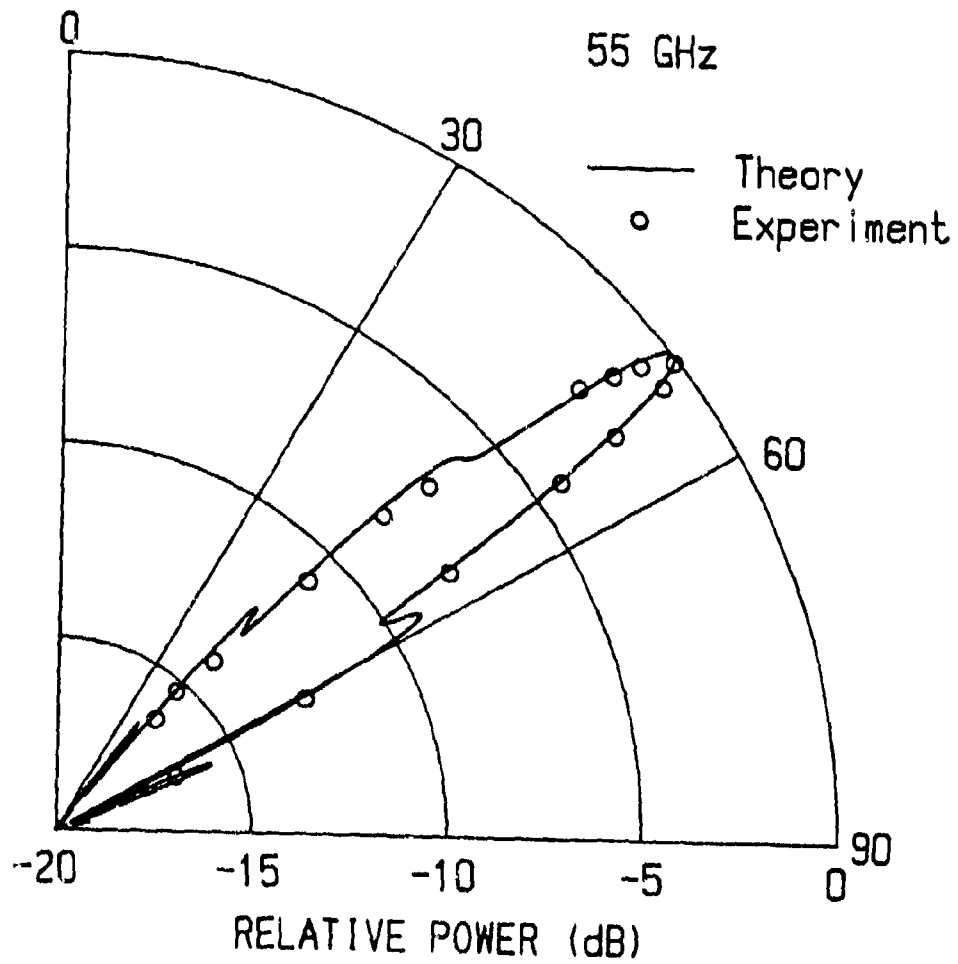


Fig. 8.26 Same as for Fig. 8.23, but for 55 GHz.

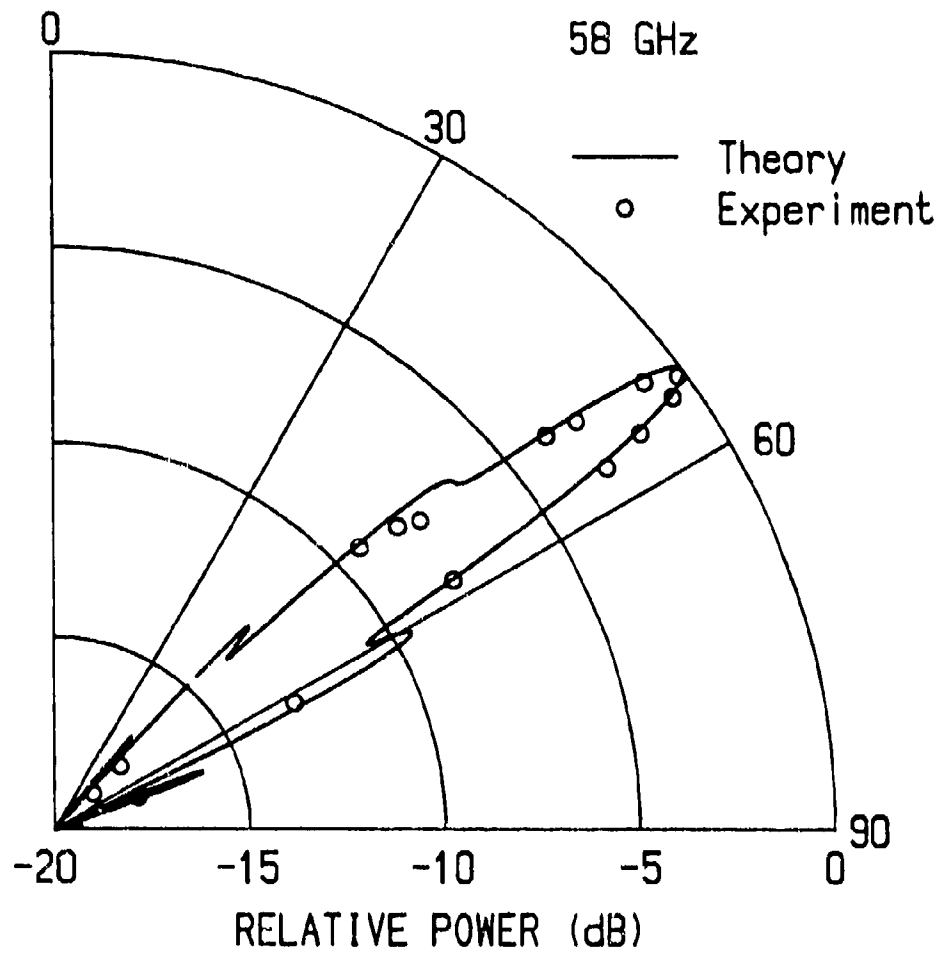


Fig. 8.27 Same as for Fig. 8.23, but for 58 GHz.

The angle θ_m of the maximum of each of these beams is the same as the angle we would find for the far field patterns, as seen from Figs. 8.19 through 8.22 and from Fig. 8.25. That angle can be obtained directly from the polar plots in Figs. 8.23 through 8.27, and it can be calculated from the value of β/k_o making use of the simple relation (2.27) of Chap. II, namely,

$$\sin \theta_m \approx \beta/k_o \quad (8.9)$$

In Fig. 8.28 we present a solid curve representing the theoretical values of θ_m obtained via (8.9) and a set of solid points that correspond to the peaks in the measured patterns in Figs. 8.23 through 8.27. As seen, the agreement is very good.

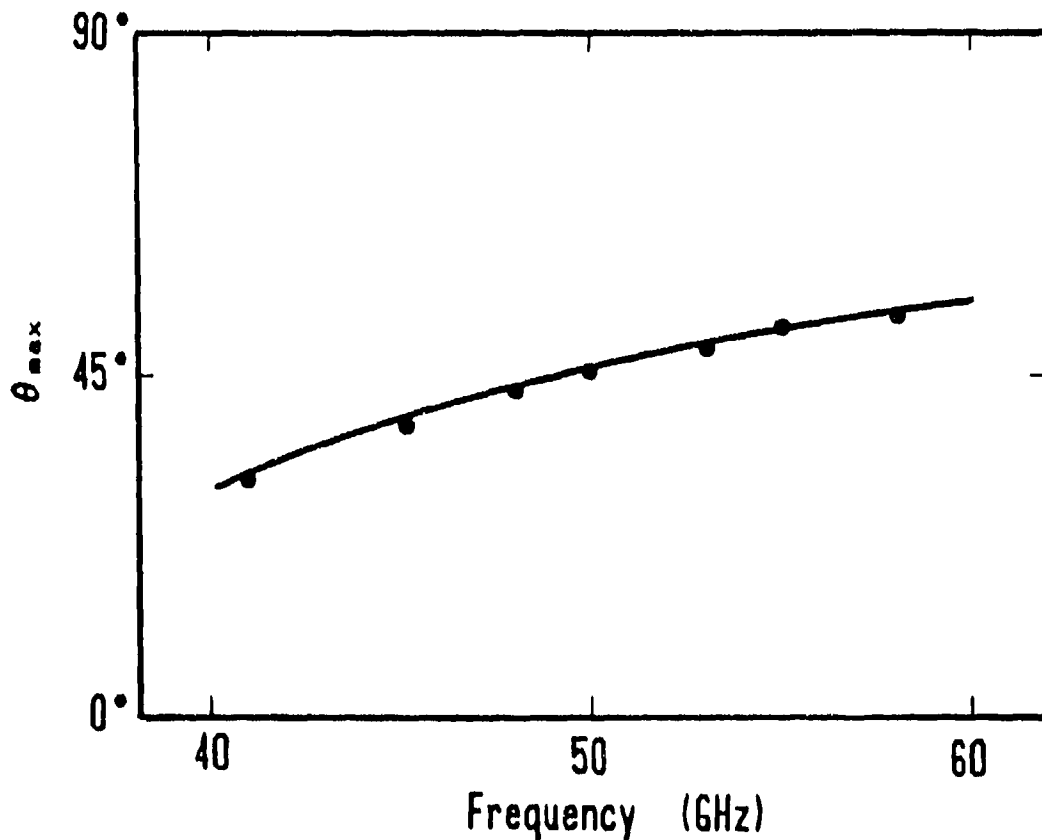


Fig. 8.28

Variation with frequency of the angle θ_m of the beam maximum. The solid line represents the theoretical result and the points correspond to measured values.

Our final concern is with the beam width $\Delta\theta$ of the far field pattern. The measured results apply only to the near field patterns, for which the beam widths are a bit larger than those for the far field patterns, as seen in Figs. 8.19 and 8.25. However, one way to determine the beam width is to examine the 3 dB level of the calculated far field pattern. A second way is to make use of the simple approximate formula (2.28) in Chap. II, which, modified slightly, is

$$\Delta\theta \approx \frac{52.1}{(L/\lambda_o) \cos \theta_m} \quad (8.10)$$

with $\Delta\theta$ in degrees.

Table 8.1 compares results for θ_m and $\Delta\theta$ derived in two different ways, and presented for three different frequencies. The results appearing under column A are calculated using the simple expressions (8.9) and (8.10); the values under column B are obtained from the calculated far field patterns. The values for beam angle θ_m appear to agree exactly, to 0.1° . The beam widths $\Delta\theta$ are also very close to each other, differing by less than 0.1° . Presumably, the values under column B, corresponding to the far field patterns, are slightly more accurate than the ones under column A, which employed the approximate expression (8.10).

It should also be noted that the values of $\Delta\theta$ remain *essentially constant* over this frequency range from 40 GHz to 60 GHz. In Chap. VII, Sec. B,3, it is shown that for the offset-groove-guide antenna, since only one medium is present, the transverse wavenumber is independent of frequency; therefore, if the beam angle θ_m is scanned by varying the frequency, the value of the beam width should remain almost exactly constant. A simple proof is presented there.

Table 8.1

Comparison of results for beam angle θ_m and beam width $\Delta\theta$, derived in two different ways and presented for three different frequencies. The numbers in columns A are computed using the simple formulas (8.9) and (8.10), whereas those in column B are obtained from the calculated far field patterns. Corresponding values are seen to agree within 0.1° .

f (GHz)	A		B	
	θ_m	$\Delta\theta$	θ_m	$\Delta\theta$
40	30.3°	4.53°	30.3°	4.49°
50	45.8°	4.49°	45.8°	4.40°
60	54.6°	4.49°	54.6°	4.40°



MISSION of Rome Air Development Center

RADC plans and executes research, development, test and selected acquisition programs in support of Command, Control, Communications and Intelligence (C³I) activities. Technical and engineering support within areas of competence is provided to ESD Program Offices (POs) and other ESD elements to perform effective acquisition of C³I systems. The areas of technical competence include communications, command and control, battle management information processing, surveillance sensors, intelligence data collection and handling, solid state sciences, electromagnetics, and propagation, and electronic reliability/maintainability and compatibility.